Monitoring Snow Cover and Snowmelt Dynamics and Assessing their Influences on Inland Water Resources

Dissertation

zur Erlangung des Doktorgrades
der Mathematisch-Naturwissenschaftlichen Fakultät
der Christian-Albrechts-Universität zu Kiel

vorgelegt von
Ya-Lun S. Tsai

München, 2021

First examiner: Prof. Dr. Natascha Oppelt
Second examiner: Dr. Andreas Dietz

Date of the oral examination: 19.01.2021

Table of contents

Acknowledgments

Firstly, I would like to thank my family, including mother Pearl, sister Mia, and father Henry, for supporting me studying abroad to achieve the doctoral degree. Without your great support in both mental and financial aspects, it would be impossible for me to survive during my struggling period and finish this dissertation. You are the heroes behind the scenes, and all deserve a big and warm hug!

I also want to sincerely thank my supervisor at Kiel University, Prof. Dr. Natascha Oppelt, for granting me the opportunity to explore this exciting yet challenging topic. Moreover, I greatly appreciate your kind helping and detailed response to my concerns during my PhD studying period.

Special thanks go to my mentor and supervisor in the German Remote Sensing Data Center (DFD) of the German Aerospace Center (DLR), Dr. Andreas Dietz and Prof. Dr. Claudia Kuenzer. Your kind guidance and valuable feedbacks are the key foundation of this dissertation. It is a pleasure to work in a great team and department.

I would also like to thank my dear colleagues of the LAX Cryo-team, including Mariel Dirscherl, Jonas Köhler, Peter Friedl, Sebastian Rößler, Zhongyang Hu, Celia Baumhoer, and Sabine Baumann. I enjoy the interesting and insightful discussions with you and have learned a lot from you. You also make me enjoy the time in the DLR and Germany!

Moreover, other LAX colleagues/friends have also greatly inspired me, including Soner Uereyen, Thorsten Hoeser, Igor Klein, Anna Wendleder, Marco Ottinger, Daniela Palacios-Lopez, Stefan Mayr, Emmanuel Da Ponte, Aiym Orynbaikyzy, Birgit Wessel, Tejas Bhagwat, Felix Reuß, and Sophie Reinermann. It is always happy for me to discuss and collaborate with you. I will miss the fun we shared and the beer we drank together.

I would like to sincerely thank Prof. Dr. Stephan van Gasselt for your countless great support since the first day I arrived in Germany. Your suggestions are always wise and helpful. Thanks for all those sincere help and supports, I would always keep in mind. The kind and generous support from the German Academic Exchange Service (DAAD) is also sincerely appreciated.

Finally, I want to thank myself for being hard-working and diligent for all these years. You have always been trying to make all efforts, especially in doing research, as you are very enthusiastic about figuring out questions and exploring the solutions. I wish you all the best in the future and achieve your dream goal – *being a great scientist!* :D

Summary

Snow is one of the most vital cryospheric components owing to its wide coverage as well as its unique physical characteristics. It not only affects the balance of numerous natural systems but also influences various socio-economic activities of human beings. Notably, the importance of snowmelt water to global water resources is outstanding, as millions of populations rely on snowmelt water for daily consumption and agricultural use. Nevertheless, due to the unprecedented temperature rise resulting from the deterioration of climate change, global snow cover extent (SCE) has been shrinking significantly, which endangers the sustainability and availability of inland water resources. Therefore, in order to understand cryo-hydrosphere interactions under a warming climate, (1) monitoring SCE dynamics and snowmelt conditions, (2) tracking the dynamics of snowmelt-influenced waterbodies, and (3) assessing the causal effect of snowmelt conditions on inland water resources are indispensable. However, for each point, there exist many research questions that need to be answered. Consequently, in this thesis, five objectives are proposed accordingly.

Firstly, to continuously monitor SCE, synthetic aperture radar (SAR) has gained more attention thanks to its cloud-penetrating and illumination-independent sensing ability compared to conventionally employed multi-spectral sensors, which are inevitably affected by cloud cover and polar darkness. Therefore, since the launch of the first continuously revisiting spaceborne SAR satellite in 1991, there have been many studies that explore the potential of using SAR for SCE detection. However, no comprehensive review was conducted. Hence, a holistic overview of existing SAR-based SCE mapping studies is provided in this thesis, which thoroughly examines the unique interactions between SAR signal and wet/dry snowpack and investigates the advantages, limitations, and trajectory of previous studies. It is found that the topic is still in a developing stage, since most studies only detect wet snow of small regions based on backscatter-based approaches, mask out the vegetated regions, and rarely validate their results. Thus, the need for a novel SCE mapping strategy is compelling.

Consequently, the second objective of this thesis is to propose a new total and wet SCE mapping strategy which is applicable in all land cover classes. The freely accessible Sentinel-1 SAR imagery is employed to derive observations including backscatter coefficient, interferometric coherence, as well as polarimetric parameters. Together with topographical factors and land cover information, an easy tuning machine learning classifier is used to detect the total SCE. Via comprehensive validations, results show that the overall accuracy, F-measure and AUC score of total SCE mapping accuracy for different land cover types (including densely vegetated forest and agricultural regions) can reach around 80%, 80%, and 70% respectively for the majority of study regions located in different mountain ranges. The accuracy can be even higher by around 5% if vegetation land cover classes are excluded. These

values confirm the robustness of the proposed land cover-dependent total SCE mapping approach. In addition, by extending the mapped total SCE with wet SCE estimated with a backscatter-based approach, SCE dynamics of different months can be revealed.

To improve SCE mapping accuracy, in the third objective, the benefits of employing vegetation indexes (leaf area index (LAI) and fractional vegetation cover (FVC)) as well as land surface temperature (LST) derived from the PROBA-V satellite and MODIS sensors, are examined. Results show that the overall accuracy, F-measure, and AUC score can be enhanced to around 90%, 90%, and 80% for all five study areas. Namely, the robustness and reliability of both proposed SAR-observation-only strategy and SAR-multi-spectral fusing strategy can be attested. Therefore, by applying the novel approach, the SCE dynamics of the whole Alps during the melting season of 2018 are clearly depicted. Moreover, based on the newly generated SCE mapping reliability maps, a relationship between densely vegetated land cover classes and lower classification reliability is found and discussed.

To fulfill the final goal of assessing the influence of snowmelt conditions on water resources, the fourth objective is to continuously track inland waterbody dynamics. The new generation spaceborne Sentinel-1 SAR and Sentinel-3 altimetry data are employed for water extent delineation and water level measurement of both the Urmia Lake and the Brahmaputra River, respectively. These publically accessible, high-resolution, cloud-free, and illumination-independent data overcome the limitations of few sites available-only in-situ gauging stations and cloud-contaminated multi-spectral sensor band-based water indexes which were commonly used in previous studies. Moreover, the utilization of freely accessible and cloud-based online SAR and altimetry data processing services guarantees high efficiency and broad applicability. Via comparisons with multi-spectral sensor-based water-covered area products and well-known water level databases, the accuracies of our estimated surface area and water level are ensured. Finally, by fusing both observations, comprehensive inland waterbody dynamics can be achieved, such as the hypsometry-based water volume change of the Lake Urmia as well as the flooded area and water level of the Brahmaputra River.

Finally, for the last objective of the present thesis, the tracked inland waterbody dynamics together with the wet SCE mapped with SAR imagery are exploited to examine the causal effects of snowmelt conditions on inland water resources. To unbiasedly quantify their interaction, rainfall and evapotranspiration records provided by the global weather model are included to mitigate the omitted error. Methodologically, the advanced DLM regression, firstly developed in the econometrics discipline, is employed due to its ability to handle multi-variables dynamics influences with temporal lags. In the lag length decision analysis, it is found that the snowmelt conditions show the longest lag length due to the unique characteristics of the SAR-based snowmelt detection approach. Eventually, the casual effect of snowmelt

conditions on inland water resources is quantified and the cryo-hydrosphere interactions can be identified. For the Lake Urmia, when increasing one percent of WSCE% during the period of zero to 80 days before, the detrended water volume would increase by 108 cubic meters; for the Brahmaputra River, when increasing one percent of WSCE% during the period of 70 to 150 days before, the water level of the investigated virtual station would increase by 0.1 meters.

Zusammenfassung

Die globale Schneebedeckung ist, aufgrund ihrer großen zusammenhängenden Flächen sowie ihrer einzigartigen physikalischen Eigenschaften, eine der wichtigsten Komponenten der Kryosphäre. Sie beeinflusst nicht nur das Gleichgewicht zahlreicher natürlicher Systeme, sondern auch verschiedene sozioökonomische Aktivitäten des Menschen. Insbesondere die Schneeschmelze ist sehr bedeutend für die globalen Wasserressourcen. Zum einen deckt sie für Millionen von Menschen den Bedarf für ihren täglichen Wasserverbrauch und zum anderen ist sie in vielen Regionen der Erde essenziell für die Erzeugung von Nahrungsmitteln. Der mit dem Klimawandel einhergehende Temperaturanstieg hingegen bewirkt einen signifikanten Rückgang der globalen Schneedecke. Dies wiederum gefährdet sowohl die Nachhaltigkeit als auch die Verfügbarkeit inländischer Wasserressourcen. Um das Verständnis der Interaktionen von Kryosphäre und Hydrosphäre unter Berücksichtigung des sich erwärmenden Klimas zu gewährleisten und zu verbessern, ist (1) die Überwachung von Dynamiken der Schneedecke und Schneeschmelze, (2) die Quantifizierung von Veränderungen von Wasserflächen bedingt durch die Schneeschmelze, sowie (3) die Bewertung von Kausalitäten zwischen Schneeschmelze und Wasserressourcen von großer Bedeutung. Die Untersuchung dieser Aspekte erfordert die Berücksichtigung vieler Forschungsfragen. Folglich ergeben sich fünf wissenschaftliche Zielstellungen, die im Rahmen dieser Forschungsarbeit aufgegriffen werden.

Erstens, hat sich Radar mit synthetischer Apertur (SAR) für ein kontinuierliches Monitoring der Schneedecke als geeignetes Instrument erwiesen. SAR Systeme liefern Bildaufnahmen der Erdoberfläche unabhängig von Witterungsbedingungen sowohl bei Tag als auch bei Nacht. Im Vergleich zu optischen Fernerkundungsinstrumenten liefern SAR Sensoren auch bei einer geschlossenen Wolkendecke Aufnahmen der Erdoberfläche. Daher wurde bereits seit dem Start der ersten satellitengestützten SAR Mission im Jahr 1991 das Potential von bildgebenden SAR Systemen zur Überwachung der Schneebedeckung in zahlreichen Studien erforscht. Um einen ganzheitlichen Überblick über die bestehenden Methoden zur Kartierung der Schneebedeckung zu liefern, werden in dieser Forschungsarbeit bereits durchgeführte Studien hinsichtlich der Potentiale und Limitierung von SAR Systemen sowie die Wechselwirkungen zwischen dem SAR Rückstreuungskoeffizienten und der trockenen und nassen Schneedecke untersucht. Die Literaturarbeit hat ergeben, dass sich die Methodenentwicklung zur Kartierung der Schneebedeckung mit SAR Sensoren noch nicht ausgereift ist. Ein Großteil der untersuchten Studien hat nur Nassschnee in kleineren Regionen auf der Grundlage des SAR Rückstreuungskoeffizienten klassifiziert. Zudem wurden vegetationsbedeckte Flächen häufig maskiert und die Ergebnisse selten validiert. Daher ist die Entwicklung einer neuartigen Methode zur Kartierung der Schneebedeckung mit SAR Daten zwingend notwendig.

Folglich besteht das zweite Ziel dieser Arbeit darin, eine neue Methode zu entwickeln, die zwischen der gesamten und der nassen Schneedecke unterscheiden kann sowie über alle Landbedeckungsklassen hinweg anwendbar ist. Zu diesem Zweck werden die frei zugänglichen Sentinel-1 SAR Aufnahmen genutzt. Neben dem Rückstreuungskoeffizienten wird die interferometrische Kohärenz sowie weitere polarimetrische Parameter berechnet. Des Weiteren werden neben SAR Parametern zusätzlich topographische Metriken sowie Informationen zur Landbedeckung in einen Machine Learning Algorithmus eingespeist um die gesamte Schneedecke zu klassifizieren. Durch umfassende Validierungsmethoden haben die Ergebnisse für verschiedene Landbedeckungsklassen (einschließlich dichte Waldflächen und landwirtschaftliche Nutzflächen) eine Gesamtgenauigkeit von 80 %, einen F-Maß von 80 % und einen AUC-Wert von 70 % für die gesamte Schneedecke ergeben. Hierbei liegt ein Großteil der Untersuchungsgebiete in Gebirgsregionen. Weiterhin ist anzumerken, dass sich die Gesamtgenauigkeit um etwa 5 % erhöht, wenn die Vegetationsklassen nicht berücksichtigt werden. Diese Metriken bestätigen die Robustheit der vorgestellten Methodik zur Erfassung der gesamten Schneebedeckung unter Berücksichtigung diverser Landbedeckungsklassen. Darüber hinaus gewährleistet die entwickelte Methode, die zwischen der gesamten und nassen Schneedecke unterscheiden kann, eine ganzheitliche Untersuchung der Schneedeckendynamiken über verschiedene Zeiträume.

Die dritte Zielstellung dieser Arbeit umfasst die erzielten Genauigkeiten der vorgestellten Methode zur Schneedeckenklassifikation zu verbessern. Zu diesem Zweck wird die zusätzliche Verwendung von Vegetationsindizes (Blattflächenindex (LAI) und partielle Vegetationsbedeckung (FVC)) sowie die vom PROBA-V und MODIS Sensoren abgeleitete Landoberflächentemperatur (LST) untersucht. Die Ergebnisse haben gezeigt, dass die Gesamtgenauigkeit (90 %), das F-Maß (90 %) und der AUC-Wert (80 %) für alle fünf Untersuchungsgebiete höher ausgefallen sind. Diese Werte bestätigen die Robustheit und Zuverlässigkeit des vorgeschlagenen SAR basierten Ansatzes sowie des fusionsbasierten Ansatzes, bestehend aus SAR und optischen Parametern. Der verbesserte Ansatz wurde daher auf die gesamte Alpenregion angewendet um die Schneedeckendynamiken während der Schmelzsaison 2018 zu analysieren. Außerdem wird auf Basis von zusätzlich erstellten Wahrscheinlichkeitskarten zur Schneedeckenklassifikation die Beziehung zwischen dicht bewachsenen Vegetationsflächen und geringer Klassifizierungszuverlässigkeit ermittelt und kritisch diskutiert.

Des Weiteren wird im Rahmen der vierten Zielstellung der Einfluss der Schneeschmelze auf Wasserressourcen durch die kontinuierliche Erfassung der Dynamiken von Binnenwasserkörpern bewertet. Hierfür werden Sentinel-1-SAR und Sentinel-3-Altimetriedaten der neuen Generation für die Abgrenzung der Oberflächengewässer und für die Messung des Wasserstandes sowohl für den Urmia See als auch den Brahmaputra verwendet. Diese frei zugänglichen und

hochaufgelösten sowie wolken- und beleuchtungsunabhängigen Daten überwinden die Einschränkungen weniger verfügbarer In-situ-Messstationen und die von Wolken beeinflussten Wasserindizes, die auf Basis von optischen Sensoren abgeleitet werden. Zudem gewährleisten frei zugängliche und cloudbasierte Datenverarbeitungsdienste eine hohe Effizienz und räumlich breite Übertragbarkeit. Die Genauigkeiten der abgeleiteten Oberflächengewässer und Wasserstandwerte werden anhand von Fernerkundungsprodukten, die auf Basis von optischen Sensordaten erstellt wurden, sowie Messerwerten zum Wasserstand aus Datenbanken bewertet. Durch die komplementäre Nutzung der klassifizierten Oberflächengewässer und des abgeleiteten Wasserstandes können schließlich die Dynamiken der Binnenwasserkörper, durch z.B. hypsometrische Kurven des Urmia Sees oder von überfluteten Gebieten entlang des Brahmaputra Flusses, umfassend analysiert werden.

Abschließend, wird im Rahmen der letzten Zielstellung dieser Forschungsarbeit, die Binnenwasserkörperdynamik zusammen mit den auf Basis von SAR Aufnahmen erstellten Daten zur nassen Schneedecke genutzt, um die Kausalitäten zwischen Schneeschmelzbedingungen und Binnenwasserressourcen zu untersuchen. Um die Wechselwirkungen genauer zu quantifizieren, werden Niederschlags- und Evaporationsdaten aus einem globalen Wettermodell in die Analysen einbezogen. Hierfür wird die DLM-Regression eingesetzt, um die dynamischen Einflüsse von mehreren Variablen mit zeitlichen Verzögerungen zu untersuchen. Die zeitlichen Verzögerungsanalysen haben ergeben, dass die Variable Schneeschmelze die längste Verzögerung aufweist. Schließlich haben wir die Kausalitäten zwischen Schneeschmelzbedingungen und Binnengewässer quantifiziert und Wechselwirkungen zwischen Kryosphäre und Hydrosphäre identifiziert.

Für das Untersuchungsgebiet des Urmia Sees würde eine Zunahme der nassen Schneedecke von einem Prozent eine Zunahme des trendbereinigten Wasservolumens um 108 Kubikmeter innerhalb einer Periode von 0 bis 80 Tage bewirken. Bei der Betrachtung des Brahmaputra Flusses hingegen würde eine Zunahme der nassen Schneedecke von einem Prozent, eine Zunahme des Wasserstandes einer untersuchten virtuellen Station um 0,1 Meter innerhalb einer Periode von 80 bis 150 Tagen bewirken.

List of Figures

List of Tables

Abbreviations and Acronyms

ALOS Advanced Land Observation Satellite
ALT Active Layer Thickness
AMI Active Microwave Instrumentation
AO Arctic Oscillation
ARDL Autoregressive Distributed Lag Model
ASI Italian Space Agency
ASTER Advanced Spaceborne Thermal Emission and Reflection Radiometer
AVHRR Advanced Very High Resolution Radiometer
AWEI Automated Water Extraction Index
BRAT Multi-Mission Radar Altimetry Toolbox
CCI+ Climate Change Initiative Extension
CoReH2O Cold Region Hydrology High-resolution Observatory
CSA Canadian Space Agency
CSK COSMO-SkyMed
DAAD German Academic Exchange Service
DAHITI Database for Hydrological Time Series of Inland Waters
DEM Digital Elevation Model
DERD Double-bounce Eigenvalue Relative Difference
DL Deep Learning
DLM Distributed Lag Model
DLR German Aerospace Center
DN Digital Numbers
DoP Degree of Polarization
ECA&D European Climate Assessment & Dataset Project
ECMWF European Centre for Medium-Range Weather Forecasts
ECV Essential Climate Variables
EM Electromagnetic
ENL Effective Number of Looks
ESA European Space Agency
FAO Food and Agriculture Organization
FDL Finite Distributed Model
FVC Fractional Vegetation Cover
GCOS Global Climate Observing System
GEE Google Earth Engine
GLWD Global Lakes and Wetlands Database
G-POD Grid Processing On Demand
GRD Ground Range Detected
GRDC Global Runoff Data Center
G-REALM Global Reservoir and Lake Global Reservoir and Lake Monitor
GSP Global SnowPack
GWP Global WaterPack
HPR Higher Posting Rate

InSAR Interferometric SAR
IPCC Intergovernmental Panel on Climate Change
ITSDA Information Theoretic Snow Detection Algorithm
IW Interferometric Wide Swath
LA Lüneburg Anisotropy
LAI Leaf Area Index
LCCS Land Cover Classification System
LIA Local Incidence Angle
Lidar Light Detection and Ranging
LRM Low-resolution Mode
LRP Long-run Propensity
LST Land Surface Temperature
LWC Liquid Water Content
MeteoSwiss Swiss Federal Office of Meteorology and Climatology
ML Machine Learning
MODFLOW Modular Three-dimensional Finite-difference Ground-water Flow Model
MODIS Moderate Resolution Imaging Spectroradiometer
NAO North Atlantic Oscillation
NASA National Aeronautics and Space Administration
NDSI Normalized Difference Snow Index
NDWI Normalized Difference Water Index
NSIDC National Snow and Ice Data Center
NTC Non Time Critical
OA Overall Accuracy
OLS Ordinary Least Squares
OOB Out-of-bag
PA Polarimetric Asymmetry
PCVE Polarimetric Contrast Variation Enhancement
PF Polarization Fraction
POE Probability of Error
PolInSAR Polarimetric Interferometric SAR
PolSAR Polarimetric SAR
PPD Polarimetric Copolarization Phase Difference
PRF Pulse Repetition Frequency
RF Random Forest
ROC Receiver Operating Characteristic Curve
ROS Rain-on-snow
RSI Radar Snow Index
RVI Radar Vegetation Index
SAR Synthetic Aperture Radar
SARvatore SAR Versatile Altimetric Toolkit for Ocean Research & Exploitation
SCD Snow Cover Duration
SCE Snow Cover Extent

SD Snow Depth
SDGs Sustainable Development Goals
SEN4SCI Sentinel for Science
SERD Single-bounce Eigenvalue Relative Difference
SLC Single Look Complex
SNAP Sentinel Application Platform
SnowEx Snow Experiment
SnowPEx Satellite Snow Product Intercomparison and Evaluation Exercise
SNR Signal-to-noise
SRAL SAR Radar Altimeter
SRTM Shuttle Radar Topographic Mission
STL Seasonal-trend Decomposition Procedures Based on Loess
SVM Support Vector Machine
SWE Snow Water Equivalent
TKK Helsinki University of Technology
TomoSAR Tomographic SAR
TOPS Terrain Observation with Progressive Scans in Azimuth
UN United Nations
UNEP United Nations Environment Programme
VS Virtual Station
VWC Volume Water Content
WCE Water-covered Extent
WSCE Wet Snow Cover Extent
WWDR World Water Development Report

1 Introduction

1.1. Research background and motivation

Snow plays an indispensable role in both, natural systems' balances and human socio-economic activities owing to its wide spatial coverage as well as its unique geophysical characteristics. According to previous studies (Pepe et al., 2005; Lemke et al., 2007; Kerr et al., 2018), snow covers approximately 47 million km^2 or around 40% of the northern hemisphere during the wintertime. Together with the distinct characteristics of snow including high thermal emissivity, low thermal conductivity, high albedo, and low surface roughness, snow acts as an unneglectable factor in the balance of global energy, climate variation, ecology, cryosphere, water resources, and economic activity.

Global energy balance

Compared to most land surfaces having an albedo in the range between 0.1 and 0.3, fresh snow has an albedo between 0.8 and 0.9 (Barry, 1996). Therefore, snow reflects a much larger proportion of solar radiation and thus influences the regional and global energy balance (Serreze et al., 2000; Barnett et al., 2005; Déry and Brown, 2007; Armstrong and Brun, 2008; Barry and Chorley, 2009). In total, snow reflects around 85% of the incoming shortwave solar radiation back into space (Warren, 1982; Perovich et al., 2002), especially in Alaska, Siberia, and northern Canada (Flanner et al., 2011), which largely regulates the energy balance of the Earth. Moreover, in the wintertime, the low thermal conductivity of snow insulates the ground surface and thus preserves the energy and moisture in the near-surface layers (Callaghan, Johansson, Brown, Groisman, Labba, Radionov, et al., 2011).

Climate variations

Snow-albedo feedback is regarded as one of the key mechanisms in the global climate system (Hall, 2004) as snow increases the surface albedo and thus reduces surface temperature (Scherrer and Appenzeller, 2006). In addition to its direct effect on soil temperature (Lawrence and Slater, 2010), studies found the evident relationship between Eurasian snow cover and atmospheric circulation patterns including Arctic Oscillation (AO), North Atlantic Oscillation (NAO) (Gutzler and Rosen, 1992; Clark and Serreze, 2000; Allen and Zender, 2010; Cohen et al., 2012) as well as the Asian monsoon (Hahn and Shukla, 1976; Yang, 1996; Peings and Douville, 2010; Saha et al., 2013; Xiao and Duan, 2016).

Ecological systems

Snow is identified as the single most critical factor influencing the biological environment in both arctic and alpine regions (Billings and Bliss, 1959; Walker et al., 1993; Callaghan, Johansson, Brown, Groisman, Labba, and Radionov, 2011). On the one hand, during wintertime, the snowpack acts as a shelter from the harsh

environment exposing to low temperature, frost or abrasion by wind-brought ice particles (Björk and Molau, 2007; Niittynen et al., 2018), and provides a warmer soil temperature and sustains microbial nutrient (Tan et al., 2014; Paradis et al., 2016). On the other hand, snow increases the plant photosynthesis (Bosiö et al., 2014) and supplies sufficient meltwater in spring/summer which facilitates the growth of vegetation(Olsen et al., 2011). Consequently, snow-covered regions usually hold the greatest diversity of species (Virtanen et al., 2003). Snow is also found to affect the phenology, behavior, and mortality of species (Madsen et al., 2007; Teja et al., 2020).

Cryospheric interactions

Snow has strong interactions with other cryospheric components (Vaughan et al., 2013). Snowfall controls the equilibrium of glacier dynamics, and snowmelt water is the dominating factor affecting subglacial drainage systems (Decaux et al., 2019; Uszczyk et al., 2019) as well as the water storage of firn (Parry et al., 2007). Snow also influences both, the radiative and physical properties of the sea ice environment (Webster et al., 2018). The high albedo of snow affects the thermodynamic processes of sea ice and the growth rate of ice thickness (Shine and Henderson‐Sellers, 1985; Ebert and Curry, 1993; Yang Y. et al., 2012; Holland and Landrum, 2015). Additionally, owing to the effective thermal insulation characteristics of snow, snow cover is regarded as one of the most critical factors affecting the thermal regime of permafrost (Zhang, 2005; Magnin et al., 2017; Zhao et al., 2018). Due to the insulation of snow, a temperature offset between air and soil is found in wintertime, which delays the thawing and reduces the variation magnitude of active layer thickness (ALT) caused by a changing air temperature (Stieglitz et al., 2003; Harris et al., 2009; Pogliotti et al., 2015; Magnin et al., 2017; Oliva et al., 2017; Beniston et al., 2018). Moreover, the snowmelt water would also change the thermal status of soil which alters the dynamics of permafrost (Romanovsky and Osterkamp, 2000).

Socio-economic influence

The stability of annual snow cover variation is linked to a wide range of socio-economic activities (Euskirchen et al., 2013). For instance, the operational period of artic road networks depends on snow cover duration, which provides a cost-efficient transportation between settlements in polar regions (Furgal and Prowse, 2008); snow anomalies and the resultant loading weight change, as well as temperature variation relate to possible damages to forest industry (Kilpeläinen et al., 2010; Callaghan, Johansson, Brown, Groisman, Labba, Radionov, et al., 2011); snow distribution and snow cover duration affect the accessibility and operational period of outdoor/ski recreation industries and winter tourism (Burakowski and Magnusson, 2012; Steiger and Abegg, 2013; Schmucki et al., 2017); indigenous cultures, resource use, and daily life rely on snow conditions (Curtis et al., 2005; Callaghan, Johansson, Brown, Groisman, Labba, Radionov, et al., 2011). Moreover, snow cover and snowmelt can also lead to disasters including floods/droughts and avalanches (Fang

et al., 2014; Favier et al., 2014; Ancey and Bain, 2015).

Water resources

The importance of springtime snowmelt water to global water resources is tremendous (Barnett et al., 2005; Chen et al., 2017; Grünewald et al., 2018; Wu et al., 2018; Armstrong et al., 2019). Since half of the global precipitation events are either snow or stem from melting snow (Field and Heymsfield, 2015), around 17% of the world population rely on snowmelt water for daily consumption and agricultural irrigation (Barnett et al., 2005). The value of snow on alpine and arctic water resources is even more crucial. More than 50% of precipitation in mountainous regions is falling as snow in Norway, the Tibet region, the Alps, and also the northern and western United States (Romanov et al., 2000; Serreze et al., 2001; Weingartner et al., 2003; Malnes et al., 2004; Barnett et al., 2005; Solberg et al., 2005; Dedieu et al., 2012; Li et al., 2017; Han et al., 2019); in northern Siberia and America, snowmelt-generated runoff accounts for 75% of total annual flow (Woo, 1980). Snowmelt water affects the runoff regimes of downstream regions not only in terms of water amount but also in distribution, quality, and seasonality (Barnett et al., 1989; Beniston et al., 2011; Schöber et al., 2014; Singh et al., 2014; Huss et al., 2017). Furthermore, snowmelt water is commonly used for hydropower production (Armstrong and Brun, 2008; Voigt et al., 2010; Callaghan, Johansson, Brown, Groisman, Labba, Radionov, et al., 2011; Kobierska et al., 2013; Mo et al., 2018).

Based on the influences mentioned above and interactions between snow and various systems, it is known that snow cover has a critical role in each natural and environmental system. Nevertheless, due to the rising temperature caused by global warming, a significant decrease in SCE has been shown globally in both, observations and models (Dye, 2002; Jylhä et al., 2008; Brown et al., 2010; McCabe and Wolock, 2010; Brown and Robinson, 2011; Derksen and Brown, 2012; Kunkel et al., 2016; Najafi et al., 2016; Hori et al., 2017; Mudryk et al., 2017; Notarnicola, 2020), which was also reported in the Fifth Assessment Report (AR5) of the Intergovernmental Panel on Climate Change (IPCC) (Pachauri et al., 2014). Hence, snow is identified as a critical climate variable within the Global Climate Observing System (GCOS) (GCOS, 2011).

Since the decrease of SCE reduces global surface albedo, which in turn increases the absorbed solar radiation, global warming and the resultant snowmelt processes would eventually be accelerated (Steffen, 1995; Armstrong and Brodzik, 2002; Dankers and De Jong, 2004; Scherrer et al., 2012; Kevin et al., 2017). This positive feedback-led acceleration is of even greater severity in alpine and arctic regions owing to the temperature amplification (Serreze and Francis, 2006; Rauscher et al., 2008; Day, 2009; Clow, 2010; Stocker et al., 2013; Wang et al., 2014; Pepin et al., 2015; Beniston et al., 2018). According to Notarnicola (2020), around 80% of the global mountain regions experienced a decline in snow cover from 2000 to 2018. Moreover, on a

global scale, winter precipitation has been shifting from snow to rainfall (Knowles et al., 2006; McCabe and Wolock, 2010; Szczypta et al., 2015). These two climate change-caused climate pattern alterations largely endanger the water resources of the countless populations relying on snowmelt water (Nijssen et al., 2001; Barnett et al., 2005; Adam et al., 2009; Schlaepfer et al., 2012), since mountainous regions are the primary water source for various river/lake systems (Beniston et al., 1997) and the decreased and earlier snowmelt water would reduce the usable runoff during the high water demanding growing season especially in the mid-latitude arid regions (Cayan et al., 2010; Seager and Vecchi, 2010; Biemans et al., 2019). Therefore, the strategy of water resource management and socio-economic development are negatively affected (Stewart et al., 2004; Barnett et al., 2005; Wang and Li, 2006; Butt and Bilal, 2011; Harma et al., 2012; Wu et al., 2018; Biemans et al., 2019).

1.2. Literature gaps and research objectives

In order to understand the interaction between snow cover and inland water resources, following goals must be fulfilled: (1) continuous monitoring of snow cover extent as well as snowmelt conditions, (2) continuous tracking of water resources variations of snowmelt-dominated waterbodies, and (3) analyzing the influence of snow cover dynamics and snowmelt conditions on inland water resources. For each point, previous studies have certain limitations and gaps which are the aims of this thesis. The current literature gaps together with the research objectives of the present thesis are summarized as follows:

Objective 1: **Reviewing the characteristics of SAR and its interactions with snow, and exploring the trends, difficulties, and opportunities of existing SAR-based SCE mapping studies**

Although there have been several SCE mapping projects relying on remote sensing including the European Space Agency's (ESA) Satellite Snow Product Intercomparison and Evaluation Exercise (SnowPEx) (Metsämäki et al., 2017) and the German Aerospace Center's (DLR) Global SnowPack (Dietz et al., 2015), they utilize multi-spectral sensors which are inevitably affected by cloud cover as well as polar darkness. Nevertheless, snow is usually located in high altitude and high latitude regions where cloud cover and polar darkness restrict the number of available optical satellite acquisitions. Consequently, continuous SCE estimation can only be fulfilled with spatial and temporal interpolations which cannot reveal true SCE conditions.

On the contrary, SAR has all-weather as well as day-and-night sensing abilities, which overcome the limitations of conventional multi-spectral sensors. Since the launch of the first continuously revisiting spaceborne SAR satellite, i.e., ERS-1 in 1991, there have been various studies that explored the benefits of using SAR for SCE mapping. Yet, no comprehensive review has been conducted to discuss the unique interactions between SAR signal and snowpack and to review the current techniques used to detect SCE with SAR imagery.

Hence, this thesis firstly investigates the background theory of using SAR imagery to detect snow, and holistically examines the SAR imagery analysis approaches together with commonly employed auxiliary data used in previous studies and investigates their advantages and restrictions. Furthermore, the advancement and trends of SAR design and SCE mapping algorithms, as well as current limitations and future opportunities are identified to reveal remaining research gaps.

Objective 2: Proposing a novel total and wet SCE mapping strategy based on freely accessible SAR imagery with all land cover classes applicability and global transferability

Based on the research gaps identified in the review paper, it is found that utilizing SAR imagery for SCE mapping is still at a developing stage. Previous SAR-based SCE detecting studies have at least one of the following limitations: (1) geological aspect: only focus on and test the algorithms in the Asian Himalaya and European Alps; (2) spatial aspect: only process at a small regional scale; (3) SAR imagery analysis algorithm: only detect wet SCE with a backscatter-threshold approach; (4) land cover aspect: rarely consider land cover information in the algorithm itself, or simply mask out the forest region; (5) classification algorithm: only employ classification algorithms which require complex tuning and have limited data handling capacities; (6) validation: seldomly validate their estimated SCE with in-situ or different remote sensing-based SCE results. These constraints largely limit the transferability of existing SAR-based SCE detection algorithms as practically they are often not operated on forested regions, or they can only detect wet snow.

Therefore, this thesis explores the potential of fusing different SAR-based informations together with topographical factors as well as land cover information to detect total and wet SCE. The detected SCE is planned to be comprehensively validated based on in-situ and reference datasets originating from multispectral data sources. Moreover, since only openly accessible datasets with global coverage are employed and five study areas located in different mountain ranges with different land cover conditions are selected for testing, the robustness and universal transferability of the proposed holistic SCE mapping method can be examined.

Objective 3: Enhancing total SCE mapping accuracy by fusing SAR- and multi-spectral sensor-based information, and providing total SCE mapping reliability map information

In the previous method paper, a globally transferable, freely accessible data-only, all land cover class-applicable total and wet SCE mapping strategy utilizing only SAR-based observations as well as topographical factors and land cover information with satisfying classifying accuracy is proposed. Nevertheless, since it is found that densely vegetated regions tend to show a lower SCE mapping accuracy, the further exploration of employing quantitative vegetation indexes should be considered. Moreover, as previous studies suggest the merit of using ground temperature

information for SCE detection, the multi-spectral sensor-derived surface temperature product is also included. In addition, since previous studies provide no uncertainty information along with the estimated SCE, this thesis aims to generate a classification reliability map. It enables the further analysis of the influences of different land cover classes on the total SCE mapping reliability. Similar as for the previously proposed method, different study areas located in different continents and hemispheres are selected and results are validated comprehensively to attest the universal applicability and robustness.

Objective 4: Proposing a cloud-free and illumination-independent inland waterbody dynamics tracking strategy using freely accessible datasets and services

To quantify the influence of snow cover dynamics as well as snowmelt conditions on inland water resources, it is necessary to firstly track the variation of inland waterbody dynamics. Previous studies focus on either water level or surface area. For tracking water surface area, multi-spectral sensor-based band ratio water indexes are commonly employed. However, in addition to the difficulty of selecting the optimized band composition, these indexes are inevitably affected by cloud cover as well as noise caused by the variation of atmospheric, illumination, and water conditions. On the other hand, for water level tracking, current studies utilize the measurements of in-situ gauging stations, yet the installation of instruments is not universally possible and the data might not be publically available.

Thus, this thesis employs the new generation of high-resolution, freely accessible spaceborne SAR and altimetry data, together with freely available online cloud-based processing services to achieve a holistic, cloud-free and illumination-independent inland waterbody dynamics tracking strategy with broad applicability and high efficiency. Furthermore, by integrating estimated water level and surface area information, the hypsometry and water volume variation of lakes as well as flooded area and water level variation of rivers can be estimated.

Objective 5: Assessing the influence of snowmelt conditions on inland water resources

To unbiasedly quantify the influence of snowmelt conditions on inland water resource variations, it is essential to include other hydrological factors which can also alter the water amount of rivers and lakes. Nevertheless, since these hydrological factors and snowmelt conditions not only are correlated but also post different lagged influences on downstream water level/volume, the conventional regression approach cannot correctly assess the causal effects of snowmelt conditions. Consequently, the sophisticated regression approach which is capable of handling multiple variables' dynamic influences with lags should be employed. Thus, in this thesis, the causal effect of wet SCE mapped with SAR imagery on the variation of inland water resources estimated by spaceborne SAR and altimetry can be unbiasedly assessed.

Therefore, cryo-hydrosphere interactions can be eventually identified.

1.3. Structure of the thesis

This thesis consists of six chapters. Chapter one provides an overview of the research background and motivations. In addition, the literature gaps of previous studies and the corresponding research objectives of the thesis are introduced. The structure of the thesis is also described.

Chapter two reviews the characteristics of SAR and its interactions with the snowpack and summarizes existing SAR-based SCE detection studies. A comprehensive discussion of limitations, opportunities, and developing trajectory of the topic is also provided. This chapter is published as:

Tsai, Y.-L.S., Dietz, A., Oppelt, N., & Kuenzer, C. (2019). Remote Sensing of Snow Cover Using Spaceborne SAR: A Review. Remote Sensing, 11, 1456

Chapter three describes the proposed novel SAR-based total and wet SCE mapping approach, including detailed methodological descriptions, results, and validations. Further discussions including the reason for inhomogeneous mapping accuracies, the influence of vegetation, as well as the achieved improvements are provided. This chapter is published as:

Tsai, Y.-L.S., Dietz, A., Oppelt, N., & Kuenzer, C. (2019). Wet and Dry Snow Detection Using Sentinel-1 SAR Data for Mountainous Areas with a Machine Learning Technique. Remote Sensing, 11, 895

Chapter four provides the descriptions of the improved total SCE mapping approach by employing the extra ground surface temperature information and vegetation indexes. The influences of different inputs on classification accuracy and the effect of different land cover classes on classification reliability are also discussed. This chapter is published as:

Tsai, Y.-L.S., Dietz, A., Oppelt, N., & Kuenzer, C. (2019). A Combination of PROBA-V/MODIS-based Products with Sentinel-1 SAR Data for Detecting Wet and Dry Snow Cover in Mountainous Areas. Remote Sensing, 11, 1904

Chapter five utilizes the SAR-based snow cover dynamics to assess the causal effect of snowmelt conditions on inland water resources. The methods of measuring water level and surface area based on altimetry and SAR respectively are described. The surveyed results together with the discussions including the cause of the different lagged effects of snow on water resources are provided. This chapter is published as:

Tsai, Y.-L.S., Klein, I., Dietz, A. and Oppelt, N. (2020). Monitoring Large-scale Inland Water Dynamics by Fusing Sentinel-1 SAR and Sentinel-3 Altimetry Data and by Analyzing Causal Effects of Snowmelt. Remote Sensing, 12, 3896

In the end, chapter six presents a synthesis of the main achievements and

contributions to previous research gaps. The overall conclusions as well as the future opportunities and challenges are elaborated as well.

2 Remote Sensing of Snow Cover Using Spaceborne SAR: A Review

Tsai, Y.-L.S., Dietz, A., Oppelt, N., & Kuenzer, C. (2019). Remote Sensing of Snow Cover Using Spaceborne SAR: A Review. Remote Sensing, 11, 1456

Abstract

The importance of snow cover extent (SCE) has been proven to strongly link with various natural phenomenon and human activities; consequently, monitoring snow cover is one the most critical topics in studying and understanding the cryosphere. As snow cover can vary significantly within short time spans and often extends over vast areas, spaceborne remote sensing constitutes an efficient observation technique to track it continuously. However, as optical imagery is limited by cloud cover and polar darkness, synthetic aperture radar (SAR) attracted more attention for its ability to sense day-and-night under any cloud and weather condition. In addition to widely applied backscattering-based method, thanks to the advancements of spaceborne SAR sensors and image processing techniques, many new approaches based on interferometric SAR (InSAR) and polarimetric SAR (PolSAR) have been developed since the launch of ERS-1 in 1991 to monitor snow cover under both dry and wet snow conditions. Critical auxiliary data including DEM, land cover information, and local meteorological data have also been explored to aid the snow cover analysis. This review presents an overview of existing studies and discusses the advantages, constraints, and trajectories of the current developments.

Keywords: Synthetic Aperture Radar; Backscattering; InSAR; PolSAR; Snow Classification; Wet Snow; Cryosphere; Data Fusion; Machine Learning

2.1. Introduction

Snow covered areas influence the global radiation balance, groundwater, runoff, glaciers, flora and fauna, and human activities such as tourism, civil engineering, and infrastructure. Within all cryospheric components, snow covers the widest area: During the wintertime, more than 40% of the northern hemisphere is covered by snow (Pepe et al., 2005; Lemke et al., 2007; Kerr et al., 2018). As a result of its multiple influences on the environment, snow cover is addressed in the Fifth Assessment Report (AR5) of the Intergovernmental Panel on Climate Change (IPCC) and is identified as a critical climate variable within the Global Climate Observing System (GCOS) (GCOS, 2011). Several snow cover projects relying on remote sensing have been conducted in recent years, including the European Space Agency (ESA)'s Satellite Snow Product Intercomparison and Evaluation Exercise (SnowPEx)

(Metsämäki et al., 2017), the German Aerospace Center (DLR)'s Global SnowPack (Dietz et al., 2015), the National Aeronautics and Space Administration (NASA)'s Snow Experiment (SnowEx) (Kim E. et al., 2017), and the ongoing ESA's Let It Snow project (Manuel et al., 2016) as well as new Climate Change Initiative Extension (CCI+) Essential Climate Variables (ECV) mission (Trofaier, 2018). Figure 2.1 gives an overview of some of the aspects related to snow cover, and also illustrates some of the more variable snow cover characteristics such as liquid water content, grain size, density, and snow water equivalent (SWE).

Snow cover reflects incoming solar radiation, as fresh snow normally has an albedo between 0.8 and 0.9 while most land surfaces have an albedo ranging between 0.1 and 0.3 (Barry, 1996); therefore, snow influences the regional and global energy balance (Serreze et al., 2000; Barnett et al., 2005; Barry and Chorley, 2009). A decrease in snow cover extent (SCE) and duration leads to a reduced albedo of the land surface, which increases the warming process and further accelerates the snowmelt process (Steffen, 1995; Armstrong and Brodzik, 2002; Dankers and De Jong, 2004; Scherrer et al., 2012; Kevin et al., 2017). Additionally, snow cover affects the conditions and spatial distribution of other cryosphere components (Vaughan et al., 2013): Snow is a prerequisite for temperate glaciers, controlling their equilibrium. The high albedo of snow preserves the retention of sea and lake ice and also influences the growth rate of ice thickness due to thermodynamic processes (freezing and melting) and snow types (dry or wet) (Shine and Henderson-Sellers, 1985; Ebert and Curry, 1993; Yang Y. et al., 2012). Snow also interacts with permafrost due to its thermal insulation characteristic, which reduces the scale of variation of active layer thickness (ALT) caused by air temperature changing (Stieglitz et al., 2003; Pogliotti et al., 2015; Beniston et al., 2018). Consequently, snow cover is regarded as one of the most critical factors affecting the thermal regime of permafrost (Magnin et al., 2017; Zhao et al., 2018).

In addition, snow cover directly affects ecology and the socioeconomic system. Studies suggested that water originating from snowmelt dominates the runoff regimes of downstream regions not only in terms of water amount but also in distribution, quality, and seasonality (Barnett et al., 1989; Beniston et al., 2011; Schöber et al., 2014; Singh et al., 2014; Huss et al., 2017). Therefore it also controls the available water resources for the inhabiting population. More than 50% of precipitation in mountainous regions is falling as snow in Norway, the French Alps, and also the northern and western United States (Romanov et al., 2000; Serreze et al., 2001; Weingartner et al., 2003; Barnett et al., 2005; Solberg et al., 2005; Dedieu et al., 2012). Moreover, snow cover and snowmelt in particular can also lead to natural disasters such as floods or avalanches (or in the absence of snow: Droughts). In order to identify possible flood events, detecting the onset of snowmelt in time is necessary (Mock and Birkeland, 2000; Pielke et al., 2005; Kvambekk and Melvold, 2010; Favier et al., 2014; Ancey and Bain, 2015). Furthermore, snow cover is also an important

aspect for winter tourism (Steiger and Abegg, 2013; Schmucki et al., 2017).

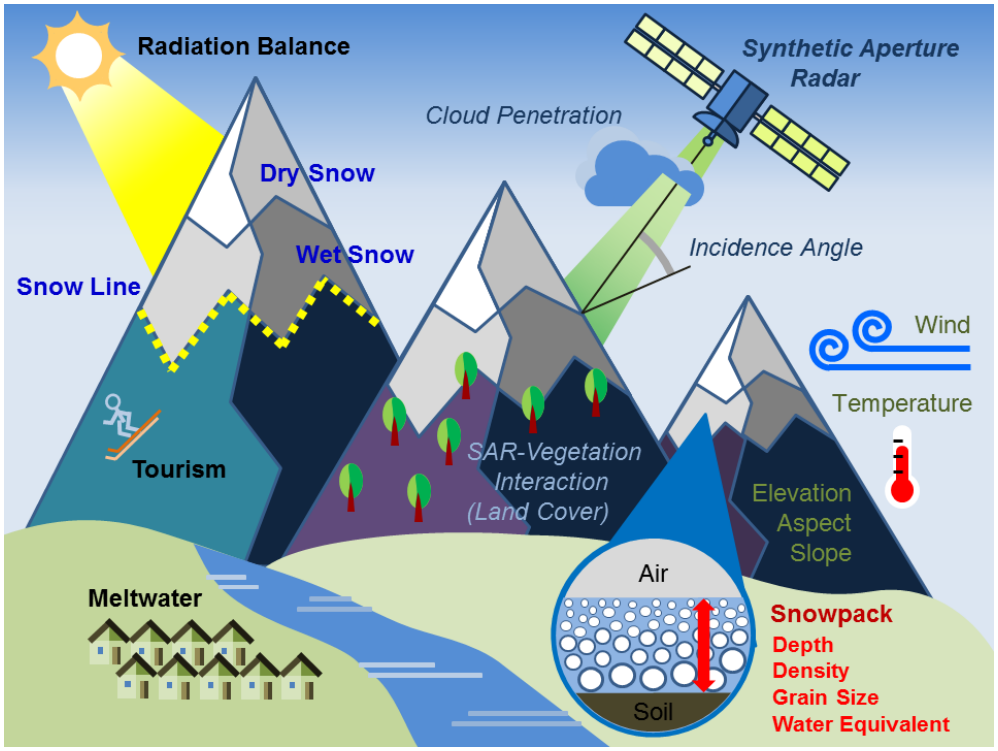

Figure 2.1 Illustration of different snow types and snow line (deep blue font), the importance of snow (black font), synthetic aperture radar (SAR)-related characteristics (font in italics), factors influence snow (green font) and snowpack parameters (red font).

Due to global warming, a significant decrease in spring SCE has been shown in both observations and models (Dye, 2002; Jylhä et al., 2008; Brown et al., 2010; McCabe and Wolock, 2010; Brown and Robinson, 2011; Najafi et al., 2016; Hori et al., 2017), and recorded in the Synthesis Report of IPCC AR5 (Pachauri et al., 2014). Climate change influences the global snow cover spatial extent as well as the duration. Beniston et al. (2018) concluded that temperature increase as well as large-scale atmospheric patterns is the most influencing factors changing global snow cover. Snow cover onset and melt dates are shifting, generally leading to shorter snow cover seasons with later onset and earlier melt (Marty et al., 2017) although these general patterns can vary on a regional scale (Bulygina et al., 2011; Dietz et al., 2014). On a global scale, winter precipitation has been shifting from snow to rainfall, which is particularly evident in regions with a more maritime climate (McCabe and Wolock, 2010). In mountain regions, the effects of climate change on snow cover are even more significant, leading to an apparent decrease of SCE and duration (Dyrrdal et al., 2013; Terzago et al., 2013; Beniston et al., 2018). Studies predicted that in the highest altitudes of the European Alps, SWE may be reduced to less than 20% of the present level by 2100 and that they may become totally snow-free in summertime (Magnusson et al., 2010; Schmucki et al., 2015). As a result of all these aspects,

continuously monitoring of snow cover is crucial.

Considering the wide areal coverage, temporal variability, inaccessibility and remote location of many snow covered regions, remote sensing is an ideal data acquisition technique for monitoring snow cover and its trends and developments on both spatial and temporal scales. Although the utilization of optical/multispectral remote sensing data for monitoring SCE has a long history compared to synthetic aperture radar (SAR) data (König et al., 2001; Dietz et al., 2012), as data from optical sensors can be affected by cloud cover as well as (polar) darkness, spaceborne SAR data offers a valuable alternative for monitoring snow cover as it is independent from clouds and illumination conditions. Due to the availability of new SAR satellites during the recent decades together with the developments of the SAR-based SCE detection algorithms, more studies have tried to detect SCE based on SAR imagery instead of optical sensors. However, there has been no comprehensive discussion of current SAR-based SCE detection approaches' theories, technical limitations, critical auxiliary data, and the so far developing trajectory as well as future possibilities. Thus, in the following sections we therefore summarize the currently available techniques to detect snow cover utilizing SAR data and thoroughly compare their advantages and drawbacks.

2.2. Characteristics of Snow and SAR

2.2.1. SAR Sensor Characteristics

Radar remote sensing is an active sensing approach, which transmits electromagnetic (EM) radiation with wavelengths between 0.3 to 0.01 m and senses their echoes from the Earth surface (Wiley, 1985; Bruder, 2013). The spatial resolution of the acquired imagery is approximately equal to one-half the length of the actual antenna and is independent from platform altitude (Chan and Koo, 2008). Comparing to other contemporary active spaceborne sensors such as scatterometers, SAR is therefore able to monitor with higher spatial resolution and thus preserves more ground surface details.

Due to its active and relatively long wavelength characteristics, SAR does not rely on solar illumination and can therefore operate both day and night. SAR can also penetrate clouds, enabling measurements of the surface under all weather and illumination conditions. These abilities are particularly valuable when it comes to snow cover monitoring, as snow-covered alpine regions are often covered by clouds and high latitudes regions are affected by polar darkness during winter (Bartsch et al., 2007). Furthermore, longer wavelengths of SAR can penetrate into the snowpack (Campbell, 2002), potentially providing information about snowpack conditions such as snow grain size and SWE (liquid/frozen water content), and can even penetrate the frozen layer on the top surface of snow (Floricioiu and Rott, 2001).

Owing to the unique sensing characteristics of SAR, the snow information recorded in

SAR imagery is fundamentally different when compared to optical/multispectral imagery. The former records surface characteristics related to the roughness and dielectric properties; the latter records the reflection/absorption of the incoming solar irradiation at the top layer of the surface (Solberg, Koren, et al., 2010). As snow, ice, and clouds are characterized by comparatively similar reflection properties in the visible and—depending on the cloud phase—the near to medium infrared part of the spectrum, confusions can occur when attempting to classify snow cover and discriminate it from ice or clouds (Harrison and Lucas, 1989; Macander et al., 2015). SAR sensors can overcome this ambiguity as they measure surface properties in a different realm in terms of a backscatter coefficient, which is a function of the wavelength of the SAR signal, and the roughness and dielectric properties of the surface rather than the reflection properties.

An additional advantage of SAR sensors is derived from the phase information they record. Different polarizations (horizontal, vertical) allow for the detection of additional physical characteristics of the surface, such as shape, material, or angle of an observed target. Furthermore, based on the phase information recorded by SAR, coherence and interferometry can be generated (Zebker and Goldstein, 1986; Goldstein et al., 1993; Touzi et al., 1999), which can indicate the deformation and stability of ground features. Such information can be analyzed to detect and quantify, e.g., glacier velocity or other moving targets (Tsai et al., 2016; Kim J.-R. et al., 2017; Tsai et al., 2018).

However, SAR also has some practical drawbacks for cryospheric application. The first is the comparatively low temporal resolution (i.e., revisit days, often longer than five days) when compared to operational optical/multispectral missions due to the trade-offs of orbit design including spatial resolution, tilt angle, swath width (Dial et al., 2003; Taini et al., 2008; Luo et al., 2017). Based on the cryosphere report given by the Global Climate Observing System (GCOS) (Key et al., 2007), the minimum requirement in terms of temporal resolution for spaceborne snowmelt area products for subsequent research of hydrology and climate is one to five days. Current optical/multispectral missions are designed with shorter, even daily revisiting time (e.g., Advanced Very High Resolution Radiometer (AVHRR), Moderate Resolution Imaging Spectroradiometer (MODIS), Sentinel-3A/B). Even though the temporal resolution is yet insufficient to provide daily imagery, the spatial resolution of recent SAR missions such as Sentinel-1 (5 × 20 m) is more than satisfactory, given that the minimum requirements expressed by GCOS are between 100 and 500 m.

Contrary to optical sensors, the geometry of SAR observations is more complex due to their synthesized multi-beam echoes transmitted and received at both, side-looking slant-range direction and azimuth direction (Curlander and McDonough, 1991). The significance and type of the resulting distortions varies by landscape and sensing angle and thus leads to foreshortening, layover and shadow effects (Lillesand and Kiefer, 1994). In addition, as the received signal for each pixel of the SAR imagery is

the sum of the random constructive and destructive phase interferences reflected from countless ground features, the resultant speckles can degrade the image quality considerably (Lillesand and Kiefer, 1994; Chan and Peng, 2003). Consequently, the interpretation and analysis of SAR images are more challenging than conventional optical observations.

The overview of different characteristics of SAR and optical sensors as well as advantages and drawbacks for snow cover monitoring are summarized in Table 2.1 and illustrated in Figure 2.1.

Table 2.1 Comparison of SAR and optical/multispectral sensors regarding their ability to detect snow cover.

Sensor	**SAR**	**Optical/Multispectral**
Sensing mode	Active	Passive
Wavelengths	0.01 ~ 0.3 m	0.3 ~ 1 µm
Spatial resolution	PALSAR-2: 3 ~ 10 m COSMO-SkyMed: 3 ~ 15 m Sentinel-1: 5 × 20 m (Stripmap mode)	Landsat-8: 15 ~ 30 m Sentinel-2: 10 ~ 20 m MODIS: 250 ~ 500 m (not included thermal band)
Temporal resolution	PALSAR-2: 14 days COSMO-SkyMed: ~5 days Sentinel-1: 6 days	Landsat-8: 16 days Sentinel-2: 5 days MODIS: 1 day
Recorded snow characteristics	Surface roughness, dielectric property	Surface reflection
Advantages	Day-and-night sensing under any weather condition; Possibility of interferometric and polarimetric information	Visually natural to interpret; High temporal resolution; Maturity of classification algorithms
Drawbacks	Low temporal resolution; Challenging to interpret due to its imaging geometry; Significant geometric distortions and speckles	Hindered by cloud, darkness; Confusion between snow, ice, and cloud

2.2.2. Interactions of Snow and SAR

Due to the penetration characteristics of the SAR signal, wet and dry snow behaves differently in SAR imagery. Practically, there are two different definitions of dry and wet snow. The first one is based on volume water content (VWC), i.e., a snowpack with VWC above 1% is considered wet snow, while snow below 1% VWC is referred to as dry snow (Ulaby and Stiles, 1980). The second definition, which is used more often, is connected to the temperature of the snowpack: At temperatures below 0 °C the snowpack is presumed to remain dry while above 0 °C the snow is considered wet (Dedieu et al., 2012; Salcedo and Cogliati, 2014; Besic et al., 2015). The temperature

definition was validated by statistical analysis of wet snow temperatures and proven advantageous when compared to the VWC approach, as measurements of temperature are easier to obtain than of VWC (Salcedo and Cogliati, 2014).

SAR observations of wet snow differ greatly from those of dry snow. As mentioned in Section 2.1, SAR signals can penetrate into the snowpack with the penetration depth depending on the wavelength of the signal. C-band SAR, for example, has a potential penetration depth of around 20 m when observing dry snow (Mätzler, 1987). Since the grain size of snow is between 0.1 and 0.3 mm (Rees, 2005), the SAR signal with its much longer wavelengths passes through the snow crystals nearly unhindered, preventing any kind of backscattering reflection from the snow crystals (Rignot et al., 2001; Langley et al., 2007). As the snowpack begins to melt, the dielectric properties of the snowpack change considerably, decreasing the penetration depth to around 3 cm while backscattering reflection from the liquid water becomes the dominant process (Mätzler and Schanda, 1984; Ulaby et al., 1986; Mätzler, 1987; Rott and Mätzler, 1987; Shi and Dozier, 1995; Ashcraft and Long, 2006; Zhou and Zheng, 2017). At a frequency higher than 1 MHz, the dielectric constants of air, ice, and water are 1.0, 3.17 ± 0.07 and 80, respectively (Evans, 1965). As the proportions of air, ice, and water within a snowpack change when melting begins, the cumulative dielectric constant also changes, leading from initially low values between 1.2 and 2.0 to much higher values (Ambach and Denoth, 1980; Arslan et al., 2001; Singh et al., 2014).

Additionally, the liquid water content of a snowpack also affects the scattering mechanism, i.e., how the multi-layered snowpack reflects the incoming SAR signal. Under dry snowpack conditions, the dominant scattering process is the sum of volume scattering of the snowpack and the surface scattering at the snow/ground interface. When the snowpack becomes wet, the surface scattering at the air/snow interface dominates the scattering mechanism (Shi and Dozier, 1995; Guneriussen, 1997; Strozzi and Matzler, 1998; Guneriussen et al., 2001; Thakur et al., 2013).

However, as the snowpack is a complex multi-layer structure, snow grain size, density, depth, stratigraphy, amount of impurities and surface roughness may affect its backscattering (Hongxing et al., 2006; Chuvieco, 2008). Surface and volume scattering is proportional to the polarization amplitude and transmissivity of the snowpack, respectively. The dielectric constant and local incidence angle (LIA) also affect the transmissivity (Snehmani et al., 2015). Table 2.2 presents an overview of each factor’s influence on the scattering of dry and wet snow as well as the backscattering characteristics. However, it must be noted that many factors affect scattering mechanisms, such as radar wavelength, polarization, incidence angle, surface roughness, and dielectric properties (Moghaddam and Saatchi, 1995; Martini et al., 2003; Eriksson et al., 2010; Besic, Vasile, Chanussot, Stankovic, Dedieu, et al., 2012; Phan et al., 2012). Longer wavelengths will produce more volume scattering due to a deeper penetration (Johansson et al., 2018).

Table 2.2 Effects of wet and dry snow on the SAR signal based on the snow physiology. “+” refers to positive correlation, “-“ to negative correlation. The number in brackets refers to the reference number.

Snow type	**Dry snow**	**Wet snow**
Backscattering source	Volume scattering from snowpack, Surface scattering at snow/ground interface	Surface scattering at air/snow interface
Dominant factors influencing scattering mechanism (Schwaizer, 2017)	Surface below snow (SAR frequency < ~10 GHz), Grain size (SAR frequency > ~10 GHz)	Liquid water content (most important), Surface roughness
Backscattering coefficient	High	Low
The relationship between snowpack parameters and the amplitude of backscattering		
Snow wetness	- (Shi and Dozier, 1993)	+ (Ambach and Denoth, 1980; Shi and Dozier, 1995; Bernier and Fortin, 1998)
Snow grain size	+ (Garrity, 1992; Snehmani et al., 2015)	insignificant (Suzuki et al., 1995)
Snow depth/thickness	+ (Garrity, 1992; Muhuri et al., 2018) + coarse-grained snowpack (Zhou and Zheng, 2017) - fine-grained snowpack (Zhou and Zheng, 2017)	- (Suzuki et al., 1995)

2.3. SAR-Based Studies and Methods to Detect Snow

The launch of SeaSat in 1978 initiated the era of utilizing spaceborne SAR sensors for global snow cover monitoring. While some snow-related studies were published with SeaSat’s L-band SAR (Rott Helmut, 1984; Rott H, 1984), studying snow cover with SAR data has become more mature since the launch of the first continuously revisiting ERS-1 (C-band) in 1991 as ERS-1 providing the opportunity to use repeat-pass multi-temporal observations, which minimizes the influence of topographic effects on the backscattering by ensuring similar sensing geometry (Löw et al., 2002) and thus produces more reliable snow cover estimations.

Consequently, the following literature review includes the results and findings from 96 snow cover studies mapping SCE with spaceborne SAR sensors after the launch of ERS-1, selected from commonly used academic search engines including Google Scholar, Web of Science, and Scopus. Studies focusing on SWE and snow depth (SD)

have been excluded from the review. Airborne-based studies are also excluded from this compilation as their temporal and spatial scopes are often limited by the mission design and thus, their insights are often not universally transferrable. The number of available publications since 1992 clearly has shown an upward trend. This implies that the present status of SAR-based snow cover monitoring is still in a developing stage (Malenovský et al., 2012; Snehmani et al., 2015).

2.3.1. SAR Sensors Used for Detecting Snow

Figure 2.2 presents an overview of commonly used spaceborne SAR sensors including their operation time span and band information. C-band SAR sensors stands out due to the longest available time series of continuous observations since 1992, which mainly thanks to the ESA's and Canadian Space Agency (CSA)'s missions, featuring ESA's pioneering ERS-1/2, Envisat, CSA's Radarsat-1/2, and the ESA milestone missions of Sentinel-1. The pioneering Active Microwave Instrumentation (AMI) C-band instrument equipped on oceanographic research-aimed ERS-1 satellite starts the era of C-band SAR for the following decades, although it was only aimed at aiding the scatterometer for deriving ocean wind and wave information (Attema et al., 2000). Together with the subsequent ESA's C-band missions, there have been a seamless time series of C-band imagery for more than 20 years. This time series became the most commonly used dataset for analyzing snow cover from SAR as the characteristics of C-band SAR is suitable for snow detection and the interchangeability of each C-band SAR sensor is guaranteed. Accordingly, the majority of published snow cover studies relying on SAR data are based on C-band sensors, with X- and L-band following on second and third position, respectively (see Figure 2.3 for a detailed overview).

Due to the longer wavelength of L-band SAR and the subsequently deeper penetration of the L-band signal into the snowpack, the snowpack remains nearly invisible in the L-band data (Strozzi, 1996). Therefore, studies about the implementation of L-band data to analyze snow cover properties are scarce although it has a longer history than X-band SAR. X-band SAR has been facilitated more often than L-band, which is due to the higher sensitivity of the X-band signal to the snowpack even when compared to C-band (Bernier and Fortin, 1998; Venkataraman et al., 2008). Moreover, multi-satellite constellations are available such as COSMO-SkyMed operated by the Italian Space Agency (ASI) and the TerraSAR-TanDEM-X twin satellite employed by Airbus Defense and Space and the German Aerospace Center (DLR).

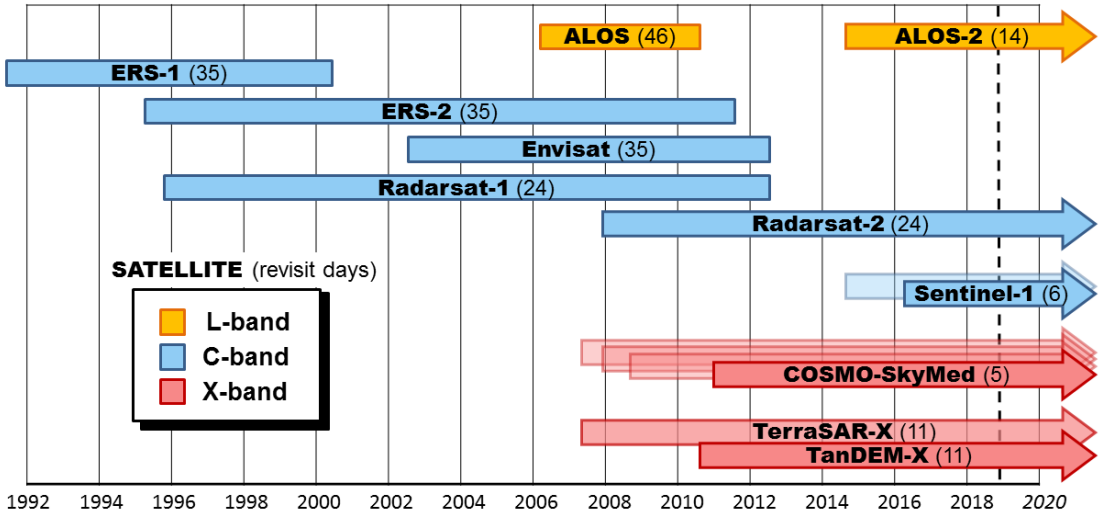

Figure 2.2 The operating periods of available satellites equipped with SAR sensors and their band as well as revisit time configurations (number in brackets referring to the revisit time in days). L-, C-, and X-band SAR refers to frequency of 1-2 GHz, 4-8 GHz, and 8-12 GHz; wavelength of 30-15 cm, 7.5-3.75 cm, and 3.75-2.5 cm, respectively (Bruder, 2013).

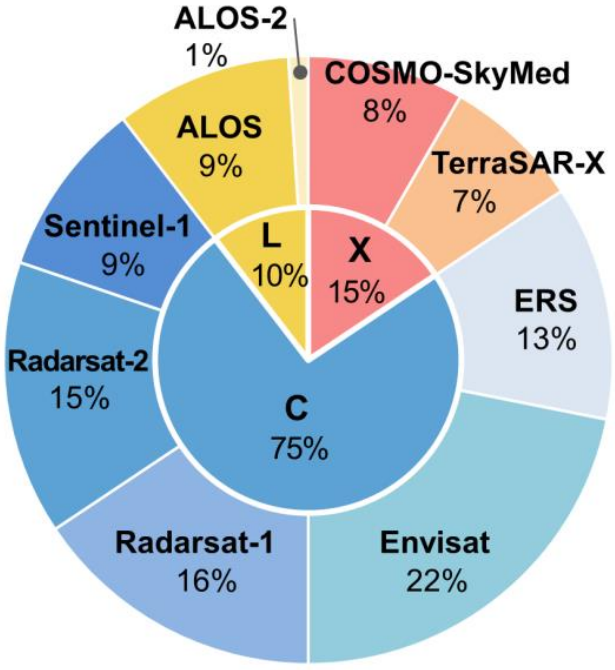

Figure 2.3 The frequency of different SAR sensors/bands being employed for snow cover studies.

2.3.2. Spatial and Temporal Scale of Snow Cover Studies

Snow covers extensive areas around the globe, including high altitudes featuring complex terrain, high latitudes, and boreal forests. It is important to get an overview of the study regions of the already conducted research. Additionally, some studies focus specifically on a certain land cover while excluding others (e.g., focusing on glaciers

or masking out any forested areas). In order to identify possible research gaps or areas where SAR-based snow cover analyses are still facing major challenges, every study incorporated in this review was evaluated by its location and land cover characteristics. Figure 2.4 presents the result of this evaluation, breaking the study regions down into study regions' types (Figure 2.4a), study mountainous regions (Figure 2.4b), and the distribution of study regions inside the European Alps (Figure 2.4c). The map presented in Figure 2.4d visualizes the locations of the studies and the frequency with which these regions have been investigated so far.

It can be observed that the majority of studies were conducted in mountainous regions, which is reasonable as these regions are frequently affected by cloud coverage so the advantage of SAR can be demonstrated. However, the relatively small number of studies conducted in forest and glacier areas was also noted although snow commonly exists in these region types. This finding suggested that the current SAR-based SCE detection studies still have further investigation potential in these regions. Regarding the hotspots of the frequently studied areas, Asian and European mountain ranges represent around 85% of available study regions, as also shown in Figure 2.4d. The European Alps have been studied most intensively (32%), followed by Himalaya (31%). Within the European Alps, most studies have been conducted in Italy and France (Figure 2.4c). Other global mountain ranges like the Andes, Caucasus, Rocky Mountains, or Ural have merely been investigated. Within the polar regions, several studies exist for Greenland and Antarctica, where the interaction between snow cover and glaciers has been investigated. The imbalance of study areas also indicates that more research is necessary in these areas.

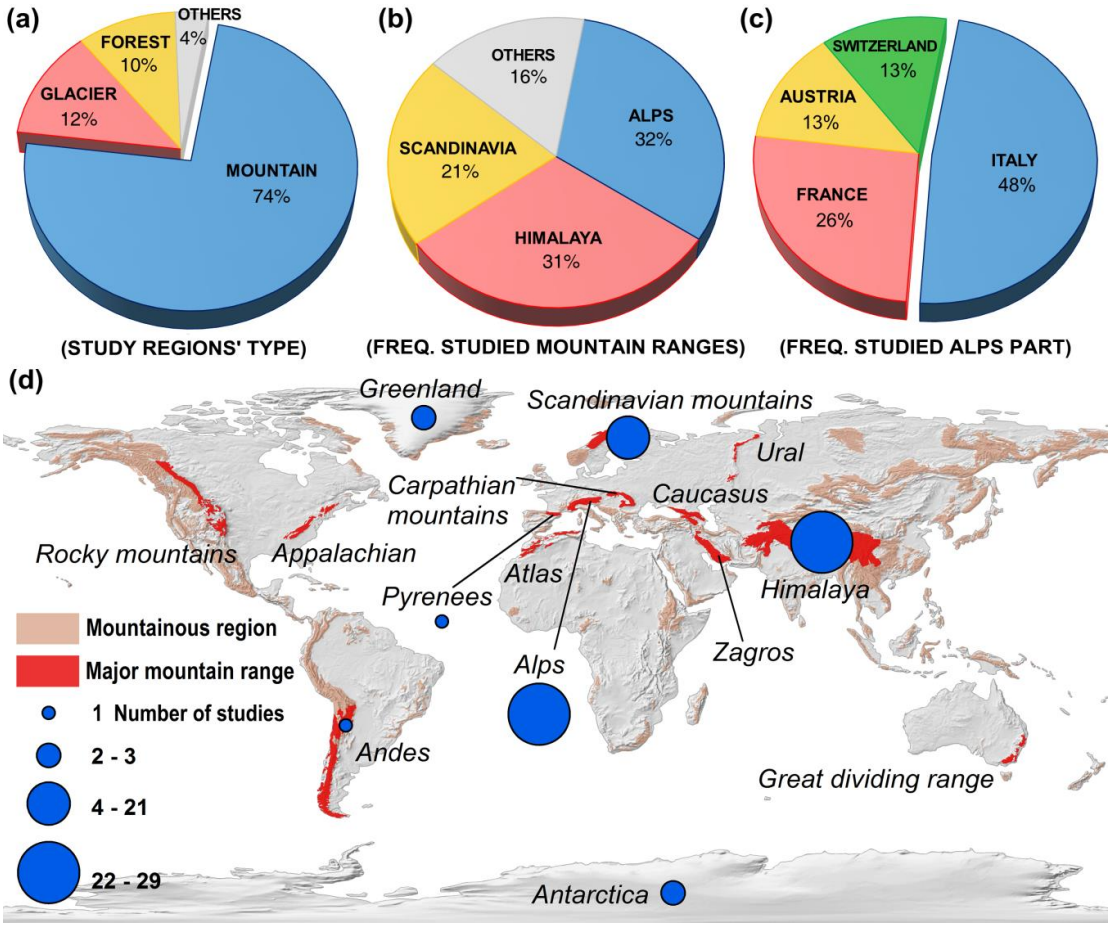

Figure 2.4 Overview of published SAR-based snow cover studies. (a) Study regions' type; (b) frequency of studied mountain ranges; (c) distribution among countries within the Alps; (d) geographic overview of performed studies.

Not only the location but also the spatial extent of the study regions is important as it can help assess the maturity and readiness of algorithms. Figure 2.5a illustrates the size of the study regions. Most of the studies were conducted on a local scale as visible in Figure 2.5a. These studies are usually limited to a specific test site, which in more than 50% of the cases is smaller than 2,500 km². Only five studies investigated areas greater than 200,000 km² (the size of Alps is around 298,128 km²). One motivation for these relatively small study sites is the spatial extent of typical SAR-data footprints itself. Many studies were designed to be conducted only within the boundary of a single SAR-footprint, which limits their extent according to the coverage of the respective SAR-mission.

When trying to evaluate the transferability of a study, not only the spatial extent is of interest, but also the amount of observations included. This information helps assess whether a proposed algorithm can work under different weather and snowpack conditions. The number of sensed years and the average number of observations conducted per sensed year is illustrated in Figure 2.5b and 2.5c, respectively. It must be noted that, even for studies we categorized as multi-year monitoring in Figure 2.5b,

none of them provide a consistent time-series of SCE result but only few random observations in each observation year. Hence, we further investigated how many observations were utilized on average for each year and study, and illustrated these findings in Figure 2.5c. Based on figures 2.5b and 5c, it can be found that more than half of the published studies investigated snow cover for one year with an average of two observations within this year to account for the dynamics of the snowpack (see Figure 2.5b and Figure 2.5c). These sparse observations indicate that current studies are still immature compared to the conventional optical-based SCE monitoring approach.

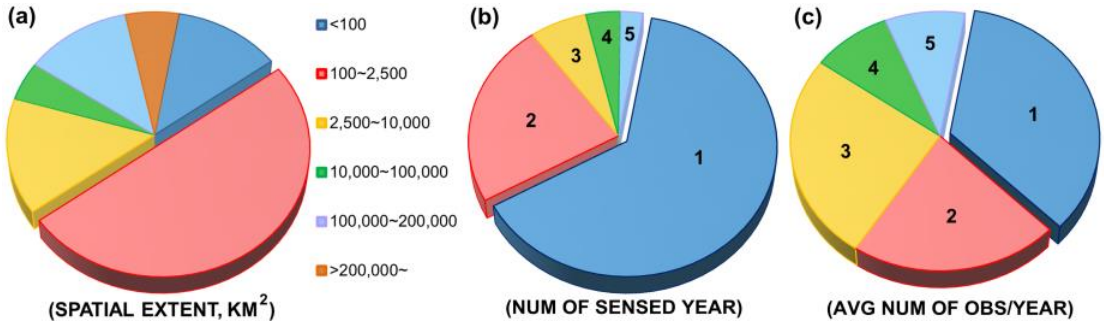

Figure 2.5 Spatial and temporal overview of published SAR-based snow cover extent (SCE) detection studies. (a) The spatial extent of studies; (b) number of sensed years; (c) average number of observations per sensed year. Note that none of the studies categorized as multi-year monitoring in (b) provide a time-series of SCE results, but only few random observations for each year. Thus the average observations conducted per sensed year of each study are illustrated in (c).

2.3.3. Employed Methods to Monitor Snow Cover with SAR data

As the development of SAR sensors and image processing techniques progresses, the sensing target of snow also changes. For the following discussion, we defined three different sensing targets of snowpack: Wet SCE, total SCE, as well as wet and dry SCE. Here we must address the difference between wet and dry SCE as well as total SCE, although the overall SCE can be retrieved by both strategies, only the former can discriminate wet and dry SCE, respectively. Namely, wet and dry SCE sensing strategies can provide more information than a total SCE approach.

2.3.3.1. Wet SCE Detection

The most commonly used approach to derive the extent of wet snow cover is by exploiting the backscatter coefficient. As outlined in Section 2.2, the backscatter coefficient drops significantly when a snowpack starts to melt, therefore containing liquid water, which decreases the dielectric constant.

The first algorithm to exploit this behavior was published by Rott and Nagler in 1995 and 2000 (1995; 2000). They relied on two SAR images (one is sensed during the snow-covered period σ^0_{ws}, and the other is a reference image σ^0_{ref} which is sensed in

either the snow-free or the dry-snow period) featuring the same imaging geometry (i.e., repeat pass pair) as well as a digital elevation model (DEM). The main workflow comprises pre-processing and wet snow mapping as illustrated in Figure 2.6. For pre-processing, the two images are calibrated, coregistered, multilooked, speckle-filtered, the scattering coefficient is transformed to a logarithmic scale (dB), the ratio between the two observations is calculated (see equation 2.1), and finally the result is geocoded. The geocoding is based on the DEM and produces a SAR layover mask, a shadow mask, and a LIA map. After pre-processing, the geocoded ratio map is classified based on a threshold to derive the binary wet snow extent. A threshold of -3 dB has proven to be robust enough to achieve satisfactory results, and was used in many subsequent studies.

$$\frac{\sigma^0_{ws}}{\sigma^0_{ref}} < -3\ \mathrm{dB}, \quad \text{wet snow} \tag{2.1}$$

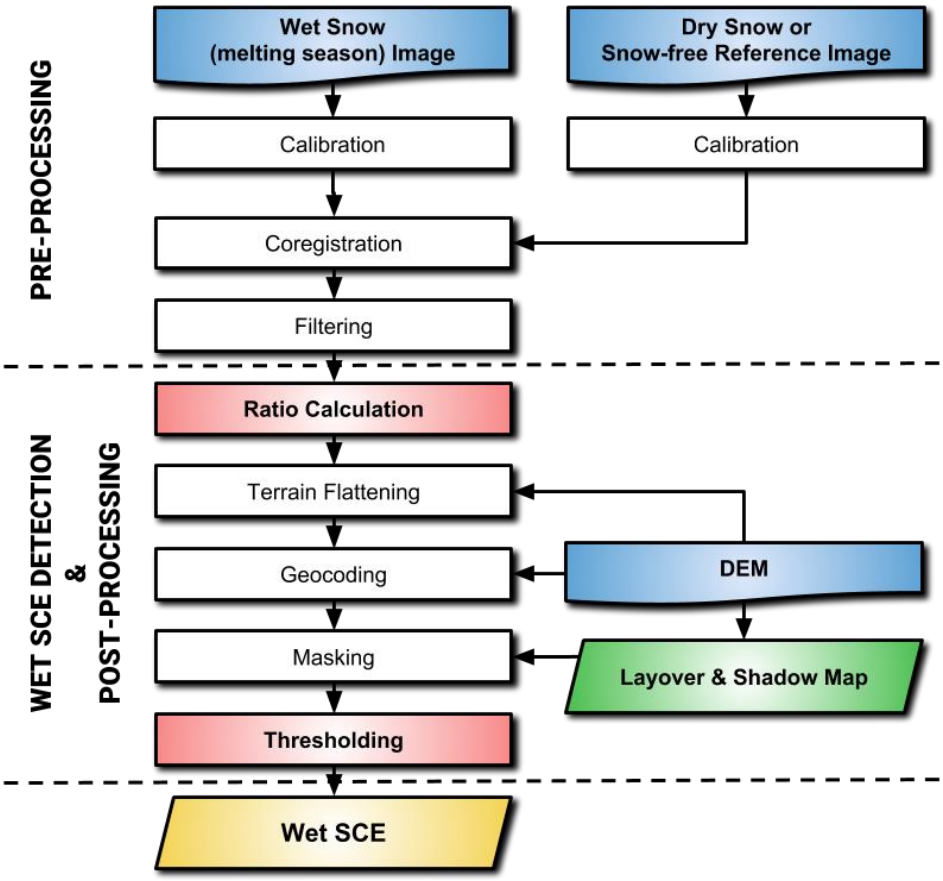

Figure 2.6 The overall workflow of the backscattering-based algorithm to detect wet snow.

As this method is easy to implement, it was applied successfully to most SAR sensors and study regions. Consequently, the backscattering coefficient-based method is known as “Nagler’s method”. Yet, this method uses only a single equation with a fixed threshold to retrieve the binary result; this result, however, is limited as the random noise of SAR would inevitably degrade the single image as mentioned in Section 2.1

and the binary snow results do not meet the real condition. Several improvements have therefore been achieved for “Nagler’s method”:

- Mapping of snow cover fraction

Binary snow cover products (i.e., a pixel is flagged as either snow covered or snow free) contain uncertainties especially along the transition between snow covered and snow free areas. Traditionally, a pixel containing more than 50% of snow cover would be considered fully snow covered in a binary product (Hall et al., 2001; Hall and Riggs, 2007; Notarnicola Claudia et al., 2013). Thus, an approach to derive fractional snow cover information from SAR-data is required. Therefore, Malnes and Guneriussen (2002) utilized a sigmoid-function based on the assumption that each pixel is a mixture of dry snow, wet snow and snow-free surface. This approach was later refined into different forms (Pettinato et al., 2006; Longepe et al., 2009).

- Refined reference image selection

Selecting a suitable image for representing the snow-free (or dry-snow) ground surface backscattering conditions is critical, as the ratio between this reference image and the observation containing the wet snow accounts for the accuracy of the wet snow detection. It is important to ensure that the reference image selection is selected carefully. Since Nagler’s first publication (2000), soil moisture has been frequently proven to bias single reference images (Baghdadi et al., 1997; Schellenberger et al., 2012). Thus, Pettinato et al. (2014) suggested reference scenes acquired under dry snow conditions recorded during wintertime. Another approach is using the average of several images originating from a similar sensing period (Ventura, Schellenberger, Notarnicola, Zebisch, Nagler, et al., 2011). However, the temporal distance between reference images has to be taken into account, ensuring that longer intervals between observations do not introduce additional uncertainties (Löw et al., 2002). Koskinen et al. (1997) selected one image observed during the melting period σ_i^0 and two reference images (one acquired at the beginning of melting period σ_w^0, and another acquired after melting period σ_g^0) to estimate the snow-free ground F_g:

$$F_g = 100 \times \frac{\sigma_i^0 - \sigma_w^0}{\sigma_g^0 - \sigma_w^0} \ \% \qquad (2.2)$$

Luojus et al. (2006) used the same formula in an approach proposed as the linear interpolation phase step. They applied the algorithm not pixel-based but at a bigger scale to eliminate the influence of SAR speckles. They also tested the usability of multi-year reference images; they concluded that the reference image does not necessarily need to be sensed in the same year as the classified melting season. Namely, a reference image from the past may be used to estimate future snow cover conditions.

Thanks to these improvements, “Nagler’s method” has remained the most commonly applied algorithm in the past 20 years. As numerous new satellites with different

wavelength designs have been launched since “Nagler’s method” was published in 2000, the -3 dB threshold value for the ratio map segmentation has also been customized for different sensors and locations (Löw et al., 2002; Magagi and Bernier, 2003; Rao et al., 2006; Venkataraman et al., 2008; Nagler et al., 2016b; Tsai Ya-Lun S, Dietz Andreas, et al., 2019b). However, as this approach cannot be applied to L-band SAR (because the backscattering values from the snow-covered scene and the reference scene containing no or dry snow are similar (Wang et al., 2015)) and can only detect wet SCE, other SAR-based algorithms have been explored as well.

2.3.3.2. Total SCE Detection

Based on the phase information of two SAR images recorded for the same location but at different observation times, the similarity of surface conditions (coherence) can be revealed based on interferometric SAR (InSAR) technique. The underlying theory of InSAR-based total snow detection is that, in comparison to snow-covered areas, the snow-free area can preserve a high coherence between two sensed dates. The reason for the decorrelation between snow-covered observations (in both dry and wet snow) is the alteration of the SAR penetrating depth and the scattering mechanism (Singh, Venkataraman, Rao, et al., 2008; Snehmani et al., 2015). Hence, in contrast to the backscattering-based approach presented in Section 3.3.1 that can only detect wet SCE, the InSAR-based approach can detect both wet and dry snow.

The first attempt of using repeat-pass InSAR techniques was conducted by Shi et al. (1997), utilizing space shuttle-based SIR-C images to create coherence maps. Later, Strozzi et al. (1999) pursued this approach, applying it to ERS images; they found that the coherence helps distinguish the SCE better than conventional backscattering-based methods. Guo et al. (2017) employed two pairs of InSAR observations sensed before and after a snowfall event, and classified the total SCE with coherence thresholds. Wang et al. (2015) proposed a more elaborate workflow to track the total SCE change in different periods. First, they used the normalized difference snow index (NDSI) derived from optical images as well as land cover information to initially estimate the tree and snow line elevation. Additionally, temperature information was incorporated to decide the actual snow condition. Finally, they applied a coherence threshold to derive the type of surface and snow cover change. Figure 2.7 illustrates the general workflow of InSAR-based algorithms to detect total snow cover.

The definition of an appropriate coherence threshold for the snow cover classification is critical. Wang et al. (2015) utilized an NDSI-based snow cover classification result to determine final coherence threshold for each area. However, using a hard threshold to classify snow cover may lead to misclassification, since the coherence values of snow-covered and snow-free areas largely overlap (Guangjun et al., 2015). To the authors’ knowledge, this problem has not been addressed in any study so far.

Another challenge for InSAR-based snow cover detection is the influence of various

additional factors on the coherence value. According to Zebker and Villasenor (1992), temporal, spatial and thermal factors influence the coherence value. Essentially, He et al. (2015) discovered that the coherence value is related to the polarization mode, land cover type, and LIA. Those factors need to be considered to improve the reliability of InSAR-based snow detection approaches.

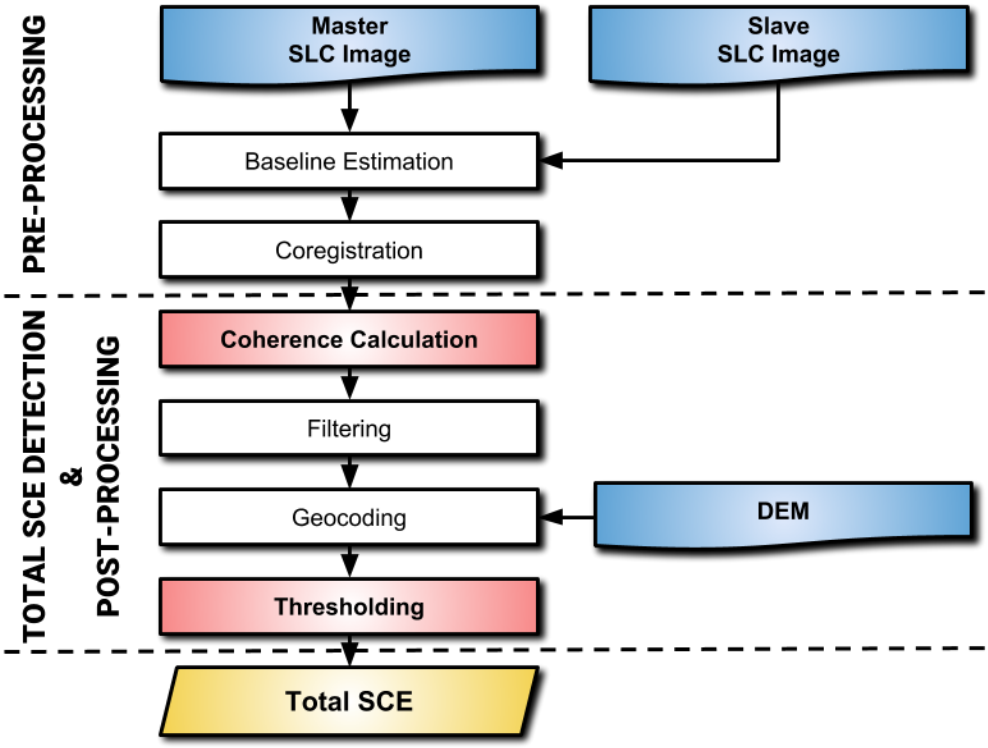

Figure 2.7 The overall workflow of interferometric SAR (InSAR)-based algorithms to detect total snow cover. Master and slave image refer to the two single look complex (SLC) SAR images used to generate an InSAR pair.

2.3.3.3. Wet and Dry SCE Detection

Initially, when polarimetric SAR (PolSAR) techniques were still immature, it was concluded that SAR is unable to detect dry snow (Malnes et al., 2004; Solberg et al., 2005; Solberg, Koren, et al., 2010). Nevertheless, as dry snow detection is crucial for applications like SWE estimation or other hydrological applications, empirical or topographical rules were applied to predict the dry snow based on the wet snow extent. Nagler and Rott (2000) presumed regions with elevations higher than the extent of the wet snow were dry snow. This method was modified (Malnes and Guneriussen, 2002; Ji et al., 2014; Thakur et al., 2016) and further improved by including measurements of air temperature (Malnes et al., 2004; Storvold and Malnes, 2004). Another approach is based on presumption of snow status change with time as shown in Pettinato et al. (2004) and Brogioni et al. (2006).

However, those wet snow based approaches to estimate the dry snow extent have proven inaccurate. Studies following Malnes's method to derive dry SCE found large

overestimations (Solberg et al., 2005; Solberg, Koren, et al., 2010). In addition, Storvold and Malnes (2004) stated their algorithm could face problems in early spring when dry snow extent could be extensive while wet snow still being absent. Moreover, these approaches do not account for the influence of wind to redistribute snow (Storvold and Malnes, 2004). Consequently, an alternative approach, i.e., PolSAR technique, was explored to detect wet and dry SCE directly from SAR imagery.

Rott (1994) proposed a depolarization approach, i.e., calculating the ratio of cross- and co-polarization of airborne AIRSAR; Shi and Dozier (1997) used SIR-C/X-SAR to test multi-frequency and multi-polarization. Early spaceborne SAR sensors; however, were generally only equipped with single polarization ability, such as ERS-1/2 (VV) and Radarsat-1 (HH). Dual polarization mode became available after the launch of ENVISAT-ASAR in 2002, offering new possibilities to explore the potential of multi-polarization repeat-pass methods for snow cover mapping.

The key of PolSAR-based wet and dry snow cover detection is to extract the geometrical scattering characteristics of ground features by decomposing the received SAR signal. The backscatter from each ground feature is composed by various unique signal-feature interactions; PolSAR decomposition therefore offers the possibility to reveal how a particular surface feature reflects the incoming SAR signal and what physical characteristics that feature might have. For instance, the frozen forest canopy leads to high correlation of the polarization due to surface backscattering during wintertime, while low correlation results from the snow-covered ground surface. Once the snow becomes wet, the polarization correlates again (Muhuri, Ratha, et al., 2017).

The development of PolSAR techniques led to numerous decomposition methods to derive PolSAR parameters. The most commonly employed decomposition parameters include Pauli decomposition (Cloude and Pottier, 1996) and H/A/$\bar{\alpha}$ (Cloude and Pottier, 1996). They decompose the coherence matrix in different ways and thus form different parameters, such as former's single/odd, double/even bounce and volume scattering. The H/A/$\bar{\alpha}$ decomposition can even reveal the scattering angle and degree of randomness of the sensed target. For detail decomposition theory and examples can refer to (Touzi et al., 2004; Zhang et al., 2008). However, as there are countless decomposition indexes, selecting the most feasible parameter is challenging. He et al. (2017) calculated the Jeffreys—Matusita (J—M) distances (Bruzzone et al., 1995) to filter feasible parameters for distinguishing dry and wet snow. Huang et al. (2011) plotted the normalized value of each parameter of each land cover type to observe their overlap. The parameters showing fewer overlapping of dry and wet snow were chosen.

Due to the various information (referring to appendix) that can be retrieved from PolSAR parameters, more details about the characteristics of snow cover can be obtained when compared to backscattering- or InSAR-based approaches. For

instance, Baghdadi et al. (1998) revealed that backscattering of wet snow is primarily caused by surface scattering; Shi and Dozier (1995) found that snow wetness is proportional to surface scattering and inversely proportional to volume scattering. In addition, the morphology of snow also influences the scattering, such that an older snowpack would have larger grain size and thus would lead to increased volume scattering (Singh et al., 2014). Singh et al. (2014) found that snow-covered regions show lower entropy, H(1-A) as well as higher polarimetric anisotropy; thus they proposed a threshold method to detect snow cover, which resulted in an accuracy comparable to a supervised Wishart classification. Reppucci et al. (2012) observed that dry snow is characterized by higher values in the Pauli surface parameter and lower value in the double-bounce parameter. Therefore, a combination of the two parameters enables to calculate the difference and then to map dry snow cover. Based on the observation that dry snow shows lower H and $\bar{\alpha}$ values, they also derived the ratio of H and $\bar{\alpha}$ to detect dry snow. Similar techniques were employed by (Park et al., 2014; Muhuri, Manickam, et al., 2017; Muhuri, Ratha, et al., 2017; Zhou and Zheng, 2017; Muhuri et al., 2018), calculating the difference of available parameters or relying on machine learning (ML) classifications to detect snow cover. Venkataraman et al. (2010; 2011) even proposed a Radar Snow Index (RSI) to estimate the total SCE based on polarization fraction parameters. To deal with the influence of underlying land cover types, Martini et al. (2006) suggested an advanced supervised polarimetric contrast variation enhancement (PCVE) to enlarge the contrast of dry snow.

Based on the research from recent years it became obvious that PolSAR-based detection of snow cover is developing quickly and that there is still potential to improve and complement existing approaches. Figure 2.8 presents an overview of the three different mainstreams of PolSAR-based wet and dry snow cover detection algorithms.

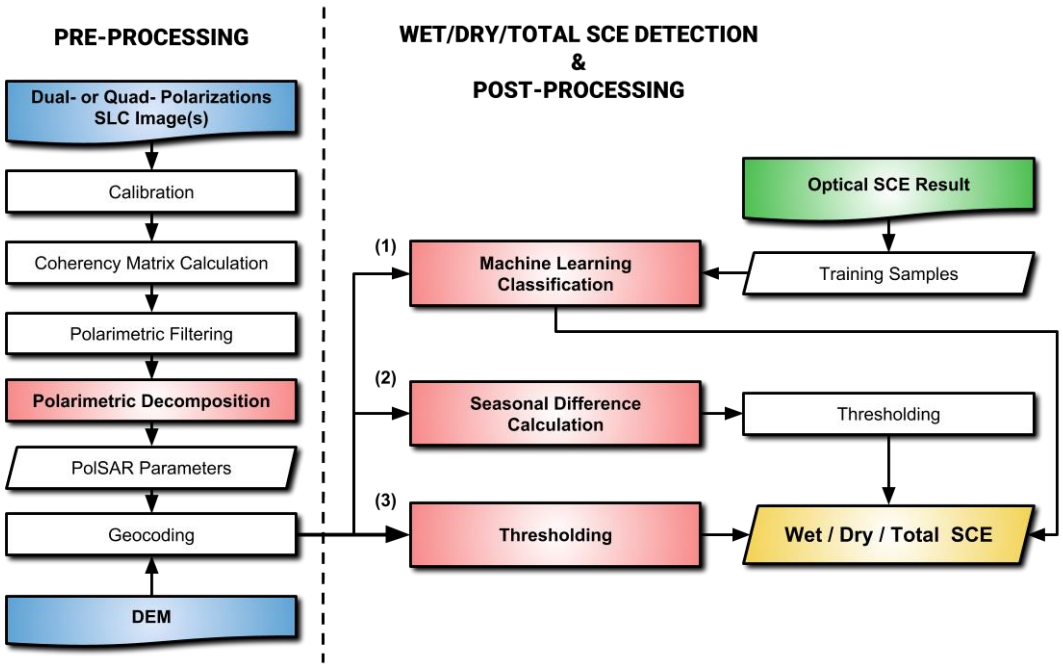

Figure 2.8 The overall workflow of polarimetric SAR (PolSAR)-based algorithms to detect wet and dry snow cover, including (1) machine learning classification trained by external SCE result; (2) the calculation of seasonal parameters' difference before thresholding, and (3) the direct thresholding.

2.3.4. Algorithms Utilized to Investigate the Different Snow Cover Types

After reviewing the advancements in detecting snow cover from SAR data within the last three decades, a comprehensive overview of the different mapping approaches for different snow cover types that can be observed relying on these approaches emerged, which is presented in Figure 2.9. When analyzing the snow type, the review revealed that more than half of the available studies focused on the retrieval of wet snow only, while 30% of the studies aimed at both, wet and dry snow (Figure 2.9a). Less than 16% of the studies were designed to retrieve total SCE or dry snow only. This mismatch does not indicate that dry snow is less important than wet snow but it clearly shows that the detection of dry snow from SAR-data is still challenging.

The different approaches to detect wet, dry, and total SCE (Figure 2.9a) can further be divided: For wet snow (Figure 2.9b), 82% of studies employed "Nagler's method", while InSAR- and PolSAR-based approaches account for 7% and 10%, respectively. Regarding dry snow (Figure 2.9c), more than 60% of the studies relied on topographic empirical determination, which is an approach frequently employed together with "Nagler's method" (see Section 3.3.3). Another 21% and 10% of the studies utilized PolSAR (including PCVE) and InSAR techniques, respectively. The remaining 7% of the studies applied logic conditional rules to identify dry snow extent. When it comes to the detection of total SCE, (Figure 2.9d), 77% of the reviewed studies relied on PolSAR while only 23% applied InSAR techniques. In summary, when reviewing

Figure 2.9, the predominance of PolSAR and InSAR for dry and total snow cover detection becomes obvious, while backscattering-based approaches are clearly the methods of choice to detect wet snow.

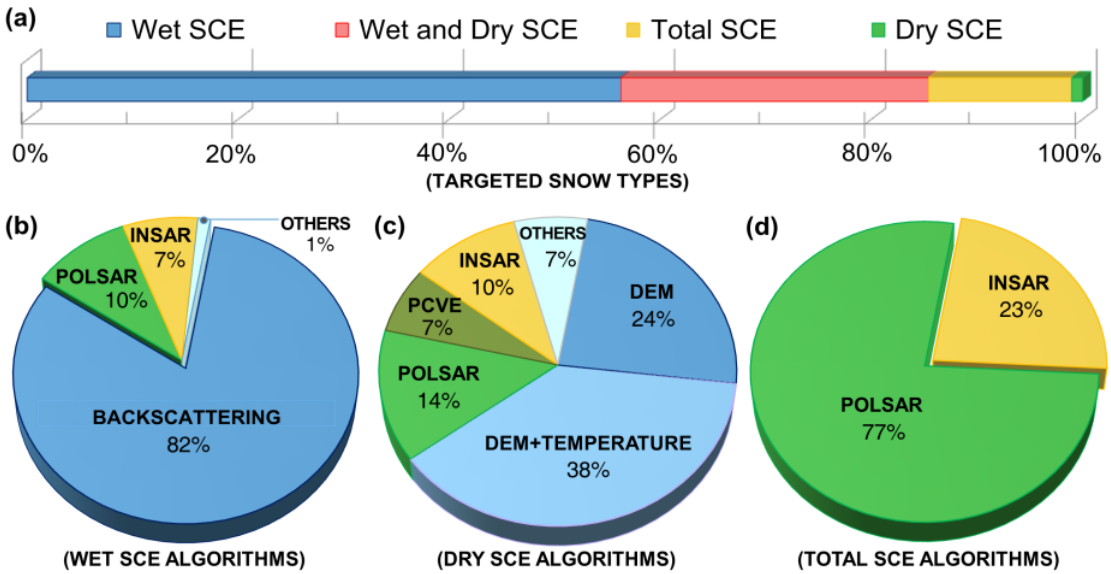

Figure 2.9 Overview of targeted snow types and corresponding algorithms. (a) Targeted snow types and employed algorithms for (b) wet (c) dry (d) total snow cover extent (SCE).

2.3.4.1. Machine Learning Classification Methods for Advanced SAR Information Analysis

Additionally to the aforementioned algorithms, ML is commonly performed on advanced SAR-derived information especially derived from PolSAR-based approaches. Because SAR images can contain a considerable amount of noise, the derived PolSAR parameters are often challenging to be manually extracted. As PolSAR-based approaches are a comparatively new technique, the number of studies employing ML classification is small (only 19%). Owing to the maturity of optical-based snow cover monitoring techniques and products, training samples for supervised algorithms are available. Thus, supervised algorithms are slightly more common than unsupervised approaches.

The most commonly employed supervised ML classification approach is the support vector machine (SVM), which is well known for its ability to solve high-dimensional non-linear classifications with only small samples (Camps-Valls and Bruzzone, 2005). Compared to maximum likelihood and decision tree methods, SVM produced higher snow cover classification accuracies (Huang et al., 2011) and thus was utilized for both InSAR-based (Guangjun et al., 2015; He et al., 2017) and PolSAR-based studies (Longepe et al., 2008; Huang et al., 2011). However, random forest (RF) also attracts attention for its simplicity and low computation load (Tsai Ya-Lun S, Dietz Andreas, et al., 2019b).

2.3.5. Quality Assessment Methods for SAR-based Snow Cover Products

In the present SAR-based mainstream algorithms, there is no straightforward method to directly generate reliability indices to allow self-validation as in other SAR-based cryospheric studies such as the signal-to-ratio value of pixel-offsets for glacier velocity tracking (Tsai et al., 2018). Thus, several studies focused on quality indicators for assessing the reliability of a snow cover products. Malnes et al. (2004) and Solberg et al. (2005) utilized a confidence flag denoting the probability for a correct classification; Schellenberger et al. (2012) introduced the probability of error (POE) to evaluate each pixel's classification reliability. Practically, validating SAR-based snow cover products using external, independent data is preferable. Overall, around half of the reviewed studies utilized snow cover products derived from spaceborne optical sensors as ground truth, with Landsat and MODIS accounting for most of the employed sensors (Figure 2.10). AVNIR-2 is used for validating PALSAR-based studies, as both sensors are mounted on the same satellite platform. Sentinel-2 is usually used for comparisons with Sentinel-1 results; Gaofen-1 (GF-1) is often utilized for validating studies in mainland China. Airborne and ground-based data account for a much smaller portion of validation approaches owing to the relatively high costs and limited spatial coverage. The fact that ~40% of the reviewed studies did not include any validation at all indicates that many of the published SAR-based snow detection techniques are in an early stage of their development.

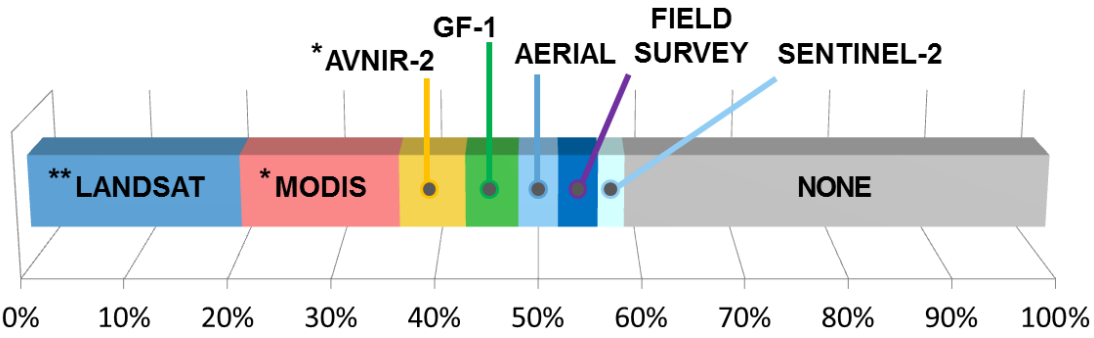

Figure 2.10 External/Ground truth data used for validating SAR-based snow cover products. *Advanced visible and near infrared radiometer type 2 (AVNIR-2) sensor onboard on Advanced land observation satellite (ALOS) satellite; moderate resolution imaging spectroradiometer (MODIS) sensor onboard on Terra and Aqua satellites; **Landsat-series missions compose different optical sensors.

In addition to conventional confusion matrix-based accuracy evaluations, Luojus et al. (2006; 2007) proposed a quantitative analysis approach based on the RMSE to check the improvement made by each refining algorithm; Reppucci et al. (2012) compared the resultant SCE with an elevation map to check whether the distribution of snow is reasonable.

2.4. Critical Auxiliary Data Necessary to Support Detecting SCE from SAR Data

In addition to the sensor types and algorithms, other critical and commonly employed datasets help improve the accuracy of the obtained snow cover classification, including DEM, land cover maps and meteorological information. As shown in Figure 2.1, these parameters directly affect snow cover distribution and condition, and it is therefore advisable to include these auxiliary datasets to the workflow. They may not be necessary to operate the SAR-based snow cover detection; they, however, can improve the quality of the results.

2.4.1. Digital Elevation Model, Influence of Topography on SAR-based Snow Detection

The influence of the topography on SAR-based snow cover detection is evident, as snow cover distribution is directly linked to elevation, aspect (facing direction of topography), and slope of the study region. Moreover, local topography affects the LIA, which largely affects the quality of SAR image pre-processing and final results.

Elevation plays a significant role in snow cover distribution. Algorithms like the wet snow-dependent dry snow detection relies on the spatial relationship between wet and dry snow cover extent and elevation (see Section 3.3.3). Haefner (2001) analyzed the seasonal difference of backscattering coefficients in various elevation zones and found larger differences in higher altitudes. Tsai et al. (2019b) also found the importance of elevation is crucial for total snow cover mapping. Aspect and slope are also critical for not only how snow is distributed but also how SAR can sense the snow. Li et al. (2012) compared the snow line altitude for several regions and discovered that glaciers facing south have higher snowline altitudes, which is caused by more intense solar radiation on south facing slopes. Park et al. (2014) identified that the seasonal difference between H and α is more pronounced for front-slope (the slope facing the sensor).

Topography not only affects snow distribution, it also affects the SAR signal viability. Based on the DEM a shadow and layover map of SAR can be generated. Steeper topography or regions closer to the nadir of the sensor would naturally lead to more SAR shadow and layover regions (Bartsch et al., 2007), where useful ground information is blocked or degraded. Hence, almost all studies calculated the mask during the geocoding step and later re-used it to mask out the results, as illustrated in Figure 2.6. However, these terrain-induced radiometric effects and the local illuminated brightness should be mitigated by adding a terrain correction based on DEM as well as the acquisition geometry of SAR (Small, 2011).

Moreover, for the backscattering-based approach, the influence of LIA on the SAR signal was already identified in Nagler's first research (2000), and confirmed by many subsequent studies (Baghdadi et al., 2000; Guneriussen et al., 2001; Löw et al., 2002; Magagi and Bernier, 2003; Besic et al., 2015). The backscattering of wet snow is more

susceptible to the variability of LIA than dry snow because the backscatter of the latter is mainly reflected from the snow/ground interface, as modeled by Malnes and Guneriussen (2002). Nagler et al. (2016b) found the backscattering from snow can decrease even more for a very high LIA, which reduces the difference between wet and dry snow. This angle-dependency influences the accuracy of backscattering-based thresholding approaches, especially for wide-swath SAR images such as ASAR and Radarsat (Storvold and Malnes, 2004; Zhou and Zheng, 2017). It was also suggested that the LIA difference between the reference and the observed image should not exceed 10° (Luojus et al., 2007). The range direction resolution would also decrease dramatically in low LIA, and the signal-to-noise ratio for low reflective surfaces decreases in high LIA (Nagler et al., 2016b). Therefore, areas with extreme LIA values should be masked out by setting LIA limitations (Rott and Nagler, 1995; Nagler and Rott, 2000; Schellenberger et al., 2012; Nagler et al., 2016b).

The influences of LIA on both InSAR-based and PolSAR-based approaches are also significant. He at al. (2015) found the coherence value increases from 0° to 30° LIA and decreases from 30° to 90° LIA. Dedieu et al. (2012) found that when the LIA is less than 35°, the dominant scattering mechanism changes from volume to single-bounce scattering. Park et al. (2014) revealed that the change of H and α caused by the snowpack would be smaller for lower LIA. Usami et al. (2016) observed that the degree of polarization decreases when the LIA increases. Furthermore, several studies found that the impact of surface roughness on the signal is more significant for high LIA (Ulaby et al., 1986; Holah et al., 2005).

2.4.2. The Influence of Land Cover (Vegetation) on Snow Detection from SAR-data

Another factor affecting SAR-based snow cover detection is land cover. This effect was first described by Koskinen et al. (1997) when they analyzed the backscattering coefficient values of different surface conditions depending on different types of land cover. Results clearly showed that the presence of vegetation significantly decreases the backscattering difference between wet snow and dry snow as well as bare ground. Schellenberger et al. (2012) also reported that snow-covered and snow-free areas in forest regions are difficult to discriminate as the backscatter is significantly influenced by canopy (Karam et al., 1995).

According to the model proposed by Pulliainen (1994), SAR backscattering relates to the transmissivity of a forest canopy, which is influenced by stem volume. The different scattering coefficient levels of grassland, crop field and dense forest confirm these results (Löw et al., 2002; Schellenberger et al., 2012). Duguay and Bernier (2012) found that backscattering coefficient is continuously increasing with increasing vegetation height. Therefore, applying only one fixed backscatter threshold to classify snow cover in a region with varying land cover may lead to inaccurate results (Löw et

al., 2002). Additionally, results from polarimetric models indicate that backscatter of dry snow is strongly sensitive to the underlying surface as the backscattering originates from the snow/ground surface interface (Martini et al., 2006; Park et al., 2014). He et al. (2017) concluded that stems of snowcapped shrubs and grass lead to higher volume scattering for dry snow than for wet snow. Dedieu et al. (2012) reported difficulties detecting snow cover in forested areas as the tree structure affects the scattering of the SAR signal (double-bounce with tree trunks, volume scattering with foliage and single scattering with forest floor). The seasonal phenology of trees (leaf fall before winter) also alters the scattering behavior. Park et al. (2014) concluded that the presence of woodlands could increase volume scattering as well as H and α.

Forest also affects InSAR-based approaches. The coherence values of InSAR are found to be commonly lower in densely vegetated regions (Guangjun et al., 2015; He et al., 2017). Thakur et al. (2013) concluded that this reduction in coherence is connected to both snow cover and the presence of forests. Kumar and Venkataraman (2011) reported that the random motion of leaves due to wind would reduce the coherence significantly.

Aforementioned studies intensively indicate that vegetation would limit the accuracy of SAR-based snow detection approaches; however, based on previous studies there is no decisive threshold for any vegetation index such as biomass or canopy closure. As a result, many studies use masks to eliminate the influence of densely forested regions. Rott and Nagler (1995; 2000) as well as Notarnicola et al. (2013) masked the agriculture areas. Practically, external land cover products (Luojus et al., 2007; Notarnicola C. et al., 2013; Guangjun et al., 2015; He et al., 2017) or land cover maps generated during the pre-processing workflow (Dedieu et al., 2012; Notarnicola et al., 2012; Thakur et al., 2013; Wang et al., 2015) may serve as masks. Masking of critical land cover regions; however, may reduce the size of the study region considerably. Therefore, Schellenberger et al. (2012) divided the backscattering ratio map for each land cover and calculated the geometric mean for each class as its threshold; Tsai et al. (2019b) built the model for each land cover type and mapped total SCE individually.

2.4.3. Utillization of Temperature and the Need for Snow Record Data

Although most SAR-based algorithms such as “Nagler’s method” (Nagler and Rott, 2000) did not require ground information as an input, meteorological data about temperature and precipitation makes estimating the snow cover conditions easier. For example, it is possible to infer the retreat of snow between two observations if the daily mean air temperature is rising (Pettinato et al., 2006) and the existence of wet snow can be postulated when surface temperature is observed to be near 0 °C (Solberg, Koren, et al., 2010). Thus, many studies included temperature information gathered by ground surveying or meteorological stations (Park et al., 2014; Pettinato et al., 2014; Singh et al., 2014; Guangjun et al., 2015; He et al., 2017; Paloscia et al.,

2017; Muhuri et al., 2018).

However, the often sparsely distributed meteorological stations hardly satisfy the required spatial resolution necessary to derive an areal inventory of surface temperatures. Hence, Malnes et al. (2004) calculated a temperature map by interpolating the data derived from meteorological station network. Another approach is utilizing spaceborne thermal imagery. Salcedo and Cogliati (2014) used atmospheric profiles of temperature and water vapor at the sensed time to derive the surface temperature based on recorded satellite radiance. Moreover, snow record data also helps to analyze the snow cover conditions. Luojus et al. (2009) utilized the snow accumulation recorded by snow stations to decide when the snowmelt period ended.

2.5. Discussion

The studies investigated in this review show that SAR-based methods to detect and characterize snow cover have been developing rapidly and profoundly within the last three decades. This development includes the design of new spaceborne SAR sensors, new algorithms to detect snow, higher spatial and temporal resolutions of the derived products, increasing accuracy, and a deeper understanding of the underlying processes. The developments identified will be discussed in more detail in the following sections.

2.5.1. The Developement of Spaceborne SAR Sensor Design

The development of SAR sensors advanced remarkably within the last 25 years in terms of instrument design, temporal and spatial coverage, and data distribution policy. Band design was limited to C-band, but has been extended to X-band, as shown in Figure 2.2. This offers new opportunities to detect and monitor snow cover, because the capabilities of X-band SAR to detect snow are superior to C-band, as outlined in Section 3.2. Moreover, study suggested that Ku-band SAR may be most suitable to detect snow cover as it can detect even shallow and dry snow (Mätzler, 1987), which was planned (but not realized) for ESA's 7th Earth Explorer mission candidate, Cold Region Hydrology High-resolution Observatory ($CoReH_2O$) satellite, meant to be equipped with X- and Ku-band SAR sensors (Rott et al., 2007).

Furthermore, the capabilities to detect snow relying on different polarizations attracted more attention. Among all snow cover detecting studies based on polarimetric information, almost all employed SAR images in full-polarimetry mode including PALSAR-1 (Venkataraman et al., 2010; Park et al., 2014; Singh et al., 2014; He et al., 2017) and Radarsat-2 (Huang et al., 2011; Dedieu et al., 2012; Reppucci et al., 2012; Callegari et al., 2016; Muhuri, Manickam, et al., 2017). Early airborne SAR and recent spaceborne studies already suggested that multi-polarization SAR—and especially fully polarimetric SAR—is more suitable to detect snow and ice than single/dual-polarization (Rott and Davis, 1991; Thakur et al., 2013; Callegari et al.,

2016). Possible reasons are that multi-polarimetric SAR has a higher sensitivity to the state of snow (Dedieu et al., 2012) and that it can greatly eliminate the topographic distortion (Singh et al., 2014).

Shortening the revisit time is another advantage of contemporary SAR missions. Practically, the time difference between two repeat-pass SAR images is the most important factor for InSAR-based approaches. Researchers have confirmed that the coherence of InSAR within snow-covered areas would decrease dramatically if the temporal difference is more than one month (Rao et al., 2006). In addition, if the revisit time is too long, more than one melting/snow fall event may have occurred in the meantime (Wang et al., 2015). In this regard, the value of the COSMO-SkyMed (CSK) constellation is remarkable. Thanks to their orbit design, four satellites (CSK1-4) significantly shorten the revisit time and thus largely eliminate temporal decorrelation (Martone et al., 2012; Rizzoli et al., 2017), which provides a potential to map SCE with a much higher temporal resolution (Notarnicola et al., 2012).

The wider swath coverage of contemporary SAR sensors allows snow monitoring in larger spatial scales, which may also reduce costs. Nagler and Rott (2005) proved that all sensing modes of ASAR images are suitable for processing “Nagler’s method”. Although the definition of wide swath mode varies for different sensors (e.g., ASAR’s 150 or 500 km, Radarsat’s 300 or 500 km, PALSAR’s 250 or 350 km, and Sentinel-1’s 250 km), it is clear that they are more efficient than traditional sensing modes providing swath widths below 100 km.

In addition to sensor’s hardware design, another important milestone is the free data policy of ESA. Before Sentinel-1, no long-term, openly accessible SAR datasets were available, which stands in contrast to the free of charge archives of optical sensors such as Landsat and MODIS. As a result, until recently the cost of spaceborne SAR data was much higher compared to optical imagery (Solberg, Koren, et al., 2010), which inevitably limited the operational use of SAR-based snow cover detection or the subsequent possibility of merging SAR and optical snow cover products.

2.5.2. The Advances of SCE-detection by SAR

Conventional backscattering-based approaches were subject to criticism for using a hard threshold to classify snow cover, as numerous factors may affect the backscattering value. For instance, in a warm winter more frequent melting/refreezing cycles would lead to bigger grain sizes and thus influencing the backscattering coefficient (Dedieu et al., 2014); sudden changes of air temperature or heavy snowfall events may cause snow metamorphism, altering the snowpack conditions (Paloscia et al., 2017). Variations of soil moisture may also disturb the backscattering coefficient values (Baghdadi et al., 1999). Moreover, the geometry of two images needs to be identical to preserve similar LIAs (Baghdadi et al., 1999). If thresholds are set too low/high, the final SCE would be under/overestimated. However, backscattering-based algorithms also show one great advantage, i.e., they do not

require training samples for classification. This fact avoids the manual selection of a classifier and saves time for the classification, which is an asset for an automated processing over longer periods or large regions.

In contrast to backscattering-based approaches, PolSAR-based algorithms have the merit of less LIA dependency. Hence, theoretically they are more suitable for mountainous terrain. Another benefit is the availability of additional information such as scattering angle and degree of randomness inherent to the polarimetric data. Furthermore, PolSAR technique only requires one image, which increases the sensing frequency and real-time monitoring capabilities. The different ways to decompose the covariance matrix, however, results in countless derived parameters; a suitable selection of included parameters and a proper filtering of redundant data therefore is critical. Moreover, the process of decomposition is more time-consuming when compared to backscattering-based approaches as it involves more matrix calculations.

InSAR-based algorithms are supported by the maturity of available InSAR processing software. The main challenge is the revisit interval of the SAR sensor and the sometimes rapid change of snow cover conditions (depending on location, weather conditions, and season). Nevertheless, it can be postulated that InSAR-based approaches may become more promising in the near future, as the revisit time of SAR sensors has enhanced significantly. Overall, the comparison of mainstream SAR-based approaches is shown in Table 2.3, which provides guidance for choosing the appropriate algorithm based on the targeted snow cover type and SAR image availability.

Table 2.3 Overall comparison of the three mainstream SAR-based snow cover detection approaches.

Detection approach	**Backscattering-based**	**InSAR-based**	**PolSAR-based**
Background theory	The backscattering coefficent reduces when snow becomes wet	Coherence loss over snow covered surfaces	Scattering mechanisms of dry and wet snow and the surface behave differently
Minimum numbers of required SAR images	2	2	1
SAR image requirements	Pair sensed at the same geometry	Pair has a short temporal baseline	Image has dual or quad polarizations
The complexity of the algorithms	Low	Medium	High

Primarily analyzed component	Backscattering coefficient	Coherence	Polarimetric parameters
LIA dependency	High	Medium	Low
The richness of derived information	Medium	Low	High
The noisiness of derived information	High	Low	Medium
Snow Type Sensing Capability			
Wet snow	Yes	No	Yes
Dry snow	No	No	Yes
Total snow	No	Yes	Yes

In addition to the aforementioned three main SAR-based approaches, other more elaborate possibilities should be further investigated, such as the information theoretic snow detection algorithm (ITSDA) proposed by Pettinato et al. (2014). A fusion of the three mainstream SAR-based approaches is another option: He et al. (2017) facilitated the information derived from all three mainstream technique to a SVM classifier to map both dry and wet SCE; Tsai et al. (2019b) utilized RF to map total SCE based on backscatter, InSAR coherence, and PolSAR H/A/$\bar{\alpha}$ parameters in five study areas around the globe. The total and wet SCE estimated by Tsai et al. (2019b) is illustrated in Figure 2.11, which demonstrates the great value of fusing all three main SAR-based approaches to derive the holistic (total + wet) SCE. The holistic SCE enables not only investigating the dynamics of SCE and snowpack by comparing different seasons' SCE conditions but also the potential of further integration with conventional optical sensor-based cloud-affected SCE results.

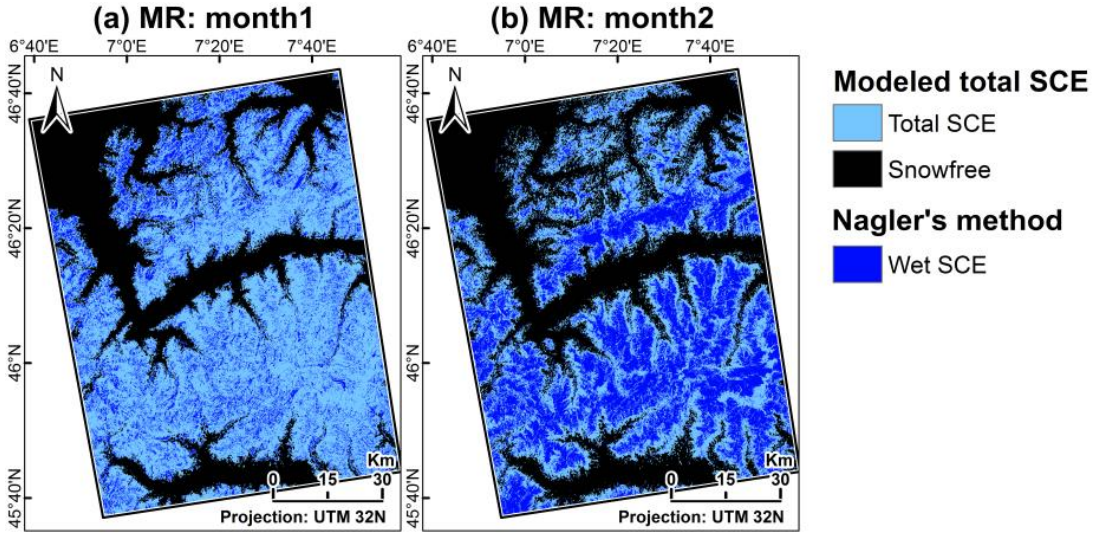

Figure 2.11 Total and wet SCE of Monte Rosa (MR) region (a) month1: 2018 March

12 (b) month2: 2018 May 11. Figures are revised from Tsai et al. (Tsai Ya-Lun S, Dietz Andreas, et al., 2019b). Note the total SCE is modeled based on backscatter, InSAR coherence, and PolSAR parameters; wet SCE is estimated based on conventional backscatter-threshold approach.

When it comes to the ML classification method, considering the recent advances in deep learning (DL) algorithms and computer hardware, there have been few attempts utilizing the neural network to detect snow in SAR imagery, such as Usami et al. (2016) and Nijhawan et al. (2018), which showed a classification accuracy that was comparable to conventional ML algorithms.

2.5.3. Solutions for Addressing SAR-vegetation Interaction

As mentioned in 4.2., the presence of vegetation would limit the viability of SAR-based snow cover classification approaches. The most successful algorithm specifically for forested regions was developed by Koskinen et al. (1997), utilizing two reference images to minimize the effect of a forest. Based on that, Luojus et al. (2006; 2006; 2007; 2009; 2009) accomplished several improvements resulting in the Helsinki University of Technology (TKK)-developed snow cover detection method aiming at boreal forest regions. Its forest compensation algorithm makes use of a semi-empirical forest backscattering model, which utilizes the stem volume information to estimate the amount of backscattering originating from the forest and further eliminates this factor from subsequent calculations.

However, in addition to the general problem of lower accuracy in open areas, the biggest limitation of the TKK method is that it requires prior knowledge of forest stem volumes, which is difficult to obtain. Thus, a purely spaceborne image-based approach to address the interaction between SAR imagery and vegetation needs to be developed. Hopefully, in the recent paper published by Tsai et al. (2019b), a land cover type-dependent classification strategy which can be applied to densely vegetated forest and agricultural regions was proposed. The method was tested in five mountainous study areas around the globe and the accuracy above 0.75 is confirmed in all regions by validation with optical-based SCE product. This study provides a novel way to map SCE in all land cover types and should be utilized in the future studies.

Additionally, the potential of utilizing PolSAR, Polarimetric Interferometric SAR (PolInSAR) as well as Tomographic SAR (TomoSAR) to estimate 3D forest structure and biomass (Minh et al., 2014; Kaasalainen et al., 2015; Sinha et al., 2015) should be further integrated into current SAR-based snow cover detection algorithms to mitigate the negative effect of vegetation. This is also proposed in ESA's 7th Earth Explorer selected mission, BIOMASS (equipped with fully polarimetric P-band SAR, planned to launch in 2020) (Heliere et al., 2014).

2.5.4. Influence of Filtering Algorithms

The speckle noise in SAR images affects all SAR-based snow cover detection algorithms, especially the backscattering-based approaches. The available options for filtering algorithms to overcome this problem include Frost filter (Nagler and Rott, 2000, 2005; Valinia et al., 2006; Ventura, Schellenberger, Notarnicola, Zebisch, Nagler, et al., 2011; Notarnicola et al., 2012; Notarnicola C. et al., 2013; Singh et al., 2014), refined Lee filter (Longepe et al., 2009; Lessard-Fontaine et al., 2012; Huang et al., 2013; He et al., 2017; Zhou and Zheng, 2017), median filter (Guneriussen et al., 2001; Malnes and Guneriussen, 2002; Thakur et al., 2013), low pass filter (Nagler, 1996; Baghdadi et al., 1997), multichannel intensity filter (Nagler et al., 2016b), binary partition tree (Reppucci et al., 2012), De Grandi filter (He GJ et al., 2016), multi-scale multilooking (Wendleder et al., 2015), and Kuan filter (Pettinato et al., 2014). Some studies attempted to compare the ability of different filters. Schellenberger et al. (2012) used the effective number of looks (ENL) and standard deviations to compare the performance of median, Gamma DEMAP and Frost filter. Results showed that the median filter performs best in a purely statistical aspect; Frost filter, however, should be selected since the median filter is not an adaptive filter, which preserves image details while smoothing speckles by using unequal weights (Tso and Mather, 1999). They also implied that the window size influences the performance of filters. Thakur et al. (2013) preferred the median filter, as other filters might cause information loss at the pixel level. However, these studies only compared few filters and so far, no extensive comparison has been made to discuss the advantages and disadvantages of all available filters in a comprehensive overview.

2.5.5. Reliability of Current Validation Approaches

As shown in Figure 2.10, around half of the available studies employed snow cover classifications based on optical sensors as ground truth to validate the SAR-based snow cover results. This approach, however, can encounter several problems. First, for studies only aiming at wet snow monitoring, the date selection of optical images is critical. Usually, late spring is selected when the snowpack theoretically melts even in the highest elevation zones (Nagler et al., 2016b). This would ensure that the SAR-based snow cover mapping detects the entire snow cover extent. However, it cannot be guaranteed that no dry snow is left.

Additionally, acquisition times of SAR and optical images differ. The resulting temporal gap leads to uncertainties, because melting processes, sudden snowfall or precipitation events all may result in different SCE in the optical and SAR data (Luojus et al., 2007). Most authors, however, selected the nearest sensed image pair, despite the time difference (e.g., 14 days between PALSAR and Landsat (Park et al., 2014), 14 days between Radarsat-2 and Landsat (Muhuri et al., 2018), six days between PALSAR and AVNIR-2 (Singh and Venkataraman, 2012)). Even though some satellites equipped with both SAR and optical sensors at the same platform (e.g., the

Advanced Land Observation Satellite (ALOS)) may acquire both images at the same time, the presence of cloud may still hinder the optical observation.

Additionally, the difference between day and night might lead to great variations, as proven by studies investigating the top layer of a snowpack, which might refreeze after a cloud-free night with low temperatures. Such a refreeze event increases the surface backscattering significantly (Floricioiu and Rott, 2001; Notarnicola C. et al., 2013) and therefore would cause a high contrast between morning and evening observations (Muhuri et al., 2018). Field surveys also revealed that the infiltration of rain may cause both, thick ice crusts within the snowpack as well as larger snow grains (Duguay and Bernier, 2012). On top of that, differing magnitudes of temperature change in each elevation zone (Bartsch et al., 2007) impede the possibility to compensate its influence on the snowpack.

When validating SAR-based snow cover classifications with products derived from optical data, the accuracy of these reference datasets is of importance. Such products are often calculated applying a threshold of 0.4 NDSI, which might cause an underestimation as only pixels containing more than 50% of snow will be selected (Crawford et al., 2013; Crawford, 2015). Some researchers therefore used 0.7 as a threshold to allow only fully snow covered pixels for detection (Schellenberger et al., 2012; Notarnicola C. et al., 2013). In addition, limiting the optical-based snow cover detection to NDSI alone may introduce errors. It is generally advised to include additional tests, such as Landsat TM band4 ≥ 0.11 (Winther and Hall, 1999) and SPOT band3 ≥ 0.11 (Xiao et al., 2004) or using an NDSI-NDVI threshold to address dense forest regions (Klein et al., 1998). Even though the need for these additional tests is well-known in the optical snow cover community, SAR-based studies often fail to include these tests. Finally, as the spatial resolutions of SAR and optical images differ, the comparison procedures generally involve resampling operations (Pettinato et al., 2006), i.e., aggregating the higher resolution snow cover product to match the coarser one. Nevertheless, the definition of SCE in the coarser pixel may affect the validation significantly (Nagler et al., 2016b).

To overcome the constraints related to comparisons between optical and SAR-based snow cover classifications, a promising alternative approach is regional or global scale weather forecasting and/or snow models as suggested in Beniston et al. (2018). Although these models are criticized for their comparatively low spatial resolution, dependency on empirical parameter setting (Lehning et al., 2002; Krol and Löwe, 2016) and the oversimplification of the snowpack (Steiger and Abegg, 2013), they can provide useful information such as ground temperature and snow accumulation amount (Wang et al., 2015; Zhou and Zheng, 2017). As the complexity and spatial resolution of such models advance, they may constitute a notable alternative for future validation approaches of SAR-based snow cover products.

2.5.6. Opportunities of Data Fusion for SAR-based Snow Cover Detection

2.5.6.1. SAR flight direction (ascending and descending)

In Nagler's study (2016a), merging ascending and descending SAR observations was mentioned as a crucial future development, which was also discussed in the Sentinel for science (SEN4SCI) scientific workshop (Malenovský et al., 2012). It was also suggested that this combination could reduce the dependency of LIA (Baghdadi et al., 1997; Callegari et al., 2016). However, only four studies utilized this solution, although Rott and Nagler already tested this approach in their pioneer paper (1995). In their paper, two ratio maps were masked with shadow and layover areas as well as regions containing extreme LIA. Then they combined the images pixel-wise based on the LIA value. Bartsch et al. (2007) applied a similar approach but considered potential thawing. The general problem when combining different flight paths is the ground temperature difference between sensing times may lead to a change of the snowpack condition (Floricioiu and Rott, 2001). Thus, Bartsch et al. (2007) recommended a separate classification threshold for each direction.

2.5.6.2. SAR polarization (co- and cross-polarization)

Several studies indicated that the influence of LIA on the backscattering difference between dry and wet snow is also polarization-related, and that cross-polarization can preserve a better difference under small LIA conditions (Strozzi et al., 1997; Nagler et al., 2016b). Hence, the combination of different polarizations could be a promising option. Nagler et al. (2016b) calculated the ratio map for VV and VH independently and fused them with their weights based on LIA. So far, however, no other study investigated this potential and, therefore, more research is required.

2.5.6.3. Combination of SAR with optical imagery

Although many studies referred to the benefit of synergizing cloud-penetrating SAR with the high spatial/temporal resolution of optical imagery, so far there are only very few studies available that actually followed this approach. In all reviewed studies, only 12 performed a fusion of optical- and SAR-based snow cover classifications. This implies that there is still some potential to develop a dedicated algorithm combining optical and SAR data for snow cover detection.

So far, most studies relied on optical-based NDSI calculation to map total SCE and then apply Nagler's method to map wet snow. Subsequently, dry, wet and total SCE can be derived (Pettinato et al., 2017; Nagler et al., 2018; Snapir et al., 2019). This simple areal calculation, however, is not a genuine fusion of the same SCE type sensed by different sensors. A possible integration is to assign weights to both SAR-based and optical-based snow cover classifications as pursued by Malnes et al. (2004), Solberg et al. (2005) and Solberg et al. (2010). In these studies, time-series of SAR-based total SCE's were merged with total snow cover derived from MODIS by applying (1) confidence values assigned to each sensor's snow cover result, and (2) a

time-dependent function defining how quickly the confidence value would decay over time. Ultimately, the algorithm would select the snow cover result with the highest confidence value for each pixel. Nevertheless, as those key parameters were selected by finding the optimal solution through trial and error, the case-dependency hinders transferability to other locations and periods. A more universally applicable combination procedure, however, is still lacking.

2.5.6.4. Combination of SAR with passive microwave imagery

Theoretically, the temperature information sensed by passive microwave sensors would support analysis and detection of SCE, as the temperature of wet and dry snow and bare ground differs. However, the coarse spatial resolution of passive microwave sensors aggravates an integration of this data into SAR processing. Moreover, Liu et al. (2006) identified SAR-derived and passive microwave-derived SCE only match for 61%. They suggested this mismatch may be due to fact that the two sensors measure different temporal-physical snow parameters as the passive microwave sensor senses snow emissivity and brightness temperature, which can be analyzed for deriving snow depth and then linked to the actual SWE. In contrast, SAR records the backscattering representing long-term morphology processes prior to the sensing time. Consequently, combining the two data sources led to biased results, which represent different temporal-physical snow parameters. A similar magnitude of mismatch was also observed by Zhou and Zheng (2017).

2.5.7. Overall Trajectory of Spaceborne SAR-Based SCE Detection and Future Possibilities

According to the available studies reviewed in the present paper, the overall trajectory of spaceborne SAR-based SCE detection may be summarized into three phases as depicted in Figure 2.12.

After the launch of ERS-1 in 1991 and before the launch of ASAR in 2002, the repeat-pass imagery of ERS-1 allowed for a bi-temporal image analysis. Using this data source, Rott and Nagler developed their pioneer wet SCE mapping algorithm based on backscattering information (1995). The same applies to their dry SCE detection approach (2000) as well as Strozzi et al.'s total SCE mapping with InSAR technique (1999). Moreover, merging different flight paths for achieving higher mapping accuracy (Rott and Nagler, 1995) and calculating fractional SCE detection (Koskinen et al., 1997) were also proposed. In this phase, most of the available studies only utilized backscattering or InSAR techniques.

New breakthroughs were achieved in the second phase after the launch of ASAR and before the launch of Sentinel-1 in 2014. Dual/quad-polarization, multi-band, and constellations of SAR sensors significantly stimulated the development of new snow cover detection methods. The rich information derived from PolSAR became achievable. For dealing with the overwhelming amount of parameters from this new source of information (appendix), machine learning classifications were introduced. In

addition, various improvements of wet SCE mapping algorithms were achieved, including the combination with optical-based SCE (Malnes et al., 2004), and proposing an algorithm with a multi-year usable reference image optimized for forest regions (Luojus K. P. et al., 2006).

Topic has already shifted into the third phase since the launch of Sentinel-1 in 2014. In the hardware aspect, the fine spatial/temporal resolution and freely accessible Sentinel-1 offer an opportunity for long-term SAR-based SCE detection. Together with the prosperity of emerging X-band SAR sensors, more SAR-based studies are foreseeable such as integration and comparison of SCE information achieved from different bands of SAR sensors. In addition, the Sentinel series' satellites constellations significantly improve the potential of multi-sensor fusion as demonstrated in Nagler et al. (2018). In the algorithm aspect, thanks to the all land cover applicable total SCE detection approach proposed by Tsai et al. (2019b), it largely solves the previous studies' limitation that SAR-based approaches cannot detect snow accurately in vegetated regions and can only monitor wet SCE. This provides a great opportunity for future studies to integrate and complement SAR-based SCE with conventional optical-sensor-based cloud-affected SCE results to achieve more comprehensive SCE dynamics information in both spatial (conquering the influence of polar darkness and frequent cloud coverage, with ~20 m spatial resolution) and temporal (long time-series, daily temporal resolution) aspects. Another key development is DL, although only few studies exploited Sentinel-1 in combination with DL techniques so far, it is foreseeable that there will be further studies utilizing it to solve the current technical challenges, including the influence of different filtering algorithms, impact of different sensing geometry, less classification accuracy in the forest regions, and fusion of heterogeneous sensors' such as Light detection and ranging (Lidar) as well as passive sensors. In validation aspect; the need of proper validation for SAR-based SCE—especially wet SCE—still needs to be addressed. Most of the previous studies did not provide reliable validation due to the limitation of sparse in situ measurements. Finally, in the application aspect, as previous studies did not fully utilize the benefit that SAR can distinguish wet and dry SCE, but only regard the wet SCE as total SCE during snow melting season (Nagler et al., 2016a), the information of wet SCE which cannot be derived from conventional optical-based approach (can only detect total SCE) should be further utilized.

Consequently, based on the trajectory and the recent developments of SAR sensors and snow detection algorithms, it can be expected that in the near future once the SAR-based SCE detection approach (1) achieves daily temporal resolution by fusing different SAR sensors' information (2) reaches satisfactory classification accuracy and global transferability as proved by Tsai et al. (2019b); SAR-based monitoring approach would replace the conventional optical-sensor-based SCE detection approach as more snowpack information can be inferred (such as wet or dry and surface roughness) and can fundamentally solve the cloud coverage and polar

darkness issues.

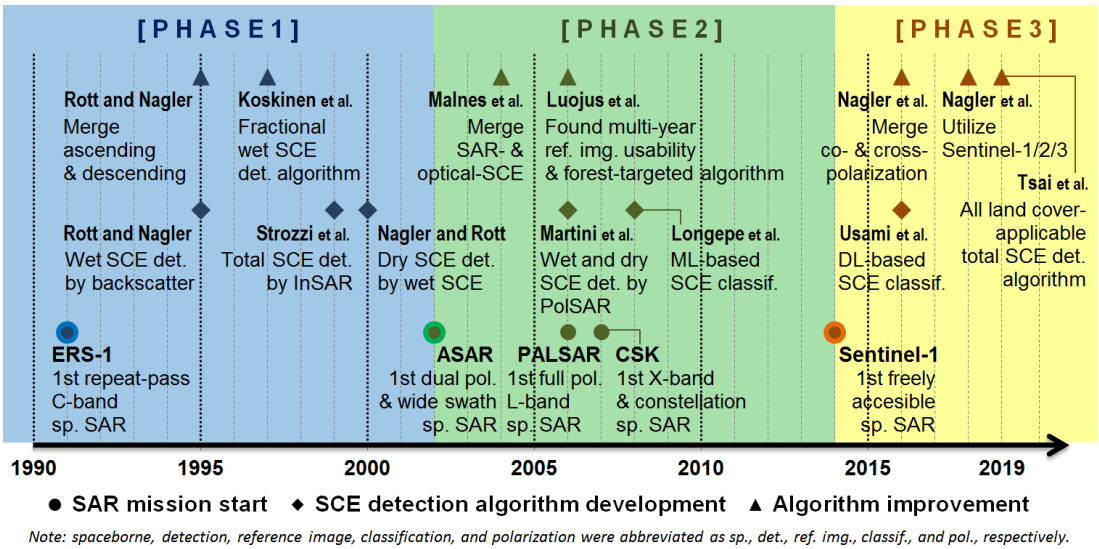

Figure 2.12 Overall development of algorithms and methods relying on spaceborne SAR data for snow cover extent (SCE) detection. The three phases denote the different main algorithms based on available SCE detection algorithms and SAR data.

2.5.8. Difficulties of Sensing Additional Snow Parameters

SWE and SD are two commonly desired snow parameters as both of them can be used to estimate the amount of water stored within a snowpack. So far, there are numerous studies aiming to identify the relationship between the information stored in SAR data and SWE as well as SD. At present, however, there is no solid conclusion to solve this challenge since various other factors affect the interactions between SAR signals and both, SWE and SD. The wetness of the snowpack, for example, would change the relative surface roughness and further affect SAR backscatter (Snehmani et al., 2015). The correlation between backscattering and SWE would therefore vary with the conditions of snow, soil (Shi and Dozier, 2000), and the surface roughness (Shi and Dozier, 1995). The relationship between SD and SAR also links to grain size, snow density, melting conditions, and temperature (Paloscia et al., 2017; Pettinato et al., 2017). Simulations suggest that the backscattering would increase with SD in a coarse-grained snowpack, but decrease in a fine-grained snowpack (Zhou and Zheng, 2017). Consequently, it is unreliable to derive SWE or SD merely from SAR information as it either requires inversions or empirical models (Arslan et al., 2001; Singh et al., 2006; Niang et al., 2007; Thakur et al., 2016).

2.6. Conclusion

Snow cover extent is one of the most important cryospheric components, as it controls global radiation balance, hydrological behavior, vegetation coverage and affects human activities. Spaceborne SAR offers the capability to quantify snow cover conditions even under clouded or nighttime conditions, which enables a better

understanding of the global snow cover dynamics. Moreover, its polarizations and phase data provide valuable information about the snowpack characteristics. Three mainstream SAR-based approaches to map snow cover have been pursued in last three decades: 1) Detecting wet snow based on SAR backscattering behavior; 2) PolSAR technique inverting the scattering mechanism of the targeted snow type; and 3) the coherence value calculated from InSAR techniques enabling estimation of total SCE.

After evaluating relevant studies published within the last three decades, we draw the following conclusions for monitoring snow cover using spaceborne SAR:

(1) C-band SAR based algorithms dominate the studies, but the recent prosperity of X-band SAR provides a promising option. Due to the long-term preference of the C-band wavelength and its better capability to detect snow when compared to L-band SAR, C-band SAR has the longest history and is utilized for snow cover detection more often than any other sensor. However, many recent studies have proven that X-band is more suitable to detect dry snow; considering the amount of new and planned X-band missions, an increase in popularity of X-band based snow cover detection algorithms therefore can be expected for the near future.

(2) Most studies focused on mountainous regions, especially the European Alps (32%) and the Asian Himalaya (31%), leading to an imbalanced distribution of study sites. The relatively small size of the study sites also implies the lack of utility of the recent wide-swath sensing mode.

(3) The majority of studies investigated snow cover for one year with an average of two observations within this year to account for the dynamics of the snowpack. These temporal aspect-limited studies indicate that there is still a gap in understanding the long-term capability of SAR-based algorithms to detect snow consistently.

(4) For detecting wet SCE, the majority of studies relied on backscattering-based approaches. More than 55% of the reviewed studies only detected wet snow, with 82% of those studies applying a backscattering-based approach proposed by Nagler et al. in 2000. However, we observed a recent increase in studies relying on InSAR- and PolSAR-based algorithms especially for the detection of dry and total SCE.

(5) This review confirms the importance of ancillary data such as a DEM, a land cover map as well as meteorological data as additional inputs into SAR-based snow detection algorithms. Based on the DEM data, information about LIA, SAR shadow and layover can be derived; land cover information is useful to mitigate the negative effects of vegetated areas on the classification accuracy, and the actual snow melting conditions can be inferred from meteorological data.

(6) Commonly employed classification methods shifted from supervised ML approach towards more sophisticated DL approaches, and the maturity of optical-based snow cover products enables a selection of suitable training samples for supervised

classifications.

(7) Technical advances in recently launched SAR missions such as wider sensing swaths, shorter revisit times and quad-polarization make SAR-based snow cover detection more promising. These technical developments and the mainstream SAR-based algorithms complement each other well, as the extended coverage can increase the efficiency of the classification, the shortened revisiting time can support InSAR-based approaches to sustain more usable coherence, and the quad-polarization can enrich the information decomposed by PolSAR-based techniques.

(8) The difficulty of SCE detection in vegetated land cover regions is recently addressed but further exploration of PolInSAR and TomoSAR techniques should be investigated. In addition, the influence of filter algorithms on the quality of the final snow cover product requires additional research.

(9) The synergy of SAR with other sensors (e.g., optical and passive microwave) to improve the quality of snow cover classifications is still immature and requires further research. The synergic use with other sensors may also help develop and establish generally accepted validation strategies.

(10) Thanks to the characteristics of SAR which can penetrate through clouds and sense ground independently of solar illumination conditions, together with the recent prosperity of different SAR satellites and advancement of ML/DL algorithms, it is foreseeable that SAR-based SCE detection approaches can complement conventional optical sensor-based SCE detection approaches in the near future as SAR provides more snowpack condition information and can fundamentally solve the cloud coverage and polar darkness limitations.

Acknowledgments: Support by the German Academic Exchange Service (DAAD) fellowship to Ya-Lun S. Tsai is gratefully acknowledged.

Appendix A

Table 2.4 The summary of included studies' SCE monitoring strategy (targeted snow type, classification method and data synergy).

Band	Sensor	Wet snow			Dry snow		Total snow	Classification		Synergy	
		Employed approach									
		Backscatter	PolSAR	InSAR	Topo-based	Others		Supervised	Un-supervised	Dual-orbits	Optical
X-Band	COSMO-SkyMed	(Ventura, Schellenberger, Notarnicola, Zebisch, Maddalena, et al., 2011; Ventura, Schellenberger, Notarnicola, Zebisch, Nagler, et al., 2011; Notarnicola et al., 2012; Schellenberger et al., 2012; Notarnicola C. et al., 2013; Pettinato et al., 2014; Paloscia et al., 2017; Pettinato et al., 2017)			(Schellenberger et al., 2012)						
	TerraSAR-X	(Besic, Vasile, Chanussot, Stankovic, Ovarlez, et al., 2012; Duguay and Bernier, 2012; Pettinato et al., 2014; Besic et al., 2015; Rizzoli et al., 2015)	(Wendleder et al., 2015)	(Rizzoli et al., 2016; Guo et al., 2017; Rizzoli et al., 2017)	(Besic, Vasile, Chanussot, Stankovic, Ovarlez, et al., 2012)	(Rizzoli et al., 2015; Rizzoli et al., 2016; Rizzoli et al., 2017)			(Rizzoli et al., 2015; Rizzoli et al., 2016; Rizzoli et al., 2017)		
C-Band	ERS-1/2	(Rott and Nagler, 1995; Nagler, 1996; Baghdadi et al., 1997; Koskinen et al., 1997; Nagler and Rott, 2000; Löw et al., 2002; Tampellini, 2003; Pettinato et al., 2004; Brogioni et al., 2006; Luojus K. P. et al., 2006; Koskinen et al., 2010; Huang et al., 2013; Salcedo and Cogliati, 2014)		(Li et al., 2001; Kumar and Venkatarama n, 2011)	(Nagler and Rott, 2000)					(Nagler and Rott, 2000)	

	Radatsat-1	(Nagler and Rott, 2000; Guneriussen et al., 2001; Haefner, 2001; Haefner et al., 2001; Löw et al., 2002; Malnes and Guneriussen, 2002; Magagi and Bernier, 2003; Anttila et al., 2005; Hongxing et al., 2006; Luojus K. et al., 2006; Pettinato et al., 2006; Luojus et al., 2007; Luojus et al., 2008; Luojus K. et al., 2009; Luojus K. P., Pulliainen J. T., Blasco Cutrona A., et al., 2009; Luojus K. P., Pulliainen J. T., Metsämäki S. J., et al., 2009; Huang et al., 2013)			(Malnes and Guneriussen, 2002)						
	ENVISAT	(Malnes et al., 2004; Pettinato et al., 2004; Solberg et al., 2004; Storvold and Malnes, 2004; Nagler and Rott, 2005; Solberg et al., 2005; Brogioni et al., 2006; Solberg et al., 2006; Storvold, Malnes, and Lauknes, 2006; Valinia et al., 2006; Bartsch et al., 2007; Longépé et al., 2008; Singh, Venkataraman, Rao, et al., 2008; Solberg et al., 2008; Valenti et al., 2008; Longepe et al., 2009; Pettinato S et al., 2009; Pettinato Simone et al., 2009; Pettianato et al., 2010; Solberg, Koren, et al., 2010; Huang et al., 2013; Thakur et al., 2013; Ji et al., 2014)		(Singh, Venkataraman, Rao, et al., 2008; Kumar and Venkataraman, 2011)	(Malnes et al., 2004; Pettinato et al., 2004; Solberg et al., 2004; Storvold and Malnes, 2004; Solberg et al., 2005; Brogioni et al., 2006; Solberg et al., 2006; Storvold, Malnes, and Lauknes, 2006; Solberg et al., 2008; Pettinato S et al., 2009; Pettinato Simone et al., 2009;				(Kumar and Venkataraman, 2011)	(Valinia et al., 2006; Bartsch et al., 2007)	(Malnes et al., 2004; Solberg et al., 2005; Solberg et al., 2006; Solberg et al., 2008; Pettinato S et al., 2009; Pettinato Simone et al., 2009; Pettianato et al.,

					Pettianato et al., 2010; Solberg, Koren, et al., 2010; Ji et al., 2014)						2010; Solberg, Koren, et al., 2010)
	Radarsat-2	(Dedieu et al., 2012; Duguay and Bernier, 2012; Lessard-Fontaine et al., 2012; Zhen et al., 2012; He Guangjun et al., 2016; Thakur et al., 2016; He et al., 2017)	(Huang et al., 2011; Dedieu et al., 2012; Zhen et al., 2012; Wendleder et al., 2015; He et al., 2017; Muhuri, Ratha, et al., 2017)	(He et al., 2017)	(Thakur et al., 2016)	(Dedieu et al., 2012; Lessard-Fontaine et al., 2012; Reppucci et al., 2012; He Guangjun et al., 2016; He et al., 2017)	(Guangjun et al., 2015; Callegari et al., 2016; He GJ et al., 2016; Muhuri, Manickam, et al., 2017; Muhuri et al., 2018)	(Huang et al., 2011; Zhen et al., 2012; Guangjun et al., 2015; Callegari et al., 2016; He Guangjun et al., 2016; He GJ et al., 2016; He et al., 2017)	(Muhuri, Manickam, et al., 2017)	(Callegari et al., 2016)	
	Sentinel-1	(Nagler et al., 2016a; Zhou and Zheng, 2017; Nagler et al., 2018; Pratola and Navarro-Sánchez, 2018; Thakur et al., 2018; Wendleder et al., 2018; Snapir et al., 2019; Tsai Ya-Lun S, Dietz Andreas, et al., 2019b)			(Zhou and Zheng, 2017)		(Nijhawan et al., 2018; Wang et al., 2018; Tsai Ya-Lun S, Dietz Andreas, et al., 2019b)	(Nijhawan et al., 2018; Tsai Ya-Lun S, Dietz Andreas, et al., 2019b)			(Nagler et al., 2018; Snapir et al., 2019)
L-Band	ALOS-1		(Longepe et al., 2008; Singh et al., 2011; Park et			(Longepe et al., 2008)	(Singh, Venkataraman, and Rao, 2008; Venkataraman et al.,	(Singh et al., 2014) (Longepe et al., 2008)	(Singh, Venkataraman, and Rao, 2008; Singh and		

			al., 2014)				2010; Singh et al., 2011; Venkatara man et al., 2011; Singh and Venkatara man, 2012; Singh et al., 2014; Wang et al., 2015)		Venkatara man, 2012)		
	ALOS-2		(Usami et al., 2016)					(Usami et al., 2016)			

Table 2.5 Summary of included studies' SCE monitoring strategy (studying region type, validation data and usage of land cover information).

		Study regions type			Validation dataset					Land cover	
										Involved analysis	Only mask
Band		Mountainous	Forest	Glacier	Landsat	MODIS	AVNIR-2	Aerial	Meteo Station		
X-Band	COSMO-SkyMed	(Ventura, Schellenberger, Notarnicola, Zebisch, Maddalena, et al., 2011; Ventura, Schellenberger, Notarnicola, Zebisch, Nagler, et al., 2011; Notarnicola et al., 2012; Schellenberger et al., 2012; Notarnicola C. et al., 2013; Pettinato et al., 2014; Paloscia et al., 2017; Pettinato et al., 2017)			(Ventura, Schellenberger, Notarnicola, Zebisch, Maddalena, et al., 2011; Ventura, Schellenberger, Notarnicola, Zebisch, Nagler, et al., 2011; Notarnicola et al., 2012; Schellenberger et al., 2012;						(Ventura, Schellenberger, Notarnicola, Zebisch, Maddalena, et al., 2011; Notarnicola C. et al., 2013; Pettinato et al., 2014)

					Notarnicola C. et al., 2013; Pettinato et al., 2014)						
	TerraSAR-X	(Besic, Vasile, Chanussot, Stankovic, Ovarlez, et al., 2012; Pettinato et al., 2014; Besic et al., 2015; Wendleder et al., 2015)	(Guo et al., 2017)	(Rizzoli et al., 2015; Rizzoli et al., 2016; Rizzoli et al., 2017)							
C-Band	ERS-1/2	(Baghdadi et al., 1997; Nagler and Rott, 2000; Li et al., 2001; Tampellini, 2003; Salcedo and Cogliati, 2014)	(Koskinen et al., 1997; Luojus K. P. et al., 2006; Koskinen et al., 2010)		(Nagler and Rott, 2000; Li et al., 2001)				(Löw et al., 2002)	(Löw et al., 2002; Luojus K. P. et al., 2006; Koskinen et al., 2010)	
	Radatsat-1	(Guneriussen et al., 2001; Haefner, 2001; Haefner et al., 2001;	(Luojus K. et al., 2006; Luojus et al.,	(Hongxing et al., 2006)		(Luojus K. et al., 2006; Luojus et		(Guneriussen et al.,		(Luojus K. et al., 2006;	

		Malnes and Guneriussen, 2002; Anttila et al., 2005; Pettinato et al., 2006)	2007; Luojus et al., 2008; Luojus K. et al., 2009; Luojus K. P., Pulliainen J. T., Blasco Cutrona A., et al., 2009; Luojus K. P., Pulliainen J. T., Metsämäki S. J., et al., 2009)			al., 2007; Luojus et al., 2008; Luojus K. et al., 2009; Luojus K. P., Pulliainen J. T., Blasco Cutrona A., et al., 2009; Luojus K. P., Pulliainen J. T., Metsämäki S. J., et al., 2009)		2001; Pettinato et al., 2006)		Luojus et al., 2007; Luojus et al., 2008; Luojus K. et al., 2009; Luojus K. P., Pulliainen J. T., Blasco Cutrona A., et al., 2009; Luojus K. P., Pulliainen J. T., Metsämäki S. J., et al., 2009)	
	ENVISAT	(Malnes et al., 2004;		(Valinia	(Solberg,	(Malnes et		(Solberg	(Pettinat		(Brogioni et

		Pettinato et al., 2004; Solberg et al., 2004; Storvold and Malnes, 2004; Nagler and Rott, 2005; Solberg et al., 2005; Brogioni et al., 2006; Solberg et al., 2006; Storvold, Malnes, and Lauknes, 2006; Bartsch et al., 2007; Longépé et al., 2008; Solberg et al., 2008; Valenti et al., 2008; Longepe et al., 2009; Pettinato S et al., 2009; Pettinato Simone et al., 2009; Pettianato et al., 2010; Solberg, Koren, et al., 2010; Thakur et al., 2013; Ji et al., 2014)		et al., 2006; Singh, Venkataraman, Rao, et al., 2008; Kumar and Venkataraman, 2011; Huang et al., 2013)	Koren, et al., 2010)	al., 2004; Storvold and Malnes, 2004; Storvold, Malnes, and Lauknes, 2006; Thakur et al., 2013; Ji et al., 2014)		, Koren, et al., 2010)	o S et al., 2009; Pettinato Simone et al., 2009; Pettianato et al., 2010)		al., 2006; Pettinato S et al., 2009; Pettinato Simone et al., 2009; Pettianato et al., 2010; Thakur et al., 2013)
	Radarsat-2	(Dedieu et al., 2012; Lessard-Fontaine et al., 2012; Reppucci et al., 2012; Guangjun	(Muhuri, Manickam, et al., 2017)	(Huang et al., 2011; Zhen et	(Dedieu et al., 2012; Lessard-Fontaine et al.,	(Thakur et al., 2016)				(Huang et al., 2011; Guangju	

		et al., 2015; He Guangjun et al., 2016; He GJ et al., 2016; Thakur et al., 2016; He et al., 2017; Muhuri, Manickam, et al., 2017; Muhuri, Ratha, et al., 2017; Muhuri et al., 2018)		al., 2012; Callegari et al., 2016)	2012; Callegari et al., 2016; He et al., 2017; Muhuri, Manickam, et al., 2017; Muhuri, Ratha, et al., 2017; Muhuri et al., 2018)					n et al., 2015; He et al., 2017; Muhuri et al., 2018)	
	Sentinel-1	(Nagler et al., 2016a; Nagler et al., 2018; Nijhawan et al., 2018; Pratola and Navarro-Sánchez, 2018; Thakur et al., 2018; Wang et al., 2018; Wendleder et al., 2018; Snapir et al., 2019; Tsai Ya-Lun S, Dietz Andreas, et al., 2019b)	(Tsai Ya-Lun S, Dietz Andreas, et al., 2019b)	(Zhou and Zheng, 2017)	(Nagler et al., 2016a; Tsai Ya-Lun S, Dietz Andreas, et al., 2019b)	(Tsai Ya-Lun S, Dietz Andreas, et al., 2019b)			(Tsai Ya-Lun S, Dietz Andreas, et al., 2019b)	(Tsai Ya-Lun S, Dietz Andreas, et al., 2019b)	
L-Band	ALOS-1	(Singh, Venkataraman, and Rao, 2008; Venkataraman et al.,		(Singh et al., 2011)	(Park et al., 2014)		(Venkataraman et al., 2010; Singh and				

		2011; Singh and Venkataraman, 2012; Park et al., 2014; Singh et al., 2014; Wang et al., 2015)					Venkataraman, 2012; Park et al., 2014; Singh et al., 2014)				
	ALOS-2	(Usami et al., 2016)									

Table 2.6 The PolSAR decomposition techniques and parameters employed in the included studies.

Decomposition type		Parameter	Wet and dry snow response	Total snow response	Employed by studies	Used for final classification	
						Wet and Dry snow	Snow-covered/ free
Backscattering		B_{HH}, B_{HV} B_{VH}, B_{VV}			(Longepe et al., 2008; Huang et al., 2011)	B_{HV} (Huang et al., 2011)	B_{HV} (Park et al., 2014)
Pauli decomposition (Cloude and Pottier, 1996)	Cloude and Pottier 1996	P_{odd} single/odd bounce, P_{dbl} double/even bounce, P_{vol} volume scattering		Low P_{dbl} and P_{vol} (Park et al., 2014)	(Huang et al., 2011; Dedieu et al., 2012; Reppucci et al., 2012; Park et al., 2014; Singh et al., 2014; He et al., 2017; Muhuri, Manickam, et al., 2017)	P_{vol} (He et al., 2017) P_{dbl} (Huang et al., 2011) All (Longepe et al., 2008)	All (Longepe et al., 2008)
H/A/$\bar{\alpha}$ (Cloude and Pottier, 1996)	Cloude and Pottier 1996	H entropy A anisotropy $\bar{\alpha}$ angle $\lambda_1, \lambda_2, \lambda_3$ 1-H H(1-A)	Low λ_3 for wet snow (Singh et al., 2014) Low $\bar{\alpha}$ for wet snow (Dedieu et al., 2012) High H for wet snow (Dedieu et al., 2012)	Low H and H(1-A) (Singh et al., 2014) Low H, $\bar{\alpha}$ (Singh et al., 2011) High A (Singh et al., 2014)	(Martini et al., 2006; Longepe et al., 2008; Singh, Venkataraman, and Rao, 2008; Huang et al., 2011; Singh et al., 2011; Venkataraman et al., 2011; Dedieu et al., 2012; Reppucci et al., 2012; Singh and Venkataraman, 2012; Park et al., 2014;	λ_3 (He Guangjun et al., 2016; He et al., 2017) H/$\bar{\alpha}$ (Dedieu et al., 2012)	λ_3 (Venkataraman et al., 2011; Singh et al., 2014) $\lambda_1, \lambda_2, \lambda_3, \bar{\alpha}$ (Callegari et al., 2016) H (Singh and Venkataraman, 2012; Park et al., 2014; Muhuri, Manickam, et al.,

					Singh et al., 2014; Callegari et al., 2016; He Guangjun et al., 2016; He et al., 2017; Muhuri et al., 2018; Tsai Ya-Lun S, Dietz Andreas, et al., 2019b)		2017) A (Singh and Venkataraman, 2012; Muhuri, Manickam, et al., 2017) α (Singh and Venkataraman, 2012)
Freeman (Freeman and Durden, 1998)	Freeman and Durden 1998	F_{odd} surface, F_{dbl} double-bounce, F_{vol} volume scattering			(Longepe et al., 2008; Singh and Venkataraman, 2012; Park et al., 2014; He et al., 2017)		
Yamaguchi (Yamaguchi et al., 2006)	Yamaguchi et al. 2006	Helix scattering of Y_{hlx} coefficient, Y_{odd} surface, Y_{dbl} double-bounce, Y_{vol} volume scattering P_s, P_d, P_v, P_c			(Singh and Venkataraman, 2012; Park et al., 2014; Singh et al., 2014; He Guangjun et al., 2016; He et al., 2017)	Y_v (He Guangjun et al., 2016; He et al., 2017)	
Touzi (Touzi, 2007)	Touzi 2007	ψ_1, ψ_2, ψ_3 $\tau_1, \tau_2, \psi\tau_3$ $\alpha_1, \alpha_2, \alpha_3$ ϕ_1, ϕ_2, ϕ_3			(Muhuri, Manickam, et al., 2017)		ψ_1 (Callegari et al., 2016) τ_1, τ_2 (Muhuri, Manickam, et al., 2017)
(Antropov et al., 2011)	Antropov et al. 2011	Generalized volume scattering			(Muhuri, Ratha, et al., 2017)		

Kennaugh (Schmitt et al., 2015)	Schmitt et al. 2015	Kennaugh elements $K_1 \sim K_9$	Low K_0 for wet snow (Wendleder et al., 2015)		(Wendleder et al., 2015)	K_0 (Wendleder et al., 2015)	
Derived parameter							
		Total power (TP)		Low TP (Singh et al., 2011)	(Singh et al., 2011)		
	Van Zyl et al. 1987	Polarization fraction (PF) (Van Zyl et al., 1987)	High PF for wet snow (Muhuri et al., 2018)	High PF (Singh et al., 2011)	(Singh et al., 2011; Venkataraman et al., 2011; Singh et al., 2014; Muhuri et al., 2018)		(Venkataraman et al., 2011; Singh et al., 2014; Muhuri et al., 2018)
	Ainsworth et al. 2002	Polarimetric asymmetry (PA) (Ainsworth et al., 2002)		High PA (Singh et al., 2014)	(Singh et al., 2014)		
	Lüneburg 2001	Lüneburg anisotropy (LA) (Lüneburg, 2001)		Low LA (Singh et al., 2014)	(Singh et al., 2014)		
	Allain et al. 2006	single-bounce eigenvalue relative difference (SERD) double-bounce eigenvalue relative difference (DERD) (Allain et al., 2006)	High SERD when snow is wet as the surface scattering dominates (Dedieu et al.,		(Dedieu et al., 2012; Singh et al., 2014)	SERD (Dedieu et al., 2012)	

			2012)				
	Lee and Pottier 2009	Copolarization Coherence (Lee J. and Pottier E., 2009)			(Singh et al., 2014)		
	Lee and Pottier 2009	polarimetric copolarization phase difference (PPD) (Lee J. and Pottier E., 2009)			(Singh et al., 2014)		
		Huynen parameter A_0			(Longepe et al., 2008)		
		Radar Vegetation Index (RVI)			(Longepe et al., 2008)		
		Degree of polarization (DoP)			(Usami et al., 2016)		

3 Wet and Dry Snow Detection Using Sentinel-1 SAR Data for Mountainous Areas with a Machine Learning Technique

Tsai, Y.-L.S., Dietz, A., Oppelt, N., & Kuenzer, C. (2019). Wet and Dry Snow Detection Using Sentinel-1 SAR Data for Mountainous Areas with a Machine Learning Technique. Remote Sensing, 11, 895

Abstract

Traditional studies on mapping wet Snow Cover Extent (SCE) often feature limitations especially in vegetated and mountainous areas. The aim of this study is to propose a new total and wet SCE mapping strategy based on freely accessible spaceborne SAR data. The approach is transferable on a global scale as well as for different land cover types (including densely vegetated forest and agricultural regions), and is based on the use of backscattering coefficient, interferometric SAR coherence, and polarimetric parameters. Furthermore, four topographical factors were included in the simple tuning of random forest-based land cover type-dependent classification strategy. Results showed the classification accuracy was above 0.75, with an F-measure higher than 0.70, in all five selected regions of interest located around globally distributed mountain ranges. Whilst excluding forest type land cover classes, the accuracy and F-measure increases to 0.80 and 0.75. In cross-location model set, the accuracy can also be maintained at 0.80 with non-forest accuracy up to 0.85. It has been found that the elevation and polarimetric parameters are the most critical factors, and that the quality of land cover information would also affect the subsequent mapping reliability. In conclusion, through comprehensive validation using optical satellite and in-situ data, our land cover-dependent total SCE mapping approach has been confirmed robustly applicable and the holistic SCE map for different months were eventually derived.

Keywords: Synthetic Aperture Radar, InSAR, PolSAR, Backscattering, Random Forest, Snow Cover Area, Land Use Land Cover, Sentinel-2, Landsat

3.1. Introduction

Snow cover is an important parameter in the context of water availability, the global radiation balance and natural disasters such as floods and avalanches. It is also a crucial resource for tourism and hydropower generation (Ancey and Bain, 2015; Huss

et al., 2017; Kevin et al., 2017; Dorji et al., 2018). Climate change has been affecting snow cover extent (SCE), its amount, and its distribution globally, generally leading to a decline of the aforementioned parameters (Bulygina et al., 2009; Brown and Robinson, 2011; Dyrrdal et al., 2013; Beniston et al., 2018). This was also stated in the Synthesis Report of Fifth Assessment Report (AR5) of the Intergovernmental Panel on Climate Change (IPCC) (Pachauri et al., 2014). The latest IPCC special report of 2018 reveals severe potential risks due to more extreme SCE changes and melting caused by global warming, which would affect winter tourism and hydrology (Hoegh-Guldberg et al., 2018). As summarized by Beniston et al. (2018) and Brown et al. (2011), because of the rising temperature as well as changes in atmospheric circulation patterns, snow depth (SD) and snow cover duration (SCD) have exhibited a decreasing trend in the past decades. Additionally, based on climate model simulations and the IPCC special report, a declining trend of SCE must be expected, with an even more severe impact on mountain regions (Schmucki et al., 2015; Beniston et al., 2018).

Because snow cover represents such an important component of the Earth's cryosphere, it is crucial to detect and monitor snow cover, its conditions and the processes that lead to its current and future developments. As a result, several international monitoring projects and products exist, comprising the National Snow and Ice Data Center (NSIDC)'s MODIS-based snow cover products (Riggs and Hall, 2015), the European Space Agency (ESA)'s GlobSnow products (Solberg, Wangensteen, et al., 2010), the German Aerospace Center (DLR)'s Global SnowPack (Dietz et al., 2015), ESA's Satellite Snow Product Inter-comparison and Evaluation Exercise (SnowPEx) (Metsämäki et al., 2017). Most of the aforementioned SCE products are based on multispectral data. Applied methods to detect snow cover from multispectral data are mature, but lack the ability to detect snow under cloud-covered conditions or during the (polar) night. Since spaceborne Synthetic Aperture Radar (SAR) has the advantage of sensing without the dependency of solar illumination and weather conditions, it has been progressively explored for SCE mapping. Moreover, regarding the information derived from backscattering and phase records, SAR data is not affected by confusions between snow and ice-clouds – a common problem occurring in multispectral imagery (Macander et al., 2015). Thus, after the launch of the ERS-1 in 1991, many studies investigated the viability of repeat-pass multi-temporal SAR-based approaches to detect SCE. The most frequently employed SAR-based approach is the backscattering-based method, also known as the "Nagler's method" (Nagler and Rott, 2000). It utilizes two SAR images sensed at snow-covered and snow-free conditions, and derives the wet SCE by thresholding the

ratio image of their backscattering coefficients value. This approach was thoroughly improved (Luojus K. P. et al., 2006; Notarnicola C. et al., 2013; Salcedo and Cogliati, 2014); hence, it has been widely applied to various new spaceborne SAR sensors (Magagi and Bernier, 2003; Venkataraman et al., 2008; Schellenberger et al., 2012; Nagler et al., 2016b).

However, as the backscattering-based approach can only map wet SCE, interferometric SAR (InSAR) as well as polarimetric SAR (PolSAR) have been additionally investigated for their potential to detect total SCE, i.e. dry SCE plus wet SCE. The coherence information derived from InSAR can map both wet and dry snow as the snow-free area would feature relatively high coherence due to more stable scatter mechanism (Singh, Venkataraman, Rao, et al., 2008; Snehmani et al., 2015). In contrast, PolSAR technique can theoretically distinguish dry snow, wet snow and snow-free areas, based on the PolSAR parameters decomposed from multi-polarization SAR image stating the geometrical scattering mechanism (Cloude and Pottier, 1996). Considering the more complicated and rich information derived from InSAR and PolSAR, these input parameters are not suitable to be analyzed with a traditional thresholding approach alone. Fortunately, acknowledging the advance of computation hardware and increased processing power in recent years, machine learning (ML) is now becoming a viable option for large scale processing of SAR data in the context of SCE detection. Several studies such as Huang et al. (2011) and Longepe et al. (2008), already tested the feasibility employed SVM with PolSAR parameters to classify dry SCE, wet SCE and bare-ground areas. He et al. (2017) utilized 36 PolSAR parameters and interferometric coherence to map the dry and wet SCE; Usami et al. (2016) even proposed using a quaternion neutral network to map the wet SCE with PALSAR-2, PolSAR information and local incidence angle (LIA).

So far, available studies are still being considered at a developing stage, which constrains their transferability to different sites and years. Currently available studies to map SCE from SAR data have at least one of the following limitations: (1) regional aspect: only focused on the Asian Himalaya and European Alps; (2) spatial aspect: only processed on a local scale; (3) temporal aspect: only monitored SCE for a year with few different observations; (4) algorithm: only detected wet SCE with Nagler's backscattering-threshold approach and did not consider topographical information; (5) vegetation: rarely considered land cover information in the algorithm itself, or simply just masked out the forest region; (6) classification: only employed SVM approaches and concluded that the tuning of the SVM and the limited data handling capacity pose severe challenges (Pal, 2005; Adam et al., 2014; Rodriguez-Galiano et al., 2015). The constraints mentioned above largely limit the currently available SAR-based SCE

detection algorithms as they are often not transferable, not operated on forest regions, or they can only detect wet snow. Consequently, the aim of the presented study is to introduce a simple tuning ML technique to detect total SCE in different regions based on spaceborne SAR imagery, and to validate this method comprehensively. The following objectives will be addressed: (1) employing openly accessible dataset with global coverage to build a universally applicable approach (2) fusing different SAR-based information as well as topographical factors to detect total SCE (3) applying the model to five regions based on each region's multi-months data to examine the model's robustness (4) utilizing a simple tuning random forest (RF) approach to solve the multi-SAR information-based classification problem (5) building a universal cross-temporal/spatial land cover-dependent classification model set (6) validating the results comprehensively based on in-situ data and reference data sets originating from multispectral data sources (7) analyzing the influence of different land cover types on the classification's accuracy.

3.2. Study Areas and Dataset

3.2.1. Study Areas

As this study intends to examine the global transferability of our approach, five regions around the globe were selected as shown in Figure 3.1, where land cover types for each region is shown (with detailed information presented in Table 3.1). Because one of our objectives is to compare the influence of different land cover types on the SCE detection, we selected regions in different continents, mountain ranges and elevation zones, increasing the overall land cover diversity.

Table 3.1 Attributes of five selected study areas along with their location, mountain range, country, and their highest peak.

Test sites	**1 (MR)**	**2 (ZG)**	**3 (MW)**	**4 (LL)**	**5 (AG)**
Hemisphere	North	North	North	North	South
Continent	Europe	Europe	Northern America	Asia	Southern America
Mountain range (Country)	Alps (Switzerland)	Alps (Germany)	Sierra Nevada (United States)	Himalaya (Nepal)	Andes (Argentina)
Highest peaks (Height)	Monte Rosa (4,634 m)	Zugspitze (2,962 m)	Mount Whitney (4,421 m)	Langtang Lirung (7,234 m)	Aconcagua (6,960 m)
Nearby city	Lausanne	Munich	Bakersfield	Kathmandu	Santiago

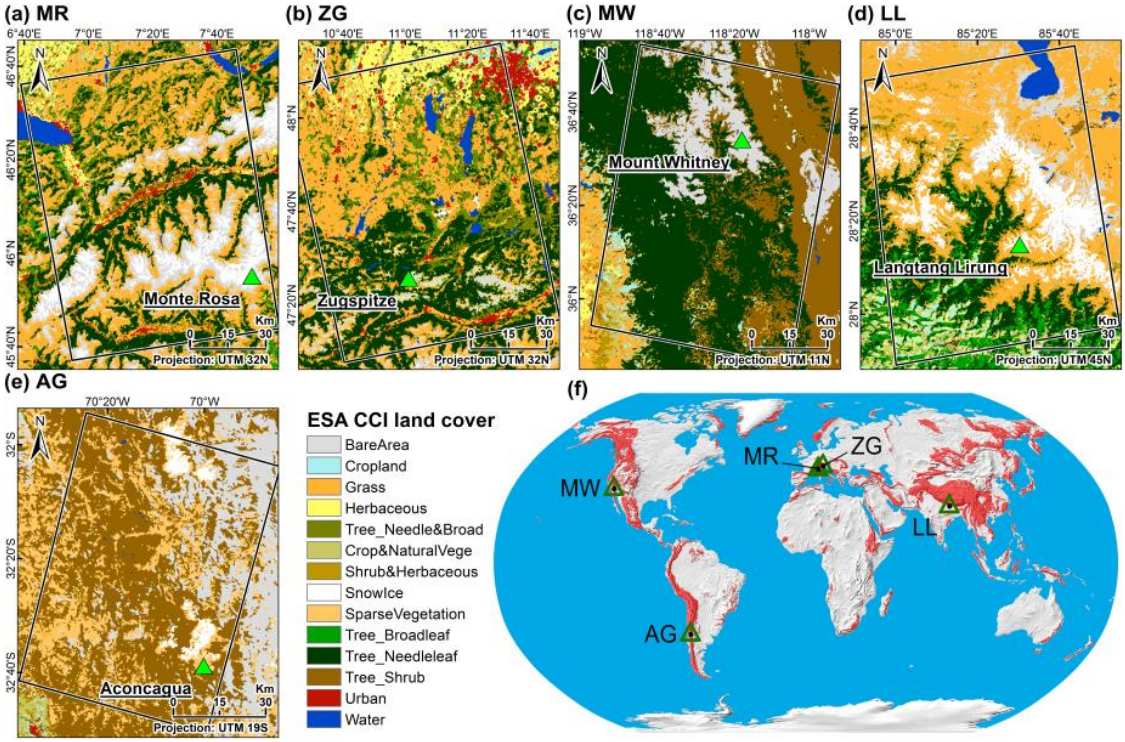

Figure 3.1 Land cover types (derived from ESA Climate Change Initiative (CCI) land cover product) for the five selected test sites: (a) Monte Rosa (MR), (b) Zugspitze (ZG), (c) Mount Whitney (MW), (d) Landtang Lirung (LL), and (e) Aconcagua (AG). Location of each region around the globe is illustrated in (f).

3.2.2. SAR Data

As this study aims at using openly accessible data sources, Sentinel-1 imagery provided by the European Space Agency (ESA) were employed. The conventional interferometric wide swath (IW) acquisition mode was used in this study. Both level 1 Single Look Complex (SLC) and Ground Range Detected (GRD) products were used, with the latter merging all sub-swath and debursting.

To validate our algorithm across different years and months/seasons, a total of three datasets (including one for the first hydrological year and two for the second hydrological year) were selected for each study area (details are shown in Figure 3.2 and Table 3.2). In order to represent snow cover conditions as well as to maximize the similarity of period sample used in each region, the months of November, February and May of the first year were selected in each region. However for MW and LL sites the months of February, April and May were chosen instead. This is due to the fact that in the MW and LL regions, the imagery were stable only after February 2017, as a result of a much rarer revisiting frequency of Sentinel-1, according to their orbit design, in comparison to European regions. Regarding AG, the only site located in the

southern hemisphere, has opposite season, the corresponding months samples were used. Two different months of imagery were used for external validation in examining the month-dependency of established model set.

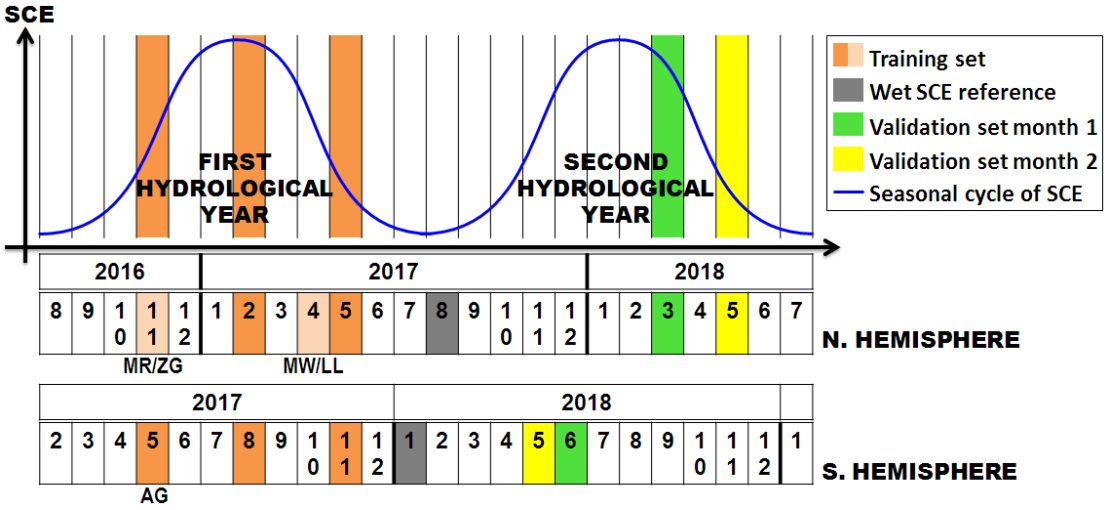

Figure 3.2 Selected date of SAR imagery for five regions in two hydrological years.

Table 3.2 Summary of the SAR data (Sentinel-1) and optical data (Sentinel-2, S2; Landsat-7/8, L7/8) used for training and validation set of this study. Note: reference image of each region for calculating wet snow cover extent (SCE) is marked with an asterisk (*); optical images employed in validation set are included in brackets after the used SAR image dates.

Training Set (First hydrological year)	**Validation Set (Second hydrological year)**	
	Month 1 (Month not included in training set)	Month 2 (Month included in training set)
Test Site 1: Monte Rosa (MR) (Sentinel-1A, Ascending, relative orbit number: 88) *(Landsat-7/8, path: 195, row: 28)*		
2016 Nov 17-29	2018 Mar 12-24 *(L7: Mar 23)*	2018 May 11-23 *(L8: May 18)*
2017 Feb 09-21		
2017 May 16-28		
* 2017 Aug 08		
Test Site 2: Zugspitze (ZG) (Sentinel-1A, Ascending, relative orbit number: 117) (Landsat-7, path: 193, row: 27) (Sentinel-2, tile number: T32TPT)		
2016 Nov 07-19	2018 Mar 14-26	2018 May 13-25

	(L7: Mar 25)	*(S2: May 07)*
2017 Feb 23- Mar 07		
2017 May 18-30		
* 2017 Aug 10		
Test Site 3: Mount Whitney (MW) (Sentinel-1A, Ascending, relative orbit number: 144) *(Landsat-7, path: 41, row: 35)*		
2017 Feb 25-Mar 09	2018 Mar 04-16 *(L7: Mar 16)*	2018 May 03-15 *(L7: May 03)*
2017 Apr 02-14		
2017 May 08-20		
* 2017 Aug 12		
Test Site 4: Landtang Lirung (LL) (Sentinel-1A, Ascending, relative orbit number: 85) *(Landsat-7, path: 141, row: 40)*		
2017 Feb 09-21	2018 Feb 28-Mar 12 *(L7: Mar 13)*	2018 May 11-23 *(L7: May 16)*
2017 Apr 10-22		
2017 May 16-28		
* 2017 Aug 08		
Test Site 5: Aconcagua (AG) (Sentinel-1B, Descending, relative orbit number: 83) *(Landsat-7/8, path: 233, row: 82)*		
2017 May 10-22	2018 Jun 10-22 *(L8: Jun 13)*	2018 May 05-17 *(L7: May 04)*
2017 Aug 14-26		
2017 Nov 06-18		
* 2018 Jan 29		

3.2.3. Auxiliary Data

In addition to SAR-derived information, it is also critical to include both land cover as well as topographical information for building a model for the total SCE classification. Considering the global availability, accessibility and data sustainability, we relied on the version 4 of the Digital Elevation Model (DEM) based on National Aeronautics and Space Administration (NASA)'s Shuttle Radar Topographic Mission (SRTM) as well as the land cover data provided by ESA Climate Change Initiative (CCI) product version 2.0.7. SRTM DEM was used to derive elevation, slope and aspect and curvature topographical information.

Even though the Advanced Spaceborne Thermal Emission and Reflection Radiometer (ASTER) DEM has 30 m spatial resolution and global coverage, which is

better when compared to the SRTMv4 DEM (around 80% global coverage and 90 m spatial resolution), SRTM was chosen as a source for the DEM as it provides higher vertical accuracy (Jarvis et al., 2008; Hirt et al., 2010; Frey and Paul, 2012; Athmania and Achour, 2014). For land cover data, we selected the ESA CCI land cover product because CCI not only provides a global coverage with 300 m resolution and quality flags denoting the number of valid observations used for classification, but is also annually updated since 1992 with the latest update in 2015.

The ESA CCI land cover product typology follows the land cover classification system (LCCS) defined by the United Nations (UN) Food and Agriculture Organization (FAO) (ESA, 2017). It originally categorizes 37 different land cover types including some detailed distinguishes such as different ratio of mosaic tree and shrub with herbaceous cover; hence all original 37 classes were re-categorized to 16 classes for our study (definition shown in Appendix A) to maintain class differences while avoiding complexity.

To train and validate our models, DLR's Global SnowPack (Dietz et al., 2015) was employed as it provides daily full globe SCE in 500 m spatial resolution without the influence of cloud coverage or polar darkness. Moreover, its daily SCE availability allows for a same-day training and validation when the Sentinel-1 scenes are acquired.

3.3. Methodology

3.3.1. SAR Imagery Processing

The processing of SAR-based observations requires several steps in order to support the three mainstream SAR-based SCE detecting approaches comprising backscattering, InSAR and PolSAR-based methods.

For backscattering-based information, each GRD SAR image was subset to the extent of the study region. Each image was calibrated, had its thermal noise removed and underwent speckle filtering with Lee sigma filter (Lee, 1983) (7×7 window size). It was then corrected for terrain flattening and distortion with the SRTM DEM, and converted to decibel (dB) units. Finally, each season's SAR dB dataset was set in relation to the summertime's reference dB image (i.e. theoretically bare/snow-free ground) (Table 3.2). It is important that, as the quantitative analysis is involved (ratio), the original intensity value or digital numbers (DN) of GRD images need to be calibrated. This is to represent the genuine brightness value based on the incidence angle information (Lavalle and Wright, 2009).

Two SLC images were co-registered for InSAR processing to estimate the coherence

value. As IW mode Sentinel-1 imagery is sensed at TOPS mode, it is necessary to respectively split each sub-swath and merge each burst, before and after co-registration. The coherence map was then terrain corrected to remove distortions. For InSAR, the temporal baseline between master and slave images should be shortened to reduce the magnitude of temporal variability that may affect the coherence value considerably (Zebker and Villasenor, 1992). Thus, the temporally nearest SAR imagery of a selected master scene was used as slave image.

Finally, for polarimetric information, each SLC image was calibrated, debursted and the polarimetric matrix was constructed. As the employed Sentinel-1 IW mode imagery only provides dual polarizations (VV and VH in all five study regions), the incoherent polarimetric C2 (2×2) complex covariance matrix formed by co- and cross-polarized complex scattering amplitudes was used (Pellizzeri, 2003; Lee J.-S. and Pottier E., 2009). The refined Lee filter (Lee, 1981) with 7×7 window size was then applied to de-speckle, and a decomposition was performed before the final terrain correction. In the presented study, the H/A/α decomposition proposed by Cloude and Pottier (Cloude and Pottier, 1996) was selected due to the availability of dual-polarizations as well as the intensive employment frequency and its viability to detect SCE (Dedieu et al., 2012; Singh and Venkataraman, 2012; Singh et al., 2014; Callegari et al., 2016). Under the commonly used assumption of reciprocal targets (i.e. scattering amplitude of VH and HV are the same) (Pellizzeri, 2003), H/A/α decomposition utilizes the eigenvalues and eigenvectors calculated from the coherency matrix, which then composes the H/A/α, representing the entropy (randomness of depolarization of scattering type), anisotropy (normalized difference of importance of scattering type) and scattering angle (dominant scattering angle and type). The comprehensive descriptions of decomposition can refer to (Cloude and Pottier, 1996; Pellizzeri, 2003).

3.3.2. Total SCE Detection

3.3.2.1. Random Forest Classification

As the aim of this study is to detect snow cover on the land surface of various regions around the globe, a simple tuning classifier which is capable of efficiently solving a two-class classification problem is necessary. According to the Global Observing System for Climate (GCOS) (Key et al., 2007), a spatial resolution of at least 100 m is necessary for snow cover mapping in mountain regions. Therefore it has been set as the output of the implemented model setup. In this study, the random forest (RF) (Breiman, 2001) was chosen to classify snow cover based on SAR observations. Compared to other supervised classifiers, RF has multiple advantages including a

relatively short training time, low computation load, capability to handle high dimensional data with missing values, support of parallel processing, simple tuning of parameters, avoiding of over-fitting, providing importance indexes of input variables, and providing an internal quality index (out-of-bag (OOB) error) (Breiman, 2001; Gislason et al., 2006; Archer and Kimes, 2008; Ali et al., 2012; Sazonau, 2012; Horning, 2013; Belgiu and Drăguţ, 2016). Due to these advantages, RF has been widely applied to many remote sensing-based classification topics (Ham et al., 2005; Pal, 2005; Cutler et al., 2007; Chan and Paelinckx, 2008; Immitzer et al., 2012; Rodriguez-Galiano et al., 2012; Feng et al., 2015; Belgiu and Drăguţ, 2016; Immitzer et al., 2016). However, it is still surprising that, so far, studies relying on RF classifiers for SCE mapping are very rare.

In the present study, the two required tuning parameters for saving memory consumption and computation time while yielding the highest classification performance after several test runs, that is, the parameters of the number of trees L and number of random features assigned to each tree θ_k, are respectively set to 600 and the default value (square root of total feature numbers). Although several studies demonstrated that *L* has less influence than θ_k on the classification accuracy (Ghosh et al., 2014; Du et al., 2015; Belgiu and Drăguţ, 2016), different *L* values were tested (ranging from 50 to 1000) in Monte Rosa (MR) region and the resultant classification accuracy and processing time are presented in Appendix B. It is found that the RF model with 600 trees can efficiently achieve on optimized accuracy. This finding agrees with previous studies suggesting that a tree number of around 500 is generally sufficient (Canovas-Garcia and Alonso-Sarria, 2015; Cánovas-García et al., 2017).

3.3.2.2. Random Forest Model Setup

For building the RF models, the selected input variables include: (1) SAR-based observations (backscattering ratio, interferometric coherence, and polarimetric H/A/α parameters as mentioned in 3.1); (2) topographical information: elevation, slope, aspect, and curvature derived from SRTM DEM; (3) land cover classes (ESA CCI land cover product); (4) total SCE (Global SnowPack daily SCE).

The RF models were established separately for each land cover class. Namely, each modelling trial consists of *N* RF models with *N* referring to the number of land cover classes in the study region. To test the influence of the three SAR observations and the four topographical factors on the RF performance, they were combined in varying setups. Firstly, uni-, dual- and three SAR observation-combined based models were tested. Then, the highest accuracy model was added with uni- and all topographical information. Eventually, the best observation-factor combination model was then

applied in two individual RF model scenarios. In the first case, each region's first year's data was used to build the model for each region individually, which were then correspondingly applied to the region's second year's data. Consequently in the second case, the input data of all test regions were merged from the first year's data to build one aggregated model, which was applied to the second year.

3.3.2.3. Data Splitting for Model Training and Validation, Calculation of Accuracy Evaluation Measurements

To establish the RF model as well as to achieve a comprehensive validation, in the presented study many different sources of data were used, including GSP, optical-based SCE, and snow depth data of meteorological stations. The overall data splitting for each region's each land cover class's model training and validation is illustrated in Figure 3.3.

First, to train the RF model, 70% of the pixels of the first year's data (including SAR-based observations and topographical factors mentioned in 3.2.2) were randomly selected and facilitated to build the model. The established model was then internally validated with 30% of the first year's GSP data which were manually omitted from building the model. It must be noted that the OOB samples, which account for around 37% of input data which were automatically not employed in the training sample when building the RF model and assigning features to the model trees, were not used for cross-validation in the presented study. The coarse resolution of GSP (500 m) would inevitably lead to spatial autocorrelation between training and OOB samples. Namely, the value between two sample sets are dependent, which could lead to overestimation of OOB accuracy (Cánovas-García et al., 2017).

Then the established RF model (only trained by first year's GSP data) was used to predict the SCE of the second year, which was then validated with additional external validation sources, including the second year's GSP (two sets of data, as shown in Table 3.2), Landsat/Sentinel-2-based SCE, and meteorological data.

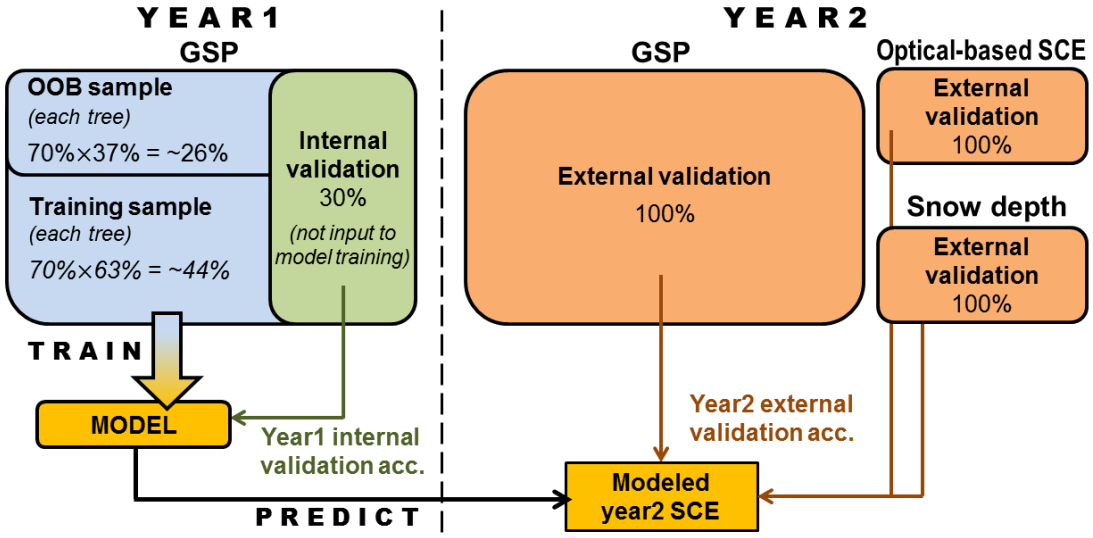

Figure 3.3 Data splitting for model training and validation including internal-, external validation, Out-of-bag (OOB) sample, and training sample based on Global SnowPack (GSP), optical-based snow cover extent (SCE), and snow depth data.

When comparing the different model inputs and setups, one of the most critical steps is to evaluate the specific model performances. Hence, an accuracy assessment was introduced, including overall accuracy, F-measure (Lewis and Gale, 1994), and 'Area Under the ROC' (receiver operating characteristic curve) (AUC) (Fawcett, 2006). These indexes provide different evaluation aspects (Sokolova et al., 2006; Ferri et al., 2009) as overall accuracy. F-measure focuses on minimizing the number of errors based on thresholding and qualitative evaluation. In contrast, AUC's purpose is to show how accurate the classes are separated, by checking how the model ranks the examples. Moreover, as it is commonly known that forest-covered areas could produce erroneous results (based on SAR data snow cover classifications (Pulliainen et al., 1994; Koskinen et al., 1997; Kumar and Venkataraman, 2011; Dedieu et al., 2012), the abovementioned accuracy measurements were also used to calculate non-forested regions separately (the criteria of forest type listed as Appendix) in order to examine the influence of vegetation.

Considering the overall accuracy, F-measure, and AUC, all of them can be derived from the confusion matrix. In this study, overall accuracy is defined as:

$$Overall\ Accuracy = \frac{pixels\ within\ true\ total\ SCE\ classified\ as\ total\ SCE\ +\ pixels\ in\ snow\ free\ classified\ as\ snow\ free}{all\ pixels} \quad (3.1)$$

The F-measure score (a.k.a. F1 score), is a composed weighted measurement which considers both, recall as well as precision. In this study, these accuracy indices were calculated as following:

$$Precision = \frac{pixels\ within\ true\ total\ SCE\ classified\ as\ \text{total}\ SCE}{pixels\ classifed\ as\ total\ SCE} \tag{3.2}$$

$$Recall = \frac{pixels\ within\ true\ total\ SCE\ classified\ as\ \text{total}\ SCE}{pixels\ within\ true\ total\ SCE} \tag{3.3}$$

$$F1\ score = \frac{precision \times recall}{precision + recall} \tag{3.4}$$

The last quality index that is calculated to evaluate the performance of the model is the AUC score, which is based on ROC. The ROC curve is plotted with False Positive Rate and True Positive Rate on the x- and y-axis, respectively. The specificity can be defined as:

$$Specificity = \frac{pixel\ not\ in\ true\ total\ SCE\ classified\ as\ not\ total\ SCE}{pixel\ not\ in\ true\ total\ SCE} \tag{3.5}$$

ROC can be interpreted as the probability of ranking randomly selected actual positive samples over randomly selected negative samples. AUC is defined as the area between the ROC and y=x function, which has a value range from 0.5 to 1.0. According to Metz (1978), AUC values range from 0.5 to 0.6, 0.6 to 0.7, 0.7 to 0.8, 0.8 to 0.9, and 0.9 to 1.0, representing bad, satisfactory, good, very good, and excellent model performance, respectively.

3.3.2.4. Tests for Selecting the Optimized Model Input Variables

As described in section 3.2.2, the possible inputs for the implemented model to detect total SCE include SAR-based observations (backscattering ratio, InSAR coherence and PolSAR H/A/α parameters, abbreviated as B, I and P), topographical parameters (elevation, aspect, slope and curvature, abbreviated as e, a, s and c), and land cover information originating from the CCI land cover product. To select the optimized input combination for the model, Monte Rosa in the Swiss Alps (MR) was chosen as a pilot study site for an in-depth accuracy assessment, as it is characterized by complex topography and land cover.

To test the influence of the SAR parameters on the model performance, different combinations of SAR-based observations were employed to train MR's model set. To assess their uncertainties, 20 iterations were processed for each trial. Resultant accuracy assessments are illustrated in Figure 3.4(a). It is obvious that for all land

cover classes, the combination of all available SAR parameters (B+I+P) produces the highest accuracy. When relying only on one SAR-based observation, using P leads to higher classification accuracy than relying on I or B. The accuracy improvement between using only single SAR parameters and the combination of all available parameters (B+I+P) is significant. Moreover, it is observed that for land cover classes that pose considerable challenges in detecting snow cover using SAR (e.g. forested areas), combining all available SAR parameters leads to a significant improvement of classification accuracy.

For evaluating the influence of topographical parameters on the model performance, elevation (e), aspect (a), slope (s), and curvature (c) were added as input parameters to the ML approach separately. Their influence on the classification accuracy is presented in Figure 3.4(b). Results show that by successively adding more topographical parameters the performance of the model increases, leading to its highest performance if all parameters are added collectively (‘asce’ case in Figure 3.4b). The overall accuracy for all land cover classes could be improved by around 8.4%, while the F1 score improved by 9.4% when compared to using only the combination of B+I+P as inputs. Even in non-forested areas, the accuracy (NF OA) rises by around 7.7%. Additionally, the AUC value could be improved by more than 12%. Of all tested topographical parameters, elevation has the biggest impact on the model performance. For example, using only B+I+P to classify snow cover within the mixed shrub and herbaceous land cover, the accuracy only reaches around 0.62. This value could be improved to 0.72 by only adding elevation (e) as an auxiliary input. By adding the remaining three topographical parameters (s+a+c), the accuracy increases to 0.74. Testing the influence of different combinations of input parameters (SAR as well as topographic), it became clear that the combination of all available SAR-based observations and all topographical parameters leads to the best model performance for classifying total snow cover. The same tests have been performed for all test sites listed in Table 3.2, which are not illustrated here for clarity, but leading to the same results as for the Monte Rosa test site. Therefore, all available SAR-based observations and all topographical parameters have been used as model inputs for the subsequently presented results.

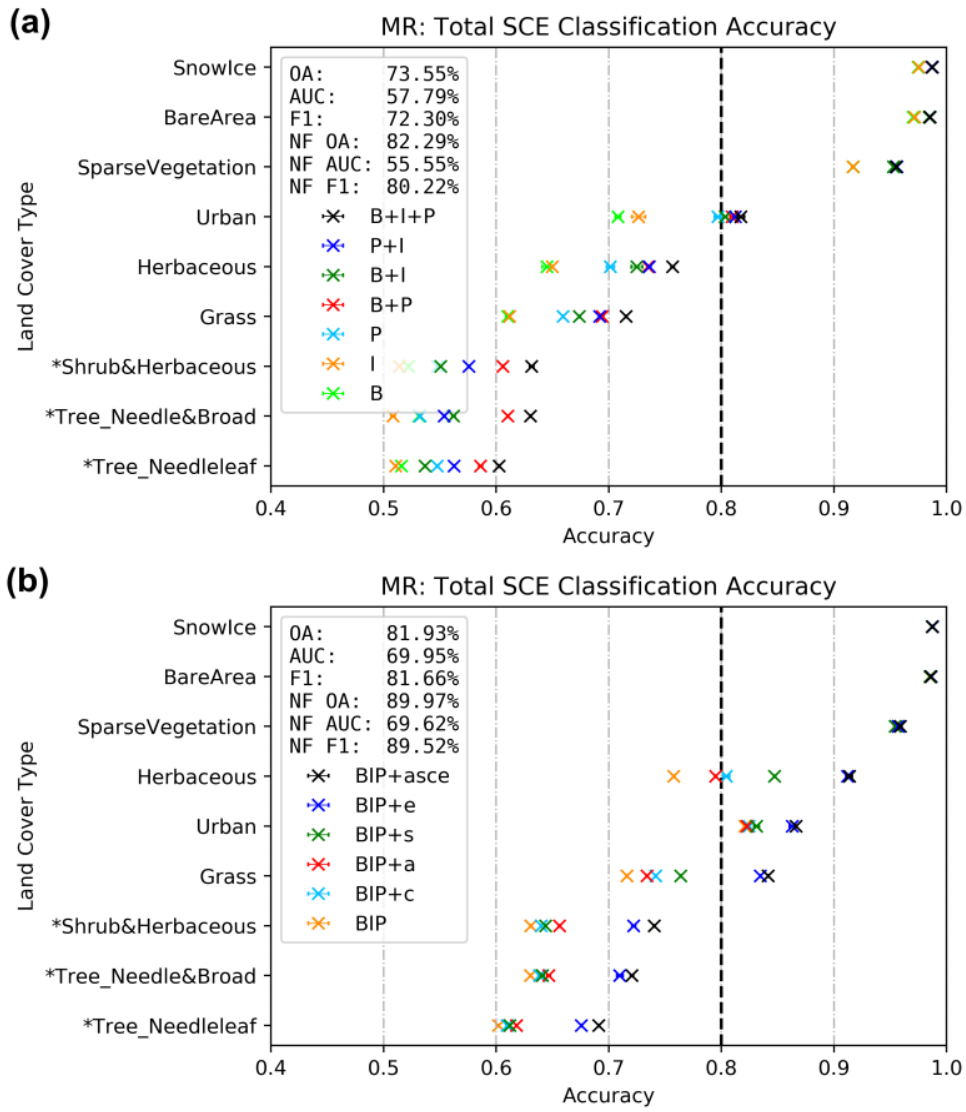

Figure 3.4 Assessment of the influence of different input combinations on the performance of the model for Monte Rosa (MR) region. SAR-based observations including backscattering ratio, InSAR coherence and PolSAR H/A/α parameters are abbreviated as B, I and P. Topographical factors including aspect, slope, curvature, and elevation are abbreviated as a, s, c, and e. Accuracy of each land cover type modeled with SAR-based observations only/ together with topographical factors is shown in (a) and (b), respectively.

3.3.3. Holistic (Total + Wet) SCE Detection and Overall Workflow Overview

The wet SCE detection was performed, in addition to the RF-based classification of the total SCE, in order to exploit the full potential of the SAR data and to discriminate between wet and dry snow. To map the wet SCE, the backscattering coefficient-based 'Nagler's method' was applied. As summarized in the introduction, this method

requires two SAR images sensed at snow-covered and snow-free conditions. It utilizes a backscattering threshold (-3 dB) to the ratio map of the two images for detecting the wet SCE. In present study, according to the feasibility of using cross-temporal reference image proved by Luojus et al. (2006), both years' SAR data observed during the snow cover season were combined with the reference scene (summertime observation) of the first year (Table 3.2).

The overall workflow of mapping total SCE, by applying a supervised RF classification model set as well as detecting wet SCE with 'Nagler's method', is illustrated in Figure 3.5.

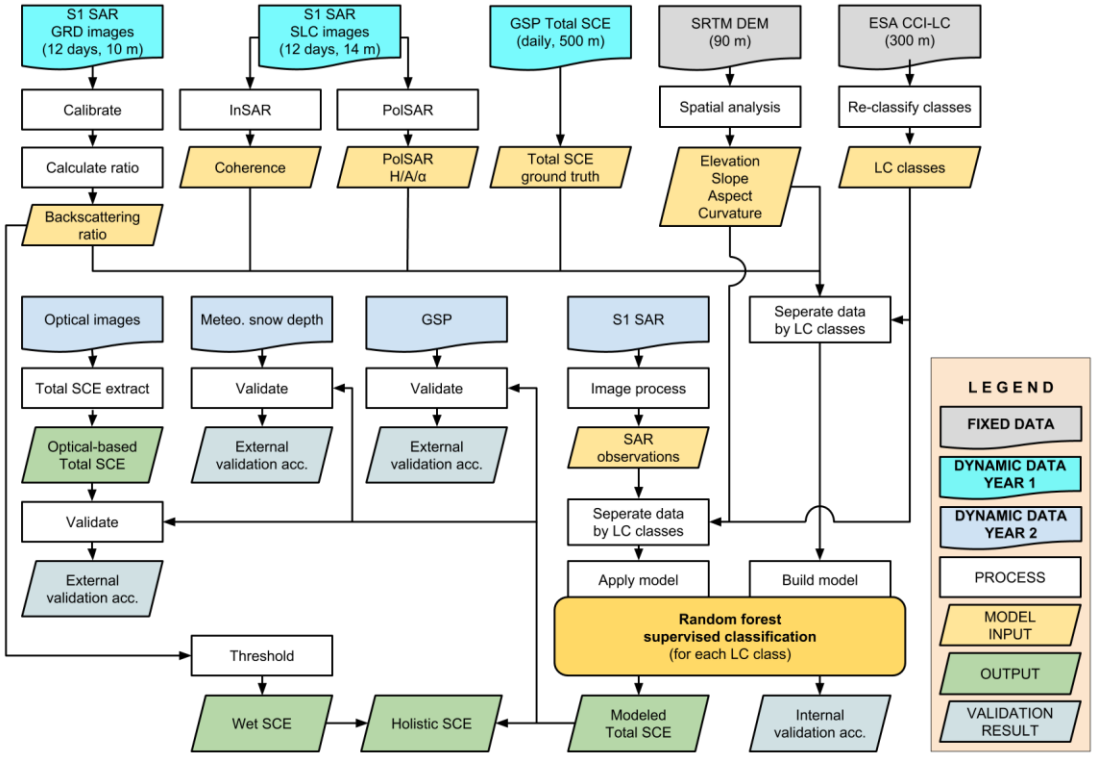

Figure 3.5 Overall workflow of mapping and validating holistic (total + wet) Snow Cover Extent (SCE) with SAR-based observations, topographical information, land cover information, and Global SnowPack (GSP) daily snow cover information.

3.4. Results

Based on the optimized input variable combinations tested in 3.2.4, the same modelling approach was applied to all five study areas. Also, to examine the transferability of the model setups, the results were comprehensively validated with different data sets (Landsat/Sentinel-2 and in-situ snow depth information). Finally, the holistic (total + wet) SCE was derived based on the modeled total SCE and wet SCE calculated from 'Nagler's method'.

3.4.1. Accuracy Assessment of Modeled Total SCE

As presented in section 2.1, five different study areas located around the globe were selected and applied with the proposed model. The total SCE mapping model set can be trained by either (1): using each region's data to train an individual model set and therefore training a region-dependent model set, or (2): merging all regions' data to train one universal model set, which was then applicable for all regions simultaneously. Depending on the intentional application of the model, it might be sufficient to have a spatially confined model which only works for a specific region. However, if it is required to derive snow cover information for several varying locations, a universal model set has to be implemented. For both cases, the performance of the model has to be known and therefore has to be assessed.

For the first (individual) case, the results of the accuracy assessment are presented in Figure 3.6(a-e). The overall accuracy of MR, ZG, MW, LL and AG are around 80%, 75%, 90%, 90%, and 80%, respectively. The F1 score for each test site is higher than 70%. AUC scores for all regions are around 70% or higher which indicates a good model performance; with the exception of ZG, with around 60%, which is still satisfying. The amount and distribution of land cover vary between the test sites and affect the overall accuracy of the model performance. The complexity of land cover types within the CCI land cover product used as auxiliary data in this study is considerably higher in the Europeans Alps and Asian Himalaya when compared to the Andes and Rocky Mountains (see Figure 3.1). As already reported in earlier SAR-based snow cover studies (Nagler and Rott, 2000; Notarnicola C. et al., 2013), lower accuracy values are achieved in grassland as well as forested areas (classes marked as * in Figure 3.6), with the exception of the LL test site. To examine the negative effect of grassland and forest areas of the classification performance, the accuracy values have also been calculated for non-forest classes (indicated in Figure 3.6 with NF OA, NF AUC, and NF F1).

As outlined above, building individual models for each test site separately can guarantee a more customized classification with higher accuracy. The overall accuracy of these individual cases including forests and grassland ranges from 75.2% to 89.6% (of which 79.4% - 98.6% excluding forests and grassland) with F1 scores ranging from 71.9% to 89.6% (of which 76.0% - 98.6% excluding forests and grassland, see Figure 3.6a-e). All input data were also merged to build a universally applicable model, which shows only slightly lower accuracy values of 81.1% of the overall accuracy (of which 84.5% excluding forests and grassland) and an F1 score of 80.4% (of which 83.9% excluding forests and grassland, see Figure 3.6f). These

values prove a good model performance. This evaluation reveals the robustness of the classification approach proposed in this study whilst merging all input data to create a globally transferable model setup; even if the model is trained universally. The sturdiness can also be exposed from the neglected accuracy difference of 20 trials for each land cover class of each region.

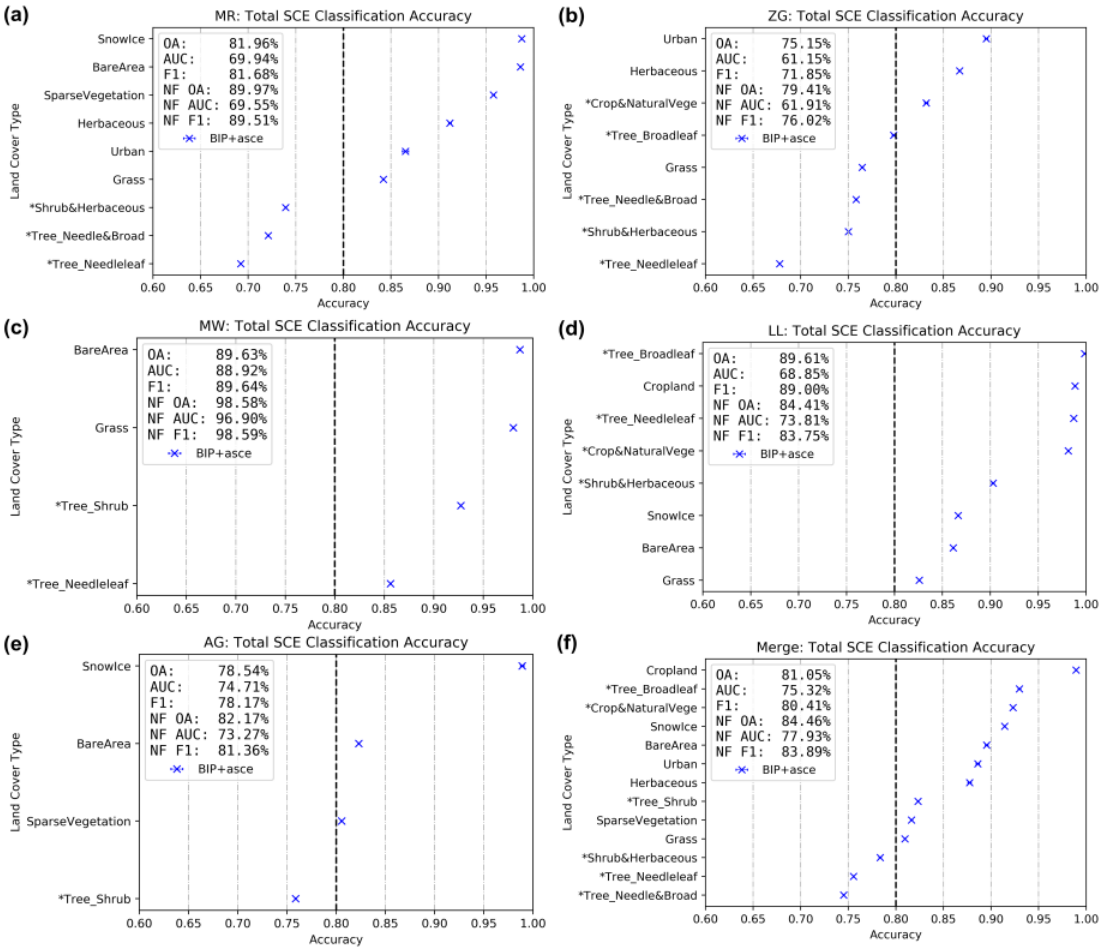

Figure 3.6 Results of each model set built in each region: (a) Monte Rosa (MR), (b) Zugspitze (ZG), (c) Mount Whitney (MW), (d) Landtang Lirung (LL), and (e) Aconcagua (AG); and the five regions' merging case (f). SAR-based observations including backscattering ratio, InSAR coherence and PolSAR H/A/α parameters are abbreviated as B, I and P. Topographical factors including aspect, slope, curvature, and elevation are abbreviated as a, s, c, and e.

3.4.2. External Validation

Although previous studies often neglect the importance of a detailed validation approach, it is indispensable to comprehensively examine the robustness and correctness of a proposed model with internal and external validation efforts. Consequently, several validation steps have been incorporated into the presented

study. It complements the internal validation illustrated in section 4.1 with addition to external validation based on the GSP, optical-based SCE and in-situ snow depth data, as illustrated in the data splitting of Figure 3.3 and workflow of Figure 3.5. The results of these accuracy assessments are presented in the following sections.

3.4.2.1. Results of the External Validation with the Global SnowPack and Landsat/Sentinel-2 Derived Snow Cover Maps

In order to examine each land cover type's influence on the model's accuracy, the comparison between the 'training accuracy' (the overall accuracy of the internal validation, calculated based on 30% of the first year's data manually kept (Figure 3.3)) and the 'validation accuracy' (the overall accuracy of the external validation, calculated based on the second year's GSP) were calculated and presented as blue and red bar in Figure 3.7, respectively. Most of the land cover types show a slightly lower accuracy for all test sites of the second year validation accuracy, with the exception of the ZG region. However, almost all land cover types within all study areas are still characterized by a satisfying accuracy (>0.6), with the exception of forested classes of the MR region. This affirms the robustness of the employed model set.

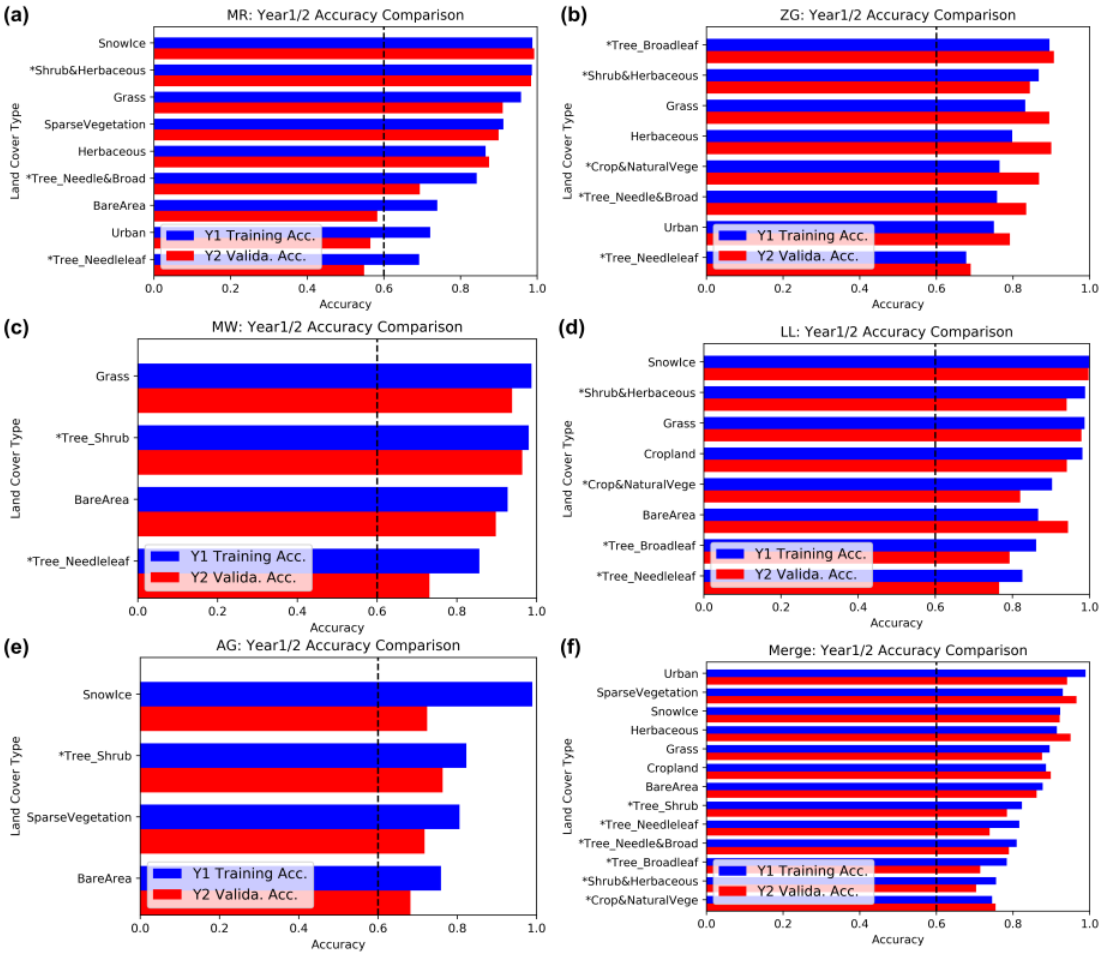

Figure 3.7 Each region's land cover type's accuracy comparison between training (first hydrological year) and validation set (second hydrological year). Model built for each region: (a) Monte Rosa (MR), (b) Zugspitze (ZG), (c) Mount Whitney (MW), (d) Landtang Lirung (LL), and (e) Aconcagua (AG); and the five regions' merging case (f).

The 500m spatial resolution GSP product may not accurately depict the actual SCE in mountain regions due to missed pixel effects and the negative influence of temporal interpolation for cloud-gap filling. Therefore, in addition to this product, higher resolution optical imagery originating from Landsat-7/8 (30 m) and Sentinel-2 (20 m) were also employed to derive SCE for validation. All available observations from these two sensors were screened for suitable data (i.e. cloud-free). The observations chosen for processing are listed in Table 3.2. The aim is to keep the observation date of the optical sensor as close as possible to the SAR data's date, which could be achieved for most cases with temporal gaps of less than one week.

To extract the optical-based total SCE, the Fmask algorithm was employed (Qiu et al., 2017). Fmask is an algorithm aiming to extract clouds, cloud shadows, snow and waterbody from Landsat 4-8 and Sentinel-2 imagery. Thanks to its mountainous Fmask function which utilizes additional DEM information, the accuracy of mapping cloud shadow and removing terrain shadow in mountainous regions is significantly improved. For parameter setting, the dilation size of cloud, cloud shadow and snow were set to 3, 3 and 0, respectively. The threshold for cloud probability was set to 10.0% for Landsat-7, 17.5% for Landsat-8, and 20.0% for Sentinel-2. The resultant total SCE and original true color composites for each study site are shown in Figure 3.8. Overall, the Fmask classification results are reasonable except for AG region showing misclassification of waterbody. However, it is also obvious that there is still serious cloud contamination. Also, due to the orbit design and sensing swath of the satellites, the study area is not always completely covered by the Landsat/Sentinel-2 observation.

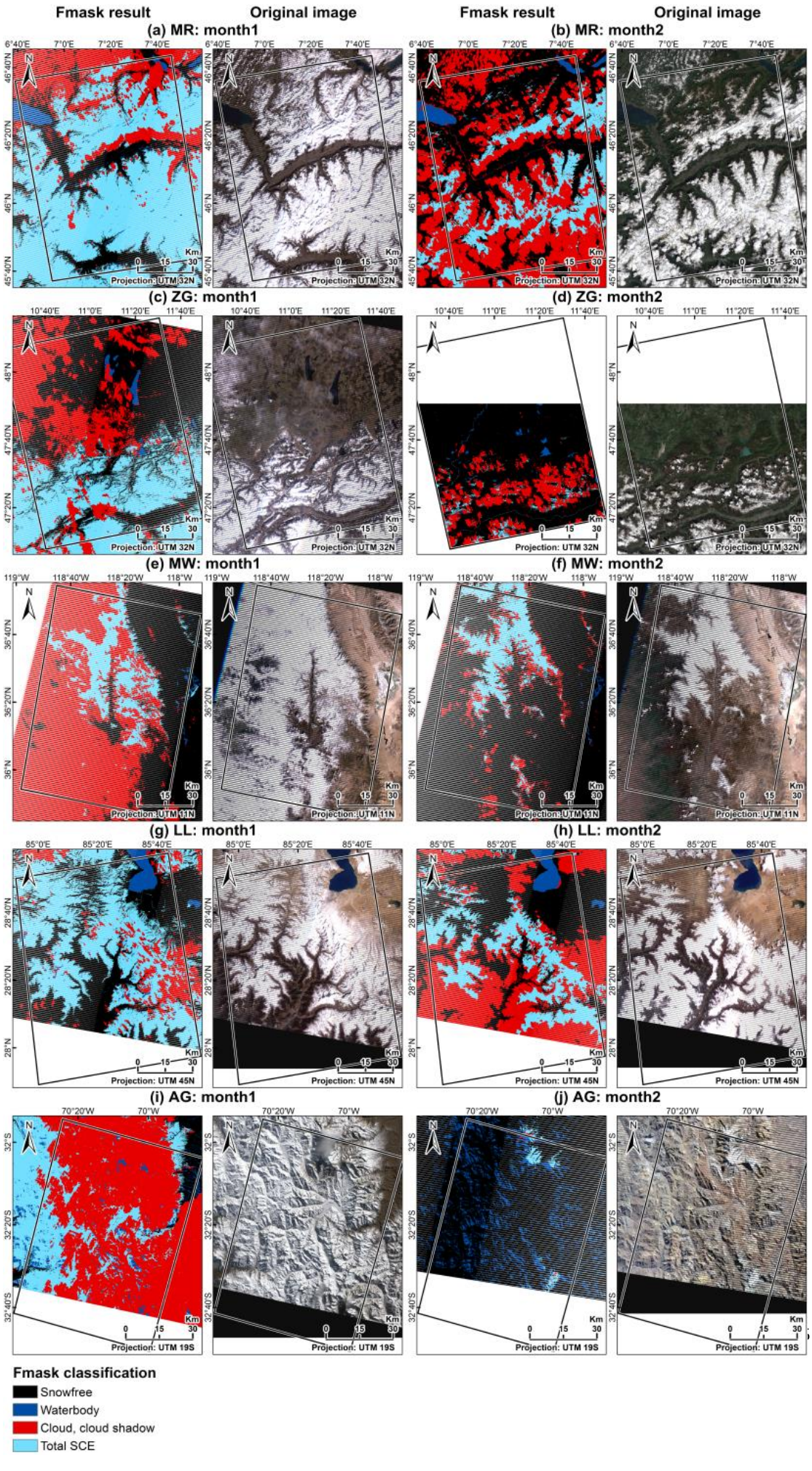
Fmask result
Original image
Fmask result
Original image
(a) MR: month1
(b) MR: month2
(c) ZG: month1
(d) ZG: month2
(e) MW: month1
(f) MW: month2
(g) LL: month1
(h) LL: month2
(i) AG: month1
(j) AG: month2
Projection: UTM 32N
Projection: UTM 11N
Projection: UTM 45N
Projection: UTM 19S
Km
Fmask classification
Snowfree
Waterbody
Cloud, cloud shadow
Total SCE

Figure 3.8 Fmask-based total snow cover extent classification derived from Landsat and Sentinel-2 as well as true-color composites for each test site: (a) Monte Rosa (MR), month 1 (Mar 23, 2018); (b) Monte Rosa, month 2 (May 18, 2018); (c) Zugspitze (ZG), month 1 (Mar 25, 2018); (d) Zugspitze, month 2 (May 07, 2018); (e) Mount Whitney (MW), month 1 (Mar 16, 2018); (f) Mount Whitney, month 2 (May 03, 2018); (g) Landtang Lirung (LL), month 1 (Mar 13, 2018); (h) Landtang Lirung, month 2 (May 16, 2018); (i) Aconcagua (AG), month 1 (Jun 13, 2018); (j) Aconcagua, month 2 (May 04, 2018).

To compare two total SCE results (the SAR-based one based on the RF classification and the optical-based classification based on Fmask), a total of 10,000 random points were equally distributed in both snow-covered as well as bare ground areas (5,000 points each). The points were distributed based on the result of the Fmask product, excluding cloud-covered areas by treating them as no-data. Although some studies reported that Fmask may tend to over-estimate cloud (Selkowitz and Forster, 2016; Nagare et al., 2017), in the present random-point-allocating method it would not damage the reliability of validation. A confusion matrix as well as evaluation indexes (overall accuracy and F1 score) were then computed for each test site and each month of the second year, and the results of this assessment are presented in Table 3.3. To simplify the interpretation, the numbers of points in each column/row of the confusion matrix were converted into a percentage of total 10,000 points. All ten months' cases show good accuracy and F1 score (> 0.72); except for month1 of AG region, which shows significant under-estimation. Under-estimation is also shown in non-used month (month1) of the first year in ZG and LL region. Furthermore, the month2 of AG region show a mild over-estimation.

Table 3.3 Confusion matrix of the accuracy assessment relying on optical-based snow cover classifications of Landsat and Sentinel-2 for each test site. The assessment includes classifications for months that were trained in the first year (month2) as well as those that were not used in the training of the first year (month1). Overall Accuracy (OA) and F1-score are depicted under the respective confusion matrix.

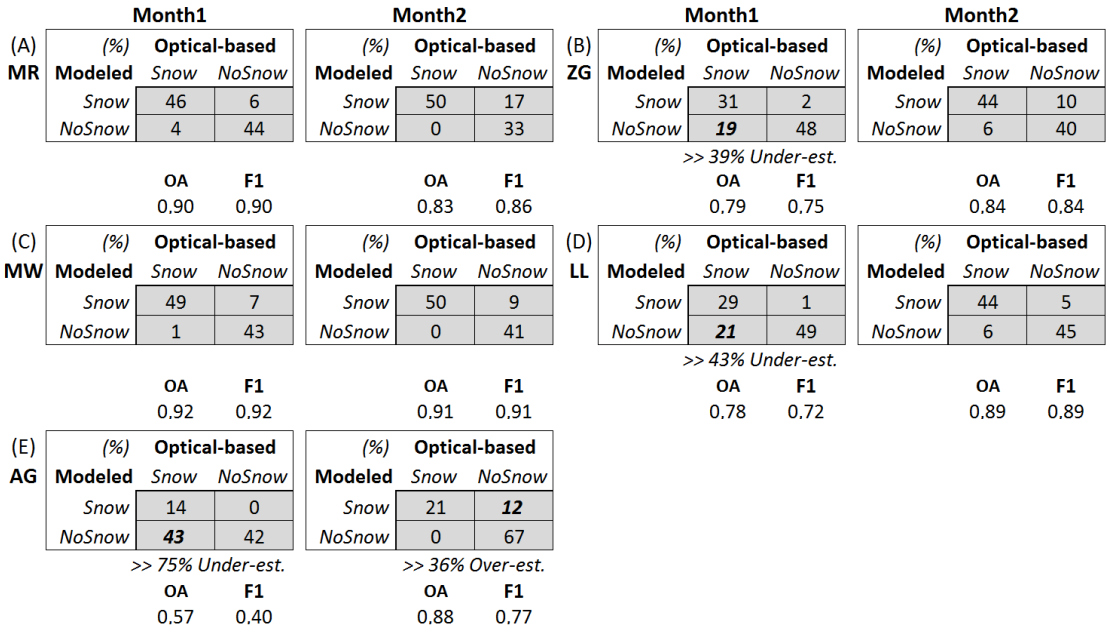

3.4.2.2. Validation Relying on In-situ Data Originating from Meteorological Stations

In addition to the validation based on satellite observations, snow depth (SD) measurements originating from meteorological stations are available for some study area. For the European region, few countries' national meteorological agencies, for example in Switzerland, provide free access to these data. Additional measurements of daily SD are available from the European Climate Assessment & Dataset Project (ECA&D) (Tank et al., 2002). The study sites MR and ZG were chosen to be validated with 28 stations of MeteoSwiss and 114 stations of ECA&D, respectively. The locations of the meteorological stations are illustrated in Figure 3.9. However, as more than 50% of the stations are located in relatively low elevation zones, which are generally completely snow-free in May, only March observations were validated for the presented study. For the study site MW, only one meteorological station was available, while for LL and AG, no suitable and freely accessible station data could be acquired. Therefore, these three regions were not validated with meteorological records. The confusion matrix, displaying the accuracy derived from the comparison of the SAR-based SCE classification with station data, is illustrated in Table 3.4. Whilst not considering the skewed observations (station records contain less 'snow-covered' data (i.e. SD higher than 0cm)), both regions achieve overall accuracy values of more than 87%. However, a slight under-estimation can be found in ZG region. This could be because there might exist a certain threshold of SD for spaceborne SAR-based approach to detect that pixel is snow-covered, such as 1 cm for MODIS snow cover product (Hall et al., 2002) and 2 cm for passive sensors (Che

et al., 2008).

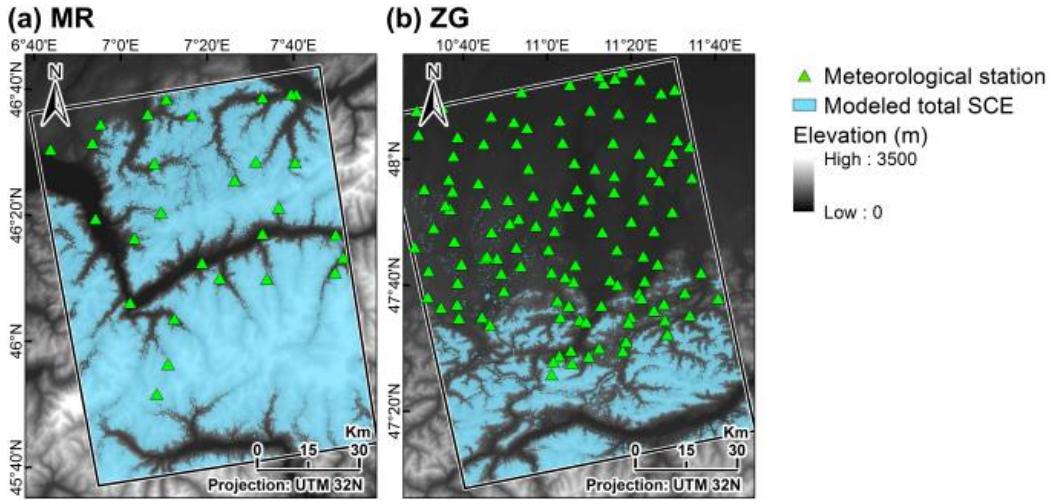

Figure 3.9 Location of meteorological stations in Monte Rosa (MR) and Zugspitze (ZG) regions.

Table 3.4 Confusion matrix of Monte Rosa (MR) and Zugspitze (ZG) regions validated with meteorological snow depth (SD) station data records of MeteoSwiss and European Climate Assessment & Dataset Project (ECA&D), respectively.

(A) MR

(%)	MeteoSwiss	
Modeled	*Snow*	*NoSnow*
Snow	7	2
NoSnow	1	18
Total Station	**OA**	
28	0,89	

(B) ZG

(%)	ECA&D	
Modeled	*Snow*	*NoSnow*
Snow	1	4
NoSnow	***11***	98
Total Station	**OA**	
114	0,87	

3.4.3. Holistic SCE Maps Including Discrimination Between Wet and Dry Snow

According to the comprehensive internal and external validation approaches relying on different data sources, all study regions turned out to achieve reliable accuracy values; with the exception of AG region, which shows comparably weaker results. As the RF classification approach relies on training data originating from optical-based products (GSP), it is not possible to train for the discrimination between wet and dry snow. However, as this information is required, we also detected the wet SCE based on Nagler's algorithm (Nagler and Rott, 2000). For the subsequent merge of the total SCE derived from the RF classification and the wet SCE derived from Nagler's classification, the presence of wet SCE is only allowed for regions where the RF classification has successfully detected snow. Figure 3.10 contains the results of this merging approach for all test sites, including month 1 and 2, to illustrate the dynamics of SCE. During March (month 1, Figure 3.10a, c, e, g, i), the total extent of snow cover is larger but wet SCE is proportionally small. As snow melt proceeds during spring

time, wet SCE increases (month 2, Figure 3.10b, d, f, and h, with AG region constituting an exception) while the total SCE decreases.

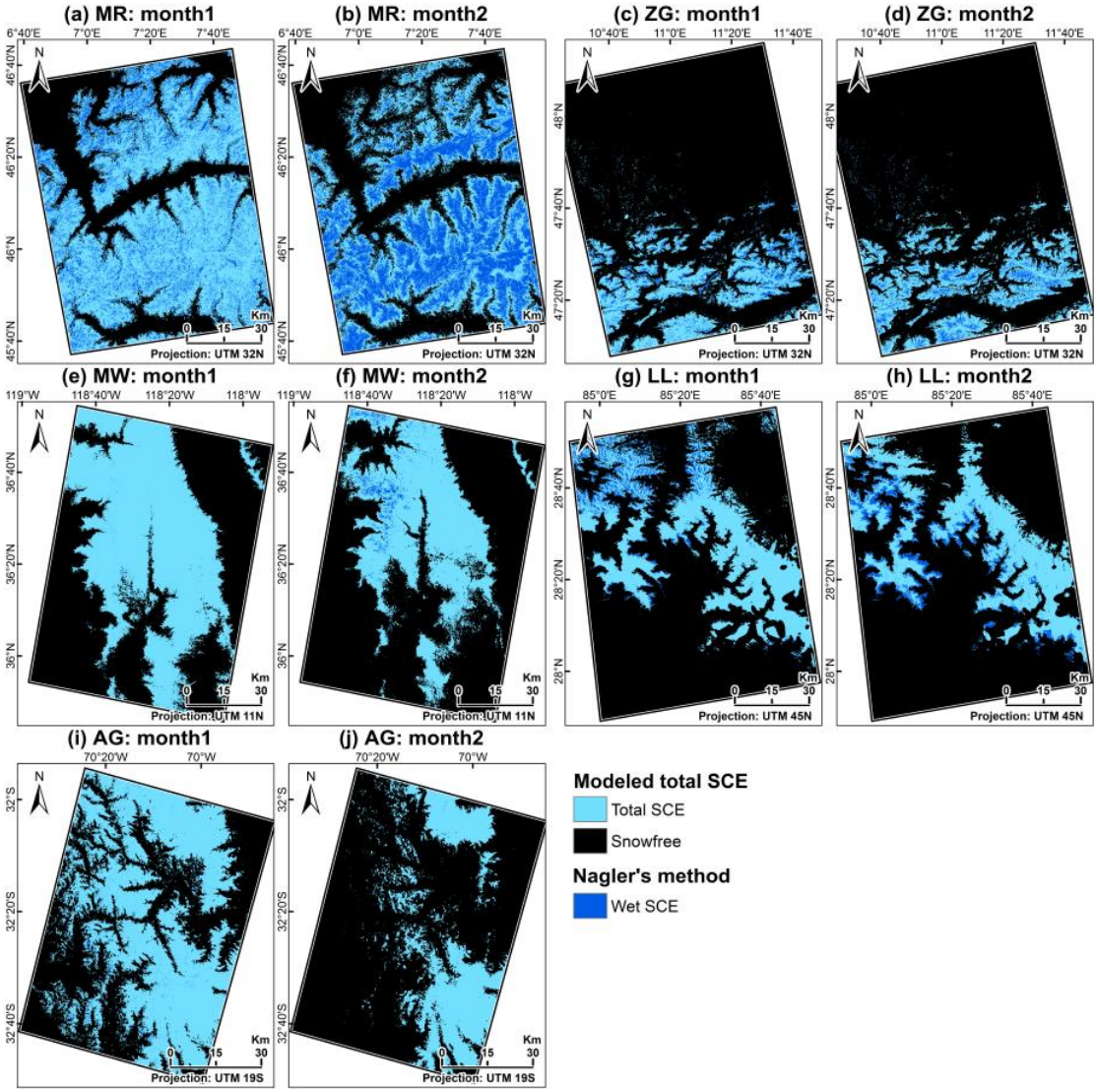

Figure 3.10 Total and wet SCE of each region's two months: (a) Monte Rosa (MR), month 1 (Mar 12, 2018); (b) Monte Rosa, month 2 (May 11, 2018); (c) Zugspitze (ZG), month 1 (Mar 14, 2018); (d) Zugspitze, month 2 (May 13, 2018); (e) Mount Whitney (MW), month 1 (Mar 04, 2018); (f) Mount Whitney, month 2 (May 03, 2018); (g) Landtang Lirung (LL), month 1 (Feb28, 2018); (h) Landtang Lirung, month 2 (May 11, 2018); (i) Aconcagua (AG), month 1 (Jun 10, 2018); (j) Aconcagua, month 2 (May 05, 2018).

3.5. Discussion

3.5.1. Influence of Different Input Factors on the Classification Accuracy

As shown in section 3.2.4, the highest classification accuracy can be obtained when including all three SAR-based observations and all four topographical factors. This

finding is not surprising as the influence of the abovementioned parameters has already been reported in previous studies (Strozzi et al., 1999; Park et al., 2014; Nagler et al., 2016a; Guo et al., 2017; Zhou and Zheng, 2017). Nevertheless, the impact of these variables has only been evaluated separately. The combination of all parameters in one single approach, as it was implemented for the presented study, turned out to achieve the best results. Topography influences the melting and distribution of snow in mountain regions and was therefore included in several approaches to map dry SCE based on wet SCE (Nagler and Rott, 2000; Malnes et al., 2004; Zhen et al., 2012; Park et al., 2014; Thakur et al., 2016). Hence, its influence on the RF-based approach implemented for the presented study is also significant. Moreover, among all three SAR-based observations and the four topographical parameters, PolSAR and elevation resulted in having the highest impact on the classification accuracy as illustrated in Figure 3.4. Comparing the classification accuracy relying on only one SAR-based observation (Figure 3.4(a)), PolSAR parameters (P) can generate the highest accuracy comparing to backscattering (B) and InSAR coherence (I). For instance, in the urban land cover type, the accuracy of the B/I/P-based cases is around 0.71, 0.72, and 0.79, respectively. Comparing the accuracy testing with only adding one topographical factor (Figure 3.4(b)), elevation shows the most significant improvement as the accuracy of grass land can improve from original 0.71 (using only SAR-based observations) to 0.83 when only adding elevation information, but only enhance to 0.72, 0.73, and 0.76 when adding aspect, curvature, and slope information. This might be because PolSAR contains much more physical information of the ground condition, such as characteristics of ground surface, than the relatively noisy backscattering and the InSAR coherence.

The importance of both PolSAR parameters and elevation can also be revealed by the ranks of importance of the variables generated by the RF model. The importance of each input variable of each land cover-targeted RF model was weighted, averaged by the percentage of land cover class for each region. The average importance of each variable for all five study areas is illustrated in Figure 3.11. Although the importance of the variables in each region is different, it is obvious that for all of the regions, elevation and PolSAR parameters have the highest importance. InSAR coherence also shows considerable contribution to the model accuracy comparing to less important variables such as slope, backscatter, aspect, and curvature. However, due to the fact that (1) all those input variables were confirmed related to snow cover by previous studies, (2) even the least important variable, i.e. curvature, still has an importance of more than 5%, (3) the importance of each input variable differs for each region, and (4) the goal of the proposed approach is to guarantee global transferability,

no input variable was trimmed out in the proposed modeling approach to ensure broader suitability and flexibility.

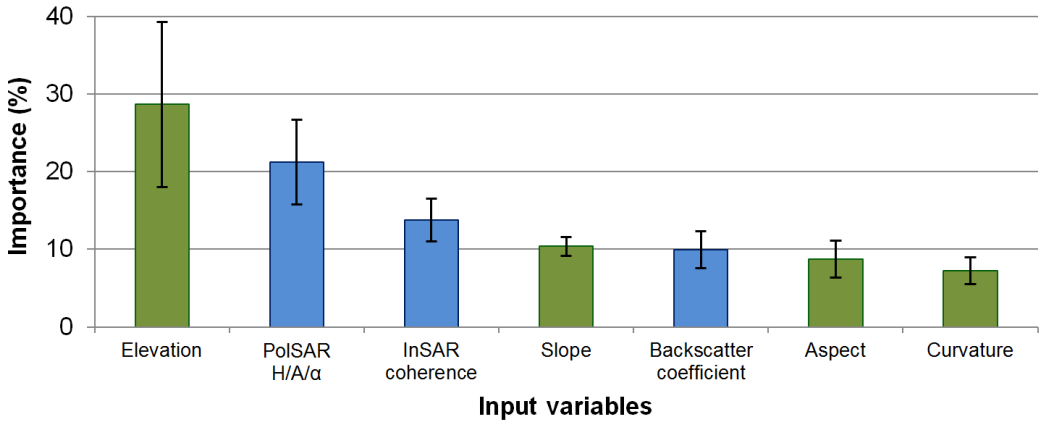

Figure 3.11 The average importance of input variables for all five study regions. Blue and green bars represent SAR-based observations and topographical factors, respectively.

3.5.2. Influence of Vegetation and Land Cover Type on the Classification Accuracy

The evaluation of the RF performance revealed that the snow cover classification accuracy varies significantly between land cover classes (compare Figure 3.4, Figure 3.6 & Figure 3.7). Densely vegetated regions tend to yield lower SCE accuracy when compared to e.g. bare area, sparse vegetation, urban areas, or even grasslands. These findings match with previous studies' conclusions: Koskinen et al. (1997) stated that the existence of vegetation will greatly reduce the difference between SCE and other land cover features. It has further been confirmed by simulation that the stem volume of forests directly relates to SAR signals (Pulliainen et al., 1994), which influences land cover classes with even less biomass such as grassland or cropland (Löw et al., 2002; Schellenberger et al., 2012). Duguay and Bernier (2012) found that the vegetation height would impact the SAR backscattering as well. Moreover, Dedieu et al. (2012) suggested that the structure and phenological change of trees would also affect how the SAR signal reflects and bounces, as it was also observed by Park et al. (2014). Venkataraman (2011) realized that the random motion of vegetation also causes dramatic loss of InSAR coherence.

3.5.3. Challenges for Validating SAR-based Snow Cover Classifications; the Case of Aconcagua (AG) Region

After validating the modeled total SCE results, some regions ended up performing better than others. The most apparent example where several factors come into play

is the AG test site. The external validation with optical-derived SCE maps (Table 3.3) proves the under-estimation of the actual SCE in month1 and the over-estimation in month2. One of the possible reasons is that the land cover product provided by of ESA CCI might be biased for this region. Some of the classes (e.g. scrubland) appear to be overestimated when checked manually, relying on very high resolution imagery from, for example, Google Earth. Around 57% of the AG region is labeled scrubland in the land cover product. When reviewing the quality flag of the ESA CCI land cover product, a lack of available input data can be constituted. As shown in Figure 3.12, the AG region's land cover product is based on considerably less input data than any other region, which might be an indicator that the quality is also poor. In addition to that, according to the ESA CCI land cover product user guidance (ESA, 2017), some specific classes such as sparse vegetation (which accounts for around 23.5% of the AG region) have relatively low classification accuracies. Considering that the total SCE mapping approach proposed in this study is land cover dependent, possible biases in the land cover product would inevitably reduce the robustness of model. As a result, a significant under- and over-estimation could be connected to this issue. To prove this assumption, we also tested the influence of erroneous land cover classes on the classification accuracy in the Monte Rosa (MR) region. First, land cover class labels were randomly shuffled, and the first year's model internal validations as well as the second year's external validation of the resultant SCE were examined (according to Figure 3.3). A decline of around 3% in overall accuracy was found in the internal cross-validation using first year GSP data, and around 20% and 31% of overestimation were shown in month1/2 validated with optical-based SCE, respectively. Based on this test, it is confirmed that the quality of land cover labelling is important.

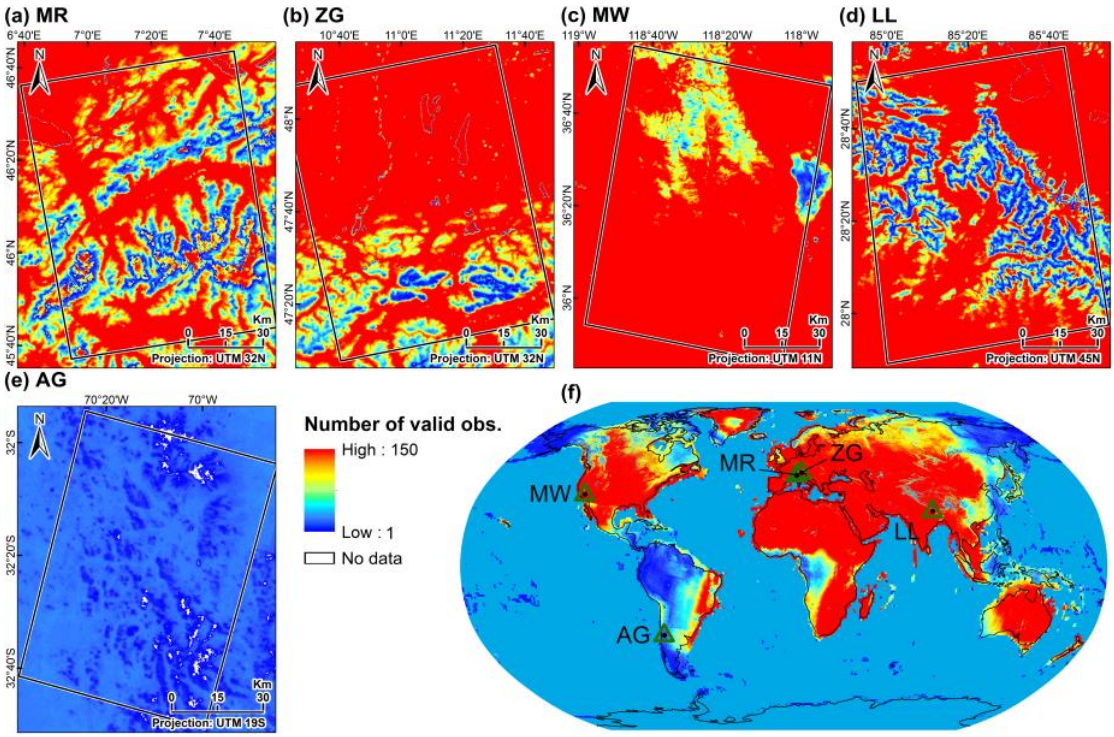

Figure 3.12 Number of available observations for the ESA CCI land cover product (based on the ESA CCI quality flag). (a) Monte Rosa (MR), (b) Zugspitze (ZG), (c) Mount Whitney (MW), (d) Landtang Lirung (LL), (e) Aconcagua (AG), (f) global overview

The influence of the topographical parameters on the classification performance is equally significant as outlined in section 3.2.4 (compare also Figure 3.4 and 3.11). Possible errors in the SRTM version 4 DEM could therefore also contribute to miss-classifications of SCE. As reported by Rodriguez et al. (2006), the SRTM DEM can have absolute height errors of more than 30 m. Since all four topographical parameters are directly derived from the height measurements, biases could cause false model presumptions that would further translate into classification errors.

Finally, the snow cover product (GSP, which is based on MODIS) utilized to train the model could be biased, too. GSP was chosen as an input because it provides daily snow cover information, which is desirable as snowfall events can occur spontaneously. The relatively coarse resolution (500 m), and the fact that clouds can cover large proportions of the study regions, contribute to uncertainties when training the model.

Any of these factors could be responsible for the relatively poor SCE classification accuracy of the AG test region. It is difficult to determine which the pivotal factor is though, as more tests would be required; while also for some input datasets (like

SRTM and GSP) no quality flag is available, which quantitatively characterizes the pixel-wise errors.

3.5.4. Uncertainties of Mapping Wet and Dry SCE in a Holistic Map; the Case of Monte Rosa (MR) Region

As shown in Figure 3.10b, it is clear that during the melting season, there is a dry SCE boundary buffering around the wet SCE especially for Alpine Monte Rosa region. The possible reasons could include both the over-estimation of our modeled total SCE and the under-estimation of wet SCE detected by “Nagler’s method”.

According to the confusion matrix comparing ‘modeled and optical-based’ total SCE as shown in Table 3.3, there is a slight over-estimation observed in month2 of Monte Rosa region caused by classification error. However, Nagler’s backscattering-based “hard” thresholding approach was also commonly found to under-estimate wet SCE, especially around the snow line where wet snow is patchy (Nagler and Rott, 2000; Malnes and Guneriussen, 2002; Pettinato et al., 2006; Storvold, Malnes, Larsen, et al., 2006). In detail, because snow has significantly lower scattering cross-section than bare ground, the stronger backscattering signals of bare soil, rock and vegetation would thus dominate that mixed pixel (Malnes et al., 2006; Pettinato et al., 2006; Storvold, Malnes, Larsen, et al., 2006). This situation mostly can only be compensated by enhancing the spatial resolution of SAR image as tested by Malnes et al. (2006).

3.5.5. Improvements Achieved in this Study

Although there have been some studies employing machine-learning to classify total SCE, the presented study utilized a novel fusion of multiple SAR-based observations and topographical factors to achieve a higher reliability. The proposed land cover-dependent model has successfully been applied in different study areas. In detail, the improvements when compared to earlier studies can be summarized as follows:

(1) The method provides global suitability and transferability

To achieve a universal, global transferability, the method needs to satisfy both data availability and model robustness. First, for data availability, all datasets being used in this study are available globally. More importantly, all input data are openly accessible, including the spaceborne SAR and optical imagery, the DEM, and the land cover product. Additionally, no field measurements for snow depth, temperature or forest’s stem volume are needed. When it comes to the model’s robustness, most of the previous studies applied the SCE mapping to a single regional site (Luojus K. P.,

Pulliainen J. T., Blasco Cutrona A., et al., 2009; He et al., 2017; Muhuri et al., 2018), which implies that they might be site-dependent approaches. In contrast, the presented method is tested in five independent regions located in different mountain ranges and even hemispheres. The achieved accuracy confirms that the proposed method can be applied to map SCE around the globe, which ensures the transferability. Moreover, merging the five regions' data to build a universal model set, a stable classification accuracy could also be confirmed.

(2) The method can efficiently deal with all land cover types, including forests

Because of challenging SAR-vegetation interactions, many existing studies simply masked out the forest or even agricultural regions (Rott and Nagler, 1995; Nagler and Rott, 2000; Luojus et al., 2007; Notarnicola C. et al., 2013; Guangjun et al., 2015; Wang et al., 2015; He et al., 2017). As illustrated in Figure 3.1, vegetation is a dominant part of land cover in all five study regions. Masking out the vegetation would significantly reduce the suitability of the SCE mapping approach to provide snow cover information for further applications. To overcome this limitation, the presented study includes all land cover types, comprising vegetation-dominated classes such as forest, scrub, grass, and cropland. The model is trained individually for each land cover type to form a land cover-dependent model set. Thanks to the simplicity and robustness of random forest classifiers, they can efficiently process various SAR observations under low computation demands.

(3) The method provides holistic wet and total SCE

Existing methods to detect snow cover from SAR data often focus on wet SCE only. The presented study proposes a method to derive both wet and total SCE, relying on a combination of an RF-based classifier to map the total SCE and a backscattering-based approach to detect wet SCE (Nagler's method). Thanks to the performance of the RF classifier, the workflow offers an option for near real-time and automatic classification of wet and dry SCE, thus enhancing the viability of spaceborne SAR data to map SCE. Since the method provides both wet and dry SCE, it could offer new ways of how remote sensing-based snow cover products can be incorporated into hydrological models.

3.5.6. Future Work

Considering the PolSAR data, existing studies have demonstrated that quad-polarization imagery can provide more satisfying results than dual-polarization, as it can reduce topographical distortions (Singh et al., 2014) and is also more sensitive to the state of snow (Dedieu et al., 2012). Thus, the potential of utilizing the

TerraSAR-X or Radarsat-2 should be explored. Moreover, their ultra-high resolution sensing mode can also enhance the accuracy of wet SCE mapping as discussed in 5.4.

Regarding the auxiliary data, one of the future developments, to improve the classification accuracy in vegetated areas will include the use of quantitative vegetation measurements, such as biomass density; the normalized difference vegetation index; or the leaf area index. The local incidence angle (LIA) of the SAR imagery related to the local topography may also be included to justify the impact of topography.

3.6. Conclusions

There are many studies available for detecting wet snow cover extent (SCE) utilizing spaceborne SAR imagery. However, there exists no properly-validated, globally transferable, total SCE mapping approach which would be applicable to all land cover classes. The presented study proposed a novel approach to map total and wet SCE based on openly accessible datasets (including SAR imagery, DEM and land cover product) with global coverage. Thanks to the simplicity and efficiency of the implemented random forest classifier, it is possible to incorporate non-linear and complex SAR-based observations (InSAR, PolSAR, backscattering). In regards to the influence of topography, four topographical factors, including elevation, slope, aspect and curvature, were also included as model inputs. The method has been applied to different mountainous locations (five regions located in different mountain ranges, continents, and hemispheres)over a period of different months and years. By extending the RF-based classification with a backscattering-based thresholding approach, information about wet SCE was additionally supplemented. Internal as well as external independent validation have been comprehensively conducted, confirming the robustness and transferability of the proposed method.

In addition to the global transferability, another merit of the presented approach is the capability to detect snow cover in vegetated areas such as forests, grass-, scrub-, and croplands. Compared to previous studies, which often masked out the forest or even agricultural regions, this study proposed a land cover-dependent classification procedure to solve this limitation. Namely, total SCE was classified with SAR observations and topographical factors in each land cover class separately, before merging each class' model to form a universal model set. To explore the influence of all inputs, the accuracy of each model set built by different combinations of SAR observations and topographical factors was evaluated. Results prove that the model set including all three SAR-based observations (InSAR, PolSAR, backscattering) as

well as all four topographical factors (elevation, slope, aspect, curvature) yields the highest classification accuracy for all land cover types. Overall accuracy, F-measure and AUC score can reach around 80%, 80%, and 70% for the majority of the regions. The accuracy can even be higher around 5% if vegetation land cover classes are excluded. It was also found that PolSAR and elevation provide more information than the remaining parameters. Additionally, when merging all input data for all test sites into one universal, general model (i.e. building a universally applicable model set), the accuracy remains satisfying. Future developments will include the incorporation of quantitative vegetation parameters (leaf area index, biomass, normalized difference vegetation index) as well as the local incidence angle of the SAR observations.

Acknowledgments: Support by the German Academic Exchange Service (DAAD) fellowship to Ya-Lun S. Tsai is gratefully acknowledged. The authors thank the providers of the meteorological data used in this article, including MeteoSwiss (the Swiss Federal Office of Meteorology and Climatology) as well as the ECA&D project (Data and metadata available at http://eca.knmi.nl).

Appendix A

Table 3.5 Re-classification of ESA CCI land cover product.

ESA CCI land cover classes	Label	Re-classified classes	Forest type
No data	0	NoData	X
Cropland, rainfed	10	Cropland	X
Herbaceous cover	11	Herbaceous	X
Tree or shrub cover	12	Tree_Shrub	O
Cropland, irrigated or post-flooding	20	Cropland	X
Mosaic cropland (>50%) / natural vegetation (tree, shrub, herbaceous cover) (<50%)	30	Crop&NaturalVege	O
Mosaic natural vegetation (tree, shrub, herbaceous cover) (>50%) / cropland (<50%)	40	Crop&NaturalVege	O
Tree cover, broadleaved, evergreen, closed to open (>15%)	50	Tree_Broadleaf	O
Tree cover, broadleaved, deciduous, closed to open (>15%)	60	Tree_Broadleaf	O
Tree cover, broadleaved, deciduous, closed (>40%)	61	Tree_Broadleaf	O
Tree cover, broadleaved, deciduous, open (15-40%)	62	Tree_Broadleaf	O
Tree cover, needleleaved, evergreen, closed to open (>15%)	70	Tree_Needleleaf	O
Tree cover, needleleaved, evergreen, closed (>40%)	71	Tree_Needleleaf	O
Tree cover, needleleaved, evergreen, open (15-40%)	72	Tree_Needleleaf	O
Tree cover, needleleaved, deciduous, closed to open (>15%)	80	Tree_Needleleaf	O
Tree cover, needleleaved, deciduous, closed (>40%)	81	Tree_Needleleaf	O
Tree cover, needleleaved, deciduous, open (15-40%)	82	Tree_Needleleaf	O
Tree cover, mixed leaf type (broadleaved and needleleaved)	90	Tree_Needle&Broad	O
Mosaic tree and shrub (>50%) / herbaceous cover (<50%)	100	Shrub&Herbaceous	O
Mosaic herbaceous cover (>50%) / tree and shrub (<50%)	110	Shrub&Herbaceous	O
Shrubland	120	Tree_Shrub	O
Shrubland evergreen	121	Tree_Shrub	O
Shrubland deciduous	122	Tree_Shrub	O
Grassland	130	Grass	X
Lichens and mosses	140	Lichens	X

Sparse vegetation (tree, shrub, herbaceous cover) (<15%)	150	SparseVegetation	X
Sparse tree (<15%)	151	SparseVegetation	X
Sparse shrub (<15%)	152	SparseVegetation	X
Sparse herbaceous cover (<15%)	153	SparseVegetation	X
Tree cover, flooded, fresh or brakish water	160	FloodedVegetation	O
Tree cover, flooded, saline water	170	FloodedVegetation	O
Shrub or herbaceous cover, flooded, fresh/saline/brakish water	180	FloodedVegetation	O
Urban areas	190	Urban	X
Bare areas	200	BareArea	X
Consolidated bare areas	201	BareArea	X
Unconsolidated bare areas	202	BareArea	X
Water bodies	210	Water	X
Permanent snow and ice	220	SnowIce	X
Total classes: 37		Total classes: 16	

Appendix B

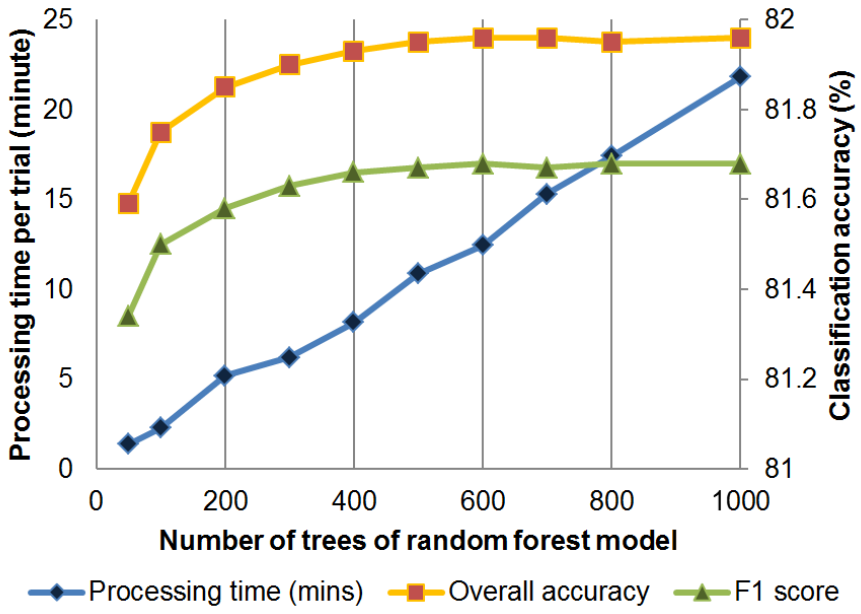

Figure 3.13 Comparison of random forest models' performance with different number of trees (tested with Monte Rosa (MR)) region.

4 A Combination of PROBA-V/MODIS-based Products with Sentinel-1 SAR Data for Detecting Wet and Dry Snow Cover in Mountainous Areas

Tsai, Y.-L.S., Dietz, A., Oppelt, N., & Kuenzer, C. (2019). A Combination of PROBA-V/MODIS-based Products with Sentinel-1 SAR Data for Detecting Wet and Dry Snow Cover in Mountainous Areas. Remote Sensing, 11, 1904

Abstract

In the presented study we explore the value of employing both, vegetation indexes as well as land surface temperature derived from PROBA-V and MODIS sensors, respectively, to support the detection of total (wet + dry) snow cover extent (SCE) based on a simple tuning machine learning approach, and provide reliability maps for further analysis. We utilize Sentinel-1-based synthetic aperture radar (SAR) observations, including backscatter coefficient, interferometric coherence, and polarimetric parameters, and four topographical factors as well as vegetation and temperature information to detect the total SCE with a land cover-dependent random forest-based approach. Our results show that the overall accuracy and F-measure are above 90% with an 'Area Under the ROC' (receiver operating characteristic curve) (AUC) score of around 80% over five study areas located in different mountain ranges, continents, and hemispheres. These accuracies are also confirmed by a comprehensive validation approach with different data sources, attesting the robustness and global transferability. Additionally, based on the reliability maps, we find an inversely proportional relationship between classification reliability and vegetation density. In conclusion, comparing to a previous study only utilizing SAR-based observations, the method proposed in the presented study provides a complementary approach to achieve a higher total SCE mapping accuracy while maintaining global applicability with reliable accuracy and corresponding uncertainty information.

Keywords: Synthetic Aperture Radar, InSAR, PolSAR, Backscatter, Machine Learning, Snow Cover Area, Land Use Land Cover, Sentinel-2, Landsat

4.1. Introduction

Global warming leads to a significant decrease of snow cover extent (SCE) as proven

in both, observations and models (Najafi et al., 2016; Hori et al., 2017). This development has also been recorded in the Synthesis Report of Fifth Assessment Report (AR5) of the Intergovernmental Panel on Climate Change (IPCC) (Pachauri et al., 2014). As SCE is an important factor for various human activities as well as the natural environment, a decrease of SCE affects and deteriorates the balance of ecosystems, the hydrological cycle of major river catchments, and the global radiation budget. The latest IPCC special report of 2018 states that extreme SCE changes could affect winter tourism and hydrology (Hoegh-Guldberg et al., 2018). In addition, several studies suggest that runoff generated by snowmelt dominates not only the amount but also the distribution, quality, and seasonality of its downstream regions (Schöber et al., 2014; Singh et al., 2014; Huss et al., 2017) and that it further controls water resources of whole populations (Barnett et al., 2005). Moreover, snow would also interact with other cryospheric components such as the equilibrium of glaciers (Beniston et al., 2018), the active layer thickness of permafrost (Pogliotti et al., 2015), and the retention of sea and lake ice (Yang Y. et al., 2012). Hence, a continuous monitoring strategy for SCE is necessary.

Although there have been various spaceborne multispectral sensor-based SCE products, such as the MODIS-based snow cover products (Riggs and Hall, 2015) and the European Space Agency (ESA)'s GlobSnow product (Solberg, Wangensteen, et al., 2010), these are still fundamentally constrained by cloud coverage, polar darkness, and the confusion between snow and ice-clouds (Bartsch et al., 2007; Macander et al., 2015). Thus, the utilization of active synthetic aperture radar (SAR) has been explored in the recent three decades (for a comprehensive review we refer to Tsai et al. (2019)). Thanks to its longer wavelength, SAR can sense ground features under all weather and solar illumination conditions. Since the first pioneer study published by Nagler and Rott (2000), various studies have been conducted utilizing the backscatter information to detect wet SCE. This is based on the fact that once the snow becomes wet, the dielectric constant of the snowpack increases significantly, leading to a dramatic shortening of the penetration depth of SAR signal (Tsai Ya-Lun S. et al., 2019). This behavior can be exploited to detect wet snow relying on a backscatter-threshold-based approach. Dry SCE, however, cannot be detected by this approach alone. Because information about the total (wet+dry) SCE is critical for further applications (e.g., hydrological modeling), interferometric SAR (InSAR) as well as polarimetric SAR (PolSAR) have been investigated (Tsai Ya-Lun S, Dietz Andreas, et al., 2019b). InSAR coherence enables total SCE mapping based on the fact that the snow-covered areas would show lower coherence due to a change of the SAR signal penetration depth (Snehmani et al., 2015), and PolSAR decomposed

parameters enable dry/wet/total SCE mapping as they can reveal the scattering mechanism of different ground features (Cloude and Pottier, 1996). For a detailed discussion and comparison of three mainstream SAR-based SCE detection approaches we refer to Tsai et al. (2019).

An important tool in detecting SCE relying on SAR data are machine learning (ML) techniques. Thanks to their strength in dealing with massive data, they allow for full exploitation of the PolSAR and InSAR parameters, as well as a combination with the conventional (often noisy) backscatter values. Although so far there have been some ML-based SCE mapping studies (Longepe et al., 2008; Huang et al., 2011; He et al., 2017), they only utilized sophisticated Support Vector Machines (SVM) for classification, which was suggested relatively challenging to tune and handle the data (Pal, 2005; Adam et al., 2014; Rodriguez-Galiano et al., 2015). Hence, a universally applicable and straightforward ML approach needed to be explored. Furthermore, most of the studies only tested their SAR-based total SCE detection algorithms on a local scale without proper validation , and often masked out the forested and agricultural regions to avoid vegetation-caused classification ambiguities (Luojus et al., 2007; Dedieu et al., 2012; He et al., 2017; Tsai Ya-Lun S. et al., 2019). Therefore, these algorithms might be site-dependent and not globally transferable.

In a previous study (Tsai Ya-Lun S, Dietz Andreas, et al., 2019b), we proposed a globally transferable, freely accessible data-only, all land cover class-applicable total and wet SCE mapping strategy utilizing only SAR-based observations (backscattering, InSAR coherence, and PolSAR parameters) as well as topographical factors. Based on a comprehensive validation approach, an overall accuracy of around 80% was confirmed. Although this accuracy level is already much higher than those of previous SAR-based studies (Tsai Ya-Lun S. et al., 2019), it is still relatively low when compare to conventional, optical sensor-based SCE detection approaches. Thus, a further enhancement of the mapping accuracy is desirable. To improve the SCE mapping accuracy, previous studies commonly employed ground temperature information derived from passive microwave sensors (Hongxing et al., 2006; Tedesco, 2007; Zhou and Zheng, 2017), as the snow-covered regions would show a lower temperature when compared to other, snow free regions. In addition to the temperature information, vegetation indexes might also help to detect SCE especially in forested regions. We found in a previous study (Tsai Ya-Lun S, Dietz Andreas, et al., 2019b) that the densely vegetated regions tend to show a lower SCE mapping accuracy when compared to e.g. bare area, sparse vegetation, and grassland. Moreover, previous studies also suggested that SAR backscatter, InSAR coherence, and PolSAR parameters are all related to vegetation types and conditions (Pulliainen, 1994;

Pulliainen et al., 1994; Park et al., 2014; He et al., 2017). Therefore, quantitative vegetation information should be added in addition to the qualitative vegetation information we already include (i.e., land cover map). Consequently, in the present study, we explore the value of including PROBA-V/MODIS-based vegetation and surface temperature products for enhancing the total SCE mapping accuracy. Also, as so far no procedure exists that provides a reliability map along with the estimated SCE, the presented study also includes a workflow for an automatically generated reliability map. Summarized, the following objectives have been addressed in this study: (1) enhancement of the mapping accuracy of total SCE by including vegetation indexes and temperature information (2) provision of reliability maps along with the modeled total SCE for further analysis (3) analysis of the influence of land cover classes with different vegetation densities on the total SCE mapping reliability.

4.2. Study Areas and Dataset

4.2.1. Study Areas

To test the transferability of our method, we selected five study areas located at different major mountainous regions around the globe with different land cover and topography, including the European Alps (Monte Rosa, (MR) and Zugspitze (ZG)), Sierra Nevada (Mount Whitney (MW)), Himalaya (Langtang Lirung (LL)), and Southern Alps in New Zealand (Aoraki (AK)). The locations and characteristics of each region are represented in Table 4.1.

Table 4.1 Attributes of the five selected study areas including Monte Rosa (MR), Zugspitze (ZG), Mount Whitney (MW), Landtang Lirung (LL), and Aoraki (AK) with their location, mountain range, country, and the highest peak.

Testing sites	**1 (MR)**	**2 (ZG)**	**3 (MW)**	**4 (LL)**	**5 (AK)**
Continent	Europe	Europe	North America	Asia	Australia
Mountain range (Country)	Alps (Switzerland)	Alps (Germany)	Sierra Nevada (U.S.A.)	Himalaya (Nepal)	Southern Alps (New Zealand)
Highest peaks (Height)	Monte Rosa (4,634 m)	Zugspitze (2,962 m)	Mount Whitney (4,421 m)	Langtang Lirung (7,234 m)	Aoraki / Mount Cook (3,724 m)

4.2.2. SAR and Optical Imagery

As we utilized a supervised classification approach, two consecutive hydrological years were chosen, with first and second year's Sentinel-1 SAR imagery used as a training and validation set, respectively. For the training set, SAR images of three different months, representing different snow cover conditions, were selected as shown in Table 4.2. Also, we included two different months (Month1: month not included in training set; Month2: month included in training set) for mapping to exclude the possibility that the selection of only a single month might influence the classification accuracy. Additionally, as the snowpack and its structure are changing continuously throughout the season, selecting different months ensures that the developed method will work under different snowpack conditions. For validating the SAR-based total SCE, optical imagery recorded during the validation year were also employed. To ensure the reliability of the validation, optical scenes from Sentinel-2 and Landsat-7/8 containing minimum cloud coverage were chosen that were recorded at similar dates as the respective Sentinel-1 imagery. Hence, the temporal gap between SAR and optical imagery for all cases is within a week. The summary of the employed SAR and optical imagery for each test site is listed in Table 4.2.

Table 4.2 Summary of the SAR data (Sentinel-1) and optical data (Sentinel-2, S2; Landsat-7/8, L7/8) used in the training and validation set. Note: reference image of each region for calculating the wet snow cover extent (SCE) is marked with an asterisk (*); optical images employed in validation set are included in brackets below the used SAR image dates.

<table>
<tr><th rowspan="2">Region</th><th rowspan="2">Training set
(First hydrological year)
* Reference image</th><th colspan="2">Validation set
(Second hydrological year)</th></tr>
<tr><th>Month1
(Month not included
in training set)</th><th>Month2
(Month included
in training set)</th></tr>
<tr><td rowspan="4">Test Site 1: Monte Rosa (MR)
(Sentinel-1A, Ascending, relative orbit number: 88)
(Landsat-7/8, path: 195, row: 28)</td><td>2016 Nov 17-29</td><td rowspan="4">2018 Mar 24-Apr 05
(L7: Mar 23)</td><td rowspan="4">2018 May 23-Jun 04
(L8: May 18)</td></tr>
<tr><td>2017 Feb 09-21</td></tr>
<tr><td>2017 May 16-28</td></tr>
<tr><td>* 2017 Aug 08</td></tr>
<tr><td rowspan="2">Test Site 2: Zugspitze (ZG)
(Sentinel-1A, Ascending, relative</td><td>2016 Nov 07-19</td><td rowspan="2">2018 Mar 26-Apr 07
(L7: Mar 25)</td><td rowspan="2">2018 May 13-25
(S2: May 07)</td></tr>
<tr><td>2017 Feb 23-Mar 07</td></tr>
</table>

orbit number: 117) *(Landsat-7, path: 193, row: 27) (Sentinel-2, tile number: T32TPT)*	2017 May 18-30		
	* 2017 Aug 10		
Test Site 3: Mount Whitney (MW) (Sentinel-1A, Ascending, relative orbit number: 144) *(Landsat-7, path: 41, row: 35)*	2017 Feb 25-Mar 09	2018 Mar 16-28 *(L7: Mar 16)*	2018 May 03-15 *(L7: May 03)*
	2017 Apr 02-14		
	2017 May 08-20		
	* 2017 Aug 12		
Test Site 4: Landtang Lirung (LL) (Sentinel-1A, Ascending, relative orbit number: 85) *(Landsat-7, path: 141, row: 40)*	2017 Feb 09-21	2018 Mar 12-24 *(L7: Mar 13)*	2018 May 11-23 *(L7: May 16)*
	2017 Apr 10-22		
	2017 May 16-28		
	* 2017 Aug 08		
Test Site 6: Aoraki (AK) (Sentinel-1B, Ascending, relative orbit number: 23) *(Landsat-7/8, path: 75, row: 90)*	2017 May 06-18	2018 Jun 30-Jul 12 *(L8: Jun 26)*	2018 May 01-13 *(L7: May 01)*
	2017 Aug 10-22		
	2017 Oct 21-Nov 02		
	* 2018 Feb 06		

4.2.3. Auxiliary Data

Due to the trade-offs between global availability, sustainability, and data quality, the SRTM digital elevation model (DEM) as well as land cover data originating from the ESA Climate Change Initiative (CCI) were used as auxiliary data. The former was employed to calculate the topographical factors (elevation, slope, aspect, curvature). The CCI land cover product was reclassified from original 37 to 16 classes to reduce redundancy (Tsai Ya-Lun S, Dietz Andreas, et al., 2019b). The daily and global SCE derived from DLR's Global SnowPack (GSP) (Dietz et al., 2015) was employed as ground truth for training the model, which has been validated using in situ and higher resolution reference data to have a accuracy of around 80% globally (Dietz et al., 2015).

In the present paper, to enhance the SCE mapping accuracy, two vegetation indexes as well as surface temperature derived from the PROBA-V satellite and MODIS sensors, respectively, were also employed. The vegetation index products including leaf area index (LAI) and fractional vegetation cover (FVC) are provided by the Copernicus Global Land Service which are calculated based on three PROBA-V bands (blue, red, and near-infrared) (Baret et al., 2016). It must be noted that a correlation between LAI and FVC might exist. However, as the classification algorithm we employed (random forest) is capable of dealing with collinearity between features and the goal of our approach is to provide a universally applicable model which can yield the highest classification accuracy, we don't consider this a problem. A possible redundancy between input variables is acceptable for ensuring flexibility.

The surface temperature is based on merging both Terra and Aqua satellite data of MODIS Level-3 8-day composite products (MOD/MYD11A2), which are averaged from clear-sky daily products (MOD/MYD11A1) based on MODIS's band 31 and 32 emissivities (Wan, 2007; Wan et al., 2015). MOD/MYD11B1 and MOD/MYD11C1 were not selected because they are resampled to a much coarser resolution (6 km and 0.05°, respectively), making them more applicable for global analysis or climate modelling applications (Wan, 2007, 2008; Mao et al., 2017). We selected the composite product instead of daily products because (1) the revisit time of Sentinel-1 SAR (12 days) is comparable with MOD/MYD11A2's 8-days period; and (2) a more complete spatial data availability can be achieved. Together with the SAR-based observations and topographical factors, the data types, sources, and spatial/temporal resolution of the data employed in the present study are listed in Table 4.3.

Table 4.3 Attributes of input data with their source, spatial and temporal resolution.

Input variable	**Data category**	**Source**	**Spatial resolution**	**Temporal resolution**
Total SCE	Ground truth	Global SnowPack	500 m	Daily
Land cover	Land cover label	ESA CCI land cover	300 m	Annually
Backscattering coefficient	SAR observation	SAR image processing (Sentinel-1)	5 × 20 m	12 days
InSAR coherence				
PolSAR entropy				
PolSAR anisotropy				
PolSAR angle				

Elevation	Topographical factor	SRTM DEM	90 m	N/A
Slope				
Aspect				
Curvature				
Leaf area index	Vegetation index	Copernicus Global Land Service (PROBA-V-based)	300 m	10 days
Fractional vegetation cover				
Land surface temperature	Temperature	MOD/MYD11A2 (MODIS-based)	1000 m	8 days

4.3. Methodology

For calculating the SAR-based observations, including backscatter ratio, InSAR coherence, and PolSAR H/A/α parameters, Sentinel-1 imagery was processed with ESA's SentiNel Application Platform (SNAP). To derive backscatter ratio, Ground Range Detected (GRD) images were calibrated, filtered, terrain corrected and flattened with SRTM DEM, and finally converted to decibel (dB) units. Each image was set in relation to a reference image originating from summer season. InSAR coherence was derived from two co-registered Single Look Complex (SLC) images, which were then terrain corrected and filtered. For PolSAR parameters, the polarimetric matrix was first constructed from the calibrated and debursted SLC images and the derived eigenvalues and eigenvectors were then used for calculating H/A/α parameters (Cloude and Pottier, 1996). For a more detailed description of the SAR pre-processing we refer to Tsai et al. (2019b).

Random forest (RF) was employed in the present study as a two-class supervised classifier owing to its simplicity of parameter tuning. It guarantees a wider applicability than algorithms such as SVM and neural network. Moreover, RF provides other benefits including a short training time, low computation load, support of parallel processing, simple tuning of parameters, avoiding of over-fitting, and providing information about the importance of the input variables (Ali et al., 2012; Sazonau, 2012; Belgiu and Drăguţ, 2016). Regarding the parameter setting, numbers of trees and the number of random features assigned to each tree, they were set to 600 and the default values (square root of total feature numbers) after several testing trials (Tsai Ya-Lun S, Dietz Andreas, et al., 2019b), respectively. For building the RF model, different input combinations (inputs are listed in Table 4.3) were tested. After finding the optimized combination, the model was applied to each land cover class individually. Accordingly, each modeling trial for each study area consists of *N* RF

models with *N* referring to the number of land cover classes. We processed the input data for two distinct scenarios: (1) single-area scenario: each region's first year data was used to build the model for each region individually, which were then correspondingly applied to the region's second year data; (2) merging-region scenario: the input data of all test regions were merged for the first year to build one aggregated model, which was then applied to the second year.

To build the models, 70% of the pixels of the first year's data (including GSP data as ground truth and the selected inputs from Table 4.3) were randomly selected and used to train the model. The trained model was then used to estimate total SCE, which was validated with internal (30% of the first year's GSP data not included in the training process) and external data (optical-based SCE data and snow depth station data). An extensive description of the data splitting is presented in Tsai et al. (2019b). For evaluating the performance of the different input and model settings, overall accuracy, F-measure (Lewis and Gale, 1994), and 'Area Under the ROC' (receiver operating characteristic curve) (AUC) (Fawcett, 2006) were calculated, which provide a comprehensive evaluation (Sokolova et al., 2006; Ferri et al., 2009). To examine the negative effect of vegetation on the classification accuracy, these measurements were also calculated separately for non-forested regions.

To select the optimized input combinations and evaluate the benefits of adding vegetation indexes and surface temperature information in addition to SAR-based observations and topographical factors employed in Tsai et al. (2019b), the Monte Rosa (MR) region in the Swiss Alps was chosen for accuracy assessment, as it features complex land cover and topography. To assess the robustness of the model, 20 iterations were processed for each trial. The results of the different classification accuracies are illustrated in Figure 4.1. It was found that adding both vegetation indexes and temperature information can yield the highest accuracy: Overall accuracy and F-measure can reach more than 93%, with an AUC score of around 84%. The original SAR-based (BIP) and topographical factors (asce)-based approach without vegetation and temperature information produced only 82% and 70%, respectively (Tsai Ya-Lun S, Dietz Andreas, et al., 2019b).

The increase in overall classification accuracy is largely due to improvements in regions covered by forests. For the mixed needle and broadleaf tree class, the original SAR-based (BIP) and topographical factors (asce) approach achieves an overall accuracy of around 71%. After including vegetation indexes and temperature information, the accuracy increases to around 87%. This demonstrates the benefit of including not only qualitative vegetation information (i.e. land cover map) but also the

quantitative vegetation information. This finding agrees with previous studies which revealed that SAR signals would largely relate to the transmissivity of vegetation (Pulliainen et al., 1994; Tsai Ya-Lun S. et al., 2019) which is correlated to the LAI and FVC (Vander Jagt et al., 2015). The accuracy improvement achieved by including temperature data is straightforward, as it provides general surface thermal information. The temperature data allows for a differentiation into cold (potentially snow covered) and warm regions (potentially snow-free). Consequently, even though the MODIS-based temperature product has a lower spatial resolution (1000 m) than the PROBA-V-based medium resolution (300 m) vegetation indexes, the SCE mapping accuracy for all land cover classes is higher when compared to the benefit gained by including the two vegetation indexes (BIP+asce+V2) . A detailed overview is illustrated in Figure 4.1.

Ultimately, nearly 90% accuracy can be achieved when all inputs are included. Therefore, all available SAR-based observations, topographical parameters, two vegetation indexes, and temperature information have been used as model inputs for the subsequently presented results. For these results, we do not filter variables based on the importance of variables calculated from RF because (1) the RF's importance metrics are found to be biased when predictor variables vary in scales of measurements or share collinearity (Strobl et al., 2007; Strobl et al., 2008); and (2) the goal of the proposed approach is to provide universal applicability and a slight redundancy of variables can ensure broader transferability and flexibility.

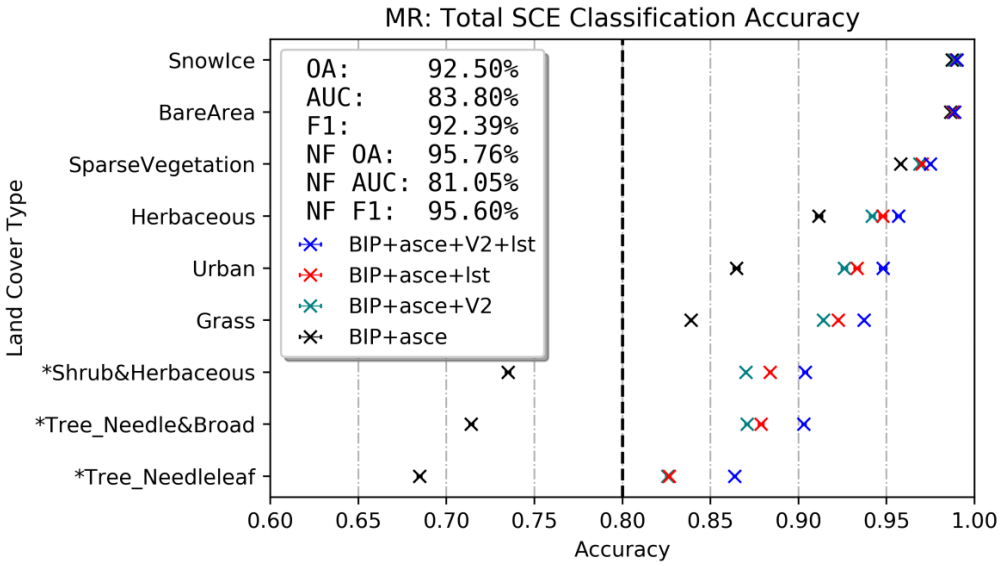

Figure 4.1 Assessment of the influence of different input combinations on the performance of the model for Monte Rosa (MR) region. Different classification

accuracies based on different input combinations are marked in different colors, and the accuracy for each land cover class is marked in the same horizontal axis. SAR-based observations, including backscatter, interferometric SAR (InSAR) coherence, and polarimetric (PolSAR) H/A/α parameters are abbreviated as B, I, and P, respectively. Topographical factors, including aspect, slope, curvature, and elevation are abbreviated as a, s, c, and e, respectively. Two vegetation indexes and land surface temperature are abbreviated as V2 and lst, respectively. Non-forest classes' overall accuracy, F measure, and area under the receiver operating characteristic curve are abbreviated as NF OA, NF F1, and NF AUC, respectively.

Based on the RF model sets, the total SCE for each month of each region's validation year can be derived. Additionally, a conventional backscatter-based wet SCE detection approach was also employed (Nagler and Rott, 2000) to utilize the full potential of the SAR data for discriminating between wet and dry snow. Reference images were selected from the summertime of the first year as shown in Table 4.2. The ratio of the backscattering coefficient values between observation and reference SAR images was set to a threshold of -3 dB to depict wet SCE. Hence, it became viable to generate holistic dry and wet SCE results based on SAR data. In the present study, both years' SAR backscatter observations were combined with the reference image (summertime observation) of the first year (Table 4.2), as the feasibility of using a cross-temporal reference image was proven by Luojus et al. (2006).

The overall workflow of mapping total SCE based on a land cover-dependent RF classification model set as well as detecting wet SCE by "Nagler's method" is illustrated in Figure 4.2.

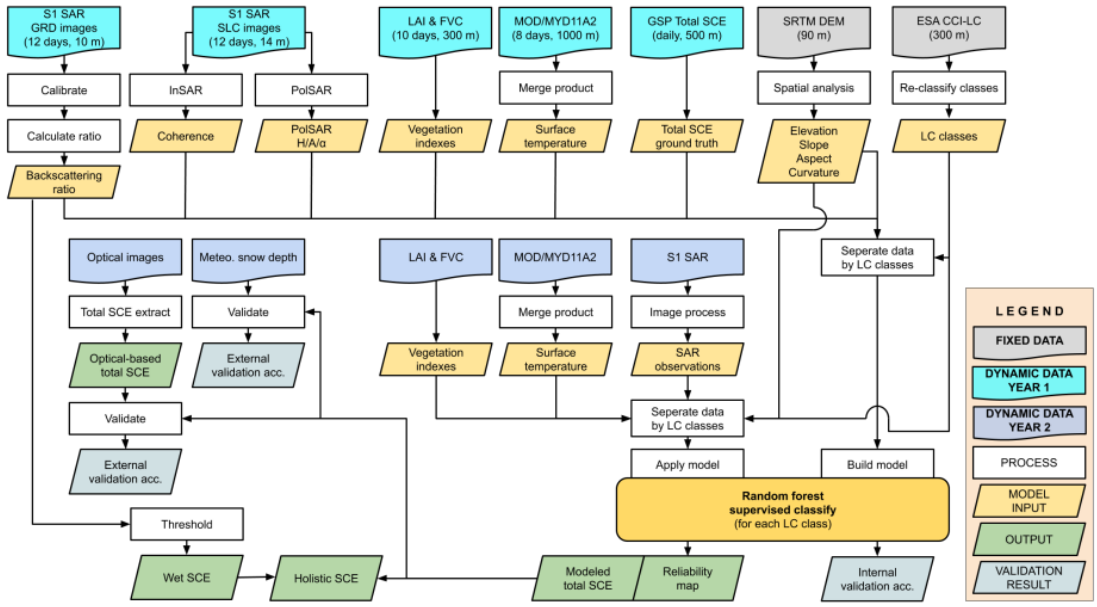

Figure 4.2 Overall workflow of mapping and validating holistic (total + wet) Snow Cover Extent (SCE) with SAR-based observations, topographical factors, vegetation indexes, temperature information, land cover information, and Global SnowPack (GSP) daily snow cover information. Single look complex, ground range detected, shuttle radar topographic mission digital elevation model, and land cover are abbreviated as SLC, GRD, SRTM DEM, and LC, respectively.

4.4. Results

4.4.1. Accuracy Assessment of the Modeled Total SCE

Based on the optimized input variable combinations tested in the Methodology section (SAR-based observations, topographical factors, vegetation indexes, and temperature information), the same modeling approach was applied to all five study areas individually. The resultant internal validation of the first year is shown in Figure 4.3. To highlight the improved classification accuracy achieved by adding vegetation indexes and temperature information, the results of using only the previous variable combination (BIP+asce) (Tsai Ya-Lun S, Dietz Andreas, et al., 2019b) are also plotted. To assess the robustness of the model, 20 iterations were processed for each trial. For the single-area scenario, the total SCE mapping accuracies of all five regions are illustrated in Figure 4.3(a-e). Overall accuracy and F-measure were around 93%, 90%, 96%, 93%, and 92% for MR, ZG, MW, LL, and AK, respectively. The AUC score for each region was also above 77%, which is more than satisfying. To compare the negative effect of vegetation on the classification accuracy, the non-forest classes were assed separately (represented in Figure 4.3 with NF OA, NF AUC, NF F1). The non-forest overall accuracy and F-measure were around 96%, 93%, 99%, 89%, and 93% for MR, ZG, MW, LL, and AK, respectively.

For the merging-region scenario (Figure 4.3(f)), a comparable accuracy was observed. Overall accuracy and F-measure were above 92% with an AUC score around 89%. This accuracy confirms the robustness of the proposed method together with the included model inputs, and that it can achieve transferability to other regions even if the model was trained universally, merging all input data to create a globally transferable model setup.

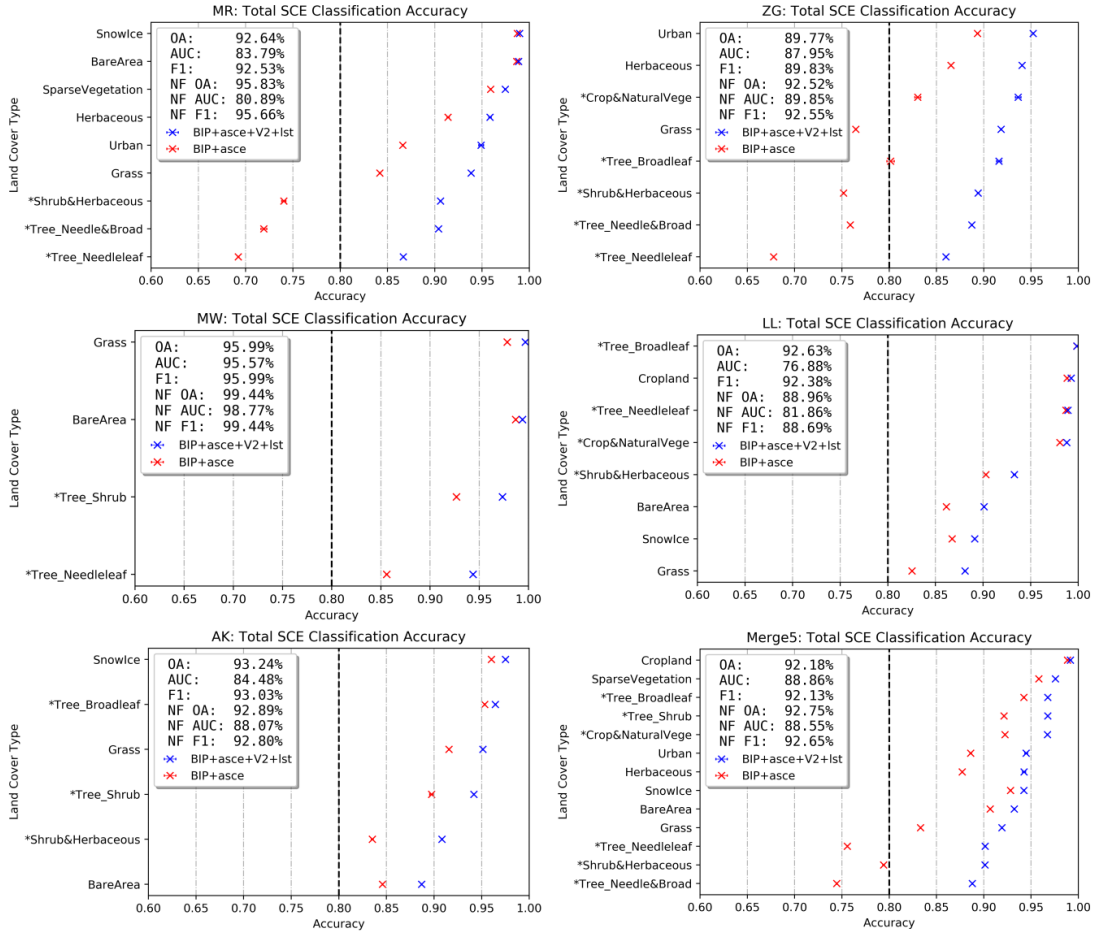

Figure 4.3 The results of each model set built in each region: (a) Monte Rosa (MR); (b) Zugspitze (ZG); (c) Mount Whitney (MW); (d) Landtang Lirung (LL); and (e) Aoraki (AK); and the five regions' merging case (f). Different classification accuracies based on different input combinations are marked in different colors, and the accuracy for each land cover class is marked in the same horizontal axis. SAR-based observations, including backscatter, interferometric SAR (InSAR) coherence, and polarimetric (PolSAR) H/A/α parameters are abbreviated as B, I, and P, respectively. Topographical factors, including aspect, slope, curvature, and elevation are abbreviated as a, s, c, and e, respectively. Two vegetation indexes and land surface temperature are abbreviated as V2 and lst, respectively.

4.4.2. External Validations with Optical-based SCE and Snow Depth Records

To thoroughly validate the modeled total SCE for the second year, two different external validation approaches were utilized, including validating with optical imagery-based SCE and meteorological snow depth information. These two datasets provide higher spatial resolution than the GSP data.

As shown in Table 4.2, high-resolution Landsat as well as Sentinel-2 data were

chosen based on the criteria of least cloud cover in the shortest temporal distance. The Fmask algorithm (Qiu et al., 2017) was then applied to each scene to derive total SCE (for detailed parameters setting refer to (Tsai Ya-Lun S, Dietz Andreas, et al., 2019b)). Based on the resultant total SCE, 10,000 random points were stratifiedly sampled in both snow-covered and snow-free areas. The confusion matrix and evaluation measurements can thus be calculated as presented in Figure 4.4. For all five regions' two validation months, overall accuracy and F-measure always maintain more than 82%. Only slight over- and under-estimation were observed in the first month of MR and LL, respectively. These evaluations confirm the robustness of the proposed model/data. The months with relatively low accuracy such as month1 of MR (82%) and month1 of LL (82%) might be affected by sudden snowfall/snowmelt events occurring during the temporal gap between the SAR and the optical image acquisitions. In study regions with no temporal gap, the accuracies are generally higher (see month2 of MW (93%) as well as month1 (90%) and month2 (91%) of AK).

To evaluate the improvement of the classification accuracy compared to the previous variable combinations (Tsai Ya-Lun S, Dietz Andreas, et al., 2019b), a confusion matrix and evaluation measurements using only SAR-based observations and topographical factors (BIP+asce) are also presented in Figure 4.4. In addition and to summarize the improvement, we used simple rules to judge the performance: (1) if the evaluation measurements of the present study are considerably higher/lower than the previous study, then we marked that case with "O"/"X"; if no significant difference is found, it is marked as "-". (2) if the present study eliminates the significant under- or over-estimation shown in the previous study, then we marked that case with another "O"; if the present study shows either under- or over-estimation which is not presented in the previous study, then we marked that case with another "X". According to these rules, we can summarize the overall improvement level for all ten months. It was found that seven cases showed an improvement while only two cases showed a worse performance; therefore, the present study can be considered as a general improvement.

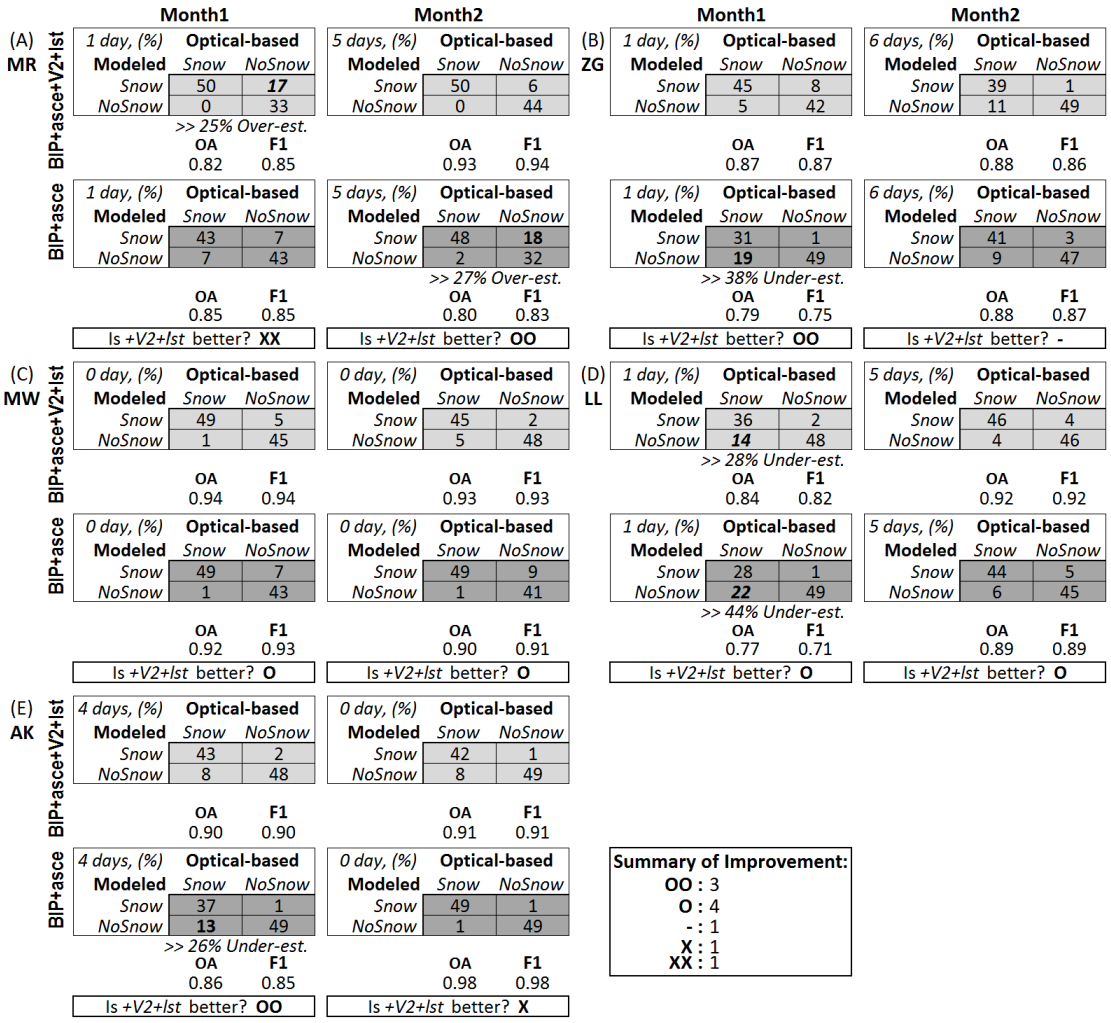

Figure 4.4 Confusion matrix of the accuracy assessment relying on optical-based snow cover classifications of Landsat and Sentinel-2 for each test site. The assessment includes classifications for months that were trained in the first year (month2) as well as those that were not used in the training of the first year (month1). Overall accuracy (OA) and F1-score are depicted under the respective confusion matrix. The temporal difference (days) between SAR observation image and optical image used for validation is mentioned on the upper-left corner of each confusion matrix. The summary of improvement depicts the improvements achieved by adding vegetation indexes and temperature information: OO for major improvement, O for slight improvement, - for no change, X for slight degradation, and XX for major degradation. The confusion matrixes marked in light and dark grey colors represent the results of using the present and previous (Tsai Ya-Lun S, Dietz Andreas, et al., 2019b) variable combination, respectively.

Another validation approach is utilizing the snow depth (SD) information of local meteorological stations. Considering the data availability, only MR and ZG regions

located in European Alps provide a suitable dataset. The daily SD records of 28 MeteoSwiss's stations and 114 stations of European Climate Assessment & Dataset Project (ECA&D) (Tank et al., 2002) were used for validation of the two regions, respectively (for exact locations of the stations refer to (Tsai Ya-Lun S, Dietz Andreas, et al., 2019b)). Due to the fact that the locations of meteorological stations are generally at a lower elevation and there is less snow in May (melting season), only SCE of March was validated. The confusion matrix between SAR-based modeled total SCE and SD (if SD is higher than 0 cm, it is defined as snow-covered) is illustrated in Figure 4.5. Overall, the accuracy was satisfyingly high, i.e., above 82% in both cases. The validation results of the SCE estimated with the previous variable combination (without vegetation and temperature information) (Tsai Ya-Lun S, Dietz Andreas, et al., 2019b) is also shown in Figure 4.5, which generally presents a lower accuracy. This finding agrees with the validation using optical-based SCE as mentioned above, i.e. the present study does demonstrate a modest improvement in classification accuracy.

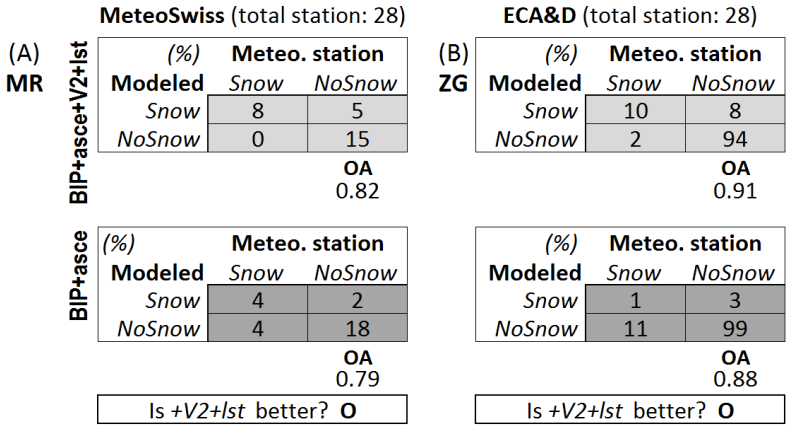

Figure 4.5 Confusion matrix of (a) Monte Rosa (MR) and (b) Zugspitze (ZG) regions validated with meteorological snow depth (SD) station data records of MeteoSwiss and European Climate Assessment & Dataset Project (ECA&D), respectively. The summary of improvement depicts the improvements achieved by adding vegetation indexes and temperature information: OO for a major improvement, O for a slight improvement, - for no change, X for a slight degradation, and XX for a major degradation. The confusion matrixes marked in light and dark grey colors represent the results of using the present and previous (Tsai Ya-Lun S, Dietz Andreas, et al., 2019b) variable combination, respectively.

4.4.3. Holistic Wet and Dry SCE Maps with Reliability Maps

Via comprehensive internal and external validation based on different data sources as mentioned in 4.1 and 4.2, it is confirmed that all five regions yield credible modeled

total SCE. Based on that and to fully utilize the advantages of SAR data, a conventional backscatter-based wet SCE detection approach (Nagler and Rott, 2000) was also employed. In the present study, the presence of wet snow is only allowed for areas where SCE has been detected by our modelling approach, which helps removing patchy wet snow caused by salt-and-pepper noise of SAR imagery. By merging both total and wet SCE, dry SCE can therefore be separately depicted as shown in Figure 4.6. It was clear that the coverage of total/wet SCE is decreasing/increasing in all five regions from month1 to month2 (Table 4.2) as the melting season starts due to rising temperature.

It should be noted that currently, there is no comprehensive way to validate the wet SCE in a comparable spatial resolution. Considering the general acceptance of the conventional backscatter-threshold-based approach for wet SCE detection in previous studies (Tsai Ya-Lun S. et al., 2019), we did not examine the quality of wet SCE in the presented study. Nevertheless, as we mentioned in (Tsai Ya-Lun S, Dietz Andreas, et al., 2019b), the conventional backscatter-threshold-based method is sometimes found to be under-estimating wet SCE especially in patchy snow-covered areas due to the mixture of different scattering characteristics of different ground surfaces.

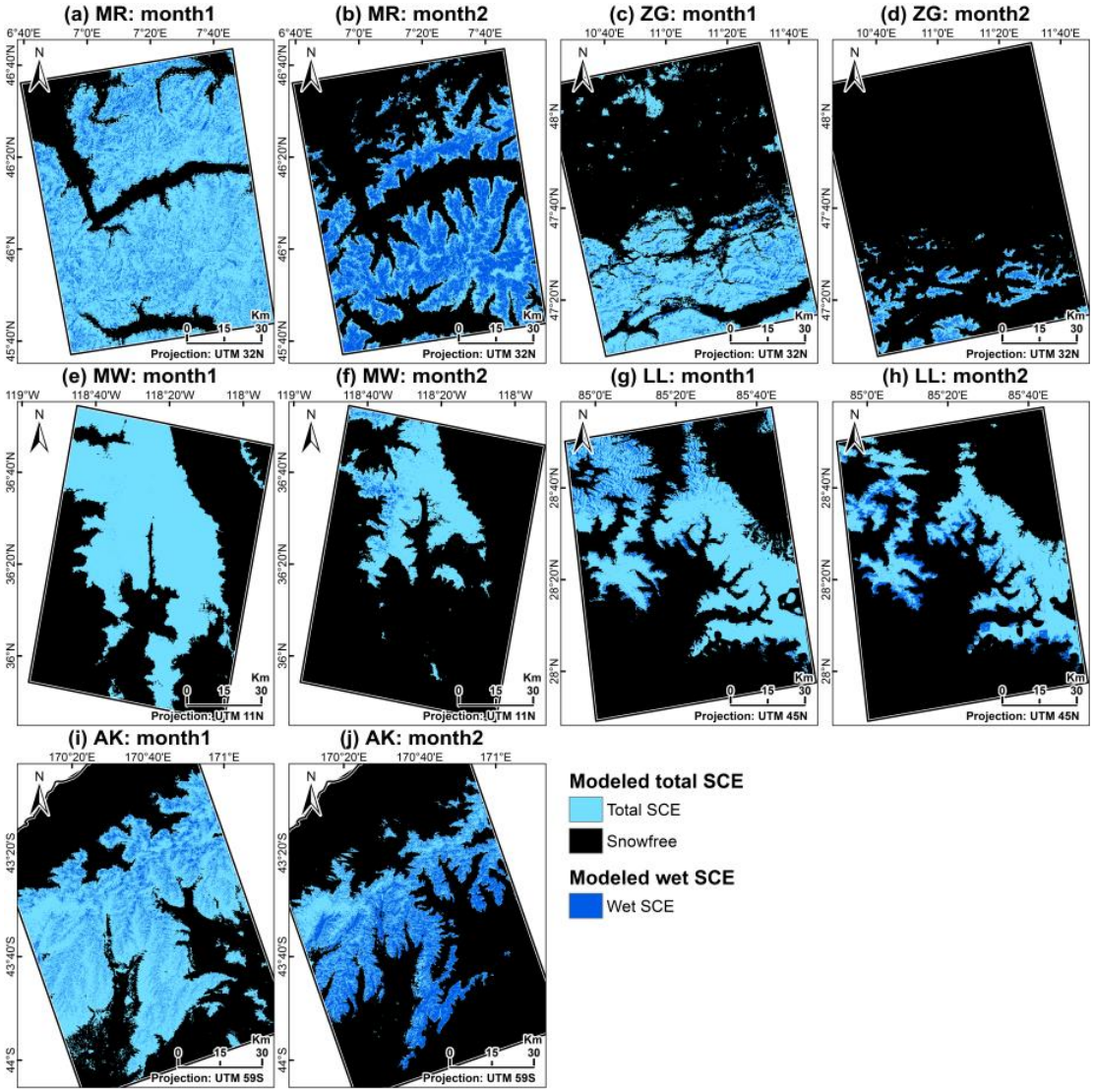

Figure 4.6 Total and wet SCE for each region's two months: (a) Monte Rosa (MR), month 1 (Mar 24, 2018); (b) Monte Rosa, month 2 (May 23, 2018); (c) Zugspitze (ZG), month 1 (Mar 26, 2018); (d) Zugspitze, month 2 (May 13, 2018); (e) Mount Whitney (MW), month 1 (Mar 16, 2018); (f) Mount Whitney, month 2 (May 03, 2018); (g) Landtang Lirung (LL), month 1 (Mar 12, 2018); (h) Landtang Lirung, month 2 (May 11, 2018); (i) Aoraki (AK), month 1 (Jun 30, 2018); (j) Aoraki, month 2 (May 01, 2018).

To overcome the limitation of previous studies, i.e. the lack of reliability information of the produced SCE (Tsai Ya-Lun S. et al., 2019) (which is state-of-the-art in other spaceborne-based cryosphere products (Tsai et al., 2018)), we utilize the advantage of RF to generate a reliability map for the modeled total SCE for each region and each month as illustrated in Figure 4.7. The reliability for the results is high except for the transition zone (or snow line) between snow-covered and snow-free areas, which is caused by ambiguities in the SAR signal within patchy snow fields (caused by a mix of bare soil, rock, vegetation, and snow) (Malnes et al., 2006; Pettinato et al., 2006;

Storvold, Malnes, Larsen, et al., 2006). However, as concluded by Malnes et al. (2006), this situation can only be compensated by enhancing the spatial resolution of the SAR imagery. Nevertheless, the reliability information along with the modeled total SCE can provide the users a valuable reference about uncertainty for further applications and analysis.

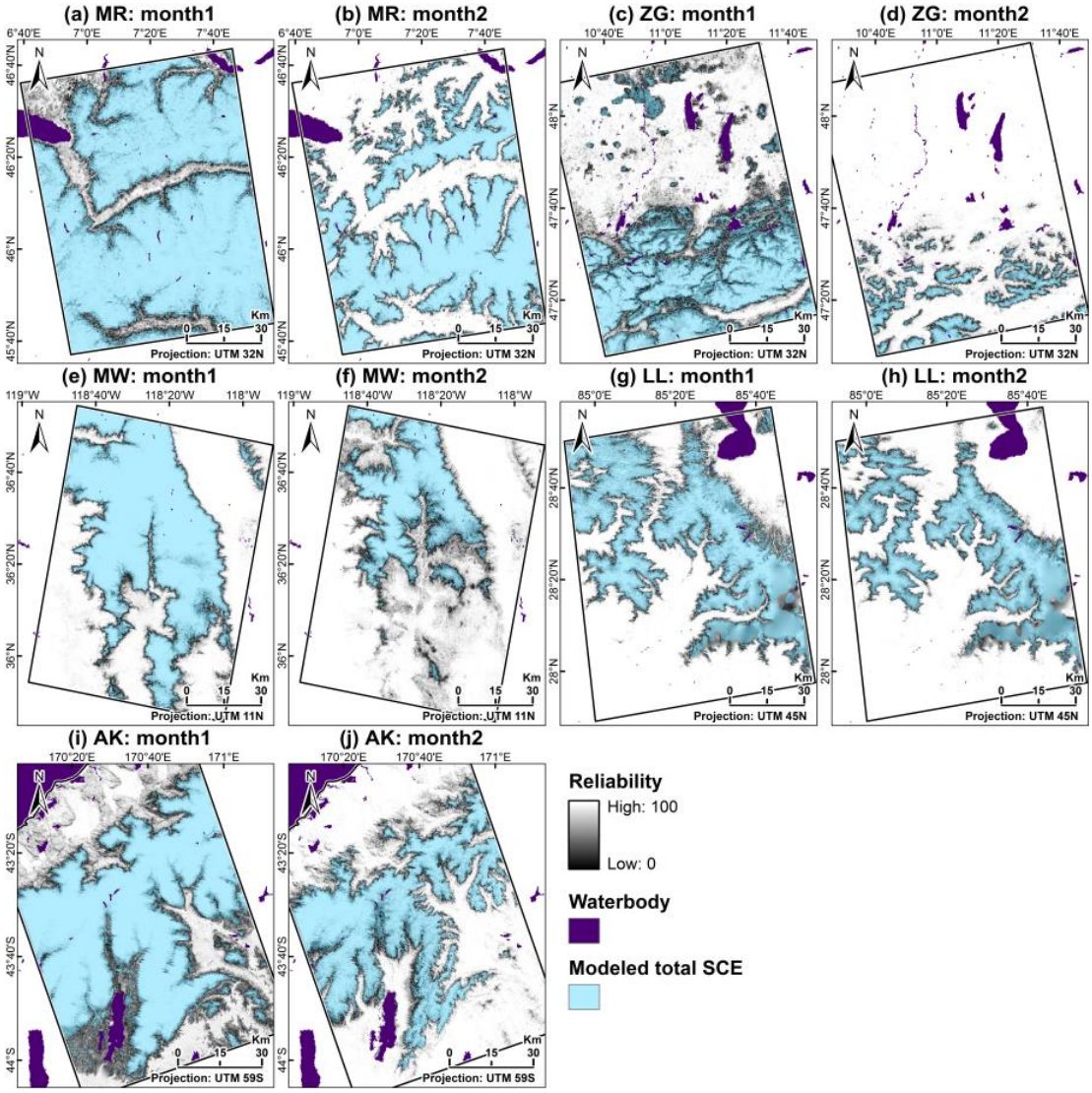

Figure 4.7 Reliability map with total SCE for each region's two months: (a) Monte Rosa (MR), month 1 (Mar 24, 2018); (b) Monte Rosa, month 2 (May 23, 2018); (c) Zugspitze (ZG), month 1 (Mar 26, 2018); (d) Zugspitze, month 2 (May 13, 2018); (e) Mount Whitney (MW), month 1 (Mar 16, 2018); (f) Mount Whitney, month 2 (May 03, 2018); (g) Landtang Lirung (LL), month 1 (Mar 12, 2018); (h) Landtang Lirung, month 2 (May 11, 2018); (i) Aoraki (AK), month 1 (Jun 30, 2018); (j) Aoraki, month 2 (May 01, 2018).

4.5. Discussion

4.5.1. The Influence of Different Input Variables Combinations to Classification Accuracy

In the Methodology section, different input combinations were tested, where the “all input included” case yields the highest classification accuracies. To clarify the misunderstanding that it would always have better modeling accuracy when including more inputs, Figure 4.8 presents the results of employing SAR local incidence angle (LIA) as well as multi-spectral data from high-resolution optical imagery. The results show that neither adding LIA (Figure 4.8(a)) nor the six different bands of Sentinel-2 (band 4, 5, 6, 7, 8, and 8A) (Figure 4.8(b)) can provide higher accuracy than the previous case only relying on the SAR-based observations and topographical factors (Tsai Ya-Lun S, Dietz Andreas, et al., 2019b). We presume that this is for two reasons: The terrain correction step in the pre-processing of the SAR-observations already eliminates most of the influence of LIA; and the snow-cloud-ice ambiguity within optical imagery largely limits the usable information. Thus, both LIA and Sentinel-2 multi-spectral data were not included in the proposed model.

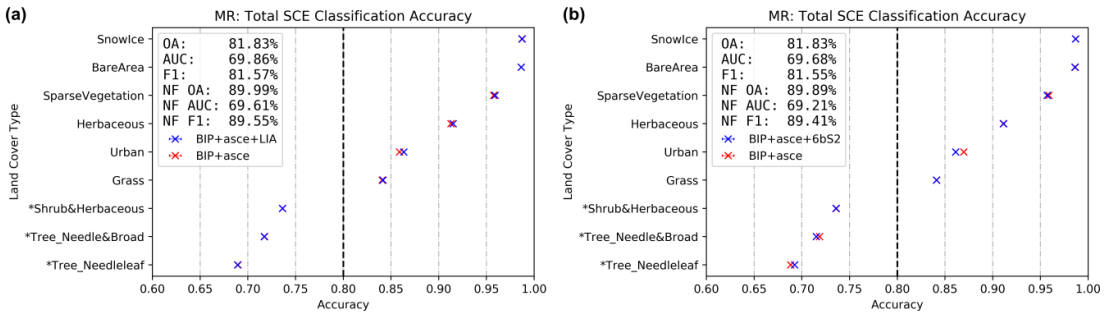

Figure 4.8 Examination of the accuracy improvement benefits of employing (a) SAR local incidence angle (LIA) and (b) Sentinel-2 multi-bands imagery on the performance of the model for Monte Rosa (MR) region. Different classification accuracies based on different input combinations are marked in different colors, and the accuracy for each land cover class is marked in the same horizontal axis. SAR-based observations, including backscatter, interferometric SAR (InSAR) coherence, and polarimetric (PolSAR) H/A/α parameters are abbreviated as B, I, and P, respectively. Topographical factors, including aspect, slope, curvature, and elevation are abbreviated as a, s, c, and e, respectively. Six bands of Sentinel-2 imagery is abbreviated as 6bS2.

4.5.2. The Influence of Different Land Cover (Vegetation) Types on the Classification Reliability

To investigate the relationship between vegetation and classification reliability, the

reliability of the second year's total SCE was analyzed based on different land cover classes as shown in Figure 4.9. The land cover classes were categorized to densely, lightly, and non-vegetated land cover classes and colored with deep green, light green, and light blue, respectively. It is obvious that generally, the reliability is inversely proportional to the density of vegetation, except for the LL region in Himalaya which may differ due to local vegetation characteristics and lower quality of the land cover map caused by more rugged terrain (Tsai Ya-Lun S, Dietz Andreas, et al., 2019b). Namely, densely vegetated classes such as shrubs, broad and needle leaf forest have the poorest reliability; they are followed by mild vegetated classes, including the grass, herbaceous, and sparse vegetation; non-forest classes like bare areas, urban, and snow/ice normally have the highest reliability. This analysis proves previous studies' findings, i.e., stem volume and vegetation height would directly influence the snow detecting abilities of SAR signals (Löw et al., 2002; Duguay and Bernier, 2012; Schellenberger et al., 2012). However, although these vegetated classes have relatively poor accuracies, most regions still provide an accuracy of more than 60% for 75% of the pixels (the tail of each box).

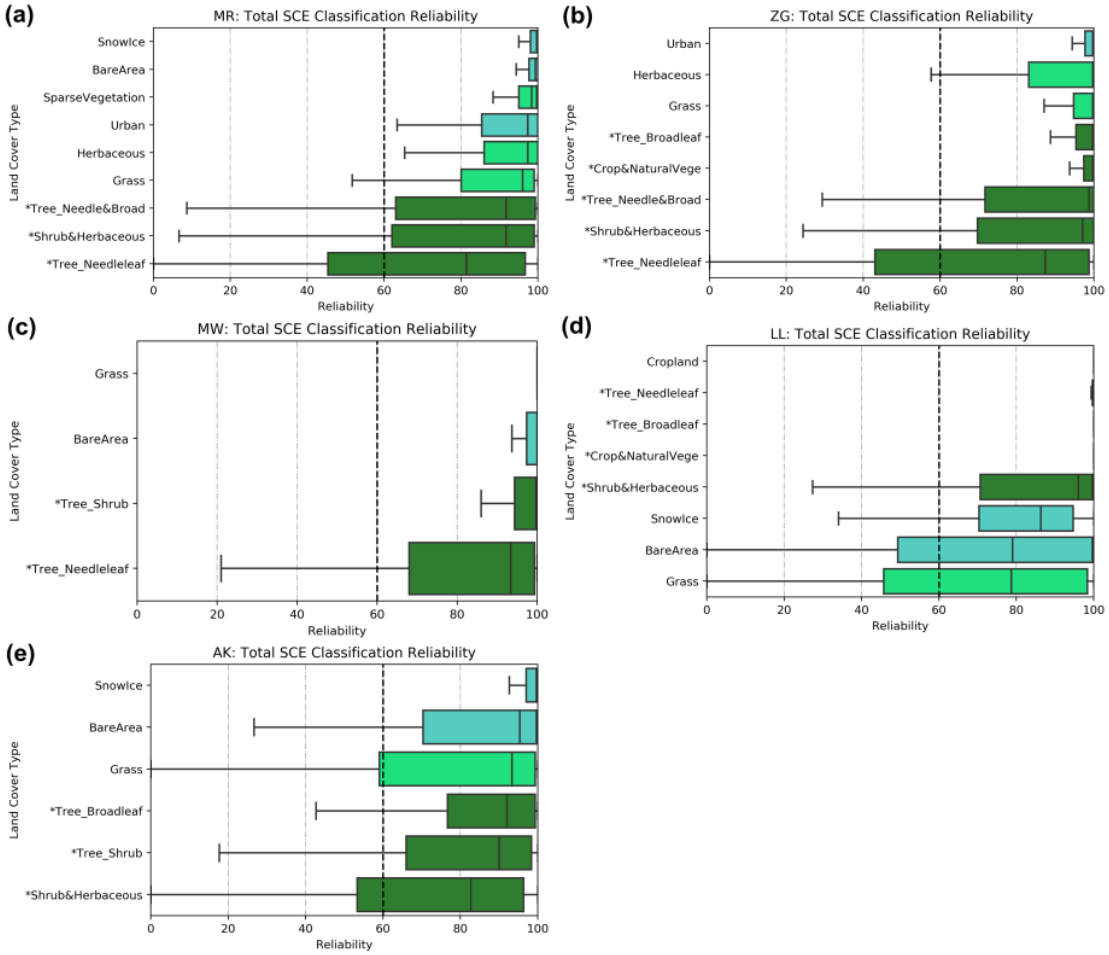

Figure 4.9 Assessment of the relationship between reliability and land cover class in

each region: (a) Monte Rosa (MR); (b) Zugspitze (ZG); (c) Mount Whitney (MW); (d) Landtang Lirung (LL); and (e) Aoraki (AK). Densely, lightly, and non-vegetated land cover classes are colored in deep green, light green, and light blue, respectively.

4.5.3 The Heterogeneity between Multispectral-based Results/Products for Model Training and Validation

Although the GSP SCE, which is used for training the model, the Landsat/Sentinel-2 Fmask-based SCE which is used for validation, and the PROBA-V-based vegetation products, which is used for modeling as well all stem from multispectral sensors, they should not be affected by considerable correlations/biases. These products are calculated with different algorithms/techniques for different purposes, and they are based on several different sensors which acquire the data at varying times. In detail, the total SCE of GSP is calculated by combining both MODIS daily snow cover products (MOD10A1 and MYD10A1) and then applying temporal interpolation, snowline determination with a DEM reference, and a seasonal filter to eliminate the effect of polar darkness and cloud coverage (Dietz et al., 2015). The GSP is therefore based on an aggregation approach. In the contrary, the Fmask-based Landsat/Sentinel-2 SCE is estimated by executing a water detection relying on the NDVI and the NIR band, cloud detection using thermal bands, and cloud shadow mapping using segmentation of objects' shapes (Qiu et al., 2017). Fmask can therefore be considered a segmentation approach. Therefore, the way how total SCE is derived from both approaches is technically different. When it comes to the PROBA-V-based LAI and FVC products, a machine learning-based approach is employed. The products are processed by neural networks with calibrated reflectance inputs, then post-processed with outlier rejection, composition, smoothing, and gap filling (Baret et al., 2016). Although being derived from multispectral data, these three datasets are calculated with different techniques, which prevents a direct correlation/bias between them. Thus, reliability of the validation can be ensured.

4.5.4. Applying the Total SCE Detection Approach to a Wider Spatial Scale – the Whole Alps

To test the robustness and transferability of the employed model and to examine the practical usability, we applied our approach to the whole Alps for the melting season of 2018 to monitor the total SCE dynamics. By utilizing the same dataset and classification routine as mentioned in Section 2.2, 2.3, and 3, we can sense the total SCE for the whole Alps from March to May of 2018. To emphasize the dynamics of the SCE visually, we only illustrate the results in 24-days interval as shown in Figure 4.10. It is clear that the pattern of the modeled total SCE matches well with the topography of the mountain ranges. A decrease of total SCE can be observed from March to May

as the snow starts to melt due to the increase of temperature. The results indicate that it is practical to depict the total SCE in both dry snow-dominated months (March) as well as wet snow-dominated months (May). This outcome confirms the maturity of our approach and that it is comparable to the conventional optical sensor-based approaches in both spatial and temporal scales.

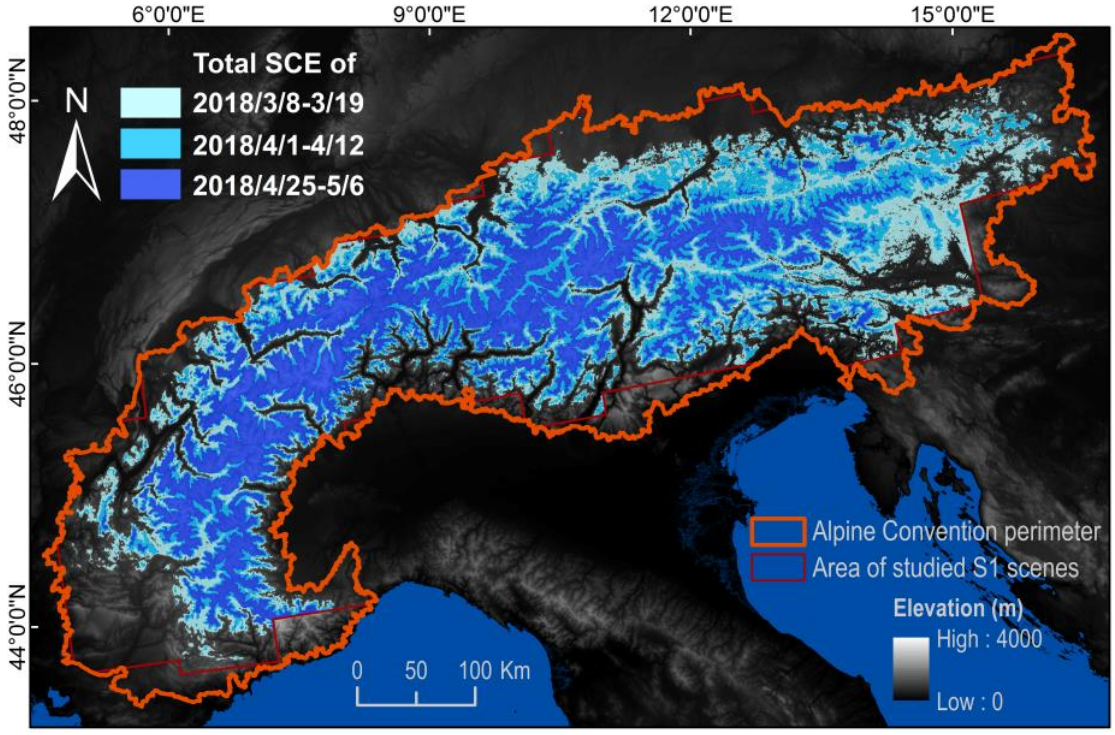

Figure 4.10 Map of the modeled total SCE for the whole Alps including 2018/3/8-3/19, 2018/4/1-4/12, and 2018/4/25-5/6 based on Sentinel-1 SAR observations, topographical factors, vegetation indexes, and temperature information. The total SCE for the different dates are colored differently.

4.5.5. Improvements Achieved in This Study and its Future Potential

In our previous study (Tsai Ya-Lun S, Dietz Andreas, et al., 2019b), we confirmed that by utilizing SAR-based observations (backscatter, InSAR coherence, and PolSAR parameters), topographical factors (elevation, slope, aspect, and curvature), and land cover information, it is possible to map the total SCE with an accuracy of around 80% (calculated based on validation with high resolution optical sensors-based SCE) which was already much higher than previous SAR-based studies (Tsai Ya-Lun S. et al., 2019). However, this level of accuracy is still generally lower than the conventional optical-based SCE detection approaches. For instance, the MODIS daily snow cover product is confirmed to have accuracy of around 90% under clear sky conditions (Dietz et al., 2015). Consequently, to improve the usability of SAR-based results, we

added two more variable sets which are derived from multi-spectral sensor-based products, including surface temperature (derived from MODIS) and vegetation indexes (derived from PROBA-V), which are commonly employed to map SCE, to enhance the classification accuracy to around 90%. These two different input variable combinations and mapping accuracies provide a comprehensive strategy for users to utilize SAR-based observations for total SCE mapping based on data availability. If a region is neither cloud covered nor affected by polar darkness, the multi-spectral sensor-based vegetation and temperature products are trustable. They allow for an RF-based SCE detection with an accuracy of around 90%, which is comparable to traditional cloud-free optical-based classification accuracies. If multi-spectral sensors are not available for a region (PROBA-V-based vegetation indexes are influenced by cloud coverage and polar darkness; the MODIS-based temperature product is also affected by cloud coverage), users can still rely on the all-weather sensible, cloud-penetrating SAR-based observations to map total SCE with an accuracy of around 80%. Although this accuracy is lower, it largely compensates the void information provided by optical sensors.

However, there is still a limitation for SAR-based SCE detection approaches. According to the Global Observing System for Climate (GCOS) (Key et al., 2007), the minimum SCE mapping requirements for the subsequent hydrological and climate applications is 1000 m spatial resolution and one to five days temporal resolution. Although the current novel spaceborne SAR sensors can easily satisfy the spatial resolution threshold (the spatial resolution of Sentinel-1 is around 20 m); their revisit time normally is longer than five days even when a multi-satellite constellation is formed (Sentinel-1A and B can shorten the revisit frequency to six days from original 12 days). Thankfully, the extension of the Sentinel-1 missions has been confirmed, and the launches of Sentinel-1C and D are planed from 2021 onwards (Torres et al., 2017). They will compose a more completed constellation system and provide a much denser SAR observation frequency which will provide a great niche for spaceborne SAR-based SCE mapping approaches.

4.6. Conclusions

Snow cover not only influences many environmental phenomena but also human activities, thus snow monitoring is a critical topic especially because recently, snow cover extent (SCE) shows a significant decreasing trend globally due to climate change. To overcome the limitations of conventional optical-based approaches, including cloud coverage and polar darkness, the utilization of spaceborne SAR is explored in the present study. Compared to our previous paper (Tsai Ya-Lun S, Dietz

Andreas, et al., 2019b) which only utilized SAR-based observations (backscatter, InSAR coherence, and PolSAR parameters) and topographical factors (elevation, slope, aspect, and curvature), the value of employing vegetation indexes (LAI and FVC) as well as land surface temperature (LST) derived from the PROBA-V satellite and MODIS sensors, respectively, has been examined. It was confirmed that the overall accuracy, F-measure, and AUC score can be enhanced from previously 80%, 80%, and 70% to around 90%, 90%, and 80% for all five study areas located in different mountain ranges, continents, and hemispheres.

Based on the satisfying accuracy among all validation trials with different data sources, the transferability of the method and data proposed in the present study was also ensured. Moreover, the newly generated reliability maps along with the modeled total SCE provides a potential for evaluating the uncertainty for further application and analysis. For instance, a relationship between lower modeled reliability with densely vegetated land cover classes was confirmed and discussed. Additionally, to examine the assumption of “more inputs can always yield better classification accuracy,” both, the SAR’s local incidence angle as well as multi-bands imagery from the high-resolution optical sensor were also tested, which did not improve the accuracy significantly. Eventually, we successfully applied our approach to map the total SCE dynamics for the whole Alps during the melting season of 2018, which confirms transferability and applicability of the approach.

Most important of all, based on the present study, we provide an alternative approach to map the total SCE (wet + dry snow) in the scenario that multi-spectral auxiliary products (LAI, FVC, LST) are trustable. Together with our previous paper (Tsai Ya-Lun S, Dietz Andreas, et al., 2019b) only relying on SAR-based observations and static topographical factors, these two different input variable settings provide users a package to achieve satisfactory total SCE mapping accuracies based on different data availability. It largely compensates the traditional limitation of optical-based SCE detection approaches and also provides extra wet SCE information which cannot be detected by optical sensors.

Acknowledgments: Support by the German Academic Exchange Service (DAAD) fellowship to Ya-Lun S. Tsai is gratefully acknowledged. The authors thank the providers of the meteorological data used in this article, including MeteoSwiss (the Swiss Federal Office of Meteorology and Climatology) as well as the ECA&D project (Data and metadata available at http://eca.knmi.nl).

5 Monitoring Large-scale Inland Water Dynamics by Fusing Sentinel-1 SAR and Sentinel-3 Altimetry Data and by Analyzing Causal Effects of Snowmelt

Tsai, Y.-L.S., Klein, I., Dietz, A. and Oppelt, N. (2020). Monitoring Large-scale Inland Water Dynamics by Fusing Sentinel-1 SAR and Sentinel-3 Altimetry Data and by Analyzing Causal Effects of Snowmelt. Remote Sensing, 12, 3896

Abstract

The warming climate is threatening to alter inland water resources on a global scale. Within all waterbody types, lake and river systems are vital not only for natural ecosystems but also for human society. Snowmelt phenology is also altered by global warming, and snowmelt is the primary water supply source for many river and lake systems around the globe. Hence, (1) monitoring snowmelt conditions, (2) tracking the dynamics of snowmelt-influenced river and lake systems, and (3) quantifying the causal effect of snowmelt conditions on these waterbodies are critical to understand the cryo-hydrosphere interactions under climate change. Previous studies utilize in-situ or multispectral sensors to track either the surface area or water level of waterbodies, which is constrained to small-scale regions and limited by cloud cover, respectively. On the contrary, in the present study, we employ the latest Sentinel-1 synthetic aperture radar (SAR) and Sentinel-3 altimetry data to grant a high resolution, cloud-free and illumination-independent comprehensive inland water dynamics monitoring strategy. Moreover, in contrast to previous studies utilizing in-house algorithms, we employ freely available cloud-based services to ensure a broad applicability with high efficiency. Based on altimetry and SAR data, water level and the water-covered extent (WCE) (surface area of lakes and the flooded area of rivers) can be successfully measured. Furthermore, by fusing water level and surface area information, for Lake Urmia we can estimate the hypsometry and derive water volume change. Additionally, for the Brahmaputra River, the variation of both water level and the flooded area can be tracked. Last but not least, together with the wet snow cover extent (WSCE) mapped with SAR imagery, we can analyze the influence of snowmelt conditions on water resource variation. The distributed lag model (DLM) initially developed in the econometrics discipline is employed, and the lagged causal effect of snowmelt conditions on inland water resources is eventually assessed.

Keywords: Snow Cover; Water Level; Surface Area; Flooded Area; Hypsometry; Distributed Lag Model

5.1. Introduction

Inland water resources play an essential role in not only the prosperity and stability of human society but also the sustainability and balance of various ecosystems. According to the reports of United Nations Environment Programme (UNEP) (2010), UN Food and Agriculture Organization (FAO) (Food and Nations, 2011), and the latest UN World Water Development Report (WWDR) 2019 (Water, 2019), transboundary surface water resources largely influence the socio-economic-ecological systems; therefore, it is enlisted as the sixth 2030 Sustainable Development Goals (SDGs). Expressly, the importance of local rivers and lakes should be noted as they are critical freshwater sources for many regions (Water, 2019) and also influence the climate (Crétaux et al., 2016). However, as studies suggested (Bhaduri et al., 2016; Costanza et al., 2016), these vague SDGs provide no dependable guideline on how to achieve them. As a result, to elaborate the practical research gap of SDG target 6.6, i.e., protect and restore water-related ecosystems, an investigation of the main drivers of change in the high-mountain cryosphere is recommended (Bhaduri et al., 2016). The importance of snowmelt water to downstream freshwater is widely recognized. Assessing this cryo-hydrosphere interaction is indispensable to understand the future trend of water resources we have in severer climate change scenarios. Due to the global warming, the shrinking of snow cover extent (SCE), earlier snowmelt season, and shorter snow cover duration has been observed almost globally as stated in the Synthesis Report of the IPCC Fifth Assessment Report (AR5) (Pachauri et al., 2014). Moreover, in the same report it is also indicated that the change of melting snow is altering hydrological systems and affecting water resources in both, quantity and quality. Thus, monitoring snowmelt conditions and the dynamics of snowmelt-influenced river and lake systems and quantifying the causal effect of snowmelt water on these waterbodies are critical. It would allow us not only to understand the impact of global warming's to inland water resources but also to assess the vulnerability and variability of regional freshwater supply.

For the observation and investigation of the influence of snowmelt on global waterbodies, the employment of spaceborne remote sensing data is preferred, owing to its high efficiency and broad applicability. As mentioned in the latest report published by UN-Water assessing the progress of SDG indicator 6.6.1 (Water, 2018), i.e., tracking time-series changes in the extent (including quality, quantity, and area) of water-related ecosystems (including rivers and lakes), the utilization of globally transferable satellite data is strongly advocated. For monitoring the snowmelt conditions, as summarized in Tsai et al. (2019), it is hardly possible to discriminate wet and dry snow with conventional multi-spectral data sources solely based on the

reflectance differences, as the spectral characteristics of both snow types share high similarity. SAR data, on the other hand, is excellent for wet SCE (WSCE) mapping: The snowmelt-caused wetness in the snowpack would change the dielectric constant of the snowpack and thus dramatically shorten the penetration depth of the SAR signal, which eventually leads to a significant decrease of the backscatter coefficient when the snowpack starts to melt (Nagler and Rott, 2000; Marin et al., 2019; Tsai Ya-Lun S. et al., 2019).

For monitoring the dynamics of river and lake systems, conventional studies focus on either water level or surface area. For tracking the surface area, multi-spectral sensor-based band ratio water indices, such as the Normalized Difference Water Index (NDWI) (McFeeters, 1996), Modified NDWI (MNDWI) (Xu, 2006), and Automated Water Extraction Index (AWEI) (Feyisa et al., 2014), are commonly used due to their simplicities. However, in addition to the difficulty of the selection among these various band ratios, these indices are based on multi-spectral sensor. Therefore, they are inevitably affected by cloud cover and polar darkness, which frequently happen for alpine regions and high latitude zones (Tsai Ya-Lun S. et al., 2019). Moreover, the spectral feature of water in the multi-spectral sensor is also affected by the variation of atmospheric/illumination conditions and water dynamics, such as water depth, sediment load, eutrophication degree, turbidity, sun angle, and sensor view angle (Klein et al., 2017; Dirscherl et al., 2020). On the contrary SAR data can be utilized for waterbody monitoring thanks to its cloud-penetrating applicability and illumination-independent characteristics. Yet it might suffer from relatively coarse resolution compared to optical sensors, the higher cost of the imagery, and most importantly, the requirement of computation-intensive processing.

Regarding the monitoring of the water level of lakes or rivers, using in-situ gauging station measurements is the optimal approach. However, although it provides the chance of continuous observations, it is not widely achievable in all lake and river systems because of the cost of instruments setup, intensive maintenance requirements, or the difficult accessibility of remote waterbodies. In fact, the number of available gauging stations has been decreasing globally (Alsdorf et al., 2007; Duan and Bastiaanssen, 2013). Also, the data might not be publically available. Another alternative is combining the surface area of a waterbody with the bathymetry of the lake or river channel to derive the water surface height. Nevertheless, accurate information of bathymetry is still needed, which is only available for very few waterbodies, which were surveyed thoroughly (Duan and Bastiaanssen, 2013; Crétaux et al., 2016). On the contrary, spaceborne altimetry provides a favorable alternative for waterbody surface height monitoring due to its global availability. Many

altimetry databases have therefore been established, including the Database for Hydrological Time Series of Inland Waters (DAHITI) (https://dahiti.dgfi.tum.de/en/) (Schwatke et al., 2015), The Global Reservoir and Lake Global Reservoir and Lake Monitor (G-REALM) (https://ipad.fas.usda.gov/cropexplorer/global_reservoir/) (Birkett et al., 2017), and Hydroweb (http://hydroweb.theia-land.fr/) (Crétaux et al., 2011). Unfortunately, because the design of spaceborne altimetry sensors is generally targeted for ocean surface surveying, i.e., a flat, isotropic, and ample reflecting surface, the footprint sizes of their echoes are enormously coarse (> 2 kilometers), and the sampling distance between these echo points is vast (Yuan et al., 2017). These characteristics hinder the viability of inland waterbody monitoring, especially for rivers, which usually have a more inhomogeneous neighboring topography (Fernandes et al., 2014). Thus, to overcome the waveform difference to the standard Brown model (Brown, 1977), a computation-intensive waveform reprocessing (retracking) analysis is usually required for inland waterbodies (Calmant et al., 2008; Crétaux et al., 2016; Cretaux et al., 2018; Wang et al., 2019). However, the selection of retrackers (ground processing techniques which estimate the range to the point of closest approach on the surface) varies in different studies and most of them use in-house algorithms or refinements (Uebbing et al., 2014; Crétaux et al., 2016; Yuan et al., 2017; Gao et al., 2019), which largely limit the transferability of the method to other regions.

With the aim to overcome these limitations for monitoring surface area and water level, in the present study, we utilize the new generation of high-resolution, freely accessible spaceborne SAR and altimetry data of Sentinel-1 and Sentinel-3, together with freely available online cloud-based processing services to achieve a comprehensive inland waterbody dynamics (time-series surface area and water level) tracking strategy with broad applicability. Although there have been some studies employing either spaceborne SAR or altimetry sensors for waterbody monitoring, yet few studies have integrated them to achieve an in-situ measurement-free approach. Also, in contrast to studies relying on multi-spectral sensors, this altimetry-SAR sensor combination provides a cloud-free and illumination-independent monitoring method. Furthermore, as the Sentinel fleet is the newest generation of spaceborne satellites with freely accessible data policy, data availability is ensured for the following decades. Last but not least, based on the depicted comprehensive waterbody dynamics together with the SAR-based WSCE maps, we can further analyze the relationship between snowmelt conditions and inland water resource variation. By employing a sophisticated regression model adopted from the econometrics domain, we guarantee a quantified and unbiased lagged influence of the snowmelt condition on

the waterbody dynamics; hence the cryo-hydrosphere interaction can be well-identified.

5.2. Study areas and data

5.2.1 Study areas

Since the goal of the present study is to (1) monitor the dynamics (both water level and surface area) of inland waterbodies and (2) quantify the lagged influence of snowmelt on inland water dynamics, we select the study sites based on the following criteria: (1) their spatial scales are wide enough to be detected by spaceborne SAR and altimetry sensors, (2) they demonstrate considerable magnitude of variation in both water level and surface area, and (3) their watersheds include snow-covered regions.

Therefore, in our study, the Lake Urmia in Iran and the Brahmaputra River are chosen.

5.2.1.1 Lake Urmia

Lake Urmia (or Orumiyeh Lake) is located in the northwest of Iran. It is the largest lake in Iran and was the largest perennial hyper-saline lake worldwide (Zarghami, 2011). This endorheic lake is situated 1273 meters above the mean sea level and is situated in the semi-arid climate zone with average annual precipitation and evaporation of around 341 and 1200 mm/yr, respectively (Djamali et al., 2008). The highest river inflows can be observed in springtime due to snowmelt (Environment, 2010). Based on its geological location and climatic characteristics, Lake Urmia and the basin encompass high biodiversity and are one of the most critical ecological habitats in the Middle East. For instance, Lake Urmia is the largest habitat of the brine shrimp *Artemia urmiana* (Karbassi et al., 2010), which is the primary food source for the migratory birds (Scott, 2001; Ahmadi et al., 2011). The islands in the lake are critical destinations for these migratory birds and also the shelter for rare species of mammals and reptiles (Kabiri et al., 2012; Sima and Tajrishy, 2013). The vibrant ecosystem led to Lake Urmia being entitled as a Wetland of International Importance by the Ramsar Convention in 1971 and a Biosphere Reserve by UNESCO in 1976 (Nouri et al., 2017).

However, recent studies show that Lake Urmia has been experiencing dramatic water depletion in recent decades mainly due to intensive anthropogenic actives (Hassanzadeh et al., 2012; Delju et al., 2013; Voss et al., 2013). The variation of its surface area is also significant as shown in Figure 5.1(a). The construction of dams and causeways, as well as the extraction of groundwater for agricultural irrigation, are

responsible for a large part of water resource loss (Eimanifar and Mohebbi, 2007; Hassanzadeh et al., 2012; Tourian et al., 2015). Together with the fact that Lake Urmia is a terminal lake with a maximum depth of only 16 meters, it is even more vulnerable to evaporation (Sorgeloos, 1986). Thus, the salinity has reached a dangerous level for species (Eimanifar and Mohebbi, 2007), and the water equilibrium has fallen to a new low standard (Tourian et al., 2015). According to Abbaspour et al. (2012), the lake might eventually dry up within a decade. The lake desiccation endangers not only the natural environment and habitat but also the nearby population of seven million inhabitants in both economic as well as health aspects (Pengra, 2012). For instance, the depleted lake bed would reveal dissolved salts crusts (Alipour, 2006), which would be exposed to the wind and cause salt-storms to the surrounding residential areas; the shrinking size of the lake would reduce its function as a mediator in the extreme climate (Kabiri et al., 2012); the dehydrated bed would also lead to species migration (Sima and Tajrishy, 2013). Moreover, the shortage of water resources might also result in a political crisis (Madani, 2014).

5.2.1.2 Brahmaputra River

The Brahmaputra River originates in the Himalayan mountain range, which is mainly fed by snowmelt water and is the third-largest river in the world by discharge (Dai et al., 2009; Immerzeel et al., 2010; Archana et al., 2012). It is a trans-boundary river, by order, it passes by China, India, Bangladesh, and eventually merges with the Ganges river and flows into the Bay of Bengal. It is called with different names in each country, including Yarlung Zangbo, Brahmaputra, and Jamuna, in China, India, and Bangladesh, respectively. As the youngest major river among the world (Archana et al., 2012), the Brahmaputra River has at least three characteristics: abundant tributaries, highly dynamic fluvial activities, and a varying river width as shown in Figure 5.1(b). Because the sediments of the Brahmaputra River bed is composed with medium to fine sand and silt which is uniformly graded and has poor transport resistance (Archana et al., 2012), the river bed and banks area are considerably mobile which leads to frequent morphological change affected by fluvial processes (Archana et al., 2012; Dubey et al., 2014; Samanta et al., 2019). Therefore, river braiding, division, and shifting often happen (Richardson and Thorne, 2001). However, although it is one of the most critical water resources in Asia, there is barely any in-situ river measurement available publically. Because of the imminent danger of flooding, such in-situ data is regarded as classified information, and even the Global Runoff Data Center (GRDC) keeps no recent observations (Finsen et al., 2014; Huang et al., 2018).

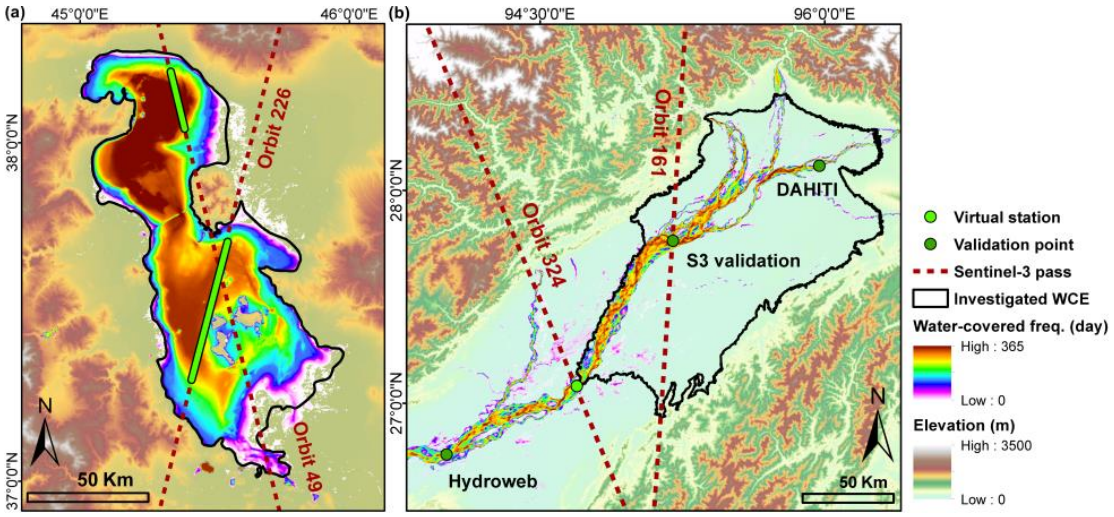

Figure 5.1 The locations of the study areas with the Sentinel-3 altimetry satellite pass ground tracks (dotted red lines) and the corresponding virtual stations (VSs) (green points). The investigated water-covered extent (WCE) (black polygon) and the average water-covered frequency of 2003 to 2018 derived from the Global WaterPack (GWP) are illustrated.

5.2.2 Data

5.2.2.1 Sentinel-1 SAR

The Sentinel-1 mission consists of two-satellites, with Sentinel-1A/B launched in April 2014 and April 2016, respectively. Its advanced terrain observation with progressive scans in azimuth (TOPS) image acquisition technique enables a high signal-to-noise (SNR) ratio in long-track direction without scalloping effect while maintaining a wide coverage like conventional ScanSAR mode (Tsai Ya-Lun S, Lin Shih-Yuan, et al., 2019). As in the present study, we only utilize the intensity information, the Level-1 Ground Range Detected (GRD) product, for which all the sub-swath have already been merged, and de-bursting is selected. To increase the efficiency of image analysis, we process the images on Google Earth Engine (GEE). It provides the archive of Sentinel-1 GRD scenes and stores them in the decibels (dB) unit. Further calibration, such as orbit file application, noise removal, radiometric calibration, and terrain corrections, are processed as well. Furthermore, this cloud-based geospatial processing platform enables a user-defined processing, which largely accelerates the time-series SAR data analysis in a wide spatial scale (Gorelick et al., 2017).

5.2.2.2 Sentinel-3 altimetry

Similar to Sentinel-1, Sentinel-3 is also composed of two satellites, with Sentinel-3A/B being launched in February 2016 and April 2018, respectively. When it comes to

inland water monitoring, compared to previous spaceborne altimetry sensors, the biggest advantage provided by the dual-frequency SAR radar altimeter (SRAL) instrument abroad on Sentinel-3 is the much finer along-track resolution. Inherited from CryoSat, Sentinel-3 uses the high pulse repetition frequency (PRF) SAR mode (or delay-Doppler) processing, which greatly improves the along-track resolution of the commonly used low-resolution mode (LRM) altimeters. It significantly increases the SNR ratio and thus enables the detection of much smaller target (EUMETSAT, 2017). Moreover, the echo reception window positioning method is also upgraded. Thanks to these improvements, Sentinel-3 is capable of monitoring finer inland waterbody. To process the altimetry data via ESA online service, Level-1 Non Time Critical (NTC) products are selected.

5.2.2.3 Auxiliary data

To include hydrological factors including rainfall and evapotranspiration, the latest European Centre for Medium-Range Weather Forecasts (ECMWF) ERA5-Land data are used. This newly released reanalysis dataset provides global meteorological variables in a much higher spatial resolution (nine kilometers) compared to previous ERA-Interim (79 kilometers) and ERA5 (31 kilometers) datasets. Currently, it covers data from 1981 to present, and eventually, it would cover the same period as ERA, i.e., 1950 to near real-time.

For examination of our water level results, the data provided by DAHITI, G-REALM, and Hydroweb are used. To compare our water-covered extent estimations, the Global WaterPack (GWP) is selected. It utilizes daily MODIS reflectance data at 250m spatial resolution and dynamically decides threshold values as well as temporal interpolation techniques to achieve daily global cloud-free water/no water classification (Klein et al., 2017).

5.3. Methodology

5.3.1 Water level calculation with Sentinel-3 altimetry

To derive the water level from Sentinel-3 altimetry data, we utilize the ESA's SAR Versatile Altimetric Toolkit for Ocean Research & Exploitation (SARvatore) service. It is based on the G-POD (Grid Processing On Demand) distributed platform, which guarantees high-speed processing and timely delivery. Another highlight of the SARvatore service is that it provides the inland water-customized processing configuration, which utilizes the higher posting rate (HPR) of 80 Hz data and processes with the new SAMOSA+ analytical retracker algorithm (Dinardo et al., 2016; Dinardo et al., 2018). By utilizing this advanced setting mode, we can reduce the

separation between two observations in along-track from the original 300 meters to 80 meters, and thus provide more valid points over the targeted waterbody. The output files include not only a L2 data in NetCDF format but a KML file containing the satellite pass ground track location. The KML file facilitates the identification of the interested regions as shown in Figure 5.1, i.e., virtual station (VS) (the intersection of altimetry's ground track and the waterbody), in the following analysis of the Multi-Mission Radar Altimetry Toolbox (BRAT). It must be noted that because both of our study targets are characterized by significant seasonal WCE change, we first utilize the GWP to identify the sub-region of a waterbody having (near) permanent water, and then analyze the altimetry data of that region to minimize the signal pollution. This step largely enhances the accuracy by avoiding taking account of river/lake bed-caused signals in the dry season. To derive the unbiased orthometric height over the inland waterbody H_{ORTHO}, i.e. the water level refers to the geoid, the following correction equation is used:

$$\mathrm{H}_{ORTHO} = \mathrm{H}_{SAT} - \mathrm{R}_{OBS} - (\Delta R_{WTC} + \Delta R_{DTC} + \Delta R_{IONO} + \Delta R_{ET} + \Delta R_{PT}) - \mathrm{N}_{GEOID} \quad (5.1)$$

where H_{SAT} is the satellite altitude above the reference geoid, R_{OBS} is the observed range, $\Delta R_{DTC}/\Delta R_{WTC}$ is the dry/wet tropospheric correction, ΔR_{IONO} is the ionospheric correction, $\Delta R_{ET}/\Delta R_{PT}$ is the earth tide and pole tide, respectively, and N_{GEOID} is the geoid height. For a full explanation of each correction refer to (EUMETSAT, 2017). Based on this formula, both propagation and geophysical biases can be compensated. Other geophysical terms, including lake tides, hydrostatic variations, thermal expansion, and wind piling-up effect are neglected as suggested by a previous study (Wang et al., 2019). For a detailed information of each correction refer to (Dumont et al., 2016; EUMETSAT, 2017). Finally, based on the corrected range, we calculate the average and standard deviation of the water level over the VS.

5.3.2 Water-covered extent (WCE) calculation with Sentinel-1 SAR

To map the water-covered extent, i.e., the lake's surface area or river's channels and flooded area, the sensitivity of SAR data to surface wetness is utilized. As the backscatter coefficient would be much lower in wet and smooth surface comparing to dry ground, it is viable to depict the water surfaces. Because our goal is to maximize the differentiation of water/non-water regions, i.e., a binary classification, the task can be separated into two parts: (1) selection of the targeted image (2) determination of the threshold. For the first point, based on the previous studies (Henry et al., 2006; Wangchuk et al., 2019) and our testing, the value difference between waterbody and the land region is more significant in VV polarization (co-polarization) than VH

(cross-polarization), so VV imagery is selected. Furthermore, we use Otsu's algorithm to decide the threshold (Otsu, 1979). It is favored for its simplicity and suitability for SAR image-based binary classification (Greifeneder et al., 2014; Wangchuk et al., 2019). Practically, the critical point is to ensure that the manually selected samples include an equal number of water/non-water pixels, as Otsu's algorithm can only handle bimodal distribution. However, sometimes it is difficult to distinguish lake/river boundary visually in some flood-caused vague scenes (as discussed in the Discussions 5.1), we only use scenes having clear waterbody boundary for training the Otsu's algorithm.

To define the targeted WCE for investigation, for Lake Urmia we use the waterbody boundary provided by the Global Lakes and Wetlands Database (GLWD) (https://www.worldwildlife.org/pages/global-lakes-and-wetlands-database) (Lehner and Döll, 2004). For the Brahmaputra River we target the part of the watershed of the VS where the terrain is a flat plain (elevation lower than 200 meters) and frequent river braiding and shifting events happen as illustrated in Figure 5.1.

5.3.3 Lake water volume estimation by hypsometry calculation and detrended volume retrieval

To estimate the water volume variation of a waterbody, it is common to use either the simplest truncated pyramid model or the power-function model; however, they are only suitable for waterbodies characterized by a regular morphology (such as reservoirs) or a bowl-shaped morphology, respectively (Nilsson et al., 2010; Sima and Tajrishy, 2013). We utilize a universally applicable approach by modeling the water volume-water level relationship from the observed surface area-water level relationship (Duan and Bastiaanssen, 2013). The processing steps include: (1) calculation of the water level difference (or water depth) relative to the minimum water level in the sensing period ($\Delta \mathrm{L} = \mathrm{L} - \mathrm{L}_{\min}$), (2) establishing a scatter plot of surface area-water level difference and model it with a polynomial function (typically second, third, or quadratic order is chosen) ($\mathrm{A} = \mathrm{f}(\Delta L)$), (3) integration of the surface area-water level difference function to derive the water volume-water level difference function ($\mathrm{V} = \int_{\Delta L_0}^{\Delta L} \mathrm{A}\, d\Delta L$), (4) ingestion of water level observations to the resultant function to derive the corresponding water volume. Details about these steps can be found in (Duan and Bastiaanssen, 2013; Muala et al., 2014). In short, by using this approach, we can estimate the "dynamic" water volume above the "static" water volume, i.e., the water volume of the time when the water level is the lowest, for any waterbody having a horizontal water surface (Hayashi and Van der Kamp, 2000).

Nevertheless, it must be noted that compared to any single point of the river, the lake is a “container,” which can store the water over time instead of merely letting the water flow by. Namely, the results of each previous hydrological year’s water budget balance (increase with snowmelt and rainfall; decrease with evapotranspiration) would affect the current “stock” of the water volume. Hence, if we directly use the original time-series water volume as the inter-annual variation, the intra-annual “container effect” could lead to a miss-interpretation. Therefore, in the present study, we employ the Seasonal-trend decomposition procedures based on Loess (STL) (Cleveland et al., 1990) to remove the intra-annual trend. This approach is suggested by previous studies (Sellinger et al., 2008; Fathian et al., 2014; Hassan and Jin, 2014). STL is an iterative non-parametric filtering procedure that uses repeated Loess (Local Regression) smoothing. The strength of STL is its robustness and computational efficiency, as well as the capacity to depict a non-linear pattern in time-series data. For details about STL refer to (Cleveland et al., 1990; Lu et al., 2003). Practically, based on the inner and outer loops with Loess processing, STL can decompose a time-series data to three components: a low-frequency long-term trend, a high-frequency seasonal variation, and residuals (or remainder). After processing STL, we subtract the decomposed long-term trend from the original time-series water volume to derive the detrended water volume, which represents the real inter-annual water volume variation.

5.3.4 WSCE mapping with Sentinel-1 SAR and hydrological factors areal calculation

Based on the finding that the backscatter coefficient of the SAR signal decreases significantly when the snowpack starts to melt and thus increases the containing liquid water (Tsai Ya-Lun S. et al., 2019), Nagler and Rott (2000) proposed a ratio-thresholding approach in 2000. It utilizes two SAR scenes (one is a wet snow-covered period image, and the other is a referenced snow-free image) and calculates their ratio image, which is then thresholded using a fixed value to derive the binary WSCE. For a detailed description of the processing steps and value setting refer to (Tsai Ya-Lun S. et al., 2019; Tsai Ya-Lun S, Dietz Andreas, et al., 2019b, 2019a).

Because the final regression analysis is watershed-based, all hydrological factors, including WSCE, rainfall, and evapotranspiration, need to be converted. Firstly, we delineate the watershed based on the SRTM DEM. For the Brahmaputra River, the VS where the Sentinel-3 track passes is used as the pour point, and the watershed of that point of that tributary is delineated. Based on the watershed, the WSCE is ratioed to derive the WSCE%; the rainfall and evapotranspiration are summed up to derive

the mean amount.

5.3.5 Hydrological econometrics regression analysis

To quantify the influence of the investigated hydrological factors (WSCE%, mean rainfall, and mean evapotranspiration) on river/lake water amount, the utilization of a regression analysis is an optimized approach. However, some factors, especially the snowmelt, would pose a lagged effect on downstream water level/volume as the snowmelt water would not only form the direct surface streamflow but also infiltrate into the ground and soil (Seyfried et al., 2009; Butt and Bilal, 2011; Abudu et al., 2012). Thus, a conventional simple regression is not viable. Consequently, we employed the advanced distributed lag model (DLM) (or finite distributed model (FDL)) in the present study for handling multiple variables' dynamic influences with lags. DLM is firstly developed in the econometrics discipline (Almon, 1965) and was recently widely applied in biomedical or environmental exposure-caused mortality studies (Yang J. et al., 2012; Allen and Sheridan, 2018). Yet, DLM is barely utilized in remote sensing and cryo-hydrology domain. DLM is a dynamic model that assumes that the effect of each independent factor on the dependent variable spreads over some time instead of a single time point. To quantify it, it defines the temporal factor by assigning a lag dimension, which is an equally-spaced and ordered time point series (Gasparrini, 2011) (in the present study, we define the minimum unit of lag dimension as ten days). The lag dimension enables the effect of a single exposure event to be distributed over a specific period of time; therefore, the holistic understanding of the cross-temporal exposure-lag-response relationship can be revealed (Gasparrini et al., 2010; Gasparrini, 2011, 2014). The multi-variable DLM can be written in the formula:

$$y_t = \alpha + \sum_{s=0}^{q1} \beta 1_s x1_{t-s} + \sum_{s=0}^{q2} \beta 2_s x2_{t-s} + \cdots + \sum_{s=0}^{qN} \beta N_s xN_{t-s} + u_t \qquad (5.2)$$

where α is the intercept; q and β is the lag length and lag coefficient (or lag weight, or short-run multiplier) of each independent variable, respectively; and u_t is the error term. The lag coefficient is solved by the ordinary least squares (OLS) technique and represents the expected change in y_t stems from the change of xN_{t-s} by one unit, holding constant other independent variables (Stock and Watson, 2015). The sum of each independent variable's lag coefficient, i.e. $\sum_{s=0}^{qN} \beta N_s$, is called the long-run multiplier, or long-run propensity (LRP), which is the cumulative effect of xN on y (Wooldridge, 2000). In the present study, we focus on the LRP value to quantify the causal effect of each factor on the water resource variation.

Practically, the most critical issue when implementing DLM is selecting a suitable lag

length for each independent variable. As in the present study, we include three variables (WSCE%, mean rainfall, and mean evapotranspiration) and based on the background knowledge it is assumed that their lag lengths should be different; therefore, it is impractical to use the conventional length decision method, i.e., successively adding/reducing lags. Previous studies utilize the prior knowledge to define the plausible lag lengths when multi-regressors are included (Teklehaimanot et al., 2004; Zhao et al., 2014). However, in our study, the lagged effect of the same hydrological factor on the water amount varies from place to place as it is affected by the distance and the regional characteristic. Thus, there is no universal pre-defined lag length estimation available. Instead, we apply the following processing steps to decide the proper lag length of each hydrological factor: (1) building of the regression of water amount (water level for the river; water volume for the lake) with each hydrological factor individually with different lag lengths and record the resultant adjusted R^2 ($\bar{R}^2$) value and the direction of the coefficient (positive or negative) (2) selection of the final lag length (starting and ending lags) of each hydrological factor based on two criteria: (a) having the coefficient direction fitting the knowledge (the coefficient of WSCE% and rainfall should be positive, while the coefficient of evapotranspiration should be negative because more snowmelt and rainfall would increase the downstream water amount, while more evapotranspiration would reduce the water supply), (b) having the ascending value of $\bar{R}^2$ (till the highest value). The theory behind our two-step approach is that the use of the $\bar{R}^2$ value helps to identify the appropriate set of regressors which can explain the variation of the dependent variable well and only selecting the lags having ascending $\bar{R}^2$ values avoids selecting an unnecessarily long lag length.

Based on the above mention techniques, the overall workflow of our study is illustrated in Figure 5.2.

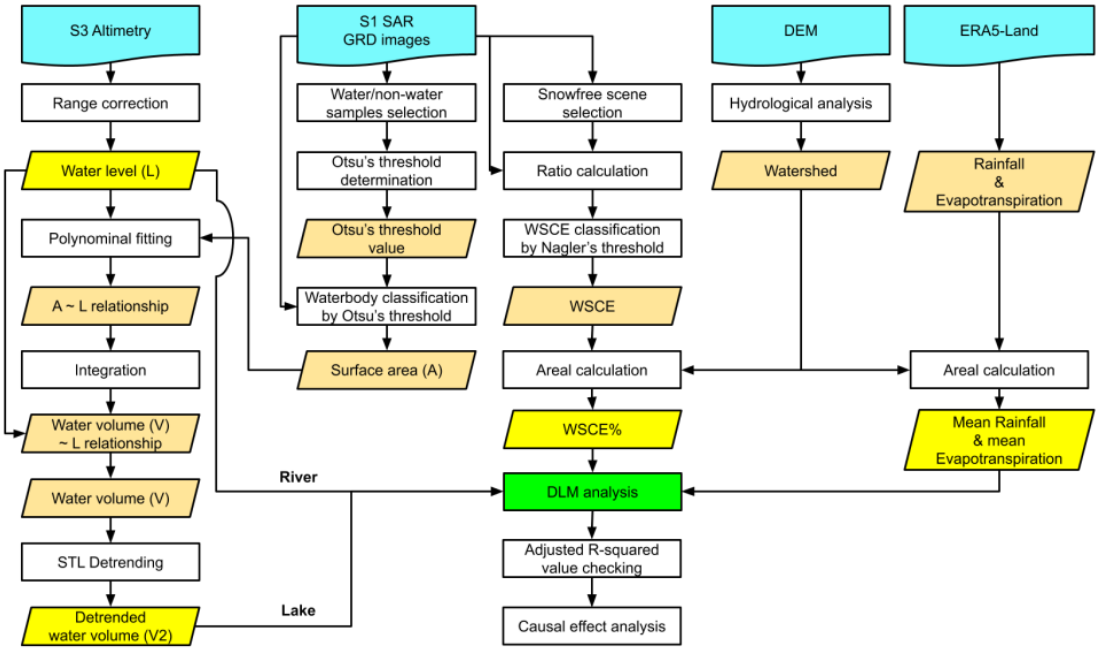

Figure 5.2 The overall workflow of the present study, including the processing of the Sentinel-1 synthetic aperture radar (SAR) and Sentinel-3 altimetry data for deriving wet snow-covered extent (WSCE), surface area, and water level. The water volume estimated from polynomial fitting and integration is detrended by the Seasonal-trend decomposition procedures based on Loess (STL). Together with the hydrological factors derived from the ERA5-Land dataset, the distributed lag model (DLM) is eventually conducted.

5.4. Results

5.4.1 Lake Urmia

5.4.1.1 Water level retrieval

Two passes of Sentinel-3 over Lake Urmia are processed via SARvatore to estimate the time-series average water level of VSs. To examine the results, the water level records provided by altimetry databases are plotted together in Figure 5.3, with the error bar representing the standard deviation of the water level among the virtual stations (VSs). As our goal is to compare their long-term trends and short-term noisy levels, and because different altimeter sensors have different instrumental biases (Calmant et al., 2013), in this figure we show the water level variation relative to each record's mean water level during our sensing period. Firstly, we can observe that there is a high consistency between the two passes' results (the locations of two passes are illustrated in Figure 5.1). Most of the time, the differences of their values are within one standard deviation. It is reasonable that two passes' results still have some differences owing to the reasons including (1) different wind-caused lake

surface wave conditions as their sensing time is not identical, (2) varying water depth on the altimetry signal penetration depth, and (3) and the different surrounding topography-caused signal pollution condition. Nevertheless, the internal consistency of each pass and their cross-consistency remain high when comparing to DAHITI and G-REALM's records. In Figure 5.3, it is evident that both of our two passes' raw results have a much smoother trend comparing to the smoothed DAHITI result (no raw data is provided by DAHITI database thus no uncertainty is plotted) and the raw G-REALM results, as these databases' results show more short-term high-frequency fluctuations. The reason is that the along-track resolution of the HPR Sentinel-3 (80 meters) we employed is much higher than the Jason-3 altimetry sensor (> 2000 meters), which is used for DAHITI and G-REALM. Hence, based on these comparisons, it is confirmed that our Sentinel-3 results generally have a higher reliability. To fuse two passes' observations for the following analysis, we utilize the weighted average calculation and then use the Gaussian smooth method to filter out the noises.

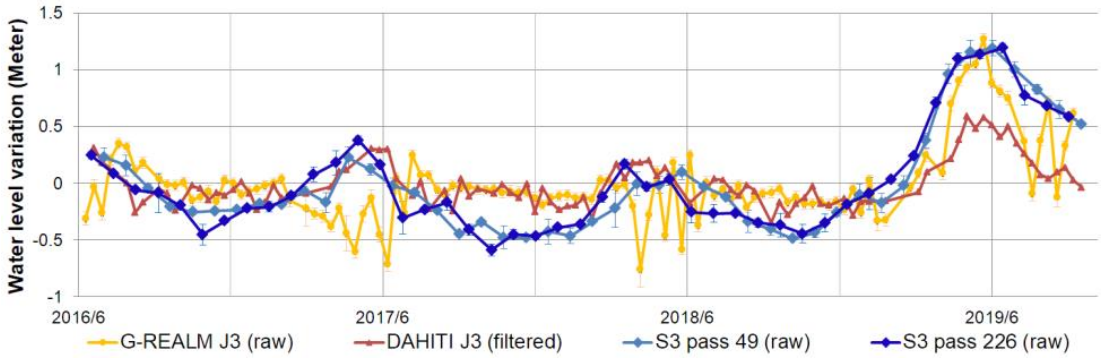

Figure 5.3 The time-series water level variation of Lake Urmia estimated with Sentinel-3. The internal cross-comparison with different Sentinel-3 passes and the external comparison with altimetry databases, including DAHITI and Hydroweb (based on Jason-3 altimetry), are illustrated. The error bars represent the standard deviation of the water level among the VSs. Note each of the variations is relative to each record's average height in the studying period.

5.4.1.2 Surface area estimation

To define the optimized Otsu's threshold value for mapping the surface area of Lake Urmia, we manually select water/non-water samples on each VV polarization scene, which shows a clear waterbody boundary. With the aim to densify the usable scenes, both ascending and descending Sentinel-1 image sets are used and processed individually. Their overall backscatter coefficient distributions and the resultant Otsu's threshold values are shown in Figure 5.4. Firstly, we can observe that both flight

direction image sets' samples intensity distributions are bimodal, which confirms the suitability of the Otsu's method. Secondly, it is found that both sets have nearly the same threshold values; therefore, we average two values to select a fixed value, i.e., -20.8 dB, to be the waterbody classification threshold for Lake Urmia.

Flight direction	Ascending	Descending
Otsu's threshold value (dB)	-20.678	-20.962
Distribution of backscatter coefficient	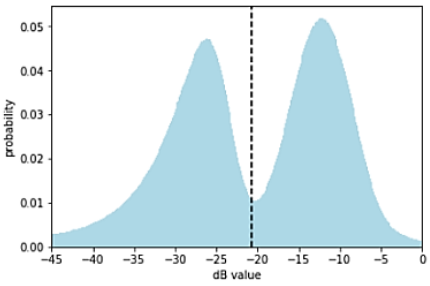	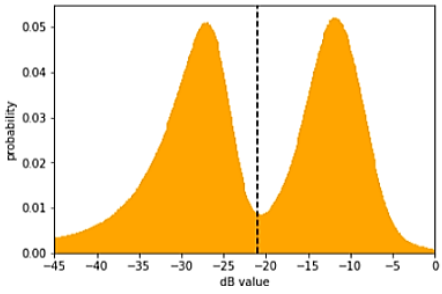

Figure 5.4 The distributions of the backscatter coefficient and the decided Otsu's threshold values of the ascending and descending of Sentinel-1 SAR imagery for Lake Urmia waterbody classification.

Based on the defined threshold value, we can classify the water-covered area of Lake Urmia, i.e., surface area, from both stacks of ascending and descending Sentinel-1 images. For cross- and external comparison, we plot the same date's surface areas estimated with ascending/descending Sentinel-1 image and the GWP product in Figure 5.5. It is evident that both of our ascending and descending results match perfectly with GWP with an R-squared value of around 0.98. These high values prove that the surface area classified with our SAR-Otsu's approach is highly reliable. Additionally, it is also interesting to realize that there is a systematic offset between our SAR-based estimation and the GWP product which is based on coarse optical sensor. Based on further analysis, we can confirm that it is because of an under-estimation of the GWP product due to high reflectance of lake soil when water level is low (see the Discussion 5.1). Thus, the reliability of our SAR-Otsu's approach for accurately delineating the surface area of Lake Urmia is ensured. Furthermore, we can map Lake Urmia's time-series surface area dynamics, as illustrated in Figure 5.14 (for details refer to the Discussion 5.1). It is obvious that the change of the surface area of Lake Urmia is dramatic. In the sensing period, the minimum and maximum surface areas are around 1126.86 (2017/10/31) and 3569.77 (2019/7/11) km². The areal difference is significant, as the maximum size is almost equal to 3.2 times the minimum surface area.

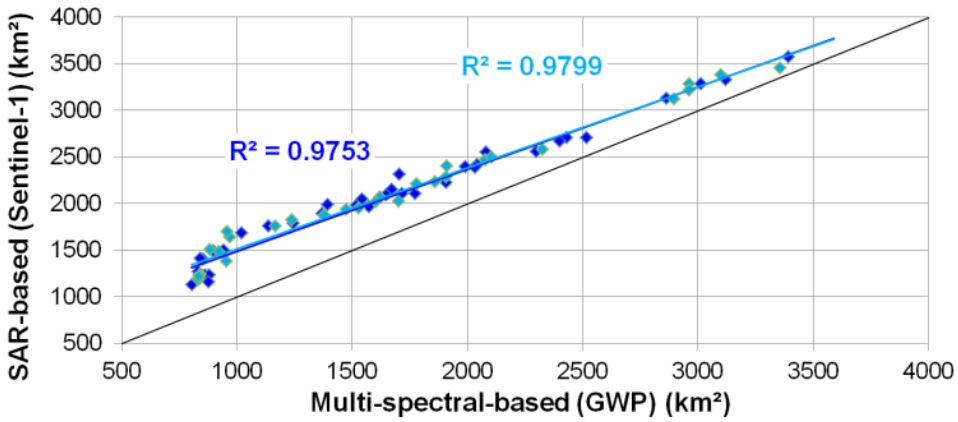

Figure 5.5 he internal cross-comparison of Lake Urmia's surface area detected by ascending and descending imagery of Sentinel-1, and the external comparison with the GWP product.

5.4.1.3 Hypsometry estimation and detrended volume retrieval

To derive the time-series water volume, the hypsometry estimated from the water level-surface area relationship is necessary. Hence, we first plot the time-series water level and surface area (derived from both ascending and descending Sentinel-1 SAR as well as the GWP) in Figure 5.6 third-order polynomial function is used for fitting as it provides the best R-squared value. Moreover, previous in-situ surveying (Alipour, 2006) and study (Sima and Tajrishy, 2013) also suggest the utilization of a third-order function for Lake Urmia's hypsometry. It is found that both of our Sentinel-1 SAR ascending (0.98) and descending (0.99) show a perfect R-squared value, while the GWP (0.94) shows a slightly poorer matching. These values suggest that both our Sentinel-3 altimetry-based water level and Sentinel-1 SAR-Otsu' approach-based surface area are reliable as they share a high consistency. The slightly lower R-square value of GWP also agrees with the previous finding of the under-estimation of GWP. Eventually, to densify the available observations, we integrate both ascending and descending SAR stacks-derived surface area to build a surface area-water level relationship, which can be written as:

$$\mathrm{A} = 1164.4 \times \mathrm{dL}^3 - 3459.1 \times \mathrm{dL}^2 + 4267.1 \times \mathrm{dL} + 1102.5 \qquad (5.3)$$

where A and dL represents the surface area and water level difference, respectively. It yields a high fitting R-squared value around 0.99.

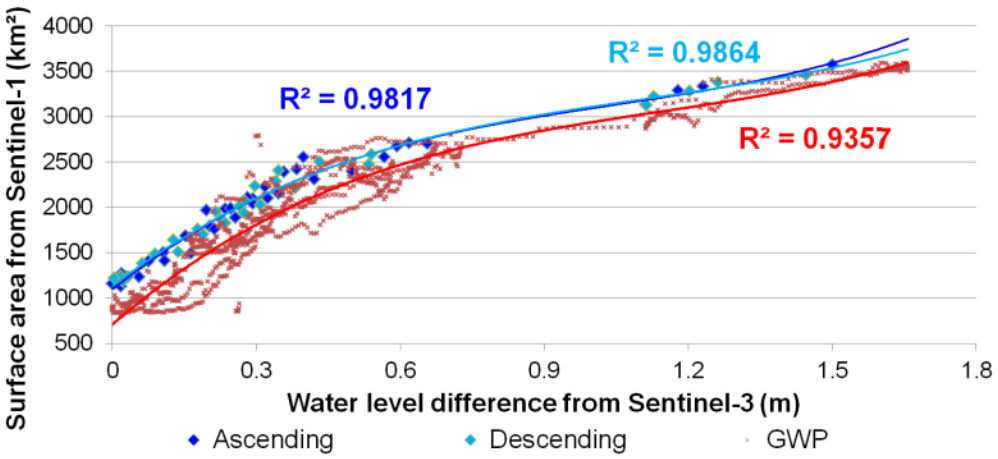

Figure 5.6 The hypsometry of Lake Urmia estimated by fitting the surface area detected by ascending and descending Sentinel-1 SAR imagery and GWP product with water level estimated by Sentinel-3 altimetry using third-order polynomial functions.

Based on the fact that the dynamic water volume should be equal to zero when the water depth (water level difference relative to the lowest water level during the sensing period) is zero, we can derive the fourth-order water volume-water level function by integrating the surface area-water level formula. Thus, Lake Urmia's water volume-water level function can be written as:

$$V = 291.10 \times dL^4 - 1153.03 \times dL^3 + 2133.55 \times dL^2 + 1102.50 \times dL \quad (5.4)$$

where V represents the dynamic water volume. Based on this equation, the time-series water volume of Lake Urmia can be derived. Nevertheless, to mitigate the bias of the container effect of the lake for the following analysis as described in the Section 3.3, the STL is then applied to estimate the detrended water volume as plotted in Figure 5.7. It is clear to observe that the trend of water volume is almost stable in the first two years, while a peak can be identified in 2019. By subtracting the trend from the estimated water volume, we can obtain the detrended water volume, which represents the real inter-annual water volume variation.

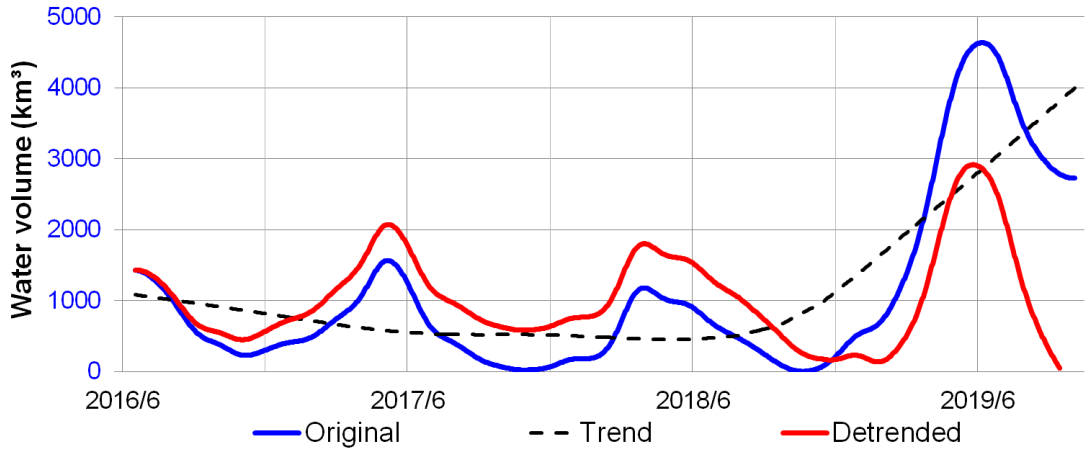

Figure 5.7 The detrended processing for Lake Urmia's time-series water volume estimation using the Seasonal-trend decomposition procedures based on Loess (STL). The estimated trend value and the original/detrended water volume are illustrated with the black, blue, and red line, respectively.

5.4.1.4 WSCE mapping and hydrological factors calculation

Both ascending and descending stacks of images of Sentinel-1 SAR are used to map the WSCE. The summertime imagery of 2018 is selected as the referenced snow-free image for calculating the ratio image. By applying the threshold value proposed by Nagler and Rott (Nagler and Rott, 2000; Tsai Ya-Lun S. et al., 2019), the time-series WSCE of each flight direction image stacks can be estimated. To examine their consistency, we plot their time-series WSCE% relative to Lake Urmia's watershed in Figure 5.8. It is found that both flight directions' results show a high agreement, which proves the internal robustness of our approach. As there is no solid way to externally validate WSCE in a comparable high-resolution (Tsai Ya-Lun S, Dietz Andreas, et al., 2019b; Tsai Ya-Lun S. et al., 2019), this cross-track comparison is used for the examination.

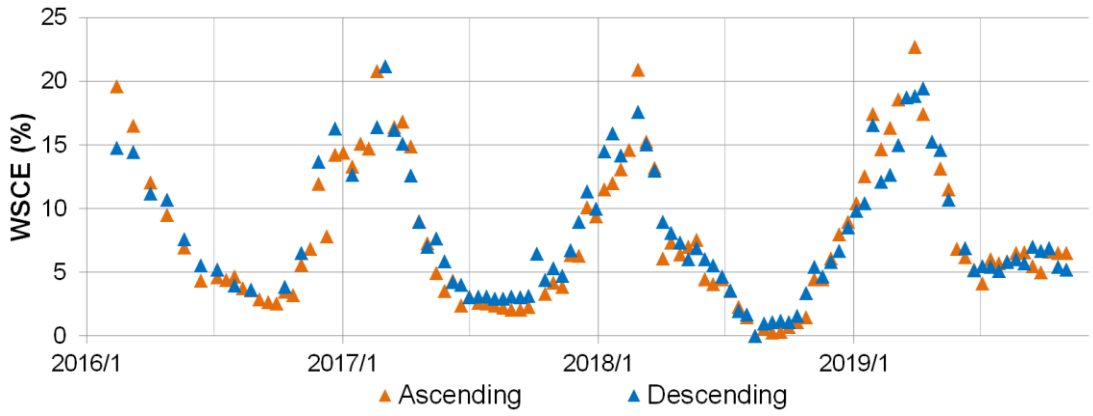

Figure 5.8 The estimation of wet snow-covered extent (WSCE) percentage of Lake Urmia watershed using ascending and descending Sentinel-1 SAR imagery.

Based on the previous data preparation, before processing the DLM analysis, we need to convert all hydrological factors to the watershed-based unit, i.e., to derive the mean evapotranspiration/rainfall and WSCE%. Together with the estimated detrended water volume, we illustrate all time-series data in Figure 5.9 to observe their relationships. Firstly, it is found that excluding rainfall shows two peaks each year; other data, including WSCE%, evapotranspiration, and detrended water volume, have only one peak annually. Also, the pattern of the evapotranspiration is nearly identical each year. Thus, we can assume that the variation of water resources of Lake Urmia cannot be perfectly explained by rainfall and evapotranspiration data only. Secondly, by comparing the time of the peak of each data, it is found that in the temporal aspect, the water volume always reaches each year's maximum value later than WSCE%. To quantify these factors' lagged and overlapping influences on the water volume variation, a hydrological analysis based on DLM is required.

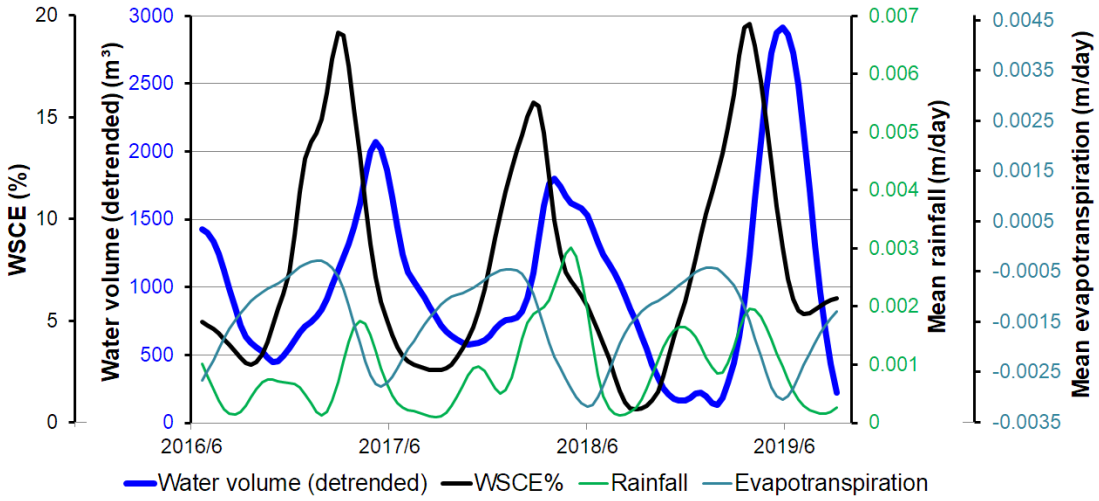

Figure 5.9 The time-series detrended water volume of Lake Urmia and the WSCE% as well as hydrological factors, including liquid rainfall and evapotranspiration.

5.4.1.5 DLM hydrological analysis

To process the DLM for quantifying the causal effects of hydrological factors on the detrended water volume variation, it is necessary to decide the proper lag length for each factor. Based on the steps and criteria mention in the Section 3.5, we summarize the determined lag length in Table 5.1. Firstly, it is found that WSCE% has the longest lag length of 80 days, rainfall has 30 days delay, and evapotranspiration shows no delay longer than ten days. As the directions of the coefficient of WSCE%, rainfall,

and evapotranspiration are always positive, positive, and negative in different lag lengths testing, respectively, we select the lag starting from zero-day for all factors. Also, we can observe that WSCE% has the highest $\bar{R}^2$ of 0.85, followed by 0.23 and 0.61 for rainfall and evapotranspiration, respectively. The high/low $\bar{R}^2$ values of WSCE%/rainfall indicate that their influential magnitudes on water volume differ considerably.

Based on the decided lag lengths, the DLM can thus be processed. The results are summarized in Table 5.1. A significant regression equation is found ($\mathrm{F}(14, 81) = 70.78, \mathrm{p} < 2.2\mathrm{e}^{-16}$) with a $\bar{R}^2$ of 0.91. The high $\bar{R}^2$ indicate that our model contains a clear explanation of the variation of the water volume. The overall F-test value of 70.78 proves that our hydrological factors with different lag lengths can reliably predict the water volume. Eventually, based on the LRP of WSCE% estimated from DLM, we can conclude the causal effect of snowmelt on water resource as: when increasing one percent of WSCE% during the period of zero to 80 days before, the detrended water volume of Lake Urmia would increase 108.5 cubic meters while holding constant other independent variables.

Table 5.1 The summaries of distributed lag model (DLM) analysis of Lake Urmia and the Brahmaputra River.

Study area	**Lake Urmia**		**Brahmaputra River**
Dependent variable	Water volume (original)	Water volume (detrended)	Water level
PRE-ANALYSIS (LAG LENGTH DECISION)			
Highest adjusted $\boldsymbol{R^2}$ (individual)			
WSCE%	0.64	0.85	0.91
Mean rainfall	0.25	0.23	0.94
Mean evapotranspiration	0.22	0.61	0.90
Lag length (days)			
WSCE%	0 ~ 60	0 ~ 80	70 ~ 150
Mean rainfall	0 ~ 20	0 ~ 30	0 ~ 20
Mean evapotranspiration	0	0	0 ~ 10
DISTRIBUTED LAG MODEL (DLM) REGRESSION ANALYSIS			
Model adjusted $\boldsymbol{R^2}$ (overall)	0.67	0.91	0.97
Long-run propensity (LRP)			

WSCE%	135.68	108.49	0.10
Mean rainfall	60695.88	-88737.6	149.186
Mean evapotranspiration	-76581.40	-120327.76	-446.02

5.4.2 Brahmaputra River

5.4.2.1 Water level retrieval

The same Sentinel-3 altimetry data processing approach is employed to estimate the time-series water level of the Brahmaputra River. Because the Brahmaputra River is a long river spreading across various geomorphologies, and the satellite pass ground track location of each spaceborne altimetry differs, there is no direct way to validate our result as the water level differs in different river sections. Nevertheless, we consider the water level of each location of the same river should share a similar pattern, with a higher correlation in shorter distance difference. Thus, in total, three VSs are utilized for comparison, including another Sentinel-3 pass (pass 161, processed by the same approach) and two Jason-3 passes (data provided by DAHITI and Hydroweb individually). Their locations and the time-series water level results are illustrated in Figure 5.1 and 5.10, respectively. Firstly, it is clear that four time-series data have highly similar trends and seasonality. Nevertheless, the magnitude of the water level variation of each location shows an ascending order from the upstream to downstream, i.e., around 3 (DAHITI), 4 (Sentinel-3 pass 161's results), 7 (Sentinel-3 pass 324's result), and 8 (Hydroweb) meters, respectively. The reason for the more significant water level change in the downstream may be due to the flatter terrain when compared to the upstream. In addition, as we observed in the Lake Urmia case, the DAHITI and Hydroweb databases contain more noises than our HPR Sentinel-3 results while the comparable patterns remain.

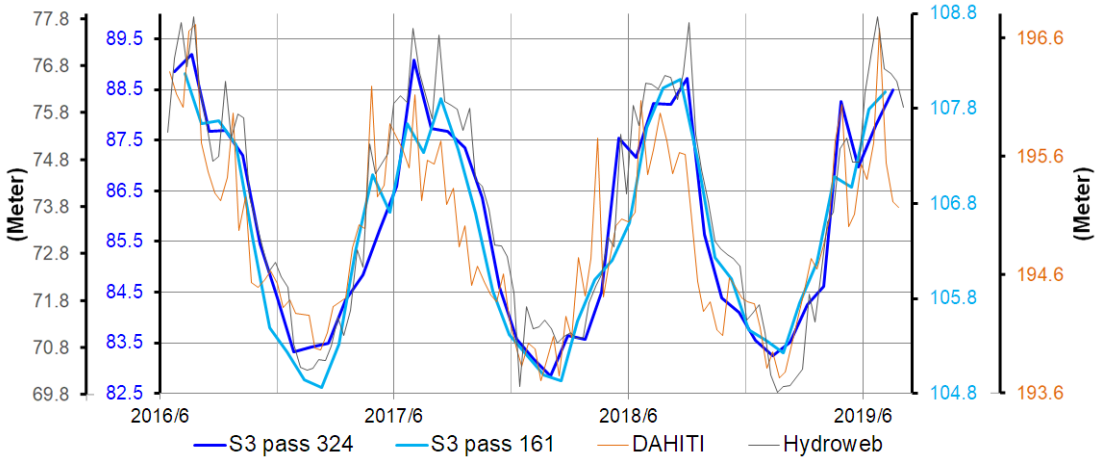

Figure 5.10 The time-series water level of the Brahmaputra River estimated with

Sentinel-3. The internal cross-comparison with different Sentinel-3 passes and the external comparison with altimetry databases are illustrated. Note the VS of each record is different, so the magnitude of water level variation differ, while the similar trends are still identifiable.

5.4.2.2 WSCE mapping and hydrological factors calculation

Both Sentinel-1 ascending and descending image stacks are used to calculate the WSCE of the Brahmaputra River. The summertime image of 2018 is selected as the referenced snow-free image.

To investigate the internal consistency, the WSCE% derived from each stack is plotted in Figure 5.11. Similar to Lake Urmia's case, a high agreement between both flight directions is observed. It suggests that the quality of our WSCE results should be trustable.

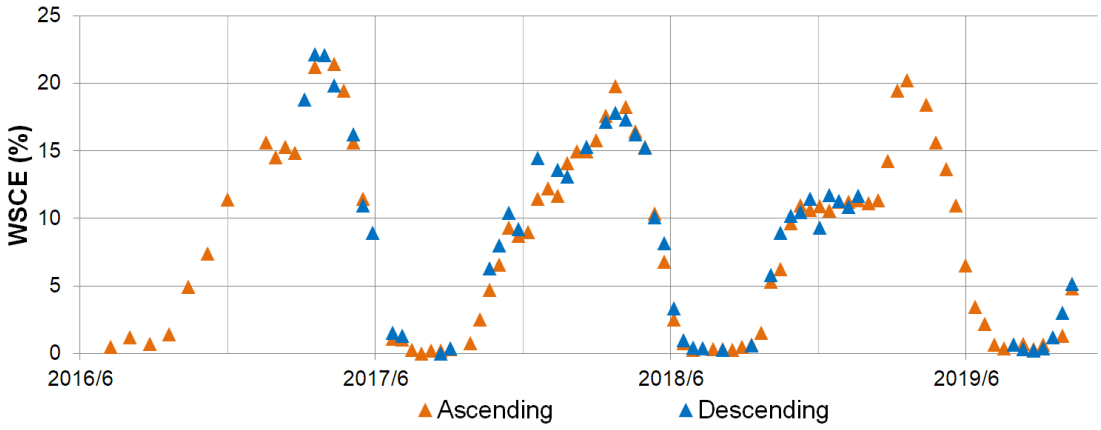

Figure 5.11 The estimation of wet snow-covered extent (WSCE) percentage of the Brahmaputra River watershed using ascending and descending Sentinel-1 SAR imagery.

We also analyze the relationship between hydrological factors and water level before the DLM processing. Their patterns during the sensing period are illustrated in Figure 5.12. Compared with the Lake Urmia case, the Brahmaputra River shows some remarkable differences. Firstly, it is observed that all four parameters have only one peak per year. Secondly, the temporal delay between the peak of water level and WSCE% is longer than the time delay of water level and rainfall. Based on these two findings, we can assume the importance of rainfall to water amount variation is higher in the Brahmaputra River than Lake Urmia. Nevertheless, since all hydrological factors and water levels show comparable seasonal patterns, the employment of DLM is indispensable to analyze their lagged causal effects on the water level.

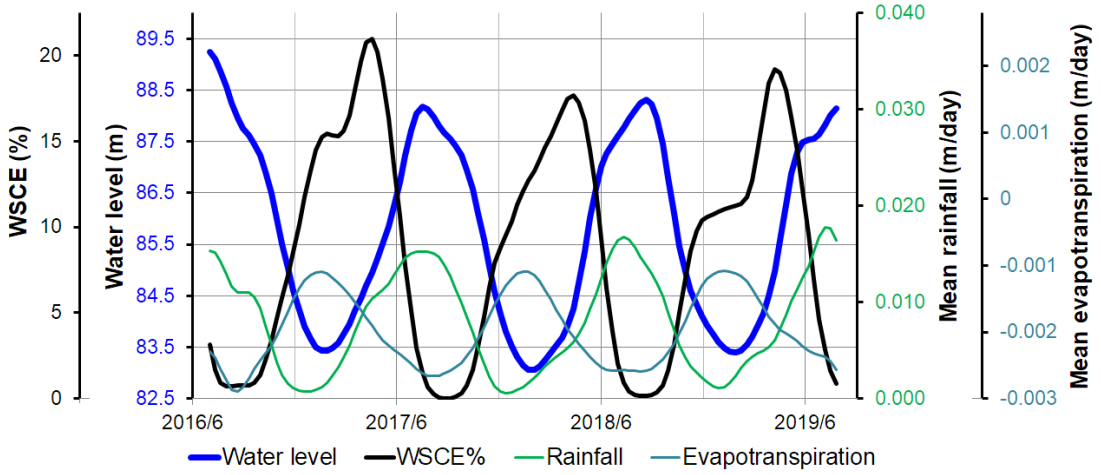

Figure 5.12 The time-series water level of the Brahmaputra River and the WSCE% as well as hydrological factors, including liquid rainfall and evapotranspiration.

5.4.2.3 DLM hydrological analysis

To decide the suitable lag length for each hydrological factor, we build regressions with each factor individually, and the resultant lag length is summarized in Table 1. Firstly, like Lake Urmia, WSCE% has the longest lag length, and evapotranspiration has the shortest lag length. However, it is found that the lag length of WSCE% is nearly two times longer than for Lake Urmia. Another critical difference is the starting lag length of WSCE% is not zero days. It is because in the periods of lag length between zero to 60 days, the direction of the WSCE%'s coefficient is negative, which violates the background knowledge. Thus, we only select the lag length from 70 to 150 days (based on the criteria described in the Methodology 3.5). Therefore, using the prior knowledge to aid the decision of lag length is critical. Secondly, when comparing the $\bar{R}^2$ values, all three hydrological factors show comparable results, i.e., higher than 0.90.

The DLM can then be processed based on the decided lag lengths of each factor; the results are summarized in Table 1. A significant regression equation is found ($\mathrm{F}(14, 73) = 198.7, \mathrm{p} < 2.2\mathrm{e}^{-16}$) with a $\bar{R}^2$ of 0.97. The high $\bar{R}^2$ indicates the variation of the water level can be perfectly explained by our model, and the F-test value of 198.7 suggests hydrological factors with different lag lengths can reliably predict the water level. Based on these examinations, we can conclude our DLM is robust. Hence, on the basis of the estimated LRP of WSCE%, the causal effect of snowmelt to water resource can be concluded as: when increasing one percent of WSCE% during the period of 70 to 150 days before, the water level of our VS of the Brahmaputra River would increase 0.1 meter while holding constant other

independent variables.

5.4.2.4 Flooded area estimation

The SAR-Otsu's approach is also utilized in the Brahmaputra River to delineate the flooding area (or the change of river channels). Both ascending and descending image stacks of Sentinel-1 are processed individually, with their backscatter coefficient distributions and the resultant Otsu's threshold values shown in Figure 5.13. Like in Lake Urmia's case, we can find comparable Otsu's threshold values. Hence, we average two values to select -16.5 dB as the fixed threshold for the waterbody classification.

Flight direction	Ascending	Descending
Otsu's threshold value (dB)	-16.375	-16.389
Distribution of backscatter coefficient	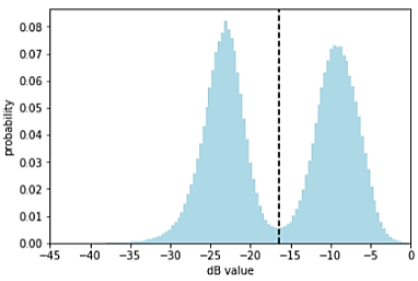	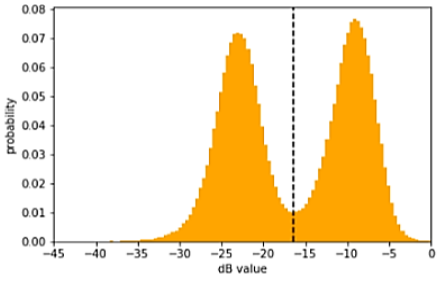

Figure 5.13 The distributions of the backscatter coefficient and the decided Otsu's threshold values of the ascending and descending of Sentinel-1 SAR imagery for mapping the flooded area of the Brahmaputra River.

For Lake Urmia we combined surface area with the water level to derive the hypsometry; on the contrary, for the Brahmaputra River, we can use the water level as the external data to examine our mapped flooded area. It is based on the fact that when the flooded area is enlarging, the water level will rise simultaneously. Thus, we plotted the time-series flooded area, water level, and WSCE% in Figure 5.14. Firstly, it is found that generally, the trends of flooded area derived from both ascending and descending Sentinel-1 SAR imagery stacks are agreeable, although internal noises and the difference between them are also clear. Moreover, their noisy levels are higher when comparing to the same descending/ascending stack-based WSCE% as illustrated in Figure 5.11. We consider it is because (1) the short-term variation of the flooded area is more abrupt and dynamic compared to the long-term gradient snowmelt process (2) the WSCE% mapping is by thresholding the ratio image relative to a referenced image (as described in the Methodology 3.4); while the flooded area is

mapped by direct applying the Otsu's threshold to each imagery, so the influence of the local incidence angle variation of each image is severer. Hence, to reduce the fluctuations, we average ascending and descending stack's results to derive a smoother trend. Secondly, by comparing the average flooded area with the water level, we can observe a temporally highly correlated pattern. It agrees with our prior knowledge and also indirectly proves the credibility of our Sentinel-1 SAR-based flooded area estimations as well as Sentinel-3 altimetry-based water level records. Finally, the synchronized flooded area and water level trend is temporally lagged when compared to the WSCE% trend. Around 110 days of the temporal gap between the peak of WSCE% and water level/flooded area are noted, which falls within the estimated lag length of WSCE% (70 to 150 days) for DLM analysis (Table 1). This agreement also strongly proves the reliability of our DLM lag length decision.

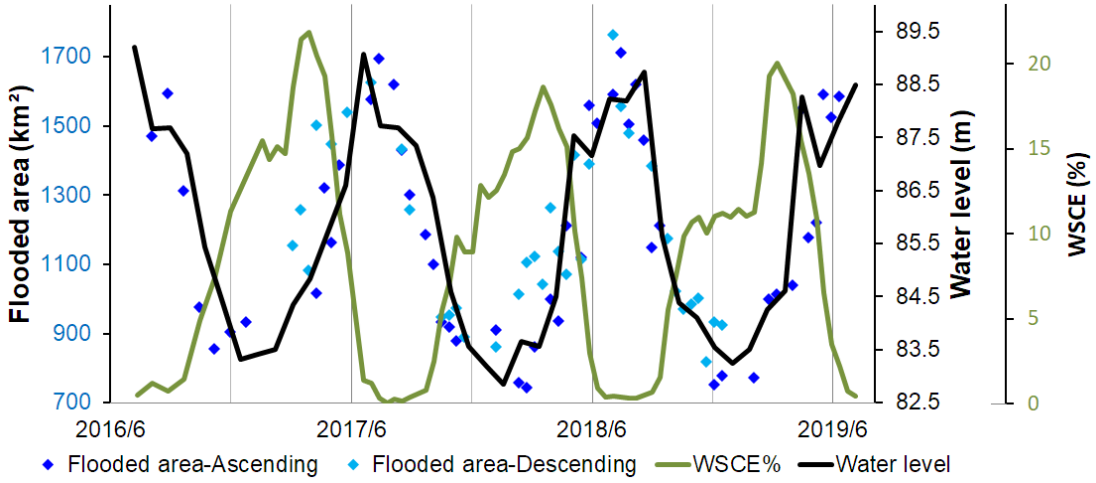

Figure 5.14 The internal cross-comparison of the Brahmaputra River's flooded area detected by ascending and descending imagery of Sentinel-1 and the comparisons with the time-series water level estimated by Sentinel-3 altimetry and the Sentinel-1 SAR-based WSCE%.

Based on the externally examined flooded area, the time-series flooding dynamics of the Brahmaputra River can be depicted. For instance, we illustrate the maximum (2019/8/9) and minimum (2018/12/12) flooded area of the middle and lower section of our study area in Figure 5.15. It is obvious that their flooded areas (river channels) significantly differ as in the dry season, the river shrinks back to the center of the wide channels mapped during the wet season. This example suggests that by using SAR-Otsu's approach, it is viable to monitor the dynamics of river channel migrations and seasonality.

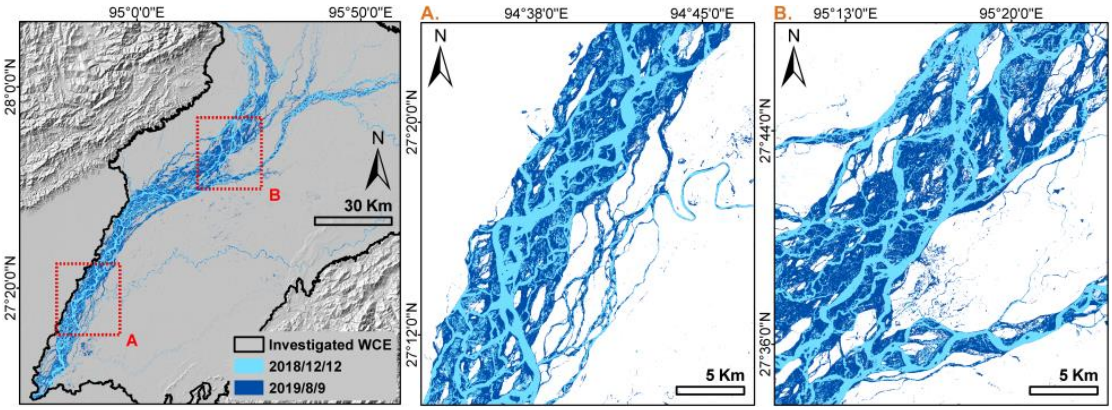

Figure 5.15 The maximum (2019/8/9) and minimum (2018/12/12) flooded area of the Brahmaputra River during the sensing period detected by the Sentinel-1 SAR imagery using the decided Otsu's threshold value.

5.5. Discussions

5.5.1 The cause of the different lake surface areas detected by Sentinel-1 SAR and GWP product

To compare the surface area mapped by SAR (Sentinel-1) and the GWP, we plot their estimations for the same dates in Figure 5.5 and 5.16. It can be observed that GWP systematically underestimates the surface area compared to SAR derived estimations. To examine that this effect is not caused by the overestimation of our SAR-based results, we plot the same date's high-resolution Sentinel-2 imagery in Figure 5.16 for comparison. It must be noted that due to the reasons that (1), there is no absolute definition of the lake boundary as stated in (Crétaux et al., 2016), (2) the calibration procedures of optical-imagery would also affect the waterbody delineation, and (3) our intention is to not include another threshold-based classification approach (such as NDWI) as it would cause another uncertainty, we compare them visually. It is clear that our SAR-based surface area agrees well with the blueish waterbody boundary observed in the Sentinel-2 scene. On the contrary, the GWP underestimates the surface area. Especially on 2017/10/31, the upper and lower parts of the lake obviously remain connected in the Sentinel-2 image, which is also delineated correctly in our Sentinel-1-based results. Nevertheless, GWP suggests the lake is separated into two parts. This underestimation-caused separation frequently happens in the dry season (as marked in Figure 5.16(b)). The reason for this underestimation is due to high reflectance signal in MODIS NIR and red bands when water is very shallow. During low water level period Lake Urmia's bright lake soil with high salt content dominates the spectral reflectance sensed by optical MODIS sensor. Therefore these shallow waters remain undetected which results in systematic bias

during low water levels because the GWP is based on a universal approach operating on global scale and cannot fit all waterbodies perfectly. On the contrary, as mentioned in the Methodology, we manually select water/non-water samples to decide the customized Otsu's threshold value for Lake Urmia.

Another finding is that the SAR-based approach can only be implemented during the lake water depletion period, i.e., dry season. As shown in Figure 5.16(b), we found that all valid SAR-based surface area estimations occur between May and October. To investigate the reasons, firstly we plot the rainfall records provided by the ERA5-Land dataset. It is found that the water depletion period is highly correlated but slightly delayed to the rainfall decreasing period. Hence, we assume the reason why the SAR imagery cannot map the lake boundary properly in the lake water accumulation period, i.e. rainfall-dominated wet season, is that series of rainfall events would cause the surrounding regions of the lake to have a wet surface due to (1) sudden flooding events of the lake and/or (2) direct ground dampening caused by the rainfall. As we classify the waterbody based on the backscatter coefficient of the SAR signal, which is mainly influenced by the surface roughness and wetness, we can hardly distinguish whether the water is in the lake or on the surface of the surrounding damped/flooded areas. Thus, in the lake water accumulation period, i.e. wet season, the SAR-based observations would dramatically over-estimate the surface area. For instance, given the example of 2019/4/7 shown in Figure 5.16(a), in the Sentinel-2 scene it is found that the surrounding area of the lake is much wetter (more blueish) and shows more small flood-caused tributaries and braids comparing to other three dates of dry season. On the contrary, the GWP estimations during wet season reveal the increasing surface water area more accurate and do not overestimate due to wet soil.

Based on the above mentioned discussions, we summarized the pros and cons of using SAR and multispectral sensors for waterbody mapping in Table 5.2.

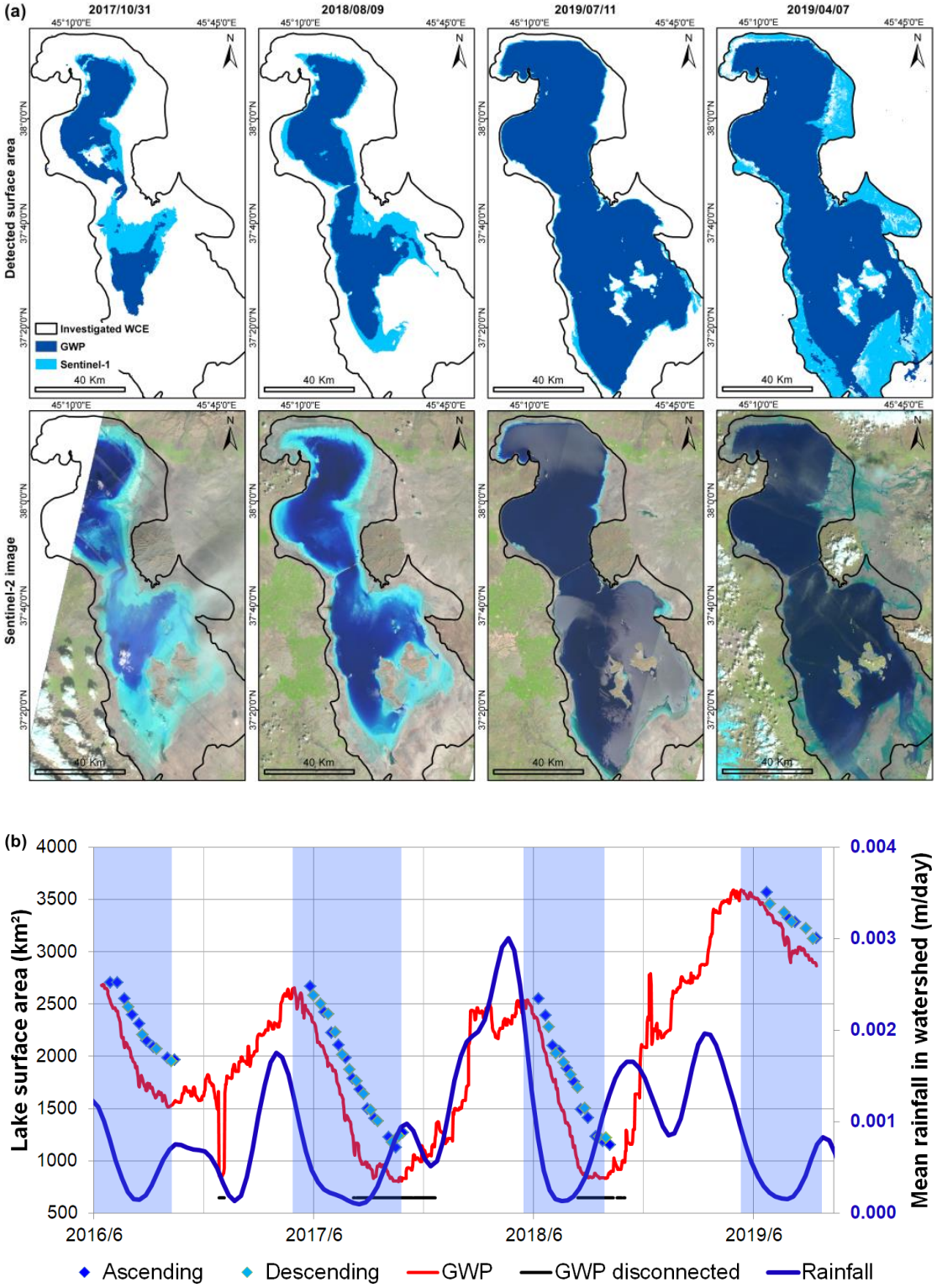

Figure 5.16 (a) The comparison of the surface area of Lake Urmia detected by Sentinel-1 SAR imagery and the GWP product, and the same date high-resolution Sentinel-2 imagery. The mean rainfall volume is plotted in (b) to identify the dry season, with the lake water depletion periods marked in blue boxes. The date which shows lake disconnection in GWP is marked with black points in (b).

The date which shows lake disconnection in GWP is marked with black points in (b).

Table 5.2 The comparison of the advantages and disadvantages of using SAR and the multi-spectral sensor for waterbody detection.

Sensor	**SAR**	**Multi-spectral**
Classification basis	Backscatter coefficient	Illumination reflectance
Primary sensing factor	Surface roughness Surface dielectric property	Bands' reflectance differences Imagery calibration
Possible noise source	Winds, flooding, soil moisture, vegetation, ice and snow cover	Cloud, mist, floating vegetation, turbidity, highly eutrophicated waters, high sediment load, ice and snow cover
Advantage	All-weather and illumination-independent sensing ability Cloud penetration	Straightforward to interpret The abundance of openly accessible sensors and images, less sensitive to soil moisture and usable during wet season
Disadvantage	Affected by wind, flooding, soil moisture	Affected by cloud and illumination conditions

5.5.2 The necessity of detrending process for lake water volume before hydrological analysis

In the present study, we employed the STL seasonal decomposition technique for detrending, i.e., removing the annual aggregation effect. The necessity of detrending can be proven by the much higher $\bar{R}^2$ value of detrended water volume (0.91) when compared to the original data (0.67), as summarized in Table 5.1. The significant enhancement of the water volume variation explanation agrees with our hypothesis: the "container effect" of lake, i.e., the intra-annual trend of water volume, would hinder the accuracy of DLM analysis between water volume and hydrological factors.

5.5.3 The lag length difference between each hydrological variable and study area

As mentioned in the Methodology section 3.5, based on the $\bar{R}^2$ value, we can decide the suitable lag length of each hydrological factor for lake and river DLM analysis. The final lag lengths of each case are summarized in Table 5.1. It is found that for both cases, the lag length of WSCE% is always the longest among three factors, and evapotranspiration has the shortest (nearly instant). This finding agrees with the prior knowledge that the snowmelt water takes a much longer time to aggregate and

eventually influence the downstream waterbody because snow-covered regions are usually locate at much higher elevation zones, which have longer distances to the downstream waterbody. Moreover, snowmelt water would not only form a direct surface streamflow but also infiltrate into the ground and soil (Seyfried et al., 2009; Butt and Bilal, 2011; Abudu et al., 2012). In contrast, although rainfall would also infiltrate to the ground, its distribution is usually broader but not limited in the high elevation zone. It might also spread over the whole watershed of the waterbody, including the waterbody itself. Hence, the lag length of rainfall is much shorter than the snowmelt. For evapotranspiration, it is straightforward that its influence is rapid, as it would immediately reduce the amount of water of the waterbody.

Additionally, it is also found that the lag length of WSCE% of the Brahmaputra River is nearly two-fold of Lake Urmia. We assume this is due to the Brahmaputra River being characterized by a much narrower and longer watershed along the tributary when compared to Lake Urmia. Consequently, the distance between the snow-covered area and the waterbody/VS is much more distant, and thus the lagged effect of the snowmelt is more significant.

5.5.4 The cause of the long lag length of the SAR sensor-based WSCE%

Another reason for the long lag length of SAR sensor-based WSCE% is because of the unique way that SAR detects snowmelt processing shows temporal offset to the real condition. Based on the in-situ measurement and modeling simulation (Marin et al., 2019), it is known that the whole snow melting process can be divided into three phases, i.e., moistening, ripening, and runoff. In each phase, the content of snow water equivalent (SWE) (the total mass of water, including both liquid and solid water, stored in the form of snow) and the liquid water content (LWC) (the mass of liquid water inside the snowpack) differ, and the backscatter coefficient of SAR also changes accordingly and results in a U-shape curve (Figure 5.17). In detail, firstly in the moistening stage, the diurnal melting-freezing cycles gradually increases the LWC and leads to the gentle decreasing of the backscatter coefficient; in the ripening stage, the LWC significantly increases (while SWE still remains the same) and the backscatter coefficient rapidly decreases and reaches the minimum value at the end of ripening stage when the snowpack is saturated; and finally during the runoff stage, as the snowmelt water releases both LWC and SWE decrease and the backscatter coefficient increases accordingly (Marin et al., 2019).

It must be noted that as the backscatter coefficient of SAR would already slightly drop in the mid of the first moistening stage, the snow would already be detected and regarded as wet snow by the backscattering ratio-threshold method (Nagler and Rott,

2000; Marin et al., 2019; Tsai Ya-Lun S. et al., 2019). However, the snowmelt water is actually released only until the final runoff stage starts. Namely, the SAR-detected wet snow-covered period would (1) happen much earlier and (2) last much longer than the real snowmelt water-releasing period, as illustrated in Figure 5.17. As a result, the lag length of WSCE% would be longer than expected as it acts more like a leading indicator of the real snowmelt water generation time.

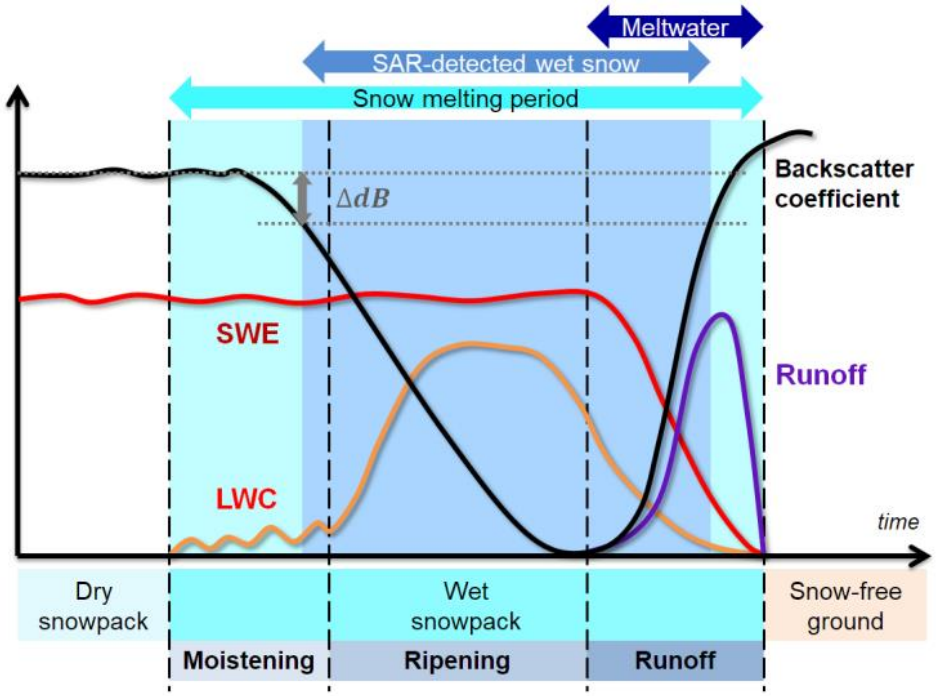

Figure 5.17 The relationship of SAR-based wet snow detection and the snowmelt processing (modified from (Marin et al., 2019)). The amount of liquid water content (LWC), snow water equivalent (SWE), and the released snowmelt runoff together with the SAR signal backscatter coefficient in different snowmelt phases are illustrated.

5.5.5 The reason of the negative LRP of rainfall in DLM of the detrended lake water volume

In sections 4.1.5 and 4.2.3, we only analyze the LRP of the WSCE%, due to the fact that we focus on depicting the casual effect of increasing WSCE on the water resource. On the contrary, the other two hydrological factors (mean rainfall and evapotranspiration) are the control variables that are not the investigated targets but help mitigating the omitted variable bias (Stock and Watson, 2015) to ensure the robustness of the DLM analysis. Including control variables is indispensable as there might have correlations between independent variables, which would mislead the estimated lag coefficient and the interested LRP.

Nevertheless, we can still analyze the coefficient of the other two hydrological factors,

as shown in Table 5.1. For evapotranspiration, in both river and lake cases the coefficients are negative, which are reasonable as more evapotranspiration would reduce the water amount. On the contrary, the coefficient of rainfall should be positive, as more rainfall would cause more water volume. However, only the case of the Brahmaputra River shows a positive value. We conclude the main reason causing the negative coefficient value of rainfall for Lake Urmia case is the detrending processing. It reduces the importance of rainfall, which is already low comparing to the river's case. In detail, by comparing the rainfall's coefficient in the Lake Urmia case estimated with the original and detrended water volume, we can be observed that the value is positive in the former scenario but becomes negative in the latter one. However, it must be noted that in both scenarios, the coefficient of WSCE% and evapotranspiration remain positive and negative, respectively, which agrees with the prior knowledge. It is because the relationship (or importance) between rainfall and water volume is much weaker than WSCE% and evapotranspiration to water volume in the lake's case (as described in the Section 4.1.4). It can also be proven by the much lower maximum $\bar{R}^2$ value of rainfall (0.23) compared to the wet SCE% (0.85) and evapotranspiration (0.61) as shown in Table 5.1. Furthermore, by comparing with the Brahmaputra River case (0.94), the lake's rainfall-water volume relationship also shows a much weaker linkage.

5.5.6 Current limitations and future goals

In the present study, we propose a cloud-free and illumination-independent comprehensive inland water monitoring approach based on freely accessible and sustainable data/tool, which provides a new way to track the dynamics of continental water resources. The econometrics' DLM also enables the accurate analysis of the lagged causal effect of snowmelt condition on the water amount. Nevertheless, there are still some limitations in our present study. Hence, future improvements are required.

Firstly, as mentioned above, it is found that the high spatial resolution, cloud-free SAR backscatter-Otsu-based surface area detection method can only be implemented in the lake water depletion period, i.e., dry season, due to the sensitivity of SAR signal to surface wetness. On the contrary, the GWP provides continuous and daily observations in all seasons, as shown in Figure 5.16(b), although it has some disadvantages such as systematic under-estimation due to high spectral reflectance of lake's bottom when water is shallow (as shown in Figure 5.5 and 5.16) and coarse spatial resolution. Yet, in a future study we would integrate both multi-spectral and SAR-sensor-based surface area to achieve a robust, high temporal and spatial

resolution continuous surface area mapping strategy.

Secondly, in our study, we use the WSCE% for representing the snowmelt condition. Although it is efficient and straightforward to depict the whole snowmelt dynamics (Marin et al., 2019; Tsai Ya-Lun S. et al., 2019; Tsai Ya-Lun S, Dietz Andreas, et al., 2019b, 2019a), it cannot provide the information of how much snowmelt water is actually generated during the snowmelt period. Instead, the measurement of either SWE or LWC should be used. Unfortunately, although there are many studies aiming at quantifying the SWE or LWC with SAR data, yet so far, there is no reliable conclusion provided (Tsai Ya-Lun S. et al., 2019). In addition to the wetness of the snowpack, other factors such as soil moisture, surface roughness, snow grain size, snow density, and temperature would also affect the SAR signal. Consequently, the utilization of either inversion technique or empirical model is usually required (Tsai Ya-Lun S. et al., 2019). The employments of multispectral and passive sensors are the alternative; however, they would be affected by either cloud cover and polar darkness or poor spatial resolution, as mentioned in the Introduction. Hence, in the future study, we would explore the SAR-SWE relationship using the inversion technique and compare the result with the passive sensor-based SWE products provided by Copernicus Global Land Service (Takala et al., 2011) and GlobSnow (Takala et al., 2011).

In addition, in the current study, we assume the water balance of Lake Urmia can be explained by WSCE, rainfall, and evapotranspiration. Because the surface water inflow can be estimated by the lagged effects of the snowmelt and rainfall water; and as the Lake Urmia is an endorheic lake so there is no stream outflow. Nevertheless, the influence of groundwater seepage and leakage are not measured in the present study due to (1) the lack of piezometric records around the lake and (2) their influences on water balance are normally trivial (Lei et al., 2013). Thus, groundwater is commonly ignored in the lake water balance studies (G Kumambala and Ervine, 2010; Kummu et al., 2014). However, to enhance the completeness of monitoring water resource variation of Lake Urmia, the hydrological models such as MODular three-dimensional finite-difference ground-water flow model (MODFLOW) (Anderson et al., 2015) or a simple groundwater input-output model (Dinka et al., 2014) could be included in the future.

Another improvement that could be considered is using the modified DLM for hydrological regression analysis. In the present DLM applied in this study, the weight of each lag is set equally. On the contrary, the advanced constrained DLM uses a lag-based smooth function, such as linear declining lag weights or polynomial/spline

distributed lag models (Gasparrini et al., 2010). These constrains would allow a more accurate estimation of each lag weight of each independent variable, as the potential multi-collinearity between different lags of each independent variable might hinder the estimation of each lag coefficient in unconstrained DLM (although the LRP, the main investigated target in the current study, would remain reliable) (Wooldridge, 2000). Moreover, the autoregressive distributed lag model (ARDL) (Pesaran et al., 2001) should also be explored as the past value of the water amount might also influence the current water amount.

Finally, rain-on-snow (ROS) hydro-meteorological phenomena should be investigated for its influence on the snowmelt-led water resource variation. It is found that ROS events would weaken the snowpack structure and accelerate the melting of snowpack due to heat transfer, which leads to an earlier and shorter melting period and even causes floods (Merz and Blöschl, 2003; McCabe et al., 2007; Pradhanang et al., 2013). Moreover, in the long-run, it can also result in a thinner springtime snowpack with less LWC and SWE, and eventually reduces the water supply in the dry season (Cohen et al., 2015; Jeong et al., 2017). Practically, when ROS events take place, they might form an icy crust on the snowpack as the relatively warm precipitation would melt the surface of snowpack and seeps through the snow, which refreezes during the nighttime (Groisman et al., 2005). This icy crust would change the surface roughness and the dielectric property and may mislead the SAR-based WSCE mapping results. Hence, the relationship between WSCE, precipitation, and SAR backscatter coefficient should be examined.

5.6. Conclusions

The significance of inland water resources has been gradually emphasized; especially in times of global warming. Within all waterbody types, lake and river systems are critical not only for the human society but also for natural ecosystems. In addition to temperature and rainfall variability, climate change alters the snowmelt phenology and snow distribution, while runoff originating from snowmelt is the primary water supply source for many river and lake systems. Therefore, monitoring the dynamics and variations of water resources as well as the snowmelt conditions is necessary to understand cryo-hydrosphere interactions under the influence of climate change. So far, only few studies addressing this question relying on remote sensing techniques exist. Most previous studies utilize either in-situ measurements or multi-spectral sensors, which are limited to small-scale regions or affected by cloud cover, respectively. In the present study, we employ the latest spaceborne Sentinel-1 SAR and Sentinel-3 altimetry data to achieve a high resolution, cloud-free and

illumination-independent comprehensive inland waterbody dynamics (time-series surface area and water level) sensing strategy. Moreover, in contrast to previous studies utilizing in-house SAR and altimetry data processing algorithms, we employ freely available cloud-based services to ensure the broad applicability and transferability.

Based on altimetry and SAR data, the water level and the water-covered extent (surface area of lakes and the flooded area of rivers) can be successfully estimated. For the surface area mapping, the SAR backscatter coefficient-based Otsu's threshold has proven to be capable of accurately classifying the waterbody boundary by comparing it with the Global WaterPack (GWP) and high-resolution Sentinel-2 imagery. Nevertheless, we found that this approach can only be implemented in the lake water depletion period, i.e., dry season, due to the fact that the rainfall-caused surface wetness over non-waterbody regions would mislead the backscatter-based classification. For water level estimation, our results show high consistency between different passes and even out-perform the well-known altimetry databases owing to the finer along-track resolution of Sentinel-3. Moreover, by fusing both, surface area and water level information, we can achieve a comprehensive inland water dynamics monitoring. For our selected study sites, such as Lake Urmia, we could estimate the hypsometry and derive the water volume change. Via utilizing the STL decomposition technique, we can mitigate the "container effect" of the lake and extract the inter-annual water variation. For the Brahmaputra River, both time-series of the water level and the flooded area can be identified and be used for cross-comparison. The synchronized trend observed between them also suggests the high reliability of our derived Sentinel-1 and Sentinel-3 results.

Last but not least, together with the WSCE mapped with SAR imagery, we can analyze the influence of snowmelt on water resource variation. With the aim to handle the lagged causal effect of snowmelt and mitigate the omitted errors in the regression, the DLM initially developed for econometric applications is employed in the present study. In the lag lengths pre-analysis, we found that WSCE% has the longest lag length compared to rainfall and evapotranspiration. It is due to the infiltration process of snowmelt water and the fact that the snow-covered area is usually located in the high elevation region, which is more distant to downstream water level investigated VS. The lag length of WSCE% is also observed to be nearly twice as long in the Brahmaputra River compared to Lake Urmia owing to the shape difference of their watersheds. Furthermore, the temporal offset between the snowmelt water generation and the SAR-based WSCE detection is also discussed, which is one reason for the long lag length. Eventually, the casual effect of snowmelt conditions on inland water

resources is unbiasedly quantified with the DLM: for Lake Urmia, when increasing one percent of WSCE% during the period of zero to 80 days before, the detrended water volume would increase by 108 cubic meters while hold still other factors; for the Brahmaputra River, when increasing one percent of WSCE% during the period of 70 to 150 days before, the water level of the investigated VS would increase 0.1 meters while other independent variables remain constant.

Acknowledgments

Support by the German Academic Exchange Service (DAAD) fellowship to Ya-Lun S. Tsai is gratefully acknowledged. Special thanks to Dr. Marco Restano (ESA-ESRIN) for supporting the SARvatore service and Mr. Yao-Chun Huang (LSE) for guiding the DLM analysis.

6 Synthesis and Outlook

6.1. Summary of achievements and contributions to research gaps

Overall, the aims of this thesis are satisfied and each objective is fulfilled. Firstly, based on the comprehensive review of existing SAR-based SCE detection studies, the limitations of previous approaches are identified, which are overcome in the proposed novel total and wet SCE detection method based on the freely accessible SAR dataset with topographical factors and land cover information. Additionally, by adding ground temperature as well as vegetation indexes, the SCE mapping accuracy is further enhanced. Eventually, based on the SAR-detected snowmelt conditions together with the waterbody dynamics tracked with publically accessible SAR and altimetry data, the causal effect of snow cover dynamics on the inland water resources are unbiasedly quantified. To elaborate the achievements done in each research objective, the summaries are provided as follows:

Objective 1: **Reviewing the characteristics of SAR as well as its interactions with snow, and exploring the trends, difficulties, and opportunities of existing SAR-based SCE mapping studies**

Chapter two (Tsai Ya-Lun S. et al., 2019) provides comprehensive introductions of SAR-snow interaction theories and reviews previous SAR-based SCE mapping studies. Further discussions including the development of SAR and mapping strategies, limitations as well as opportunities of future studies are also described.

Firstly, the unique interactions between SAR signal and wet/dry snowpack are discussed. The water content of the snowpack largely affects the penetration depth of the SAR signal and alters the scattering mechanisms correspondingly. This background knowledge provides the basis for the SAR-based SCE mapping strategy.

Second, the previously published studies since the launch of the first revisiting spaceborne SAR sensor are reviewed thoroughly in different aspects. For instance, for SAR sensor comparison, C-band SAR-based algorithms dominate the studies, but the recent prosperity of X-band SAR provides a promising alternative. Their significant differences in employed frequencies are due to the penetration characteristics and histories of different wavelength sensors. Geologically and spatially, an imbalanced distribution of local-scale study sites is found, where most studies focus on mountainous regions, especially the European Alps and the Asian Himalaya. Regarding the land cover aspect, many studies simply mask out the forested and agricultural regions. With respect to the temporal aspect, the majority of studies investigate snow cover for only one year with an average of two observations within

this year to account for the dynamics of the snowpack. Last but not least, for the employed SCE detection algorithms, more than 55% of the reviewed studies only detect wet snow, with 82% of those studies applying a backscatter-based approach. These findings indicate that there still exists a gap for SAR-based SCE mapping approaches being maturely usable.

Nevertheless, it is also found that recent technical advancements provide promising opportunities for future studies, such as wider sensing swaths, shorter revisit times and quad-polarizations of SAR sensors, which largely highlights the potentials of using InSAR and PolSAR techniques for SCE detection. The need for synergy of SAR with other sensors to improve the quality of SCE mapping is also suggested. Eventually, the future potential of complementing or even replacing the conventional multi-spectral sensor-based SCE detection approaches with the SAR-based method is foreseen.

Objective 2: Proposing a novel total and wet SCE mapping strategy based on freely accessible SAR imagery with all land cover classes applicability and global transferability

To overcome the limitations of previous studies which usually only detect wet SCE in non-forested regions, the novel total and wet SCE mapping strategy is proposed in chapter three (Tsai Ya-Lun S, Dietz Andreas, et al., 2019b). Various new dataset as well as processing approaches are employed.

Firstly, to guarantee the global transferability, the freely accessible spaceborne Sentinel-1 SAR imagery is selected. Secondly, the land cover information is included which is used to build the SCE classifier for each land cover class. Thirdly, in addition to the commonly used backscatter coefficient, interferometric SAR coherence as well as polarimetric parameters are included to fully capture the snow-caused surface features. Fourthly, since in the review paper, it is realized that the elevation information is commonly used for dry SCE detection, the global DEM dataset is utilized as well. Furthermore, with the aim of comprehensively depicting topographical characteristics, other factors including slope, aspect, and curvature are also employed. Last but not least, an easy tuning machine learning classification algorithm is used to ensure the broad applicability and high flexibility.

Five different study areas located in different mountain ranges, continents, and hemispheres are selected to test the universal applicability of the proposed approach. Moreover, on the contrary to most previous studies having no validation for the mapped SCE, in the thesis, various datasets at different scales are used for

comprehensive validations, including internal cross-validation, external multi-spectral sensor-based SCE products/maps as well as in-situ snow depth records.

Results show that the overall accuracy, F-measure and AUC score of total SCE mapping accuracy for different land cover types (including densely vegetated forest and agricultural regions) can reach around 80%, 80%, and 70% respectively for the majority of regions. The accuracy can even be higher by around 5% if vegetation land cover classes are excluded. Additionally, when merging all input data for all test sites to build a universally applicable model set, the accuracy remains satisfying. These values confirm the robustness of the proposed land cover-dependent total SCE mapping approach. By extending the mapped total SCE with a backscatter-based thresholding approach, information about wet SCE is additionally provided. It is also found that the quality of land cover information affects SCE mapping accuracy. Eventually, the suggestions for employing other auxiliary data such as quantitative vegetation measurements are given.

Objective 3: Enhancing total SCE mapping accuracy by fusing SAR- and multi-spectral sensor-based information, and providing total SCE mapping reliability information

With the aim of improving the total SCE mapping accuracy, the employment of ground temperature information as well as vegetation indexes derived from multi-spectral sensors are included in chapter four (Tsai Ya-Lun S, Dietz Andreas, et al., 2019a). Moreover, the newly generated classification reliability map provided along with the estimated SCE enables further analysis possibilities.

Compared to the previously proposed total SCE mapping strategy (chapter three), which only uses SAR-based observations, topographical factors, and land cover information, further auxiliary data should be considered to enhance SCE mapping accuracy. Based on the review paper (chapter two), it is realized that ground temperature information is commonly employed as snow-covered regions naturally show a lower temperature. Thus, in chapter four, the ground temperature product derived from the emissivity bands of a multi-spectral sensor is used. On the other hand, as found in the results of the previously proposed mapping strategy, the existence of dense vegetation decreases classification accuracy. Previous studies also reveal that vegetation affects SAR backscatter, coherence, and PolSAR parameters; therefore, two different but related vegetation indexes (leaf area index (LAI) and fractional vegetation cover (FVC)) are also employed in the refined SCE mapping strategy.

Although including more data would inevitably increase the collinearity and complexity of the analyzed dataset, thanks to the strength of machine learning of handling non-linear high dimensionality, it would not result in biased results. Moreover, since the goal of this thesis is to provide a universally applicable mapping strategy that yields the highest SCE classification accuracy, mild redundancy between input variables is acceptable for ensuring flexibility.

Based on comprehensive validation trials, results show that the overall accuracy, F-measure, and AUC score can be enhanced from previously 80%, 80%, and 70% to around 90%, 90%, and 80% for all five study areas. Thus, the robustness and the universal transferability of the proposed strategy can be ensured; therefore, the SCE dynamics of the melting season of 2018 for the whole Alps are depicted. Moreover, with the newly generated SCE detection reliability map, the evaluation of uncertainty can be conducted and enables further analysis. For instance, it is found that densely vegetated regions have lower reliability, which matches the expectation.

More importantly, together with the proposed SAR observations and static topographical factors-based SCE mapping approach (objective 3), these two different input datasets provide users a comprehensive package to achieve satisfactory total SCE mapping accuracies based on data availability. It largely compensates the limitation of the traditional multi-spectral sensor-only SCE detection method and further yields wet SCE information, which cannot be depicted by multi-spectral sensors.

Objective 4: Proposing a cloud-free and illumination-independent inland waterbody dynamics tracking strategy using freely accessible datasets and services

To assess the influence of SCE variation on inland water resources, tracking inland waterbody dynamics is necessary. In chapter five, the new generation spaceborne Sentinel-1 and Sentinel-3 are used to detect water surface area and level respectively, in a cloud-free and illumination-independent manner. Moreover, the freely available online cloud-based processing services enable broad applicability and high efficiency. Eventually, the hypsometry and water volume variation of lakes as well as the flooded area and the water level variation of rivers can be estimated.

For surface area (water-covered area) detection, compared to most previous studies utilizing multi-spectral sensor-based band ratio water indexes, which suffer from cloud cover and noise caused by variations of atmospheric/illumination conditions, in chapter five, the cloud-penetrating and illumination-independent Sentinel-1 SAR

imagery is used. Since the SAR signal is sensitive to surface wetness and roughness, the water-covered/non-water areas can clearly be distinguished based on the backscatter coefficient with Otsu's algorithm.

On the contrary, for water level monitoring, rather than using in-situ gauging measurements or combining bathymetry surveying with surface area detection, which is not always publically accessible or universally available, the utilization of spaceborne Sentinel-3 active altimetry sensor is explored in chapter five. It has global data availability and free accessibility similar to Sentinel-1, and has a much finer footprint size compared to previous spaceborne altimetry sensors, which is much suitable for inland water level tracking.

To analyze both Sentinel-1 SAR and Sentinel-3 altimetry data, the Google Earth Engine as well as the ESA SARvatore cloud-based, publically available processing services are utilized. These platforms guarantee high speed data processing and a broad applicability. Moreover, SARvatore enables an advanced inland waterbody analysis and avoids the use of non-transferable in-house algorithms commonly adopted in previous studies.

Via comparison with multi-spectral sensor-based waterbody area products, it is found that the proposed Sentinel-1-based surface area usually can reliably classify the water-covered area. For water level estimation, the Sentinel-3-based results even outperform the well-known water level databases.

Finally, by fusing results of both water level and water-covered extent (surface area of lakes and the flooded area of rivers), the comprehensive inland waterbody dynamics can be tracked: for Lake Urmia in Iran, the hypsometry and derived water volume change can be estimated; for the Brahmaputra River, the variation of both water level and the flooded area can be tracked.

Objective 5: Assessing the influence of snowmelt conditions on inland water resources

Based on the fulfillment of all previous objectives, not only the SCE dynamics and snowmelt conditions can be mapped by SAR imagery, but also the inland waterbody dynamics can be tracked. Therefore, via the employment of the sophisticated regression method developed in the econometrics discipline and inclusion of hydrological factors, the causal effect of snowmelt conditions on water resources can be eventually quantified in chapter five.

Firstly, to unbiasedly quantify the influence of snowmelt conditions on water resources,

the inclusion of other factors sharing impact on water amount variation is critical. Hence, both rainfall and evapotranspiration data derived from the high-resolution global weather forecast model are employed as the control variables for mitigating the omitted error. By including these two hydrological factors, the correlations between them and snowmelt phenology would not undermine the credibility of regression analysis.

Secondly, since snowmelt water would not only form the direct surface streamflow but also infiltrate into the ground and soil, it has a temporally lagged effect on the downstream water amount variation. Thus, to tackle the lagged and overlapped influences of snowmelt as well as hydrological factors on water resources, traditional regression algorithms are not suitable owing to their poor collinearity handling abilities. On the contrary, the advanced DLM firstly developed in the econometrics discipline, which excels in dealing with multi-variables' dynamics influences with lags is employed in chapter five. To process the DLM, deciding the suitable lag length for each variable is vital, yet there is no universal rule for decision. Therefore, the background knowledge- and adjusted R^2-based lag length decision approach is proposed. Furthermore, by analyzing the lag length, it is found that compared to rainfall and evapotranspiration, the snowmelt conditions have the longest lag length. It is due to the distant location of snow-covered regions to waterbodies and the unique characteristics of the SAR-based snowmelt detection approach.

Finally, the causal effect of snowmelt conditions on inland water resources is unbiasedly quantified: for the Lake Urmia, when increasing one percent of WSCE% during the period of zero to 80 days before, the detrended water volume would increase by 108 cubic meters while hold still other factors; for the Brahmaputra River, when increasing one percent of WSCE% during the period of 70 to 150 days before, the water level of the investigated virtual station would increase by 0.1 meters while other independent variables remain constant. Namely, cryo-hydrosphere interactions can be identified.

6.2. Overall conclusions

Snow cover extent (SCE) is one of the most critical cryospheric components owing to its ample coverage as well as its unique physical characteristics. It not only affects the balance of numerous natural systems but also influences various socio-economic activities of human beings. Nevertheless, due to the rapidly rising global temperature caused by the deterioration of climate change, SCE has been decreasing globally, which largely endangers the sustainability and availability of inland water resources as millions of people rely on snowmelt water for daily consumption and agricultural

irrigation. Therefore, in order to understand the cryo-hydrosphere interactions under a warming climate, (1) monitoring SCE dynamics and snowmelt conditions, (2) tracking the dynamics of snowmelt-influenced waterbodies, and (3) assessing the causal effect of snowmelt conditions on inland water resources are indispensable.

To continuously monitor SCE, employing spaceborne remote sensing techniques is necessary. Since the conventional multi-spectral sensor-based approach would be inevitably affected by cloud cover and polar darkness, the utilization of cloud-penetrating and illumination-independent SAR offers a promising alternative. Thanks to its valuable polarization information as well as phase data, more detailed features of the snowpack can be identified. Moreover, based on the sensitivity of the SAR signal to water content, the snowmelt conditions can be well depicted. Nevertheless, based on the comprehensive review of previous SAR-based SCE detection studies as described in chapter two, it is found that there still exists a gap for being maturely usable. For instance, the majority of studies only detect wet SCE of small scale regions with a backscatter-based approach, mask out the forested and even agricultural regions, and rarely validate their results. Consequently, the need to propose a new SCE mapping strategy is desired.

Therefore, in chapter three, the novel total and wet SCE mapping strategy is proposed. By using the freely accessible spaceborne Sentinel-1 SAR imagery, data availability and sustainability are ensured. Also, based on the rich SAR-derived information, including the backscatter coefficient, interferometric coherence, and polarimetric parameters, together with the land cover information as well as topographical factors including elevation, slope, aspect, and curvature, the total SCE can be well depicted in all land cover classes (including densely vegetated forest and agricultural regions). Moreover, to facilitate the analysis of non-linear and complex SAR-based observations, the flexible but robust machine learning RF classification algorithm is used. Via comprehensive validations with multi-spectral sensor-based SCE products and in-situ snow depth records, results show that the overall accuracy, F-measure and AUC score of total SCE mapping accuracy can reach around 80%, 80%, and 70% for the majority of study areas located in different mountain ranges. By excluding the vegetation land cover classes, the accuracy can even increase by around 5%. Furthermore, when merging all input data for all test sites to build a universally applicable model set, the accuracy remains satisfying. These high values attest the reliability of the proposed land cover-dependent total SCE mapping approach. In addition, by extending the mapped total SCE with wet SCE estimated with a backscatter-based approach, holistic SCE dynamics for different months can be revealed.

To further explore the potential of enhancing total SCE mapping accuracy, the value of employing vegetation indexes (LAI and FVC) as well as land surface temperature (LST) derived from the PROBA-V satellite and MODIS sensors respectively, are examined in chapter four. Results show that the overall accuracy, F-measure, and AUC score can be enhanced to around 90%, 90%, and 80% for all five study areas located in different mountain ranges, continents, and hemispheres. Additionally, based on the newly generated reliability maps, a relationship between densely vegetated land cover classes and lower classification reliability is found. Eventually, the proposed approach is applied to depict the SCE dynamics of the whole Alps during the melting season of 2018.

With the aim of assessing the influences of SCE dynamics on inland water resources, in chapter five, the utilization of new generation publically accessible spaceborne Sentinel-3 altimetry as well as Sentinel-1 SAR are used to detect the water level and surface area of the Urmia Lake and the Brahmaputra River, respectively. The employment of spaceborne altimetry and SAR provide a high-resolution, cloud-free, and illumination-independent continuous water dynamics monitoring, instead of few sites available-only in-situ gauging stations and cloud-contaminated multi-spectral sensor band-based water indexes which was commonly used in previous studies. Via validations with well-known water level databases and multi-spectral sensor-based water boundary products, it is confirmed that the altimetry data-derived water level and SAR backscatter-Otsu-based surface area are accurate. Furthermore, by integrating both observations, the comprehensive inland waterbody dynamics can be achieved, such as the hypsometry-based water volume change of the Lake Urmia as well as the flooded area and water level of the Brahmaputra River.

Finally, together with the wet SCE mapped with SAR imagery, the causal effect of snowmelt conditions on water resource variations can be identified. To unbiasedly quantify the influence of snowmelt, rainfall, and evapotranspiration measurements provided by the global weather model are also included to mitigate the omitted error. The advanced DLM regression was firstly developed in the econometrics discipline and is employed as it can handle multi-variables' dynamics influences with temporal lags. In the lag length pre-analysis, snowmelt conditions show the longest lag length due to the distant location of snow-covered region to downstream waterbodies and the unique characteristics of the SAR-based snowmelt detection approach. At last, the casual effect of snowmelt conditions on inland water resources is unbiasedly quantified and cryo-hydrosphere interactions can be identified. For the Lake Urmia, when increasing one percent of WSCE% during the period of zero to 80 days before, the detrended water volume would increase by 108 cubic meters; for the Brahmaputra

River, when increasing one percent of WSCE% during the period of 70 to 150 days before, the water level of the investigated virtual station would increase 0.1 meters.

6.3. Future opportunities and challenges

In this thesis, many significant improvements and breakthroughs are achieved, such as (1) proposing novel SAR-based total and wet SCE mapping strategies which are applicable for all land cover classes with universal applicability, (2) proposing an advanced inland waterbody dynamics tracking approach by fusing Sentinel-1 SAR and Sentinel-3 altimetry data, and (3) quantifying the unbiased causal effect of snowmelt conditions on inland water resources using a sophisticated model. However, there remain many open questions and challenges, which should be explored in future studies. Thankfully, based on the practical experiences gained in this thesis, many suggestions and insights can be given as follows:

For SCE detection, the current thesis utilizes the C-band Sentinel-1 SAR imagery due to its global coverage, public accessibility, and highly sustainable mission design which guarantees the widest applicability among all currently existing spaceborne SAR sensors. Moreover, it is promising to foresee the launch of Sentinel-1C&D, which would provide even denser observations. Therefore, the temporal decorrelation of InSAR can be reduced and the strength of using interferometric coherence for SCE classification can be significantly enhanced. Nevertheless, in addition to Sentinel-1 constellation, since previous studies found the X-band SAR has higher sensitivity to the snowpack due to its shorter wavelength (see chapter two), the utilization of X-band SAR sensors such as COSMO-SkyMed and TerraSAR- X should be further considered. Also, as summarized in the review chapter and demonstrated in the method chapters, polarimetric information is highly helpful for SCE detection. Yet Sentinel-1 satellites only provide dual polarizations which limit the potential of conducting other polarimetric decomposition techniques such as Freeman–Durden decomposition (Freeman and Durden, 1998), Touzi decomposition (Touzi, 2006), and Yamaguchi decomposition (Yamaguchi et al., 2005). These advanced techniques provide much more surface feature characteristics but require quad-polarization SAR imagery. Therefore, the value of Radarsat-2 and PALSAR-2 should be further examined.

Methodologically, for SCE mapping, other auxiliary datasets such as soil moisture should be employed to remove the soil moisture-caused SAR signal change. However, the interaction between soil moisture and SAR signal together with the SWE/LWC of the snowpack is a highly complex topic due to their non-linearity and multi-factor-driven characteristics, as reviewed in (Ali et al., 2015; Karthikeyan et al.,

2017; LIU et al., 2019). Therefore, this issue requires extensive future studies to investigate. Another methodological improvement that can be conducted is the utilization of deep learning techniques, i.e., an advanced neural network-based classification/segmentation. As summarized in chapter two, although currently there are only a few studies that exploited DL techniques, it is foreseeable that the utilization of DL in this topic would prevail in the near future. Nevertheless, it must be noted that although DL might help to tackle the complex vegetation-SAR signal interaction and even the soil moisture-snow-SAR signal relationship mentioned above, generally during the training step of DL, it requires a much longer training period with a much higher computational power compared to the easy tuning/training RF used in the thesis. More importantly, to avoid overfitting which commonly happens in DL, corresponding procedures are not only time-consuming but also largely relying on experiences. For SAR-based DL classification, this drawback is expected to be even more severe due to the typical randomly distributed salt-and-pepper noises on SAR imagery. Because of these potential drawbacks and considering the currently proposed simple tuning RF-based SCE detection method can already guarantee a mapping accuracy of around 80%, the utilization of DL is not urgently required.

In the validation aspect, as thoroughly discussed in chapters two and three, currently there is no simple method to validate the mapped wet SCE. Most previous studies simply assume that there only exists wet snow in late spring and directly validate estimated wet SCE with multi-spectral sensor-based total SCE results. Nevertheless, the possibility of the existence of dry snow remains considerable. The difficulty of wet SCE validation results from both, the ambiguous definition of “wet snow” for SAR imagery and the highly dynamic variation of LWC. For instance, the LWC in the snowpack might largely differ in the morning and at night due to temperature-caused melting and refreezing. Also, since the SAR-based wet SCE detection approach is based on the backscatter coefficient value, which is affected by not only the targeted LWC but also other factors such as soil moisture and random noise, it is difficult to establish a consistent snow LWC-SAR backscatter coefficient relationship. Another similarly difficult snowmelt sensing alternative is to use SAR to directly invert the LWC instead of wet SCE mapping. However, this topic is still developing owing to both the natural complexity of the interaction between SAR signal and LWC of snowpack and the wide range of other possible signal-contaminating factors such as soil moisture and surface vegetation. Therefore, future studies examining both, field survey and SAR signal are still demanded.

Regarding the inland waterbody dynamics tracking approach, both, the surface area and water level retrieving methods can be further refined. For instance, to distinguish

the surface area of waterbodies, in addition to the backscatter coefficient used in the current thesis, the interferometric coherence as well as polarimetric parameters should be explored. It is due to the fact that the InSAR coherence would show a much lower value over the water surface owing to the strong phase decorrelation. For the polarimetric technique, based on suitable decomposition methods, the surface roughness and scattering mechanism of the SAR signal can be identified, which can largely facilitate water area delineation. Moreover, to overcome the limitation of the current SAR-based surface area detection method (i.e., can only be implemented during dry seasons), the fusion of both, multi-spectral and SAR imagery should be considered. For water level retrieval, the comparison of Sentinel-3 with other altimetry sensors such as Jason-3 is worth investigating. Via cross-comparison between different spaceborne altimetry missions, the systematic error of each sensor can be identified and mitigated.

Finally, for quantifying the influence of snowmelt conditions on water resources, various potentials can be investigated in the future, as discussed in chapter five. Firstly, in contrast to the WSCE% utilized in the thesis, the measurement of LWC should be chosen as it can more clearly reveal the snowmelt phenology. Nevertheless, as discussed above, inverting the LWC from SAR is still immature and requires plenty of studies. Secondly, the influence of groundwater seepage and leakage can be examined. Although previous studies suggest that their effects are generally ignorable, yet to enhance the completeness of assessing water resource variation, employing corresponding ground hydrological models should be considered. Thirdly, a modified DLM which uses a lag-based smooth function for weight assignment can be explored. In contrast to currently used universally weighted DLM, these constraints would provide a more accurate estimation of each lag weight of each variable. Finally, based on the fact that rain-on-snow (ROS) events would not only accelerate the snowmelt process but also affect the backscatter coefficient of the SAR signal on the snowpack, ROS events should be identified and their influence on water amount variation should be measured.

References

Abbaspour, M., Javid, A., Mirbagheri, S., Givi, F. A. and Moghimi, P. (2012). Investigation of lake drying attributed to climate change. *International Journal of Environmental Science and Technology, 9*(2), 257-266.

Abudu, S., Cui, C.-l., Saydi, M. and King, J. P. (2012). Application of snowmelt runoff model (SRM) in mountainous watersheds: A review. *Water Science and Engineering, 5*(2), 123-136.

Adam, E., Mutanga, O., Odindi, J. and Abdel-Rahman, E. M. (2014). Land-use/cover classification in a heterogeneous coastal landscape using RapidEye imagery: evaluating the performance of random forest and support vector machines classifiers. *International Journal of Remote Sensing, 35*(10), 3440-3458.

Adam, J. C., Hamlet, A. F. and Lettenmaier, D. P. (2009). Implications of global climate change for snowmelt hydrology in the twenty-first century. *Hydrological Processes: An International Journal, 23*(7), 962-972.

Ahmadi, R., Mohebbi, F., Hagigi, P., Esmailly, L. and Salmanzadeh, R. (2011). Macro-invertebrates in the Wetlands of the Zarrineh estuary at the south of Urmia Lake (Iran). *International Journal of Environmental Research, 5*(4), 1047-1052.

Ainsworth, T., Cloude, S. and Lee, J. (2002). *Eigenvector analysis of polarimetric SAR data.* Paper presented at the Geoscience and Remote Sensing Symposium, 2002. IGARSS'02. 2002 IEEE International.

Ali, I., Greifeneder, F., Stamenkovic, J., Neumann, M. and Notarnicola, C. (2015). Review of machine learning approaches for biomass and soil moisture retrievals from remote sensing data. *Remote Sensing, 7*(12), 16398-16421.

Ali, J., Khan, R., Ahmad, N. and Maqsood, I. (2012). Random forests and decision trees. *International Journal of Computer Science Issues (IJCSI), 9*(5), 272.

Alipour, S. (2006). Hydrogeochemistry of seasonal variation of Urmia salt lake, Iran. *Saline systems, 2*(1), 9.

Allain, S., Ferro-Famil, L. and Pottier, E. (2006). *A polarimetric classification from PolSAR data using SERD/DERD parameters.* Paper presented at the 6th European Conference on Synthetic Aperture Radar, EUSAR 2006, Dresden, Germany.

Allen, M. J. and Sheridan, S. C. (2018). Mortality risks during extreme temperature events (ETEs) using a distributed lag non-linear model. *International journal of biometeorology, 62*(1), 57-67.

Allen, R. and Zender, C. (2010). Effects of continental-scale snow albedo anomalies on the wintertime Arctic oscillation. *Journal of Geophysical Research: Atmospheres, 115*(D23).

Almon, S. (1965). The distributed lag between capital appropriations and expenditures. *Econometrica: Journal of the Econometric Society*, 178-196.

Alsdorf, D. E., Rodríguez, E. and Lettenmaier, D. P. (2007). Measuring surface water from space. *Reviews of geophysics, 45*(2).

Ambach, W. and Denoth, A. (1980). The dielectric behaviour of snow: a study versus liquid water content.

Ancey, C. and Bain, V. (2015). Dynamics of glide avalanches and snow gliding. *Reviews of geophysics, 53*(3), 745-784.

Anderson, M. P., Woessner, W. W. and Hunt, R. J. (2015). *Applied groundwater modeling: simulation of flow and advective transport*: Academic press.

Antropov, O., Rauste, Y. and Häme, T. (2011). Volume scattering modeling in PolSAR decompositions: Study of ALOS PALSAR data over boreal forest. *IEEE Transactions on Geoscience and Remote Sensing, 49*(10), 3838-3848.

Anttila, S., Metsämäki, S., Pulliainen, J. and Luojus, K. (2005). *From EO data to snow covered area (SCA) end products using automated processing system.* Paper presented at the Geoscience and Remote Sensing Symposium, 2005. IGARSS'05. Proceedings. 2005 IEEE International.

Archana, S., RD, G. and Nayan, S. (2012). RS-GIS based assessment of river dynamics of Brahmaputra River in India. *Journal of Water Resource and Protection, 2012*.

Archer, K. J. and Kimes, R. V. (2008). Empirical characterization of random forest variable importance measures. *Computational Statistics & Data Analysis, 52*(4), 2249-2260. doi: https://doi.org/10.1016/j.csda.2007.08.015

Armstrong, R. L. and Brodzik, M. J. (2002). Hemispheric-scale comparison and evaluation of passive-microwave snow algorithms. *Annals of Glaciology, 34*, 38-44.

Armstrong, R. L. and Brun, E. (2008). *Snow and climate: physical processes, surface energy exchange and modeling*: Cambridge University Press.

Armstrong, R. L., Rittger, K., Brodzik, M. J., Racoviteanu, A., Barrett, A. P., Khalsa, S.-J. S., Raup, B., Hill, A. F., Khan, A. L. and Wilson, A. M. (2019). Runoff from glacier ice and seasonal snow in High Asia: separating melt water sources in river flow. *Regional Environmental Change, 19*(5), 1249-1261.

Arslan, A., Wang, H., Pulliainen, J. and Hallikainen, M. (2001). Effective permittivity of wet snow using strong fluctuation theory. *Progress in Electromagnetics Research, 31*, 273-290.

Ashcraft, I. S. and Long, D. G. (2006). Comparison of methods for melt detection over Greenland using active and passive microwave measurements. *International Journal of Remote Sensing, 27*(12), 2469-2488.

Athmania, D. and Achour, H. (2014). External Validation of the ASTER GDEM2, GMTED2010 and CGIAR-CSI- SRTM v4.1 Free Access Digital Elevation Models (DEMs) in Tunisia and Algeria. *Remote Sensing, 6*(5), 4600.

Attema, E., Desnos, Y.-L. and Duchossois, G. (2000). Synthetic aperture radar in Europe: ERS, Envisat, and beyond. *Johns Hopkins APL technical digest, 21*(1), 155-161.

Baghdadi, N., Fortin, J.-P. and Bernier, M. (1999). Accuracy of wet snow mapping using simulated Radarsat backscattering coefficients from observed snow cover characteristics. *International Journal of Remote Sensing, 20*(10), 2049-2068.

Baghdadi, N., Gauthier, Y. and Bernier, M. (1997). Capability of multitemporal ERS-1 SAR data for wet-snow mapping. *Remote Sensing of Environment, 60*(2), 174-186.

Baghdadi, N., Gauthier, Y., Bernier, M. and Fortin, J.-P. (2000). Potential and limitations of RADARSAT SAR data for wet snow monitoring. *IEEE Transactions on Geoscience and Remote Sensing, 38*(1), 316-320.

Baghdadi, N., Livingstone, C. E. and Bernier, M. (1998). Airborne C-band SAR measurements of wet snow-covered areas. *IEEE Transactions on Geoscience and Remote Sensing, 36*(6), 1977-1981.

Baret, F., Weiss, M., Verger, A. and Smets, B. (2016). ATBD FOR LAI, FAPAR AND FCOVER FROM PROBA-V PRODUCTS AT 300M RESOLUTION (GEOV3).

Barnett, T. P., Adam, J. C. and Lettenmaier, D. P. (2005). Potential impacts of a warming climate on water availability in snow-dominated regions. *Nature, 438*(7066), 303-309.

Barnett, T. P., Dümenil, L., Schlese, U., Roeckner, E. and Latif, M. (1989). The effect of Eurasian snow cover on regional and global climate variations. *Journal of the Atmospheric Sciences, 46*(5), 661-686.

Barry, R. G. (1996). The parameterization of surface albedo for sea ice and its snow cover. *Progress in Physical Geography, 20*(1), 63-79.

Barry, R. G. and Chorley, R. J. (2009). *Atmosphere, weather and climate*: Routledge.

Bartsch, A., Jansa, J., Schöner, M. and Wagner, W. (2007). *Monitoring of spring snowmelt with Envisat ASAR WS in the Eastern Alps by combination of ascending and descending orbits.* Paper presented at the Proceedings of Envisat Symposium.

Belgiu, M. and Drăguţ, L. (2016). Random forest in remote sensing: A review of applications and future directions. *ISPRS Journal of Photogrammetry and Remote Sensing, 114*, 24-31.

Beniston, M., Diaz, H. and Bradley, R. (1997). Climatic change at high elevation sites: an overview. *Climatic Change, 36*(3-4), 233-251.

Beniston, M., Farinotti, D., Stoffel, M., Andreassen, L. M., Coppola, E., Eckert, N., Fantini, A., Giacona, F., Hauck, C. and Huss, M. (2018). The European mountain cryosphere: a review of its current state, trends, and future challenges. *The Cryosphere, 12*(2), 759.

Beniston, M., Stoffel, M. and Hill, M. (2011). Impacts of climatic change on water and natural hazards in the Alps: can current water governance cope with future challenges? Examples from the European "ACQWA" project. *Environmental science & policy, 14*(7), 734-743.

Bernier, M. and Fortin, J.-P. (1998). The potential of times series of C-band SAR data to monitor dry and shallow snow cover. *IEEE Transactions on Geoscience and Remote Sensing, 36*(1), 226-243.

Besic, N., Vasile, G., Chanussot, J., Stankovic, S., Dedieu, J.-P., d'Urso, G., Boldo, D. and Ovarlez, J.-P. (2012). *Dry snow backscattering sensitivity on density change for swe estimation.* Paper

presented at the Geoscience and Remote Sensing Symposium (IGARSS), 2012 IEEE International.

Besic, N., Vasile, G., Chanussot, J., Stankovic, S., Ovarlez, J.-P., d'Urso, G., Boldo, D. and Dedieu, J.-P. (2012). *Stochastically based wet snow mapping with SAR data.* Paper presented at the Geoscience and Remote Sensing Symposium (IGARSS), 2012 IEEE International.

Besic, N., Vasile, G., Dedieu, J.-P., Chanussot, J. and Stankovic, S. (2015). Stochastic Approach in Wet Snow Detection Using Multitemporal SAR Data. *IEEE Geoscience and Remote Sensing Letters, 12*(2), 244-248. doi: 10.1109/lgrs.2014.2334355

Bhaduri, A., Bogardi, J., Siddiqi, A., Voigt, H., Vörösmarty, C., Pahl-Wostl, C., Bunn, S. E., Shrivastava, P., Lawford, R. and Foster, S. (2016). Achieving sustainable development goals from a water perspective. *Frontiers in Environmental Science, 4*, 64.

Biemans, H., Siderius, C., Lutz, A., Nepal, S., Ahmad, B., Hassan, T., von Bloh, W., Wijngaard, R., Wester, P. and Shrestha, A. (2019). Importance of snow and glacier meltwater for agriculture on the Indo-Gangetic Plain. *Nature Sustainability, 2*(7), 594-601.

Billings, W. D. and Bliss, L. (1959). An alpine snowbank environment and its effects on vegetation, plant development, and productivity. *Ecology, 40*(3), 388-397.

Birkett, C. M., Ricko, M., Beckley, B. D., Yang, X. and Tetrault, R. L. (2017). *G-REALM: A lake/reservoir monitoring tool for drought monitoring and water resources management.* Paper presented at the AGU Fall Meeting Abstracts.

Björk, R. G. and Molau, U. (2007). Ecology of alpine snowbeds and the impact of global change. *Arctic, Antarctic, and Alpine Research, 39*(1), 34-43.

Bosiö, J., Stiegler, C., Johansson, M., Mbufong, H. N. and Christensen, T. R. (2014). Increased photosynthesis compensates for shorter growing season in subarctic tundra—8 years of snow accumulation manipulations. *Climatic Change, 127*(2), 321-334.

Breiman, L. (2001). Random forests. *Machine learning, 45*(1), 5-32.

Brogioni, M., Macelloni, G., Paloscia, S., Pampaloni, P., Pettinato, S. and Santi, E. (2006). *Monitoring snow cover characteristics with multifrequency active and passive microwave sensors.* Paper presented at the Geoscience and Remote Sensing Symposium, 2006. IGARSS 2006. IEEE International.

Brown, G. (1977). The average impulse response of a rough surface and its applications. *IEEE transactions on antennas and propagation, 25*(1), 67-74.

Brown, R., Derksen, C. and Wang, L. (2010). A multi-data set analysis of variability and change in Arctic spring snow cover extent, 1967–2008. *Journal of Geophysical Research: Atmospheres, 115*(D16).

Brown, R. D. and Robinson, D. A. (2011). Northern Hemisphere spring snow cover variability and change over 1922–2010 including an assessment of uncertainty. *The Cryosphere, 5*(1), 219-229.

Bruder, J. A. (2013). IEEE Radar standards and the radar systems panel. *IEEE Aerospace and Electronic Systems Magazine, 28*(7), 19-22.

Bruzzone, L., Roli, F. and Serpico, S. B. (1995). An extension of the Jeffreys-Matusita distance to multiclass cases for feature selection. *IEEE Transactions on Geoscience and Remote Sensing, 33*(6), 1318-1321.

Bulygina, O., Groisman, P. Y., Razuvaev, V. and Korshunova, N. (2011). Changes in snow cover characteristics over Northern Eurasia since 1966. *Environmental Research Letters, 6*(4), 045204.

Bulygina, O., Razuvaev, V. and Korshunova, N. (2009). Changes in snow cover over Northern Eurasia in the last few decades. *Environmental Research Letters, 4*(4), 045026.

Burakowski, E. and Magnusson, M. (2012). Climate impacts on the winter tourism economy in the United States.

Butt, M. J. and Bilal, M. (2011). Application of snowmelt runoff model for water resource management. *Hydrological Processes, 25*(24), 3735-3747.

Cánovas-García, F., Alonso-Sarría, F., Gomariz-Castillo, F. and Oñate-Valdivieso, F. (2017). Modification of the random forest algorithm to avoid statistical dependence problems when classifying remote sensing imagery. *Computers & Geosciences, 103*, 1-11.

Callaghan, T. V., Johansson, M., Brown, R. D., Groisman, P. Y., Labba, N. and Radionov, V. (2011). Changing snow cover and its impacts.

Callaghan, T. V., Johansson, M., Brown, R. D., Groisman, P. Y., Labba, N., Radionov, V., Bradley, R. S., Blangy, S., Bulygina, O. N. and Christensen, T. R. (2011). Multiple effects of changes in Arctic snow cover. *Ambio, 40*(1), 32-45.

Callegari, M., Carturan, L., Marin, C., Notarnicola, C., Rastner, P., Seppi, R. and Zucca, F. (2016). A Pol-SAR Analysis for Alpine Glacier Classification and Snowline Altitude Retrieval. *IEEE Journal of Selected Topics in Applied Earth Observations and Remote Sensing, 9*(7), 3106-3121. doi: 10.1109/jstars.2016.2587819

Calmant, S., da Silva, J. S., Moreira, D. M., Seyler, F., Shum, C., Crétaux, J. F. and Gabalda, G. (2013). Detection of Envisat RA2/ICE-1 retracked radar altimetry bias over the Amazon basin rivers using GPS. *Advances in Space Research, 51*(8), 1551-1564.

Calmant, S., Seyler, F. and Cretaux, J. F. (2008). Monitoring continental surface waters by satellite altimetry. *Surveys in geophysics, 29*(4-5), 247-269.

Campbell, B. A. (2002). *Radar remote sensing of planetary surfaces*: Cambridge University Press.

Camps-Valls, G. and Bruzzone, L. (2005). Kernel-based methods for hyperspectral image classification. *IEEE Transactions on Geoscience and Remote Sensing, 43*(6), 1351-1362.

Canovas-Garcia, F. and Alonso-Sarria, F. (2015). Optimal combination of classification algorithms and feature ranking methods for object-based classification of submeter resolution Z/I-Imaging DMC imagery. *Remote Sensing, 7*(4), 4651-4677.

Cayan, D. R., Das, T., Pierce, D. W., Barnett, T. P., Tyree, M. and Gershunov, A. (2010). Future dryness in the southwest US and the hydrology of the early 21st century drought. *Proceedings of the National Academy of Sciences, 107*(50), 21271-21276.

Chan, A. K. and Peng, C. (2003). *Wavelets for sensing technologies* (Vol. 1): Artech House.

Chan, J. C.-W. and Paelinckx, D. (2008). Evaluation of Random Forest and Adaboost tree-based ensemble classification and spectral band selection for ecotope mapping using airborne hyperspectral imagery. *Remote Sensing of Environment, 112*(6), 2999-3011.

Chan, Y. K. and Koo, V. C. (2008). An introduction to synthetic aperture radar (SAR). *Progress in Electromagnetics Research, 2*, 27-60.

Che, T., Li, X., Jin, R., Armstrong, R. and Zhang, T. (2008). Snow depth derived from passive microwave remote-sensing data in China. *Annals of Glaciology, 49*, 145-154.

Chen, Y., Li, Z., Fang, G. and Deng, H. (2017). Impact of climate change on water resources in the Tianshan Mountians. *Central Asia. Acta Geographica Sinica, 72*(1), 18-26.

Chuvieco, E. (2008). Environmental remote sensing: Earth observation from space. *Ariel, Barcelona*.

Clark, M. P. and Serreze, M. C. (2000). Effects of variations in East Asian snow cover on modulating atmospheric circulation over the North Pacific Ocean. *Journal of Climate, 13*(20), 3700-3710.

Cleveland, R. B., Cleveland, W. S., McRae, J. E. and Terpenning, I. (1990). STL: A seasonal-trend decomposition. *Journal of official statistics, 6*(1), 3-73.

Cloude, S. R. and Pottier, E. (1996). A review of target decomposition theorems in radar polarimetry. *IEEE Transactions on Geoscience and Remote Sensing, 34*(2), 498-518.

Clow, D. W. (2010). Changes in the timing of snowmelt and streamflow in Colorado: a response to recent warming. *Journal of Climate, 23*(9), 2293-2306.

Cohen, J., Ye, H. and Jones, J. (2015). Trends and variability in rain-on-snow events. *Geophysical Research Letters, 42*(17), 7115-7122.

Cohen, J. L., Furtado, J. C., Barlow, M. A., Alexeev, V. A. and Cherry, J. E. (2012). Arctic warming, increasing snow cover and widespread boreal winter cooling. *Environmental Research Letters, 7*(1), 014007.

Costanza, R., Fioramonti, L. and Kubiszewski, I. (2016). The UN Sustainable Development Goals and the dynamics of well-being. *Frontiers in Ecology and the Environment, 14*(2), 59-59.

Crétaux, J.-F., Abarca-del-Río, R., Berge-Nguyen, M., Arsen, A., Drolon, V., Clos, G. and Maisongrande, P. (2016). Lake volume monitoring from space. *Surveys in geophysics, 37*(2), 269-305.

Crétaux, J.-F., Jelinski, W., Calmant, S., Kouraev, A., Vuglinski, V., Bergé-Nguyen, M., Gennero, M.-C., Nino, F., Del Rio, R. A. and Cazenave, A. (2011). SOLS: A lake database to monitor in the Near Real Time water level and storage variations from remote sensing data. *Advances in Space Research, 47*(9), 1497-1507.

Crawford, C. J. (2015). MODIS Terra Collection 6 fractional snow cover validation in mountainous terrain during spring snowmelt using Landsat TM and ETM+. *Hydrological Processes, 29*(1), 128-138.

Crawford, C. J., Manson, S. M., Bauer, M. E. and Hall, D. K. (2013). Multitemporal snow cover mapping in mountainous terrain for Landsat climate data record development. *Remote Sensing of Environment, 135*, 224-233.

Cretaux, J.-F., Berge-Nguyen, M., Calmant, S., Jamangulova, N., Satylkanov, R., Lyard, F., Perosanz, F., Verron, J., Samine Montazem, A. and Le Guilcher, G. (2018). Absolute calibration or validation of the altimeters on the Sentinel-3A and the Jason-3 over Lake Issykkul (Kyrgyzstan). *Remote Sensing, 10*(11), 1679.

Curlander, J. C. and McDonough, R. N. (1991). *Synthetic aperture radar* (Vol. 396): John Wiley & Sons New York, NY, USA.

Curtis, T., Kvernmo, S. and Bjerregaard, P. (2005). Changing living conditions, life style and health. *International Journal of Circumpolar Health, 64*(5), 442-450.

Cutler, D. R., Edwards Jr, T. C., Beard, K. H., Cutler, A., Hess, K. T., Gibson, J. and Lawler, J. J. (2007). Random forests for classification in ecology. *Ecology, 88*(11), 2783-2792.

Déry, S. J. and Brown, R. D. (2007). Recent Northern Hemisphere snow cover extent trends and implications for the snow-albedo feedback. *Geophysical Research Letters, 34*(22).

Dai, A., Qian, T., Trenberth, K. E. and Milliman, J. D. (2009). Changes in continental freshwater discharge from 1948 to 2004. *Journal of Climate, 22*(10), 2773-2792.

Dankers, R. and De Jong, S. M. (2004). Monitoring snow-cover dynamics in Northern Fennoscandia with SPOT VEGETATION images. *International Journal of Remote Sensing, 25*(15), 2933-2949.

Day, C. A. (2009). Modelling impacts of climate change on snowmelt runoff generation and streamflow across western US mountain basins: a review of techniques and applications for water resource management. *Progress in Physical Geography, 33*(5), 614-633.

Decaux, L., Grabiec, M., Ignatiuk, D. and Jania, J. (2019). Role of discrete water recharge from supraglacial drainage systems in modeling patterns of subglacial conduits in Svalbard glaciers. *The Cryosphere, 13*(3), 735-752.

Dedieu, J.-P., Besic, N., Vasile, G., Mathieu, J., Durand, Y. and Gottardi, F. (2014). *Dry snow analysis in alpine regions using RADARSAT-2 full polarimetry data. Comparison with in situ measurements.* Paper presented at the Geoscience and Remote Sensing Symposium (IGARSS), 2014 IEEE International.

Dedieu, J.-P., De Farias, G. B., Castaings, T., Allain-Bailhache, S., Pottier, E., Durand, Y. and Bernier, M. (2012). Interpretation of a RADARSAT-2 fully polarimetric time-series for snow cover studies in an Alpine context–first results. *Canadian Journal of Remote Sensing, 38*(3), 336-351.

Delju, A., Ceylan, A., Piguet, E. and Rebetez, M. (2013). Observed climate variability and change in Urmia Lake Basin, Iran. *Theoretical and Applied Climatology, 111*(1-2), 285-296.

Derksen, C. and Brown, R. (2012). Spring snow cover extent reductions in the 2008–2012 period exceeding climate model projections. *Geophysical Research Letters, 39*(19).

Dial, G., Bowen, H., Gerlach, F., Grodecki, J. and Oleszczuk, R. (2003). IKONOS satellite, imagery, and products. *Remote Sensing of Environment, 88*(1-2), 23-36.

Dietz, A. J., Conrad, C., Kuenzer, C., Gesell, G. and Dech, S. (2014). Identifying changing snow cover characteristics in central Asia between 1986 and 2014 from remote sensing data. *Remote Sensing, 6*(12), 12752-12775.

Dietz, A. J., Kuenzer, C. and Dech, S. (2015). Global SnowPack: a new set of snow cover parameters for studying status and dynamics of the planetary snow cover extent. *Remote Sensing Letters, 6*(11), 844-853.

Dietz, A. J., Kuenzer, C., Gessner, U. and Dech, S. (2012). Remote sensing of snow–a review of available methods. *International Journal of Remote Sensing, 33*(13), 4094-4134.

Dinardo, S., Fenoglio-Marc, L., Buchhaupt, C., Becker, M., Scharroo, R., Fernandes, M. J. and Benveniste, J. (2018). Coastal sar and plrm altimetry in german bight and west baltic sea. *Advances in Space Research, 62*(6), 1371-1404.

Dinardo, S., Restano, M., Ambrózio, A. and Benveniste, J. (2016). *SAR altimetry processing on demand service for Cryosat-2 and Sentinel-3 AT ESA G-POD.* Paper presented at the Proceedings of the 2016 conference on Big Data from Space (BiDS'16), Santa Cruz de Tenerife, Spain.

Dinka, M. O., Loiskandl, W. and Ndambuki, J. M. (2014). Hydrologic modelling for Lake Basaka: development and application of a conceptual water budget model. *Environmental Monitoring and Assessment, 186*(9), 5363-5379.

Dirscherl, M., Dietz, A. J., Kneisel, C. and Kuenzer, C. (2020). Automated Mapping of Antarctic Supraglacial Lakes Using a Machine Learning Approach. *Remote Sensing, 12*(7), 1203.

Djamali, M., de Beaulieu, J.-L., Shah-hosseini, M., Andrieu-Ponel, V., Ponel, P., Amini, A., Akhani, H., Leroy, S. A., Stevens, L. and Lahijani, H. (2008). A late Pleistocene long pollen record from Lake Urmia, NW Iran. *Quaternary Research, 69*(3), 413-420.

Dorji, T., Hopping, K. A., Wang, S., Piao, S., Tarchen, T. and Klein, J. A. (2018). Grazing and spring snow counteract the effects of warming on an alpine plant community in Tibet through effects on the dominant species. *Agricultural and Forest Meteorology, 263*, 188-197. doi: https://doi.org/10.1016/j.agrformet.2018.08.017

Du, P., Samat, A., Waske, B., Liu, S. and Li, Z. (2015). Random forest and rotation forest for fully polarized SAR image classification using polarimetric and spatial features. *ISPRS Journal of Photogrammetry and Remote Sensing, 105*, 38-53.

Duan, Z. and Bastiaanssen, W. (2013). Estimating water volume variations in lakes and reservoirs from four operational satellite altimetry databases and satellite imagery data. *Remote Sensing of Environment, 134*, 403-416.

Dubey, A. K., Gupta, P., Dutta, S. and Kumar, B. (2014). Evaluation of satellite-altimetry-derived river stage variation for the braided Brahmaputra River. *International Journal of Remote Sensing, 35*(23), 7815-7827.

Duguay, Y. and Bernier, M. (2012). *The use of RADARSAT-2 and TerraSAR-X data for the evaluation of snow characteristics in subarctic regions.* Paper presented at the Geoscience and Remote Sensing Symposium (IGARSS), 2012 IEEE International.

Dumont, J., Rosmorduc, V., Carrere, L., Picot, N., Bronner, E., Couhert, A., Guillot, A., Desai, S., Bonekamp, H. and Figa, J. (2016). Jason-3 products handbook: SALP-MU-M-OP-16118-CN.

Dye, D. G. (2002). Variability and trends in the annual snow-cover cycle in Northern Hemisphere land areas, 1972–2000. *Hydrological Processes, 16*(15), 3065-3077.

Dyrrdal, A. V., Saloranta, T., Skaugen, T. and Stranden, H. B. (2013). Changes in snow depth in Norway during the period 1961–2010. *Hydrology Research, 44*(1), 169-179.

Ebert, E. E. and Curry, J. A. (1993). An intermediate one-dimensional thermodynamic sea ice model for investigating ice-atmosphere interactions. *Journal of Geophysical Research: Oceans, 98*(C6), 10085-10109.

Eimanifar, A. and Mohebbi, F. (2007). Urmia Lake (northwest Iran): a brief review. *Saline systems, 3*(1), 5.

Environment, I. D. o. (2010). Integrated management plan for Lake UrmiaBasin (1st ed.) (prepared in Cooperation with UNEP/GEF).

Eriksson, L. E., Borenäs, K., Dierking, W., Berg, A., Santoro, M., Pemberton, P., Lindh, H. and Karlson, B. (2010). Evaluation of new spaceborne SAR sensors for sea-ice monitoring in the Baltic Sea. *Canadian Journal of Remote Sensing, 36*(sup1), S56-S73.

ESA. (2017). Land Cover CCI Product User Guide Version 2.0, CCI-LC-PUGV2.

EUMETSAT. (2017). Sentinel-3 SRAL Marine User Handbook.

Euskirchen, E. S., Goodstein, E. S. and Huntington, H. P. (2013). An estimated cost of lost climate regulation services caused by thawing of the Arctic cryosphere. *Ecological applications, 23*(8), 1869-1880.

Evans, S. (1965). Dielectric properties of ice and snow–a review. *Journal of Glaciology, 5*(42), 773-792.

Fang, S., Xu, L., Pei, H., Liu, Y., Liu, Z., Zhu, Y., Yan, J. and Zhang, H. (2014). An integrated approach to snowmelt flood forecasting in water resource management. *IEEE transactions on industrial informatics, 10*(1), 548-558.

Fathian, F., Dehghan, Z. and Eslamian, S. (2014). Analysis of water level changes in Lake Urmia based on data characteristics and non-parametric test. *International Journal of Hydrology Science and Technology, 4*(1), 18-38.

Favier, P., Bertrand, D., Eckert, N. and Naaim, M. (2014). A reliability assessment of physical vulnerability of reinforced concrete walls loaded by snow avalanches. *Natural Hazards and Earth System Sciences, 14*(3), 689-704.

Fawcett, T. (2006). An introduction to ROC analysis. *Pattern Recognition Letters, 27*(8), 861-874.

Feng, Q., Liu, J. and Gong, J. (2015). UAV Remote Sensing for Urban Vegetation Mapping Using Random Forest and Texture Analysis. *Remote Sensing, 7*(1), 1074.

Fernandes, M. J., Lázaro, C., Nunes, A. L. and Scharroo, R. (2014). Atmospheric corrections for altimetry studies over inland water. *Remote Sensing, 6*(6), 4952-4997.

Ferri, C., Hernández-Orallo, J. and Modroiu, R. (2009). An experimental comparison of performance measures for classification. *Pattern Recognition Letters, 30*(1), 27-38.

Feyisa, G. L., Meilby, H., Fensholt, R. and Proud, S. R. (2014). Automated Water Extraction Index: A new technique for surface water mapping using Landsat imagery. *Remote Sensing of Environment, 140*, 23-35.

Field, P. and Heymsfield, A. (2015). Importance of snow to global precipitation. *Geophysical Research Letters, 42*(21), 9512-9520.

Finsen, F., Milzow, C., Smith, R., Berry, P. and Bauer-Gottwein, P. (2014). Using radar altimetry to update a large-scale hydrological model of the Brahmaputra river basin. *Hydrology Research, 45*(1), 148-164.

Flanner, M. G., Shell, K. M., Barlage, M., Perovich, D. K. and Tschudi, M. (2011). Radiative forcing and albedo feedback from the Northern Hemisphere cryosphere between 1979 and 2008. *Nature Geoscience, 4*(3), 151-155.

Floricioiu, D. and Rott, H. (2001). Seasonal and short-term variability of multifrequency, polarimetric radar backscatter of alpine terrain from SIR-C/X-SAR and AIRSAR data. *IEEE Transactions on Geoscience and Remote Sensing, 39*(12), 2634-2648.

Food and Nations, A. O. o. t. U. (2011). *The state of the world's land and water resources for food and agriculture: Managing systems at risk*: Earthscan.

Freeman, A. and Durden, S. L. (1998). A three-component scattering model for polarimetric SAR data. *IEEE Transactions on Geoscience and Remote Sensing, 36*(3), 963-973.

Frey, H. and Paul, F. (2012). On the suitability of the SRTM DEM and ASTER GDEM for the compilation of topographic parameters in glacier inventories. *International Journal of Applied Earth Observation and Geoinformation, 18*, 480-490. doi: https://doi.org/10.1016/j.jag.2011.09.020

Furgal, C. and Prowse, T. (2008). Northern Canada From Impacts to Adaptation: Canada in a Changing Climate 2007 ed D Lemmen. *F Warren, E Bush and J Lacroix (Ottawa: Natural Resources Canada)*.

G Kumambala, P. and Ervine, A. (2010). Water balance model of Lake Malawi and its sensitivity to climate change. *The Open Hydrology Journal, 4*(1).

Gao, Q., Makhoul, E., Escorihuela, M. J., Zribi, M., Quintana Seguí, P., García, P. and Roca, M. (2019). Analysis of retrackers' performances and water level retrieval over the ebro river basin using sentinel-3. *Remote Sensing, 11*(6), 718.

Garrity, C. (1992). Characterization of snow on floating ice and case studies of brightness temperature changes during the onset of melt. *Microwave remote sensing of sea ice*, 313-328.

Gasparrini, A. (2011). Distributed lag linear and non-linear models in R: the package dlnm. *Journal of statistical software, 43*(8), 1.

Gasparrini, A. (2014). Modeling exposure–lag–response associations with distributed lag non-linear models. *Statistics in medicine, 33*(5), 881-899.

Gasparrini, A., Armstrong, B. and Kenward, M. G. (2010). Distributed lag non-linear models. *Statistics in medicine, 29*(21), 2224-2234.

GCOS, W. a. (2011). *Systematic Observation Requirements for Satellite-Based Data Products for Climate – 2011 Update*: GCOS - 154. Geneva: WMO GCOS.

Ghosh, A., Fassnacht, F. E., Joshi, P. and Koch, B. (2014). A framework for mapping tree species combining hyperspectral and LiDAR data: Role of selected classifiers and sensor across three spatial scales. *International Journal of Applied Earth Observation and Geoinformation, 26*, 49-63.

Gislason, P. O., Benediktsson, J. A. and Sveinsson, J. R. (2006). Random Forests for land cover classification. *Pattern Recognition Letters, 27*(4), 294-300. doi: https://doi.org/10.1016/j.patrec.2005.08.011

Goldstein, R. M., Engelhardt, H., Kamb, B. and Frolich, R. M. (1993). Satellite radar interferometry for monitoring ice sheet motion: application to an Antarctic ice stream. *Science, 262*(5139), 1525-1530.

Gorelick, N., Hancher, M., Dixon, M., Ilyushchenko, S., Thau, D. and Moore, R. (2017). Google Earth Engine: Planetary-scale geospatial analysis for everyone. *Remote Sensing of Environment, 202*, 18-27.

Grünewald, T., Wolfsperger, F. and Lehning, M. (2018). Snow farming: conserving snow over the summer season. *The Cryosphere, 12*(1), 385.

Greifeneder, F., Wagner, W., Sabel, D. and Naeimi, V. (2014). Suitability of SAR imagery for automatic flood mapping in the Lower Mekong Basin. *International Journal of Remote Sensing, 35*(8), 2857-2874.

Groisman, P. Y., Knight, R. W., Easterling, D. R., Karl, T. R., Hegerl, G. C. and Razuvaev, V. N. (2005). Trends in intense precipitation in the climate record. *Journal of Climate, 18*(9), 1326-1350.

Guangjun, H., Pengfeng, X., Xuezhi, F., Xueliang, Z., Zuo, W. and Ni, C. (2015). Extracting Snow Cover in Mountain Areas Based on SAR and Optical Data. *IEEE Geoscience and Remote Sensing Letters, 12*(5), 1136-1140. doi: 10.1109/lgrs.2014.2386275

Guneriussen, T. (1997). Backscattering properties of a wet snow cover derived from DEM corrected ERS-1 SAR data. *International Journal of Remote Sensing, 18*(2), 375-392.

Guneriussen, T., Johnsen, H. and Lauknes, I. (2001). Snow cover mapping capabilities using RADARSAT standard mode data. *Canadian Journal of Remote Sensing, 27*(2), 109-117.

Guo, C., Tong, L., Chen, Y. and Yang, X. (2017). *Snow extraction using X-band multi-temporal coherence based on insar technology.* Paper presented at the Geoscience and Remote Sensing Symposium (IGARSS), 2017 IEEE International.

Gutzler, D. S. and Rosen, R. D. (1992). Interannual variability of wintertime snow cover across the Northern Hemisphere. *Journal of Climate, 5*(12), 1441-1447.

Haefner, H. (2001). Small-Scale Monitoring of Wet Snowcover with Radarsat-ScanSAR Data. *EARSeL eProceedings*(1), 339-346.

Haefner, H., Small, D., Biegger, S., Hoffmann, H. and Nuesch, D. (2001, Apr 2001). *Estimation of snow cover over large mountainous areas using Radarsat ScanSAR.* Paper presented at the Remote Sensing and Hydrology, New Mexico, USA.

Hahn, D. G. and Shukla, J. (1976). An apparent relationship between Eurasian snow cover and Indian monsoon rainfall. *Journal of the Atmospheric Sciences, 33*(12), 2461-2462.

Hall, A. (2004). The role of surface albedo feedback in climate. *Journal of Climate, 17*(7), 1550-1568.

Hall, D. K. and Riggs, G. A. (2007). Accuracy assessment of the MODIS snow products. *Hydrological Processes: An International Journal, 21*(12), 1534-1547.

Hall, D. K., Riggs, G. A., Salomonson, V. V., Barton, J., Casey, K., Chien, J., DiGirolamo, N., Klein, A., Powell, H. and Tait, A. (2001). Algorithm theoretical basis document (ATBD) for the MODIS snow and sea ice-mapping algorithms. *Nasa Gsfc*.

Hall, D. K., Riggs, G. A., Salomonson, V. V., DiGirolamo, N. E. and Bayr, K. J. (2002). MODIS snow-cover products. *Remote Sensing of Environment, 83*(1-2), 181-194.

Ham, J., Chen, Y., Crawford, M. M. and Ghosh, J. (2005). Investigation of the random forest framework for classification of hyperspectral data. *IEEE Transactions on Geoscience and Remote Sensing, 43*(3), 492-501.

Han, P., Long, D., Han, Z., Du, M., Dai, L. and Hao, X. (2019). Improved understanding of snowmelt runoff from the headwaters of China's Yangtze River using remotely sensed snow products and hydrological modeling. *Remote Sensing of Environment, 224*, 44-59.

Harma, K. J., Johnson, M. S. and Cohen, S. J. (2012). Future water supply and demand in the Okanagan Basin, British Columbia: a scenario-based analysis of multiple, interacting stressors. *Water Resources Management, 26*(3), 667-689.

Harris, C., Arenson, L. U., Christiansen, H. H., Etzelmüller, B., Frauenfelder, R., Gruber, S., Haeberli, W., Hauck, C., Hoelzle, M. and Humlum, O. (2009). Permafrost and climate in Europe: Monitoring and modelling thermal, geomorphological and geotechnical responses. *Earth-Science Reviews, 92*(3-4), 117-171.

Harrison, A. R. and Lucas, R. M. (1989). Multi-spectral classification of snow using NOAA AVHRR imagery. *International Journal of Remote Sensing, 10*(4-5), 907-916.

Hassan, A. A. and Jin, S. (2014). Lake level change and total water discharge in East Africa Rift Valley from satellite-based observations. *Global and Planetary Change, 117*, 79-90.

Hassanzadeh, E., Zarghami, M. and Hassanzadeh, Y. (2012). Determining the main factors in declining the Urmia Lake level by using system dynamics modeling. *Water Resources Management, 26*(1), 129-145.

Hayashi, M. and Van der Kamp, G. (2000). Simple equations to represent the volume–area–depth relations of shallow wetlands in small topographic depressions. *Journal of Hydrology, 237*(1-2), 74-85.

He, G., Feng, X., Xiao, P., Xia, Z., Wang, Z., Chen, H., Li, H. and Guo, J. (2017). Dry and Wet Snow Cover Mapping in Mountain Areas Using SAR and Optical Remote Sensing Data. *IEEE Journal of Selected Topics in Applied Earth Observations and Remote Sensing, 10*(6), 2575-2588. doi: 10.1109/jstars.2017.2673409

He, G., Hao, Y., Xiao, P., Feng, X., Li, H. and Wang, Z. (2016). *Snow recognition in mountain areas based on SAR and optical remote sensing data.* Paper presented at the Geoscience and Remote Sensing Symposium (IGARSS), 2016 IEEE International.

He, G., Jiang, J., Xia, Z., Hao, Y., Xiao, P., Feng, X. and Wang, Z. (2016). *Snow cover extraction in mountain areas using RadarSat-2 polarimetrie SAR data.* Paper presented at the Ground Penetrating Radar (GPR), 2016 16th International Conference on.

Heliere, F., Fois, F., Arcioni, M., Bensi, P., Fehringer, M. and Scipal, K. (2014). *Biomass P-band SAR interferometric mission selected as 7th Earth Explorer Mission.* Paper presented at the EUSAR 2014; 10th European Conference on Synthetic Aperture Radar; Proceedings of.

Henry, J. B., Chastanet, P., Fellah, K. and Desnos, Y. L. (2006). Envisat multi-polarized ASAR data for flood mapping. *International Journal of Remote Sensing, 27*(10), 1921-1929.

Hirt, C., Filmer, M. and Featherstone, W. (2010). Comparison and validation of the recent freely available ASTER-GDEM ver1, SRTM ver4. 1 and GEODATA DEM-9S ver3 digital elevation models over Australia. *Australian Journal of Earth Sciences, 57*(3), 337-347.

Hoegh-Guldberg, O., Jacob, D., Taylor, M., Bindi, M., Brown, S., Camilloni, I., Diedhiou, A., Djalante, R., Ebi, K. and Engelbrecht, F. (2018). Impacts of 1.5 ºC global warming on natural and human systems.

Holah, N., Baghdadi, N., Zribi, M., Bruand, A. and King, C. (2005). Potential of ASAR/ENVISAT for the characterization of soil surface parameters over bare agricultural fields. *Remote Sensing of Environment, 96*(1), 78-86.

Holland, M. M. and Landrum, L. (2015). Factors affecting projected Arctic surface shortwave heating and albedo change in coupled climate models. *Philosophical Transactions of the Royal Society A: Mathematical, Physical and Engineering Sciences, 373*(2045), 20140162.

Hongxing, L., Lei, W. and Jezek, K. C. (2006). Automated delineation of dry and melt snow zones in Antarctica using active and passive microwave observations from space. *IEEE Transactions on Geoscience and Remote Sensing, 44*(8), 2152-2163. doi: 10.1109/tgrs.2006.872132

Hori, M., Sugiura, K., Kobayashi, K., Aoki, T., Tanikawa, T., Kuchiki, K., Niwano, M. and Enomoto, H. (2017). A 38-year (1978–2015) Northern Hemisphere daily snow cover extent product derived using consistent objective criteria from satellite-borne optical sensors. *Remote Sensing of Environment, 191*, 402-418.

Horning, N. (2013). Introduction to decision trees and random forests. *Am. Mus. Nat. Hist*.

Huang, L., Li, Z., Tian, B.-S., Chen, Q., Liu, J.-L. and Zhang, R. (2011). Classification and snow line detection for glacial areas using the polarimetric SAR image. *Remote Sensing of Environment, 115*(7), 1721-1732. doi: 10.1016/j.rse.2011.03.004

Huang, L., Li, Z., Tian, B.-s., Chen, Q. and Zhou, J.-m. (2013). Monitoring glacier zones and snow/firn line changes in the Qinghai–Tibetan Plateau using C-band SAR imagery. *Remote Sensing of Environment, 137*, 17-30. doi: 10.1016/j.rse.2013.05.016

Huang, Q., Long, D., Du, M., Zeng, C., Qiao, G., Li, X., Hou, A. and Hong, Y. (2018). Discharge estimation in high-mountain regions with improved methods using multisource remote sensing: A case study of the Upper Brahmaputra River. *Remote Sensing of Environment, 219*, 115-134.

Huss, M., Bookhagen, B., Huggel, C., Jacobsen, D., Bradley, R. S., Clague, J. J., Vuille, M., Buytaert, W., Cayan, D. R. and Greenwood, G. (2017). Toward mountains without permanent snow and ice. *Earth's Future, 5*(5), 418-435.

Immerzeel, W. W., Van Beek, L. P. and Bierkens, M. F. (2010). Climate change will affect the Asian water towers. *Science, 328*(5984), 1382-1385.

Immitzer, M., Atzberger, C. and Koukal, T. (2012). Tree Species Classification with Random Forest Using Very High Spatial Resolution 8-Band WorldView-2 Satellite Data. *Remote Sensing, 4*(9), 2661.

Immitzer, M., Vuolo, F. and Atzberger, C. (2016). First Experience with Sentinel-2 Data for Crop and Tree Species Classifications in Central Europe. *Remote Sensing, 8*(3), 166.

Jarvis, A., Reuter, H. I., Nelson, A. and Guevara, E. (2008). Hole-filled SRTM for the globe Version 4.

Jeong, D. I., Sushama, L. and Khaliq, M. N. (2017). Attribution of spring snow water equivalent (SWE) changes over the northern hemisphere to anthropogenic effects. *Climate Dynamics, 48*(11-12), 3645-3658.

Ji, X., Chen, Y., Tong, L., Jia, M., Tan, L. and Fan, S. (2014). *Area retrieval of melting snow in alpine areas.* Paper presented at the Geoscience and Remote Sensing Symposium (IGARSS), 2014 IEEE International.

Johansson, A. M., Brekke, C., Spreen, G. and King, J. A. (2018). X-, C-, and L-band SAR signatures of newly formed sea ice in Arctic leads during winter and spring. *Remote Sensing of Environment, 204*, 162-180.

Jylhä, K., Fronzek, S., Tuomenvirta, H., Carter, T. R. and Ruosteenoja, K. (2008). Changes in frost, snow and Baltic sea ice by the end of the twenty-first century based on climate model projections for Europe. *Climatic Change, 86*(3-4), 441-462.

König, M., Winther, J. G. and Isaksson, E. (2001). Measuring snow and glacier ice properties from satellite. *Reviews of geophysics, 39*(1), 1-27.

Kaasalainen, S., Holopainen, M., Karjalainen, M., Vastaranta, M., Kankare, V., Karila, K. and Osmanoglu, B. (2015). Combining lidar and synthetic aperture radar data to estimate forest biomass: status and prospects. *Forests, 6*(1), 252-270.

Kabiri, K., Pradhan, B., Sharifi, A., Ghobadi, Y. and Pirasteh, S. (2012). *Manifestation of remotely sensed data coupled with field measured meteorological data for an assessment of degradation of Urmia Lake, Iran.* Paper presented at the Asia Pacific Conference on Environmental Science and Technology. APEST, Kuala Lumpur, Malaysia.

Karam, M. A., Amar, F., Fung, A. K., Mougin, E., Lopes, A., Le Vine, D. M. and Beaudoin, A. (1995). A microwave polarimetric scattering model for forest canopies based on vector radiative transfer theory. *Remote Sensing of Environment, 53*(1), 16-30.

Karbassi, A., Bidhendi, G. N., Pejman, A. and Bidhendi, M. E. (2010). Environmental impacts of desalination on the ecology of Lake Urmia. *Journal of Great Lakes Research, 36*(3), 419-424.

Karthikeyan, L., Pan, M., Wanders, N., Kumar, D. N. and Wood, E. F. (2017). Four decades of microwave satellite soil moisture observations: Part 1. A review of retrieval algorithms. *Advances in Water Resources, 109*, 106-120.

Kerr, Y. H., Mahmoodi, A., Mialon, A., Al Biltar, A., Rodriguez-Fernandez, N., Richaume, P., Cabot, F., Wigneron, J. P., Waldteufel, P. and Ferrazzoli, P. (2018). Soil Moisture Retrieval Algorithms: The SMOS Case: Elsevier.

Kevin, J.-P. W., Kotlarski, S., Scherrer, S. C. and Schär, C. (2017). The Alpine snow-albedo feedback in regional climate models. *Climate Dynamics, 48*(3-4), 1109-1124.

Key, J., Drinkwater, M. and Ukita, J. (2007). IGOS cryosphere theme report. *WMO/TD, 1405*, 100.

Kilpeläinen, A., Gregow, H., Strandman, H., Kellomäki, S., Venäläinen, A. and Peltola, H. (2010). Impacts of climate change on the risk of snow-induced forest damage in Finland. *Climatic Change, 99*(1-2), 193-209.

Kim, E., Gatebe, C., Hall, D., Newlin, J., Misakonis, A., Elder, K., Marshall, H. P., Heimstra, C., Brucker, L. and De Marco, E. (2017). *Overview of SnowEx Year 1 Activities*.

Kim, J.-R., Lin, S.-Y., Yun, H.-W., Tsai, Y.-L., Seo, H.-J., Hong, S. and Choi, Y. (2017). Investigation of Potential Volcanic Risk from Mt. Baekdu by DInSAR Time Series Analysis and Atmospheric Correction. *Remote Sensing, 9*(2), 138.

Klein, A. G., Hall, D. K. and Riggs, G. A. (1998). Improving snow cover mapping in forests through the use of a canopy reflectance model. *Hydrological Processes, 12*(10), 1723-1744.

Klein, I., Gessner, U., Dietz, A. J. and Kuenzer, C. (2017). Global WaterPack–A 250 m resolution dataset revealing the daily dynamics of global inland water bodies. *Remote Sensing of Environment, 198*, 345-362.

Knowles, N., Dettinger, M. D. and Cayan, D. R. (2006). Trends in snowfall versus rainfall in the western United States. *Journal of Climate, 19*(18), 4545-4559.

Kobierska, F., Jonas, T., Zappa, M., Bavay, M., Magnusson, J. and Bernasconi, S. M. (2013). Future runoff from a partly glacierized watershed in Central Switzerland: A two-model approach. *Advances in Water Resources, 55*, 204-214.

Koskinen, J. T., Pulliainen, J. T. and Hallikainen, M. T. (1997). The use of ERS-1 SAR data in snow melt monitoring. *IEEE Transactions on Geoscience and Remote Sensing, 35*(3), 601-610.

Koskinen, J. T., Pulliainen, J. T., Luojus, K. P. and Takala, M. (2010). Monitoring of snow-cover properties during the spring melting period in forested areas. *IEEE Transactions on Geoscience and Remote Sensing, 48*(1), 50-58.

Krol, Q. and Löwe, H. (2016). Analysis of local ice crystal growth in snow. *Journal of Glaciology, 62*(232), 378-390.

Kumar, V. and Venkataraman, G. (2011). SAR interferometric coherence analysis for snow cover mapping in the western Himalayan region. *International Journal of Digital Earth, 4*(1), 78-90. doi: 10.1080/17538940903521591

Kummu, M., Tes, S., Yin, S., Adamson, P., Józsa, J., Koponen, J., Richey, J. and Sarkkula, J. (2014). Water balance analysis for the Tonle Sap Lake–floodplain system. *Hydrological Processes, 28*(4), 1722-1733.

Kunkel, K. E., Robinson, D. A., Champion, S., Yin, X., Estilow, T. and Frankson, R. M. (2016). Trends and extremes in Northern Hemisphere snow characteristics. *Current Climate Change Reports, 2*(2), 65-73.

Kvambekk, Å. S. and Melvold, K. (2010). Long-term trends in water temperature and ice cover in the subalpine lake, Øvre Heimdalsvatn, and nearby lakes and rivers. *Hydrobiologia, 642*(1), 47-60.

Lüneburg, E. (2001). *Foundations of the mathematical theory of polarimetry*: EML Consultants Ltd., Colombo, Sri Lanka, Tech. Rep. N00014-00-M-0152.

Löw, A., Ludwig, R. and Mauser, W. (2002). *Land use dependent snow cover retrieval using multitemporal, multisensoral SAR-images to drive operational flood forecasting models.* Paper presented at the Proceedings of EARSeL-LISSIG-Workshop Observing our Cryosphere from Space.

Langley, K., Hamran, S.-E., Hogda, K. A., Storvold, R., Brandt, O., Hagen, J. O. and Kohler, J. (2007). Use of C-band ground penetrating radar to determine backscatter sources within glaciers. *IEEE Transactions on Geoscience and Remote Sensing, 45*(5), 1236-1246.

Lavalle, M. and Wright, T. (2009). Absolute radiometric and polarimetric calibration of ALOS PALSAR products. *Document Issue (1), Revision (3)*.

Lawrence, D. M. and Slater, A. G. (2010). The contribution of snow condition trends to future ground climate. *Climate Dynamics, 34*(7-8), 969-981.

Lee, J.-S. (1981). Refined filtering of image noise using local statistics. *Computer graphics and image processing, 15*(4), 380-389.

Lee, J.-S. (1983). Digital image smoothing and the sigma filter. *Computer vision, graphics, and image processing, 24*(2), 255-269.

Lee, J.-S. and Pottier, E. (2009). *Polarimetric radar imaging: from basics to applications*: CRC press.

Lee, J. and Pottier, E. (2009). Polarimetric Radar Imaging: From Basics to Applications. *Optical Science and Engineering*.

Lehner, B. and Döll, P. (2004). Development and validation of a global database of lakes, reservoirs and wetlands. *Journal of Hydrology, 296*(1-4), 1-22.

Lehning, M., Bartelt, P., Brown, B., Fierz, C. and Satyawali, P. (2002). A physical SNOWPACK model for the Swiss avalanche warning: Part II. Snow microstructure. *Cold Regions Science and Technology, 35*(3), 147-167.

Lei, Y., Yao, T., Bird, B. W., Yang, K., Zhai, J. and Sheng, Y. (2013). Coherent lake growth on the central Tibetan Plateau since the 1970s: Characterization and attribution. *Journal of Hydrology, 483*, 61-67.

Lemke, P., Ren, J., Alley, R. B., Allison, I., Carrasco, J., Flato, G., Fujii, Y., Kaser, G., Mote, P. and Thomas, R. H. (2007). *Observations: changes in snow, ice and frozen ground*. Cambridge University Press: Cambridge, UK

Lessard-Fontaine, A., Allain, S., Dedieu, J.-P. and Durand, Y. (2012). *Multi-temporal wet snow mapping in alpine context using polarimetric Radarsat-2 time-series.* Paper presented at the Geoscience and Remote Sensing Symposium (IGARSS), 2012 IEEE International.

Lewis, D. D. and Gale, W. A. (1994). *A sequential algorithm for training text classifiers.* Paper presented at the Proceedings of the 17th annual international ACM SIGIR conference on Research and development in information retrieval.

Li, D., Wrzesien, M. L., Durand, M., Adam, J. and Lettenmaier, D. P. (2017). How much runoff originates as snow in the western United States, and how will that change in the future? *Geophysical Research Letters, 44*(12), 6163-6172.

Li, Z., Guo, H., Li, X. and Wang, C. (2001). *SAR Interferometry coherence analysis for snow mapping.* Paper presented at the Geoscience and Remote Sensing Symposium, 2001. IGARSS'01. IEEE 2001 International.

Lillesand, T. M. and Kiefer, R. W. (1994). Remote sensing and photo interpretation. *John Wiley and Sons: New York*, 750.

LIU, C.-a., CHEN, Z.-x., Yun, S., CHEN, J.-s., Hasi, T. and PAN, H.-z. (2019). Research advances of SAR remote sensing for agriculture applications: A review. *Journal of Integrative Agriculture, 18*(3), 506-525.

Longépé, N., Allain, S. and Pottier, E. (2008). *Toward an Operational Method for Refined Snow Characterization Using Dual-Polarization C-Band SAR Data.* Paper presented at the Geoscience and Remote Sensing Symposium, 2008. IGARSS 2008. IEEE International.

Longepe, N., Allain, S., Ferro-Famil, L., Pottier, E. and Durand, Y. (2009). Snowpack Characterization in Mountainous Regions Using C-Band SAR Data and a Meteorological Model. *IEEE Transactions on Geoscience and Remote Sensing, 47*(2), 406-418. doi: 10.1109/tgrs.2008.2006048

Longepe, N., Shimada, M., Allain, S. and Pottier, E. (2008). *Capabilities of full-polarimetric PALSAR/ALOS for snow extent mapping.* Paper presented at the Geoscience and Remote Sensing Symposium, 2008. IGARSS 2008. IEEE International.

Lu, H., Raupach, M. R., McVicar, T. R. and Barrett, D. J. (2003). Decomposition of vegetation cover into woody and herbaceous components using AVHRR NDVI time series. *Remote Sensing of Environment, 86*(1), 1-18.

Luo, X., Wang, M., Dai, G. and Chen, X. (2017). A novel technique to compute the revisit time of satellites and its application in remote sensing satellite optimization design. *International Journal of Aerospace Engineering, 2017*.

Luojus, K., Kärnä, J.-P., Hallikainen, M. and Pulliainen, J. (2006). *Development of techniques to retrieve Snow Covered Area (SCA) in boreal forests from space-borne microwave observations.* Paper presented at the Geoscience and Remote Sensing Symposium, 2006. IGARSS 2006. IEEE International Conference on.

Luojus, K., Pulliainen, J. and Metsämäki, S. (2009). *Evaluation of the single reference image snow-covered area estimation method for the boreal forest zone.* Paper presented at the Geoscience and Remote Sensing Symposium, 2009 IEEE International, IGARSS 2009.

Luojus, K., Pulliainen, J., Metsämäki, S., Molera, G., Nakari, R., Kärnä, J.-P. and Hallikainen, M. (2008). *Development of sar-based snow-covered area estimation method for borel forest zone.* Paper presented at the Geoscience and Remote Sensing Symposium, 2008. IGARSS 2008. IEEE International.

Luojus, K. P., Pulliainen, J. T., Blasco Cutrona, A., Metsämäki, S. J. and Hallikainen, M. T. (2009). Comparison of SAR-Based Snow-Covered Area Estimation Methods for the Boreal Forest Zone. *IEEE Geoscience and Remote Sensing Letters, 6*(3), 403-407. doi: 10.1109/lgrs.2009.2014786

Luojus, K. P., Pulliainen, J. T., Metsämäki, S. J. and Hallikainen, M. T. (2006). Accuracy assessment of SAR data-based snow-covered area estimation method. *IEEE Transactions on Geoscience and Remote Sensing, 44*(2), 277-287. doi: 10.1109/tgrs.2005.861414

Luojus, K. P., Pulliainen, J. T., Metsämäki, S. J. and Hallikainen, M. T. (2007). Snow-Covered Area Estimation Using Satellite Radar Wide-Swath Images. *IEEE Transactions on Geoscience and Remote Sensing, 45*(4), 978-989. doi: 10.1109/tgrs.2006.888864

Luojus, K. P., Pulliainen, J. T., Metsämäki, S. J. and Hallikainen, M. T. (2009). Enhanced SAR-Based Snow-Covered Area Estimation Method for Boreal Forest Zone. *IEEE Transactions on Geoscience and Remote Sensing, 47*(3), 922-935. doi: 10.1109/tgrs.2008.2006047

Mätzler, C. (1987). Applications of the interaction of microwaves with the natural snow cover. *Remote Sensing Reviews, 2*(2), 259-387.

Mätzler, C. and Schanda, E. (1984). Snow mapping with active microwave sensors. *Remote Sensing, 5*(2), 409-422.

Macander, M. J., Swingley, C. S., Joly, K. and Raynolds, M. K. (2015). Landsat-based snow persistence map for northwest Alaska. *Remote Sensing of Environment, 163*, 23-31.

Madani, K. (2014). Water management in Iran: what is causing the looming crisis? *Journal of environmental studies and sciences, 4*(4), 315-328.

Madsen, J., Tamstorf, M., Klaassen, M., Eide, N., Glahder, C., Rigét, F., Nyegaard, H. and Cottaar, F. (2007). Effects of snow cover on the timing and success of reproduction in high-Arctic pink-footed geese Anser brachyrhynchus. *Polar biology, 30*(11), 1363-1372.

Magagi, R. and Bernier, M. (2003). Optimal conditions for wet snow detection using RADARSAT SAR data. *Remote Sensing of Environment, 84*(2), 221-233.

Magnin, F., Westermann, S., Pogliotti, P., Ravanel, L., Deline, P. and Malet, E. (2017). Snow control on active layer thickness in steep alpine rock walls (Aiguille du Midi, 3842 m asl, Mont Blanc massif). *Catena, 149*, 648-662.

Magnusson, J., Jonas, T., López-Moreno, I. and Lehning, M. (2010). Snow cover response to climate change in a high alpine and half-glacierized basin in Switzerland. *Hydrology Research, 41*(3-4), 230-240.

Malenovský, Z., Rott, H., Cihlar, J., Schaepman, M. E., García-Santos, G., Fernandes, R. and Berger, M. (2012). Sentinels for science: Potential of Sentinel-1, -2, and -3 missions for scientific observations of ocean, cryosphere, and land. *Remote Sensing of Environment, 120*, 91-101. doi: 10.1016/j.rse.2011.09.026

Malnes, E. and Guneriussen, T. (2002). *Mapping of snow covered area with Radarsat in Norway.* Paper presented at the Geoscience and Remote Sensing Symposium, 2002. IGARSS'02. 2002 IEEE International.

Malnes, E., Storvold, R. and Lauknes, I. (2004). *Near real time snow covered area mapping with Envisat ASAR wideswath in Norwegian mountainous areas.* Paper presented at the ESA ENVISAT & ERS Symposium.

Malnes, E., Storvold, R., Lauknes, I. and Pettinato, S. (2006). Multi-polarisation measurements of snow signatures with air-and satelliteborne SAR. *EARSeL eProceedings, 5*(1), 111.

Manuel, G., Gascoin, S., Hagolle, O., L'helguen, C. and Klempka, T. (2016). *Let it snow - operational snow cover product from Sentinel-2 and Landsat-8 data.* Paper presented at the Living planet symposium 2016, Prague, Czech Republich.

Mao, K., Ma, Y., Tan, X. a., Shen, X., Liu, G., Li, Z., Chen, J. and Xia, L. (2017). Global surface temperature change analysis based on MODIS data in recent twelve years. *Advances in Space Research, 59*(2), 503-512.

Marin, C., Bertoldi, G., Premier, V., Callegari, M., Brida, C., Hürkamp, K., Tschiersch, J., Zebisch, M. and Notarnicola, C. (2019). Use of Sentinel-1 radar observations to evaluate snowmelt dynamics in alpine regions.

Martini, A., Ferro-Famil, L. and Pottier, E. (2003). *Polarimetric study of scattering from dry snow cover in alpine areas.* Paper presented at the Geoscience and Remote Sensing Symposium, 2003. IGARSS'03. Proceedings. 2003 IEEE International.

Martini, A., Ferro-Famil, L., Pottier, E. and Dedieu, J. P. (2006). Dry snow discrimination in alpine areas from multi-frequency and multi-temporal SAR data. *IEE Proceedings - Radar, Sonar and Navigation, 153*(3), 271. doi: 10.1049/ip-rsn:20045104

Martone, M., Bräutigam, B. and Krieger, G. (2012). *Decorrelation effects in bistatic TanDEM-X data.* Paper presented at the Geoscience and Remote Sensing Symposium (IGARSS), 2012 IEEE International.

Marty, C., Schlögl, S., Bavay, M. and Lehning, M. (2017). How much can we save? Impact of different emission scenarios on future snow cover in the Alps. *The Cryosphere, 11*(1), 517.

McCabe, G. J., Clark, M. P. and Hay, L. E. (2007). Rain-on-snow events in the western United States. *Bulletin of the American Meteorological Society, 88*(3), 319-328.

McCabe, G. J. and Wolock, D. M. (2010). Long-term variability in Northern Hemisphere snow cover and associations with warmer winters. *Climatic Change, 99*(1-2), 141-153.

McFeeters, S. K. (1996). The use of the Normalized Difference Water Index (NDWI) in the delineation of open water features. *International Journal of Remote Sensing, 17*(7), 1425-1432.

Merz, R. and Blöschl, G. (2003). A process typology of regional floods. *Water Resources Research, 39*(12).

Metsämäki, S., Ripper, E., Mattila, O.-P., Fernandes, R., Schwaizer, G., Luojus, K., Nagler, T., Bojkov, B. and Kern, M. (2017). *Evaluation of Northern Hemisphere and regional snow extent products within ESA SnowPEx-project.* Paper presented at the Geoscience and Remote Sensing Symposium (IGARSS), 2017 IEEE International.

Metz, C. E. (1978). *Basic principles of ROC analysis.* Paper presented at the Seminars in nuclear medicine.

Minh, D. H. T., Le Toan, T., Rocca, F., Tebaldini, S., d'Alessandro, M. M. and Villard, L. (2014). Relating P-band synthetic aperture radar tomography to tropical forest biomass. *IEEE Transactions on Geoscience and Remote Sensing, 52*(2), 967-979.

Mo, B., Helseth, A. and Warland, G. (2018). *Modeling and Quantifying the Importance of Snow Storage Information for the Nordic Power System.* Paper presented at the 2018 15th International Conference on the European Energy Market (EEM).

Mock, C. J. and Birkeland, K. W. (2000). Snow avalanche climatology of the western United States mountain ranges. *Bulletin of the American Meteorological Society, 81*(10), 2367-2392.

Moghaddam, M. and Saatchi, S. (1995). Analysis of scattering mechanisms in SAR imagery over boreal forest: Results from BOREAS'93. *IEEE Transactions on Geoscience and Remote Sensing, 33*(5), 1290-1296.

Muala, E., Mohamed, Y. A., Duan, Z. and Van der Zaag, P. (2014). Estimation of reservoir discharges from Lake Nasser and Roseires Reservoir in the Nile Basin using satellite altimetry and imagery data. *Remote Sensing, 6*(8), 7522-7545.

Mudryk, L., Kushner, P., Derksen, C. and Thackeray, C. (2017). Snow cover response to temperature in observational and climate model ensembles. *Geophysical Research Letters, 44*(2), 919-926.

Muhuri, A., Manickam, S. and Bhattacharya, A. (2017). Scattering Mechanism Based Snow Cover Mapping Using RADARSAT-2 C-Band Polarimetric SAR Data. *IEEE Journal of Selected Topics in Applied Earth Observations and Remote Sensing, 10*(7), 3213-3224. doi: 10.1109/jstars.2017.2681719

Muhuri, A., Manickam, S., Bhattacharya, A. and Snehmani. (2018). Snow Cover Mapping Using Polarization Fraction Variation With Temporal RADARSAT-2 C-Band Full-Polarimetric SAR Data Over the Indian Himalayas. *IEEE Journal of Selected Topics in Applied Earth Observations and Remote Sensing*, 1-18. doi: 10.1109/JSTARS.2018.2817687

Muhuri, A., Ratha, D. and Bhattacharya, A. (2017). Seasonal Snow Cover Change Detection Over the Indian Himalayas Using Polarimetric SAR Images. *IEEE Geoscience and Remote Sensing Letters, 14*(12), 2340-2344. doi: 10.1109/lgrs.2017.2764123

Nagare, M., Aoki, H. and Kaneko, E. (2017). *A unified method of cloud detection and removal robust to spectral variability.* Paper presented at the 2017 IEEE International Geoscience and Remote Sensing Symposium (IGARSS).

Nagler, T. (1996). *Methods and analysis of synthetic aperture radar data from ERS-1 and X-SAR for snow and glacier applications.* Leopold-Franzens-Universität Innsbruck.

Nagler, T. and Rott, H. (2000). Retrieval of wet snow by means of multitemporal SAR data. *IEEE Transactions on Geoscience and Remote Sensing, 38*(2), 754-765.

Nagler, T. and Rott, H. (2005). *Snow classification algorithm for Envisat ASAR.* Paper presented at the Envisat & ERS Symposium.

Nagler, T., Rott, H., Ossowska, J., Schwaizer, G., Small, D., Malnes, E., Luojus, K., Metsämäki, S. and Pinnock, S. (2018). *Snow Cover Monitoring by Synergistic Use of Sentinel-3 Slstr and Sentinel-L Sar Data.* Paper presented at the IGARSS 2018-2018 IEEE International Geoscience and Remote Sensing Symposium.

Nagler, T., Rott, H., Ripper, E., Bippus, G. and Hetzenecker, M. (2016a). Advancements for Snowmelt Monitoring by Means of Sentinel-1 SAR. *Remote Sensing, 8*(12), 348. doi: 10.3390/rs8040348

Nagler, T., Rott, H., Ripper, E., Bippus, G. and Hetzenecker, M. (2016b). Advancements for snowmelt monitoring by means of sentinel-1 SAR. *Remote Sensing, 8*(4), 348.

Najafi, M. R., Zwiers, F. W. and Gillett, N. P. (2016). Attribution of the spring snow cover extent decline in the Northern Hemisphere, Eurasia and North America to anthropogenic influence. *Climatic Change, 136*(3-4), 571-586.

Niang, M., Dedieu, J.-P., Durand, Y., Mérindol, L., Bernier, M. and Dumont, M. (2007). *New inversion method for snow density and snow liquid water content retrieval using C-band data from ENVISAT/ASAR alternating polarization in alpine environment.* Paper presented at the Proc. ENVISAT Symp.

Niittynen, P., Heikkinen, R. K. and Luoto, M. (2018). Snow cover is a neglected driver of Arctic biodiversity loss. *Nature Climate Change, 8*(11), 997-1001.

Nijhawan, R., Das, J. and Raman, B. (2018). A hybrid of deep learning and hand-crafted features based approach for snow cover mapping. *International Journal of Remote Sensing*, 1-15.

Nijssen, B., O'Donnell, G. M., Hamlet, A. F. and Lettenmaier, D. P. (2001). Hydrologic sensitivity of global rivers to climate change. *Climatic Change, 50*(1-2), 143-175.

Nilsson, K. A., Trout, K. E. and Ross, M. A. (2010). General model to represent multiple wetland and lake stage-storage behavior. *Journal of Hydrologic Engineering, 15*(10), 786-795.

Notarnicola, C. (2020). Hotspots of snow cover changes in global mountain regions over 2000–2018. *Remote Sensing of Environment, 243*, 111781.

Notarnicola, C., Duguay, M., Moelg, N., Schellenberger, T., Tetzlaff, A., Monsorno, R., Costa, A., Steurer, C. and Zebisch, M. (2013). Snow cover maps from MODIS images at 250 m resolution, Part 1: Algorithm description. *Remote Sensing, 5*(1), 110-126.

Notarnicola, C., Ratti, R., Maddalena, V., Schellenberger, T., Ventura, B. and Zebisch, M. (2013). Seasonal Snow Cover Mapping in Alpine Areas Through Time Series of COSMO-SkyMed Images. *IEEE Geoscience and Remote Sensing Letters, 10*(4), 716-720. doi: 10.1109/lgrs.2012.2219848

Notarnicola, C., Schellenberger, T., Ventura, B., Zebisch, M., Maddalena, V., Ratti, R. and Tampellini, L. (2012). *Time series analysis of dual-pol COSMO-SkyMed images for monitoring snow cover in alpine areas.* Paper presented at the Geoscience and Remote Sensing Symposium (IGARSS), 2012 IEEE International.

Nouri, H., Mason, R. J. and Moradi, N. (2017). Land suitability evaluation for changing spatial organization in Urmia County towards conservation of Urmia Lake. *Applied Geography, 81*, 1-12.

Oliva, M., Hrbacek, F., Ruiz-Fernández, J., de Pablo, M. Á., Vieira, G., Ramos, M. and Antoniades, D. (2017). Active layer dynamics in three topographically distinct lake catchments in Byers Peninsula (Livingston Island, Antarctica). *Catena, 149*, 548-559.

Olsen, M., Callaghan, T., Reist, J., Reiersen, L., Dahl-Jensen, D., Granskog, M., Goodison, B., Hovelsrud, G., Johansson, M. and Kallenborn, R. (2011). The changing Arctic cryosphere and likely consequences: An overview. *Ambio, 40*(1), 111-118.

Otsu, N. (1979). A threshold selection method from gray-level histograms. *IEEE transactions on systems, man, and cybernetics, 9*(1), 62-66.

Pachauri, R. K., Allen, M. R., Barros, V. R., Broome, J., Cramer, W., Christ, R., Church, J. A., Clarke, L., Dahe, Q. and Dasgupta, P. (2014). *Climate change 2014: synthesis report. Contribution of Working Groups I, II and III to the fifth assessment report of the Intergovernmental Panel on Climate Change*: Ipcc.

Pal, M. (2005). Random forest classifier for remote sensing classification. *International Journal of Remote Sensing, 26*(1), 217-222.

Paloscia, S., Pettinato, S., Santi, E. and Valt, M. (2017). COSMO-SkyMed Image Investigation of Snow Features in Alpine Environment. *Sensors (Basel), 17*(1). doi: 10.3390/s17010084

Paradis, M., Lévesque, E. and Boudreau, S. (2016). Greater effect of increasing shrub height on winter versus summer soil temperature. *Environmental Research Letters, 11*(8), 085005.

Park, S.-E., Yamaguchi, Y., Singh, G., Yamaguchi, S. and Whitaker, A. C. (2014). Polarimetric SAR Response of Snow-Covered Area Observed by Multi-Temporal ALOS PALSAR Fully Polarimetric Mode. *IEEE Transactions on Geoscience and Remote Sensing, 52*(1), 329-340. doi: 10.1109/tgrs.2013.2240000

Parry, V., Nienow, P., Mair, D., Scott, J., Hubbard, B., Steffen, K. and Wingham, D. (2007). Investigations of meltwater refreezing and density variations in the snowpack and firn within the percolation zone of the Greenland ice sheet. *Annals of Glaciology, 46*, 61-68.

Peings, Y. and Douville, H. (2010). Influence of the Eurasian snow cover on the Indian summer monsoon variability in observed climatologies and CMIP3 simulations. *Climate Dynamics, 34*(5), 643-660.

Pellizzeri, T. M. (2003). Classification of polarimetric SAR images of suburban areas using joint annealed segmentation and "H/A/α" polarimetric decomposition. *ISPRS Journal of Photogrammetry and Remote Sensing, 58*(1-2), 55-70.

Pengra, B. (2012). The Drying of Iran's Lake Urmia and its Environmental Consequences. UNEP Global Environmental Alert Service (GEAS) Bulletin.

Pepe, M., Brivio, P., Rampini, A., Nodari, F. R. and Boschetti, M. (2005). Snow cover monitoring in Alpine regions using ENVISAT optical data. *International Journal of Remote Sensing, 26*(21), 4661-4667.

Pepin, N., Bradley, R. S., Diaz, H., Baraër, M., Caceres, E., Forsythe, N., Fowler, H., Greenwood, G., Hashmi, M. and Liu, X. (2015). Elevation-dependent warming in mountain regions of the world. *Nature Climate Change, 5*(5), 424-430.

Perovich, D., Grenfell, T., Light, B. and Hobbs, P. (2002). Seasonal evolution of the albedo of multiyear Arctic sea ice. *Journal of Geophysical Research: Oceans, 107*(C10), SHE 20-21-SHE 20-13.

Pesaran, M. H., Shin, Y. and Smith, R. J. (2001). Bounds testing approaches to the analysis of level relationships. *Journal of applied econometrics, 16*(3), 289-326.

Pettianato, S., Santi, E., Brogioni, M., Macelloni, G., Paloscia, S. and Pampaloni, P. (2010). *An operational algorithm for snow cover mapping by using optical and SAR data.* Paper presented at the ESA Living Planet Symposium.

Pettinato, S., Malnes, E. and Haarpaintner, J. (2006). *Snow cover maps with satellite borne SAR: A new approach in harmony with fractional optical SCA retrieval algorithms.* Paper presented at the Geoscience and Remote Sensing Symposium, 2006. IGARSS 2006. IEEE International.

Pettinato, S., Poggi, P., Macelloni, G., Paloscia, S., Pampaloni, P. and Crepaz, A. (2004). *Mapping snow cover in alpine areas with ENVISAT/SAR images.* Paper presented at the Proc. of the Envisat & ERS Symp.

Pettinato, S., Santi, E., Brogioni, M., Macelloni, G., Paloscia, S. and Pampaloni, P. (2009). *Snow cover mapping by using optical and SAR data.* Paper presented at the Image and Signal Processing for Remote Sensing XV.

Pettinato, S., Santi, E., Brogioni, M., Paloscia, S. and Pampaloni, P. (2009). *An operational algorithm for snow cover mapping in hydrological applications.* Paper presented at the Geoscience and Remote Sensing Symposium, 2009 IEEE International, IGARSS 2009.

Pettinato, S., Santi, E. and Paloscia, S. (2017). *Investigation of alpine snow features using cosmo-skymed images.* Paper presented at the Geoscience and Remote Sensing Symposium (IGARSS), 2017 IEEE International.

Pettinato, S., Santi, E., Paloscia, S., Aiazzi, B., Baronti, S. and Garzelli, A. (2014). Snow cover area identification by using a change detection method applied to COSMO-SkyMed images. *Journal of Applied Remote Sensing, 8*(1), 084684.

Phan, X.-V., Ferro-Famil, L., Gay, M., Durand, Y., Dumont, M., Allain, S. and D'Urso, G. (2012). Analysis of snowpack properties and structure from TerraSAR-X data, based on multilayer backscattering and snow evolution modeling approaches. *arXiv preprint arXiv:1211.3278*.

Pielke, R. A., Doesken, N., Bliss, O., Green, T., Chaffin, C., Salas, J. D., Woodhouse, C. A., Lukas, J. J. and Wolter, K. (2005). Drought 2002 in Colorado: an unprecedented drought or a routine drought? *pure and applied geophysics, 162*(8-9), 1455-1479.

Pogliotti, P., Guglielmin, M., Cremonese, E., Morra di Cella, U., Filippa, G., Pellet, C. and Hauck, C. (2015). Warming permafrost and active layer variability at Cime Bianche, Western European Alps. *The Cryosphere, 9*(2), 647-661.

Pradhanang, S. M., Frei, A., Zion, M., Schneiderman, E. M., Steenhuis, T. S. and Pierson, D. (2013). Rain-on-snow runoff events in New York. *Hydrological Processes, 27*(21), 3035-3049.

Pratola, C. and Navarro-Sánchez, V. D. (2018). *Snow Cover Monitoring in Hardangervidda and Sierra Nevada Protected Areas by using Sentinel-L Time Series.* Paper presented at the IGARSS 2018-2018 IEEE International Geoscience and Remote Sensing Symposium.

Pulliainen, J. T. (1994). *Investigation on the backscattering properties of Finnish boreal forests at C-and X-band: A semi-empirical modeling approach.*

Pulliainen, J. T., Heiska, K., Hyyppa, J. and Hallikainen, M. T. (1994). Backscattering properties of boreal forests at the C-and X-bands. *IEEE Transactions on Geoscience and Remote Sensing, 32*(5), 1041-1050.

Qiu, S., He, B., Zhu, Z., Liao, Z. and Quan, X. (2017). Improving Fmask cloud and cloud shadow detection in mountainous area for Landsats 4–8 images. *Remote Sensing of Environment, 199*, 107-119.

Rao, Y., Venkataraman, G. and Singh, G. (2006). *ENVISAT-ASAR data analysis for snow cover mapping over Gangotri region.* Paper presented at the Microwave Remote Sensing of the Atmosphere and Environment V.

Rauscher, S. A., Pal, J. S., Diffenbaugh, N. S. and Benedetti, M. M. (2008). Future changes in snowmelt-driven runoff timing over the western US. *Geophysical Research Letters, 35*(16).

Rees, W. G. (2005). *Remote sensing of snow and ice*: CRC press.

Reppucci, A., Banque, X., Zhan, Y., Alonso, A. and López-Martinez, C. (2012). Estimation of snow pack characteristics by means of polarimetric SAR data. *Remote Sensing for Agriculture, Ecosystems, and Hydrology, 8531*, 85310Z. doi: 10.1117/12.974598

Richardson, W. R. and Thorne, C. R. (2001). Multiple thread flow and channel bifurcation in a braided river: Brahmaputra–Jamuna River, Bangladesh. *Geomorphology, 38*(3-4), 185-196.

Riggs, G. A. and Hall, D. K. (2015). *MODIS snow products collection 6 user guide*: National Snow and Ice Data Center.

Rignot, E., Echelmeyer, K. and Krabill, W. (2001). Penetration depth of interferometric synthetic-aperture radar signals in snow and ice. *Geophysical Research Letters, 28*(18), 3501-3504.

Rizzoli, P., Martone, M. and Brautigam, B. (2015). *Greenland ice sheet snow facies identification approach using TanDEM-X interferometric data.* Paper presented at the Geoscience and Remote Sensing Symposium (IGARSS), 2015 IEEE International.

Rizzoli, P., Martone, M., Brautigam, B., Rott, H. and Moreira, A. (2016). *Multi-Temporal Investigation of Greenland Ice Sheet Snow Facies using TanDEM-X Mission Data.* Paper presented at the Living Planet Symposium.

Rizzoli, P., Martone, M., Rott, H. and Moreira, A. (2017). Characterization of Snow Facies on the Greenland Ice Sheet Observed by TanDEM-X Interferometric SAR Data. *Remote Sensing, 9*(12), 315. doi: 10.3390/rs9040315

Rodriguez-Galiano, V., Sanchez-Castillo, M., Chica-Olmo, M. and Chica-Rivas, M. (2015). Machine learning predictive models for mineral prospectivity: An evaluation of neural networks, random forest, regression trees and support vector machines. *Ore Geology Reviews, 71*, 804-818.

Rodriguez-Galiano, V. F., Chica-Olmo, M., Abarca-Hernandez, F., Atkinson, P. M. and Jeganathan, C. (2012). Random Forest classification of Mediterranean land cover using multi-seasonal imagery and multi-seasonal texture. *Remote Sensing of Environment, 121*, 93-107. doi: https://doi.org/10.1016/j.rse.2011.12.003

Rodriguez, E., Morris, C. S. and Belz, J. E. (2006). A global assessment of the SRTM performance. *Photogrammetric Engineering & Remote Sensing, 72*(3), 249-260.

Romanov, P., Gutman, G. and Csiszar, I. (2000). Automated monitoring of snow cover over North America with multispectral satellite data. *Journal of Applied Meteorology, 39*(11), 1866-1880.

Romanovsky, V. E. and Osterkamp, T. (2000). Effects of unfrozen water on heat and mass transport processes in the active layer and permafrost. *Permafrost and Periglacial Processes, 11*(3), 219-239.

Rott, H. (1984). The analysis of backscattering properties from SAR data of mountain regions. *IEEE Journal of Oceanic Engineering, 9*(5), 347-355.

Rott, H. (1984). Synthetic aperture radar capabilities for snow and glacier monitoring. *Advances in Space Research, 4*(11), 241-246.

Rott, H. (1994). Thematic studies in alpine areas by means of polarimetric SAR and optical imagery. *Advances in Space Research, 14*(3), 217-226.

Rott, H., Cline, D., Nagler, T., Pulliainen, J., Rebhan, H. and Yueh, S. (2007). *CoReH2O-A dual frequency SAR mission for hydrology and climate research.* Paper presented at the Geoscience and Remote Sensing Symposium, 2007. IGARSS 2007. IEEE International.

Rott, H. and Davis, R. E. (1991). *Multi-parameter airborne SAR experiments at an alpine test site.* Paper presented at the Geoscience and Remote Sensing Symposium, 1991. IGARSS'91. Remote Sensing: Global Monitoring for Earth Management., International.

Rott, H. and Mätzler, C. (1987). Possibilities and limits of synthetic aperture radar for snow and glacier surveying. *Annals of Glaciology, 9*, 195-199.

Rott, H. and Nagler, T. (1995). *Monitoring temporal dynamics of snowmelt with ERS-1 SAR.* Paper presented at the Geoscience and Remote Sensing Symposium, 1995. IGARSS'95.'Quantitative Remote Sensing for Science and Applications', International.

Saha, S. K., Pokhrel, S. and Chaudhari, H. S. (2013). Influence of Eurasian snow on Indian summer monsoon in NCEP CFSv2 freerun. *Climate Dynamics, 41*(7-8), 1801-1815.

Salcedo, A. P. and Cogliati, M. G. (2014). Snow Cover Area Estimation Using Radar and Optical Satellite Information. *Atmospheric and Climate Sciences, 04*(04), 514-523. doi: 10.4236/acs.2014.44047

Samanta, A., Tripathy, G. R. and Das, R. (2019). Temporal variations in water chemistry of the (lower) Brahmaputra River: Implications to seasonality in mineral weathering. *Geochemistry, Geophysics, Geosystems, 20*(6), 2769-2785.

Sazonau, V. (2012). Implementation and evaluation of a random forest machine learning algorithm. *University of Manchester, UK*.

Schöber, J., Schneider, K., Helfricht, K., Schattan, P., Achleitner, S., Schöberl, F. and Kirnbauer, R. (2014). Snow cover characteristics in a glacierized catchment in the Tyrolean Alps-Improved spatially distributed modelling by usage of Lidar data. *Journal of Hydrology, 519*, 3492-3510.

Schellenberger, T., Ventura, B., Zebisch, M. and Notarnicola, C. (2012). Wet Snow Cover Mapping Algorithm Based on Multitemporal COSMO-SkyMed X-Band SAR Images. *IEEE Journal of Selected Topics in Applied Earth Observations and Remote Sensing, 5*(3), 1045-1053. doi: 10.1109/jstars.2012.2190720

Scherrer, S., Ceppi, P., Croci-Maspoli, M. and Appenzeller, C. (2012). Snow-albedo feedback and Swiss spring temperature trends. *Theoretical and Applied Climatology, 110*(4), 509-516.

Scherrer, S. C. and Appenzeller, C. (2006). Swiss Alpine snow pack variability: major patterns and links to local climate and large-scale flow. *Climate Research, 32*(3), 187-199.

Schlaepfer, D. R., Lauenroth, W. K. and Bradford, J. B. (2012). Consequences of declining snow accumulation for water balance of mid-latitude dry regions. *Global Change Biology, 18*(6), 1988-1997.

Schmitt, A., Wendleder, A. and Hinz, S. (2015). The Kennaugh element framework for multi-scale, multi-polarized, multi-temporal and multi-frequency SAR image preparation. *ISPRS Journal of Photogrammetry and Remote Sensing, 102*, 122-139.

Schmucki, E., Marty, C., Fierz, C. and Lehning, M. (2015). Simulations of 21st century snow response to climate change in Switzerland from a set of RCMs. *International Journal of Climatology, 35*(11), 3262-3273.

Schmucki, E., Marty, C., Fierz, C., Weingartner, R. and Lehning, M. (2017). Impact of climate change in Switzerland on socioeconomic snow indices. *Theoretical and Applied Climatology, 127*(3-4), 875-889.

Schwaizer, G. (2017, 03 - 07 July 2017). *SAR/Optical Applications to Ice and Snow.* Paper presented at the ESA Training Course on Radar and Optical Remote Sensing, Vilnius, Lithuania.

Schwatke, C., Dettmering, D., Bosch, W. and Seitz, F. (2015). DAHITI–an innovative approach for estimating water level time series over inland waters using multi-mission satellite altimetry. *Hydrology and Earth System Sciences 19 (10): 4345-4364*.

Scott, D. A. (2001). The birds of Lake Orumiyeh and adjacent wetlands, Islamic Republic of Iran. *Ornithology Unit of the Department of the Environment in the 1970s. Retrieved from http://www. wetlands. org/reports/ris/2IR003_Annex. pdf*.

Seager, R. and Vecchi, G. A. (2010). Greenhouse warming and the 21st century hydroclimate of southwestern North America. *Proceedings of the National Academy of Sciences, 107*(50), 21277-21282.

Selkowitz, D. and Forster, R. (2016). An automated approach for mapping persistent ice and snow cover over high latitude regions. *Remote Sensing, 8*(1), 16.

Sellinger, C. E., Stow, C. A., Lamon, E. C. and Qian, S. S. (2008). Recent water level declines in the Lake Michigan− Huron System. *Environmental Science & Technology, 42*(2), 367-373.

Serreze, M., Walsh, J., Chapin, F. S., Osterkamp, T., Dyurgerov, M., Romanovsky, V., Oechel, W., Morison, J., Zhang, T. and Barry, R. (2000). Observational evidence of recent change in the northern high-latitude environment. *Climatic Change, 46*(1-2), 159-207.

Serreze, M. C., Clark, M. P. and Frei, A. (2001). Characteristics of large snowfall events in the montane western United States as examined using snowpack telemetry (SNOTEL) data. *Water Resources Research, 37*(3), 675-688.

Serreze, M. C. and Francis, J. A. (2006). The Arctic amplification debate. *Climatic Change, 76*(3-4), 241-264.

Seyfried, M., Grant, L., Marks, D., Winstral, A. and McNamara, J. (2009). Simulated soil water storage effects on streamflow generation in a mountainous snowmelt environment, Idaho, USA. *Hydrological Processes: An International Journal, 23*(6), 858-873.

Shi, J. and Dozier, J. (1993). Measurements of snow-and glacier-covered areas with single-polarization SAR. *Annals of Glaciology, 17*, 72-76.

Shi, J. and Dozier, J. (1995). Inferring snow wetness using C-band data from SIR-C's polarimetric synthetic aperture radar. *IEEE Transactions on Geoscience and Remote Sensing, 33*(4), 905-914.

Shi, J. and Dozier, J. (1997). Mapping seasonal snow with SIR-C/X-SAR in mountainous areas. *Remote Sensing of Environment, 59*(2), 294-307.

Shi, J. and Dozier, J. (2000). Estimation of snow water equivalence using SIR-C/X-SAR. II. Inferring snow depth and particle size. *IEEE Transactions on Geoscience and Remote Sensing, 38*(6), 2475-2488.

Shi, J., Hensley, S. and Dozier, J. (1997). *Mapping snow cover with repeat pass synthetic aperture radar.* Paper presented at the Geoscience and Remote Sensing, 1997. IGARSS'97. Remote Sensing-A Scientific Vision for Sustainable Development., 1997 IEEE International.

Shine, K. and Henderson-Sellers, A. (1985). The sensitivity of a thermodynamic sea ice model to changes in surface albedo parameterization. *Journal of Geophysical Research: Atmospheres, 90*(D1), 2243-2250.

Sima, S. and Tajrishy, M. (2013). Using satellite data to extract volume–area–elevation relationships for Urmia Lake, Iran. *Journal of Great Lakes Research, 39*(1), 90-99.

Singh, G., Kumar, V., Mohite, K., Venkatraman, G. and Rao, Y. (2006). *Snow wetness estimation in Himalayan snow covered regions using ENVISAT-ASAR data.* Paper presented at the Microwave Remote Sensing of the Atmosphere and Environment V.

Singh, G. and Venkataraman, G. (2012). Application of incoherent target decomposition theorems to classify snow cover over the Himalayan region. *International Journal of Remote Sensing, 33*(13), 4161-4177.

Singh, G., Venkataraman, G. and Rao, Y. (2008). *The H/A/Alpha polarimetric decomposition theorem and complex wishart distribution for snow cover monitoring.* Paper presented at the Geoscience and Remote Sensing Symposium, 2008. IGARSS 2008. IEEE International.

Singh, G., Venkataraman, G., Rao, Y. S. and Kumar, V. (2008). *InSAR coherence measurement techniques for snow cover mapping in Himalayan region.* Paper presented at the Geoscience and Remote Sensing Symposium, 2008. IGARSS 2008. IEEE International.

Singh, G., Venkataraman, G., Yamaguchi, Y. and Park, S.-E. (2014). Capability Assessment of Fully Polarimetric ALOS–PALSAR Data for Discriminating Wet Snow From Other Scattering Types in Mountainous Regions. *IEEE Transactions on Geoscience and Remote Sensing, 52*(2), 1177-1196. doi: 10.1109/tgrs.2013.2248369

Singh, G., Yamaguchi, Y., Venktaraman, G. and Park, S.-E. (2011). *Potential assessment of SAR in compact and full polarimetry mode for snow detection.* Paper presented at the Geoscience and Remote Sensing Symposium (IGARSS), 2011 IEEE International.

Sinha, S., Jeganathan, C., Sharma, L. and Nathawat, M. (2015). A review of radar remote sensing for biomass estimation. *International Journal of Environmental Science and Technology, 12*(5), 1779-1792.

Small, D. (2011). Flattening gamma: Radiometric terrain correction for SAR imagery. *IEEE Transactions on Geoscience and Remote Sensing, 49*(8), 3081-3093.

Snapir, B., Momblanch, A., Jain, S., Waine, T. and Holman, I. P. (2019). A method for monthly mapping of wet and dry snow using Sentinel-1 and MODIS: Application to a Himalayan river basin. *International Journal of Applied Earth Observation and Geoinformation, 74*, 222-230.

Snehmani, Singh, M. K., Gupta, R. D., Bhardwaj, A. and Joshi, P. K. (2015). Remote sensing of mountain snow using active microwave sensors: a review. *Geocarto International, 30*(1), 1-27. doi: 10.1080/10106049.2014.883434

Sokolova, M., Japkowicz, N. and Szpakowicz, S. (2006). *Beyond accuracy, F-score and ROC: a family of discriminant measures for performance evaluation.* Paper presented at the Australasian joint conference on artificial intelligence.

Solberg, R., Amlien, J., Koren, H., Eikvil, L., Malnes, E. and Storvold, R. (2004). *Multi-sensor and time-series approaches for monitoring of snow parameters.* Paper presented at the Geoscience and Remote Sensing Symposium, 2004. IGARSS'04. Proceedings. 2004 IEEE International.

Solberg, R., Amlien, J., Koren, H., Eikvil, L., Malnes, E. and Storvold, R. (2005). *Multi-sensor/multitemporal approaches for snow cover area monitoring*. Paper presented at the EARSeL LIS-SIG Workshop, Berne.

Solberg, R., Huseby, R. B., Koren, H. and Malnes, E. (2008). *Time-series fusion of optical and SAR data for snow cover area mapping.* Paper presented at the Proceedings of 5th EARSeL LIS-SIG Workshop: Remote Sensing of Land Ice and Snow.

Solberg, R., Koren, H., Amlien, J., Malnes, E., Schuler, D. V. and Orthe, N. K. (2010). The development of new algorithms for remote sensing of snow conditions based on data from the catchment of Øvre Heimdalsvatn and the vicinity. *Hydrobiologia, 642*(1), 35-46. doi: 10.1007/s10750-010-0157-3

Solberg, R., Koren, H., Malnes, E., Haarpaintner, J. and Lauknes, I. (2006). *An approach for multisensor harmonization in snow cover area mapping.* Paper presented at the Geoscience and Remote Sensing Symposium, 2006. IGARSS 2006. IEEE International Conference on.

Solberg, R., Wangensteen, B., Metsämäki, S., Nagler, T., Sandner, R., Rott, H., Wiesmann, A., Luojus, K., Kangwa, M. and Pulliainen, J. (2010). GlobSnow snow extent product guide product version 1.0. *European Space Angency, Finland*.

Sorgeloos, P. (1986). *Brine shrimp Artemia in coastal saltworks: hydrobiological key to improved salt production and inexpensive source of food for vertically integrated aquaculture.* Paper presented at the Proc. International Meeting on" Saltworks Conversion for Aquaculture", Trapani, Italy.

Steffen, K. (1995). Surface energy exchange at the equilibrium line on the Greenland ice sheet during onset of melt. *Annals of Glaciology, 21*, 13-18.

Steiger, R. and Abegg, B. (2013). The sensitivity of Austrian ski areas to climate change. *Tourism Planning & Development, 10*(4), 480-493.

Stewart, I. T., Cayan, D. R. and Dettinger, M. D. (2004). Changes in snowmelt runoff timing in western North America under abusiness as usual'climate change scenario. *Climatic Change, 62*(1-3), 217-232.

Stieglitz, M., Déry, S., Romanovsky, V. and Osterkamp, T. (2003). The role of snow cover in the warming of arctic permafrost. *Geophysical Research Letters, 30*(13).

Stock, J. H. and Watson, M. W. (2015). *Introduction to econometrics*.

Stocker, T. F., Qin, D., Plattner, G., Tignor, M., Allen, S., Boschung, J., Nauels, A., Xia, Y., Bex, V. and Midgley, P. (2013). Contribution of working group I to the fifth assessment report of the intergovernmental panel on climate change. *Climate change*.

Storvold, R. and Malnes, E. (2004). *Snow covered area retrieval using ENVISAT ASAR wideswath in mountainous areas.* Paper presented at the Geoscience and Remote Sensing Symposium, 2004. IGARSS'04. Proceedings. 2004 IEEE International.

Storvold, R., Malnes, E., Larsen, Y., Høgda, K., Hamran, S., Mueller, K. and Langley, K. (2006). SAR remote sensing of snow parameters in norwegian areas—Current status and future perspective. *Journal of Electromagnetic Waves and Applications, 20*(13), 1751-1759.

Storvold, R., Malnes, E. and Lauknes, I. (2006). *Using ENVISAT ASAR wideswath data to retrieve snow covered area in mountainous regions.* Paper presented at the EARSeL eProceedings.

Strobl, C., Boulesteix, A.-L., Kneib, T., Augustin, T. and Zeileis, A. (2008). Conditional variable importance for random forests. *BMC bioinformatics, 9*(1), 307.

Strobl, C., Boulesteix, A.-L., Zeileis, A. and Hothorn, T. (2007). Bias in random forest variable importance measures: Illustrations, sources and a solution. *BMC bioinformatics, 8*(1), 25.

Strozzi, T. (1996). *Backscattering measurements of snowcovers at 5.3 and 35 ghz*: Universitat Bern, Fakultat der Philosophisch-naturwissenschaftlichen.

Strozzi, T. and Matzler, C. (1998). Backscattering measurements of alpine snowcovers at 5.3 and 35 GHz. *IEEE Transactions on Geoscience and Remote Sensing, 36*(3), 838-848.

Strozzi, T., Wegmuller, U. and Matzler, C. (1999). Mapping wet snowcovers with SAR interferometry. *International Journal of Remote Sensing, 20*(12), 2395-2403.

Strozzi, T., Wiesmann, A. and Mätzler, C. (1997). Active microwave signatures of snow covers at 5.3 and 35 GHz. *Radio Science, 32*(2), 479-495.

Suzuki, M., Sasaki, M., Murata, K., Fujino, K. and Takeda, K. (1995). *Evaluation of the data obtained by satellite-borne microwave sensor for snowpack observation.* Paper presented at the Geoscience and Remote Sensing Symposium, 1995. IGARSS'95.'Quantitative Remote Sensing for Science and Applications', International.

Szczypta, C., Gascoin, S., Houet, T., Hagolle, O., Dejoux, J.-F., Vigneau, C. and Fanise, P. (2015). Impact of climate and land cover changes on snow cover in a small Pyrenean catchment. *Journal of Hydrology, 521*, 84-99.

Taini, G., Pietropaolo, A. and Notarantonio, A. (2008). *Criteria and trade-offs for LEO orbit design.* Paper presented at the Aerospace Conference, 2008 IEEE.

Takala, M., Luojus, K., Pulliainen, J., Derksen, C., Lemmetyinen, J., Kärnä, J.-P., Koskinen, J. and Bojkov, B. (2011). Estimating northern hemisphere snow water equivalent for climate research through assimilation of space-borne radiometer data and ground-based measurements. *Remote Sensing of Environment, 115*(12), 3517-3529.

Tampellini, M. L. (2003, 29 Sep- 3 Oct 2003). *Monitoring of Glacier and Snow Cover Changes in Alpine Region using Remote Sensing Data.* Paper presented at the 54th International Astronautical Congress of the International Astronautical Federation (IAF), the International Academy of Astronautics and the International Institute of Space Law, Bremen, Germany.

Tan, B., Wu, F.-z., Yang, W.-q. and He, X.-h. (2014). Snow removal alters soil microbial biomass and enzyme activity in a Tibetan alpine forest. *Applied Soil Ecology, 76*, 34-41.

Tank, A. K., Wijngaard, J., Können, G., Böhm, R., Demarée, G., Gocheva, A., Mileta, M., Pashiardis, S., Hejkrlik, L. and Kern-Hansen, C. (2002). Daily dataset of 20th-century surface air temperature and precipitation series for the European Climate Assessment. *International Journal of Climatology, 22*(12), 1441-1453.

Tedesco, M. (2007). Snowmelt detection over the Greenland ice sheet from SSM/I brightness temperature daily variations. *Geophysical Research Letters, 34*(2).

Teja, C., Pokrovsky, I., Lecomte, N., Tomas, A., Burnham, K., Dietz, A., Franke, A., Gauthier, G., Karl-Otto, J. and Kidd, J. (2020). Arctic avian predators synchronise their spring migration with the northern progression of snowmelt. *Scientific Reports (Nature Publisher Group), 10*(1).

Teklehaimanot, H. D., Lipsitch, M., Teklehaimanot, A. and Schwartz, J. (2004). Weather-based prediction of Plasmodium falciparum malaria in epidemic-prone regions of Ethiopia I. Patterns of lagged weather effects reflect biological mechanisms. *Malaria journal, 3*(1), 41.

Terzago, S., Fratianni, S. and Cremonini, R. (2013). Winter precipitation in Western Italian Alps (1926–2010). *Meteorology and Atmospheric Physics, 119*(3-4), 125-136.

Thakur, P., Garg, V., Nikam, B., Singh, S., Chouksey, A., Dhote, P., Aggarwal, S., Chauhan, P. and Kumar, A. (2018). Snow Cover and Glacier Dynamics Study Using C-And L-Band SAR Datasets in Parts of North West Himalaya. *International Archives of the Photogrammetry, Remote Sensing & Spatial Information Sciences*.

Thakur, P. K., Aggarwal, S. P., Arun, G., Sood, S., Senthil Kumar, A., Mani, S. and Dobhal, D. P. (2016). Estimation of Snow Cover Area, Snow Physical Properties and Glacier Classification in Parts of Western Himalayas Using C-Band SAR Data. *Journal of the Indian Society of Remote Sensing, 45*(3), 525-539. doi: 10.1007/s12524-016-0609-y

Thakur, P. K., Garg, P. K., Aggarwal, S. P., Garg, R. D. and Mani, S. (2013). Snow Cover Area Mapping Using Synthetic Aperture Radar in Manali Watershed of Beas River in the Northwest Himalayas. *Journal of the Indian Society of Remote Sensing, 41*(4), 933-945. doi: 10.1007/s12524-012-0236-1

Torres, R., Lokas, S., Di Cosimo, G., Geudtner, D. and Bibby, D. (2017). *Sentinel 1 evolution: Sentinel-1C and-1D models.* Paper presented at the 2017 IEEE International Geoscience and Remote Sensing Symposium (IGARSS).

Tourian, M., Elmi, O., Chen, Q., Devaraju, B., Roohi, S. and Sneeuw, N. (2015). A spaceborne multisensor approach to monitor the desiccation of Lake Urmia in Iran. *Remote Sensing of Environment, 156*, 349-360.

Touzi, R. (2006). Target scattering decomposition in terms of roll-invariant target parameters. *IEEE Transactions on Geoscience and Remote Sensing, 45*(1), 73-84.

Touzi, R. (2007). Target scattering decomposition in terms of roll-invariant target parameters. *IEEE Transactions on Geoscience and Remote Sensing, 45*(1), 73-84.

Touzi, R., Boerner, W., Lee, J. and Lueneburg, E. (2004). A review of polarimetry in the context of synthetic aperture radar: concepts and information extraction. *Canadian Journal of Remote Sensing, 30*(3), 380-407.

Touzi, R., Lopes, A., Bruniquel, J. and Vachon, P. W. (1999). Coherence estimation for SAR imagery. *IEEE Transactions on Geoscience and Remote Sensing, 37*(1), 135-149.

Trofaier, A. M. (2018). Monitoring Snow & Ice from space. *Copernicus Pan European High Resolution Snow and Ice Monitoring Product -User consultation workshop*.

Tsai, Y.-L., Kim, J.-R., Save, H. and Lin, S.-Y. (2016). *Monitoring Groundwater Depletion of Northwest India using SAR Interferometry* Paper presented at the AGU Fall Meeting Abstracts.

Tsai, Y.-L. S., Dietz, A., Oppelt, N. and Kuenzer, C. (2019a). A Combination of PROBA-V/MODIS-based Products with Sentinel-1 SAR Data for Detecting Wet and Dry Snow Cover in Mountainous Areas. *Remote Sensing, 11*(16), 1904.

Tsai, Y.-L. S., Dietz, A., Oppelt, N. and Kuenzer, C. (2019). Remote Sensing of Snow Cover Using Spaceborne SAR: A Review. *Remote Sensing, 11*(12), 1456.

Tsai, Y.-L. S., Dietz, A., Oppelt, N. and Kuenzer, C. (2019b). Wet and Dry Snow Detection Using Sentinel-1 SAR Data for Mountainous Areas with a Machine Learning Technique. *Remote Sensing, 11*(8), 895.

Tsai, Y.-L. S., Lin, S.-Y., Kim, J.-R. and Choi, Y. (2019). Analysis of the seasonal velocity difference of the Greenland Russell glacier using multi-sensor data. *Terrestrial, Atmospheric & Oceanic Sciences, 30*(4).

Tsai, Y., Lin, S. and Kim, J. (2018). Tracking Greenland Russell Glacier Movements Using Pixel-offset Method. *Journal of Photogrammetry and Remote Sensing, 23*(3), 173-189. doi: 10.6574/JPRS.201809_23(3).0003

Tso, B. and Mather, P. (1999). Crop discrimination using multi-temporal SAR imagery. *International Journal of Remote Sensing, 20*(12), 2443-2460.

Uebbing, B., Kusche, J. and Forootan, E. (2014). Waveform retracking for improving level estimations from TOPEX/Poseidon, Jason-1, and Jason-2 altimetry observations over African lakes. *IEEE Transactions on Geoscience and Remote Sensing, 53*(4), 2211-2224.

Ulaby, F. T., Moore, R. K. and Fung, A. K. (1986). *Microwave Remote Sensing: Active and Passive: 3: From Theory to Applications*: Artech House.

Ulaby, F. T. and Stiles, W. H. (1980). The active and passive microwave response to snow parameters: 2. Water equivalent of dry snow. *Journal of Geophysical Research: Oceans, 85*(C2), 1045-1049.

UNEP. (2010). Africa Water Atlas. Division of Early Warning and Assessment (DEWA): United Nations Environment Programme (UNEP) Nairobi, Kenya.

Usami, N., Muhuri, A., Bhattacharya, A. and Hirose, A. (2016). PolSAR wet snow mapping with incidence angle information. *IEEE Geoscience and Remote Sensing Letters, 13*(12), 2029-2033.

Uszczyk, A., Grabiec, M., Laska, M., Kuhn, M. and Ignatiuk, D. (2019). Importance of snow as component of surface mass balance of Arctic glacier (Hansbreen, southern Spitsbergen).

Valenti, L., Small, D. and Meier, E. (2008). *Snow cover monitoring using multi-temporal Envisat/ASAR data.* Paper presented at the Proc. of 5th EARSeL LISSIG (Land, Ice, Snow) Workshop.

Valinia, A., Rao, Y. S., Uratsuka, S., Venkataraman, G., Singh, G. and Misra, T. (2006). ENVISAT-ASAR data analysis for snow cover mapping over Gangotri region. *Microwave Remote Sensing of the Atmosphere and Environment, 6410*, 641007. doi: 10.1117/12.693845

Van Zyl, J. J., Zebker, H. A. and Elachi, C. (1987). Imaging radar polarization signatures: Theory and observation. *Radio Science, 22*(04), 529-543.

Vander Jagt, B. J., Durand, M. T., Margulis, S. A., Kim, E. J. and Molotch, N. P. (2015). On the characterization of vegetation transmissivity using LAI for application in passive microwave remote sensing of snowpack. *Remote Sensing of Environment, 156*, 310-321.

Vaughan, D. G., Comiso, J. C., Allison, I., Carrasco, J., Kaser, G., Kwok, R., Mote, P., Murray, T., Paul, F. and Ren, J. (2013). Observations: cryosphere. *Climate change, 2103*, 317-382.

Venkataraman, G., Singh, G. and Kumar, V. (2008). *Snow cover area monitoring using multi-temporal TerraSAR-X data.* Paper presented at the Third TerraSAR-X Science Team Meeting, DLR, Germany.

Venkataraman, G., Singh, G. and Yamaguchi, Y. (2010). *Fully polarimetric ALOS PALSAR data applications for snow and ice studies.* Paper presented at the Geoscience and Remote Sensing Symposium (IGARSS), 2010 IEEE International.

Venkataraman, G., Singh, G., Yamaguchi, Y. and Park, S.-E. (2011). *Methodology development for snow discrimination using SAR polarimetry techniques.* Paper presented at the Synthetic Aperture Radar (APSAR), 2011 3rd International Asia-Pacific Conference on.

Ventura, B., Schellenberger, T., Notarnicola, C., Zebisch, M., Maddalena, V., Ratti, R., Tampellini, L. and Du, J. (2011). *Analysis of snow changes in alpine regions with X-band data: electromagnetic analysis and snow cover mapping.* Paper presented at the SAR Image Analysis, Modeling, and Techniques XI.

Ventura, B., Schellenberger, T., Notarnicola, C., Zebisch, M., Nagler, T., Rott, H., Maddalena, V., Ratti, R. and Tampellini, L. (2011). *Snow cover monitoring in alpine regions with cosmo-skymed images by using a multitemporal approach and depolarization ratio.* Paper presented at the Analysis of Multi-temporal Remote Sensing Images (Multi-Temp), 2011 6th International Workshop on the.

Virtanen, R., Dirnböck, T., Dullinger, S., Grabherr, G., Pauli, H., Staudinger, M. and Villar, L. (2003). Patterns in the plant species richness of European high mountain vegetation *Alpine biodiversity in Europe* (pp. 149-172): Springer.

Voigt, T., Füssel, H.-M., Gärtner-Roer, I., Huggel, C., Marty, C. and Zemp, M. (2010). Impacts of climate change on snow, ice, and permafrost in Europe: Observed trends, future projections, and socio-economic relevance. *ETC/ACC Technical Paper, 13*, 1-117.

Voss, K. A., Famiglietti, J. S., Lo, M., De Linage, C., Rodell, M. and Swenson, S. C. (2013). Groundwater depletion in the Middle East from GRACE with implications for transboundary water management in the Tigris-Euphrates-Western Iran region. *Water Resources Research, 49*(2), 904-914.

Walker, D., Halfpenny, J. C., Walker, M. D. and Wessman, C. A. (1993). Long-term studies of snow-vegetation interactions. *BioScience, 43*(5), 287-301.

Wan, Z. (2007). Collection-5 MODIS land surface temperature products users' guide. *ICESS, University of California, Santa Barbara*.

Wan, Z. (2008). New refinements and validation of the MODIS land-surface temperature/emissivity products. *Remote Sensing of Environment, 112*(1), 59-74.

Wan, Z., Hook, S. and Hulley, G. (2015). MOD11A1 MODIS/Terra Land Surface Temperature. *Emissivity Daily L3 Global 1km SIN Grid, 6*.

Wang, H., Chu, Y., Huang, Z., Hwang, C. and Chao, N. (2019). Robust, Long-term Lake Level Change from Multiple Satellite Altimeters in Tibet: Observing the Rapid Rise of Ngangzi Co over a New Wetland. *Remote Sensing, 11*(5), 558.

Wang, J. and Li, S. (2006). Effect of climatic change on snowmelt runoffs in mountainous regions of inland rivers in Northwestern China. *Science in China Series D: Earth Sciences, 49*(8), 881-888.

Wang, Q., Fan, X. and Wang, M. (2014). Recent warming amplification over high elevation regions across the globe. *Climate Dynamics, 43*(1-2), 87-101.

Wang, S., Yang, B., Zhou, Y., Wang, F., Zhang, R. and Zhao, Q. (2018). Snow Cover Mapping and Ice Avalanche Monitoring from the Satellite Data of the Sentinels. *International Archives of the Photogrammetry, Remote Sensing & Spatial Information Sciences, 42*(3).

Wang, Y., Wang, L., Li, H., Yang, Y. and Yang, T. (2015). Assessment of Snow Status Changes Using L-HH Temporal-Coherence Components at Mt. Dagu, China. *Remote Sensing, 7*(12), 11602-11620. doi: 10.3390/rs70911602

Wangchuk, S., Bolch, T. and Zawadzki, J. (2019). Towards automated mapping and monitoring of potentially dangerous glacial lakes in Bhutan Himalaya using Sentinel-1 Synthetic Aperture Radar data. *International Journal of Remote Sensing, 40*(12), 4642-4667.

Warren, S. G. (1982). Optical properties of snow. *Reviews of geophysics, 20*(1), 67-89.

Water, U. (2018). Progress on water-related ecosystems: Piloting the monitoring methodology and initial findings for SDG indicator 6.6. 1. *UN Environment on behalf of UN Water ISBN*(978-92), 807-3712.

Water, U. (2019). World Water Development Report.

Webster, M., Gerland, S., Holland, M., Hunke, E., Kwok, R., Lecomte, O., Massom, R., Perovich, D. and Sturm, M. (2018). Snow in the changing sea-ice systems. *Nature Climate Change, 8*(11), 946-953.

Weingartner, R., Barben, M. and Spreafico, M. (2003). Floods in mountain areas—an overview based on examples from Switzerland. *Journal of Hydrology, 282*(1-4), 10-24.

Wendleder, A., Dietz, A. J. and Schork, K. (2018). *Mapping Snow Cover Extent Using Optical and SAR Data.* Paper presented at the IGARSS 2018-2018 IEEE International Geoscience and Remote Sensing Symposium.

Wendleder, A., Heilig, A., Schmitt, A. and Mayer, C. (2015). *Monitoring of Wet Snow and Accumulations at High Alpine Glaciers Using Radar Technologies.* Paper presented at the ISPRS - International Archives of the Photogrammetry, Remote Sensing and Spatial Information Sciences.

Wiley, C. A. (1985). Synthetic aperture radars. *IEEE Transactions on Aerospace and Electronic Systems*(3), 440-443.

Winther, J.-G. and Hall, D. K. (1999). Satellite-derived snow coverage related to hydropower production in Norway: Present and future. *International Journal of Remote Sensing, 20*(15-16), 2991-3008.

Woo, M.-k. (1980). Hydrology of a small lake in the Canadian High Arctic. *Arctic and Alpine Research, 12*(2), 227-235.

Wooldridge, J. (2000). Basic regression analysis with time series data. *Wooldridge JM. Introductory econometrics: a modern approach. Cincinnati, Ohio: South-Western College Publishing*.

Wu, X., Che, T., Li, X., Wang, N. and Yang, X. (2018). Slower snowmelt in spring along with climate warming across the Northern Hemisphere. *Geophysical Research Letters, 45*(22), 12,331-312,339.

Xiao, X., Zhang, Q., Boles, S., Rawlins, M. and Moore III, B. (2004). Mapping snow cover in the pan-Arctic zone, using multi-year (1998-2001) images from optical VEGETATION sensor. *International Journal of Remote Sensing, 25*(24), 5731-5744.

Xiao, Z. and Duan, A. (2016). Impacts of Tibetan Plateau snow cover on the interannual variability of the East Asian summer monsoon. *Journal of Climate, 29*(23), 8495-8514.

Xu, H. (2006). Modification of normalised difference water index (NDWI) to enhance open water features in remotely sensed imagery. *International Journal of Remote Sensing, 27*(14), 3025-3033.

Yamaguchi, Y., Moriyama, T., Ishido, M. and Yamada, H. (2005). Four-component scattering model for polarimetric SAR image decomposition. *IEEE Transactions on Geoscience and Remote Sensing, 43*(8), 1699-1706.

Yamaguchi, Y., Yajima, Y. and Yamada, H. (2006). A four-component decomposition of POLSAR images based on the coherency matrix. *IEEE Geoscience and Remote Sensing Letters, 3*(3), 292-296.

Yang, J., Ou, C.-Q., Ding, Y., Zhou, Y.-X. and Chen, P.-Y. (2012). Daily temperature and mortality: a study of distributed lag non-linear effect and effect modification in Guangzhou. *Environmental Health, 11*(1), 63.

Yang, S. (1996). ENSO–snow–monsoon associations and seasonal–interannual predictions. *International Journal of Climatology: A Journal of the Royal Meteorological Society, 16*(2), 125-134.

Yang, Y., Leppäranta, M., Cheng, B. and Li, Z. (2012). Numerical modelling of snow and ice thicknesses in Lake Vanajavesi, Finland. *Tellus A: Dynamic Meteorology and Oceanography, 64*(1), 17202.

Yuan, C., Gong, P., Zhang, H., Guo, H. and Pan, B. (2017). Monitoring water level changes from retracked Jason-2 altimetry data: a case study in the Yangtze River, China. *Remote Sensing Letters, 8*(5), 399-408.

Zarghami, M. (2011). Effective watershed management; case study of Urmia Lake, Iran. *Lake and Reservoir Management, 27*(1), 87-94.

Zebker, H. A. and Goldstein, R. M. (1986). Topographic mapping from interferometric synthetic aperture radar observations. *Journal of Geophysical Research: Solid Earth, 91*(B5), 4993-4999.

Zebker, H. A. and Villasenor, J. (1992). Decorrelation in interferometric radar echoes. *IEEE Transactions on Geoscience and Remote Sensing, 30*(5), 950-959.

Zhang, L., Zou, B., Cai, H. and Zhang, Y. (2008). Multiple-component scattering model for polarimetric SAR image decomposition. *IEEE Geoscience and Remote Sensing Letters, 5*(4), 603-607.

Zhang, T. (2005). Influence of the seasonal snow cover on the ground thermal regime: An overview. *Reviews of geophysics, 43*(4).

Zhao, J.-y., Chen, J., Wu, Q.-b. and Hou, X. (2018). Snow cover influences the thermal regime of active layer in Urumqi River Source, Tianshan Mountains, China. *Journal of Mountain Science, 15*(12), 2622-2636.

Zhao, X., Chen, F., Feng, Z., Li, X. and Zhou, X.-H. (2014). The temporal lagged association between meteorological factors and malaria in 30 counties in south-west China: a multilevel distributed lag non-linear analysis. *Malaria journal, 13*(1), 57.

Zhen, L., Lei, H., Quan, C. and Bang-sen, T. (2012). Glacier Snow Line Detection on a Polarimetric SAR Image. *IEEE Geoscience and Remote Sensing Letters, 9*(4), 584-588. doi: 10.1109/lgrs.2011.2175697

Zhou, C. and Zheng, L. (2017). Mapping Radar Glacier Zones and Dry Snow Line in the Antarctic Peninsula Using Sentinel-1 Images. *Remote Sensing, 9*(12), 1171. doi: 10.3390/rs9111171

Statement of authorship

I hereby certify that I have authored this Dissertation entitled “Monitoring Snow Cover and Snowmelt Dynamics and Assessing their Influences on Inland Water Resources” independently and without undue assistance from third parties. No other than the resources and references indicated in this thesis have been used. I am aware that violations of this declaration may lead to subsequent withdrawal of the degree. The work has not previously been presented in the same or a similar format to another examination body in Germany or abroad.

I confirm that I acknowledge the doctoral regulations of the Faculty of Mathematics and Natural Sciences of Kiel University.

München, 2021
Ya-Lun S. Tsai

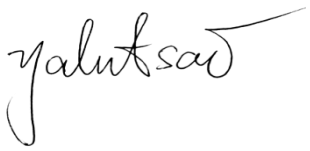

Eidesstattliche Erklärung

I hereby certify that apart from the supervisor's guidance, the content and design of this thesis entitled “Monitoring Snow Cover and Snowmelt Dynamics and Assessing their Influences on Inland Water Resources” is all my own work and without undue assistance from third parties. No other than the resources and references indicated in this thesis have been used. This thesis has not been submitted either partially or wholly as part of a doctoral degree to another examining body. This thesis has not been published or submitted for publication. No academic degree has ever been withdrawn. I confirm that this thesis has been prepared subject to the Rules of Good Scientific Practice of the German Research Foundation and doctoral regulations of the Faculty of Mathematics and Natural Sciences of Kiel University.

München, 2021
Ya-Lun S. Tsai